J-PARC

ANNUAL REPORT 2015

Vol.2: Materials and Life Science Experimental Facility

MLF ANNUAL REPORT

J-PARC MLF
Materials and Life Science Division
J-PARC Center
http://j-parc.jp/MatLife/en/

J-PARC was jointly constructed and is now operated by the High Energy Accelerator Research Organization (KEK) and the Japan Atomic Energy Agency (JAEA).

CROSS
Comprehensive Research Organization for Science and Society
http://www.cross-tokai.jp/

J-PARC 17-01

Preface

Toshiji Kanaya
Division Head of Materials and Life Science Division, MLF

In this introduction, we will outline the J-PARC MLF activities in 2015. The user operation in 2015A started on April 19th, 2015, with a beam power of 500 kW. However, after an incident with the target vessel on April 30th, the user program had to be halted. To accommodate the experiments that were not conducted due to the incident, we decided to cancel the call for proposals for the 2015B period. We investigated the cause in detail, and concluded that a part of the welded surface between two steel plates was not completed properly during the fabrication process, which caused a crack and repetitive thermal stress during the operating period. We changed the welding method for the shroud of a spare target vessel, and replaced the target vessel with a new one. On October 27th, the neutron production for the user program resumed with a 500-kW proton beam. However, the user operation stopped on November 20th, due to an unexpected problem with the target vessel. It occurred inside the target shroud and was different from what happened in April. We should note that the problems with the target did not cause any leakage of radioactive materials.

After the trouble in November, the users insisted strongly that we resume the MLF operation, so we decided to use an alternative spare target with a mechanically robust structure but without a helium gas bubbling system that is needed for a stable operation with a power above 300 kW. After replacing the target, on February 20th, we resumed the user operation with a beam power of 200 kW. At the same time, the performance of the helium refrigerator of the cryogenic hydrogen circulation system for the moderators deteriorated. Then, after a 3-week user operating period, we stopped the user operation for maintenance of the refrigerator.

We continue our efforts to improve the robustness of the target vessel by eliminating welds and/or bolts as much as possible. On February 22nd, an international design review assessed the adequacy of the improvements in the design of the target vessel.

The operational efficiency in MLF finally reached 35.1% in 2015. The number of unique users was 628 (559 for neutron, 69 for muon), and the number of proposals for general use was 305 (268 for neutron, 37 for muon), about half of the numbers for a normal year because of the cancellation of the call for proposals in 2015B. The fraction of industrial use was 16.4% of the approved proposals.

In 2015, we conducted many activities in MLF, such as workshops and schools. From May 31st to June 3rd, the 7th workshop on NEUtron WAVElength-dependent imaging (NEUWAVE7) was held in the Ibaraki Prefectural Culture Center in Mito. The 1st Japan-Korean Joint Workshop on Polarized Neutron Reflectometry also took place at J-PARC on July 30th, 2015. From December 1st to 5th, the joint school of the 7th AONSA Neutron School and the 3rd MLF School was held. The school included 41 young researchers and graduate students from Japan, Korea, Australia, Indonesia, India, China, Taiwan, Malaysia, the United States, and Iran. Quantum Beam Science Festa 2015, which included the 7th MLF Symposium and the 33rd PF Symposium, was held on March 15th and 16th at Epochal Tsukuba.

The High Energy Accelerator Research Organization (KEK), the Japan Atomic Energy Agency (JAEA), and ANSTO signed an arrangement for cooperation in the field of neutron science at Manly, Sydney, on July 20th at the opening of the 2nd Asia-Oceania Conference on Neutron Scattering. The 1st workshop for J-PARC/ANSTO MOU collaboration was held at J-PARC.

As for the Muon Science Facility (MUSE) in MLF, the Muon Section staff focused their efforts into reinvestigation of the beamline components and instruments to ensure the safety of the resuming operations of the D-, U-, and S-lines after the fire incident in the MUSE. Finally, the MUSE was cleared for restarting the operation.

The superconducting solenoid coils (SSC) and their cooling system were partially damaged in the Great East Japan Earthquake in 2011 and fixed to operate temporarily before the complete restoration. During the shutdown period in the summer of 2015, the superconducting solenoid coils (SSC) on the D-line were replaced. Good news for MUSE in November 2015 were the successful delivery of the first surface muon beam to the S1 area at the end of new S-line and the generation of the first ultra-slow muon in the U-line.

We will do our best to ensure stable operations in J-PARC MLF and produce fruitful results in science and industry.

Preface

Hideaki Yokomizo
Director, CROSS-Tokai

Five years have passed since CROSS-Tokai commenced operations in support of the user program of the Public Beamlines at Materials and Life Science Experimental Facility of J-PARC (J-PARC MLF). Pursuant to the Provision of the "Act on the Promotion of Public Utilization of the Specific Advanced Large Research Facilities", under which CROSS was appointed a Registered Institution for Facilities Use Promotion, we have been fully engaged in facility promotion activities, such as operating a fair and open proposal selection system for the MLF Public Beamlines, providing high-quality user support and promoting facility utilization for both academic and industrial researchers.

In 2015, CROSS-Tokai supported the user programs with seven fully-operational Public Beamlines: BL01 *4SEASONS*, BL02 *DNA*, BL11 *PLANET*, BL15 *TAIKAN*, BL17 *SHARAKU,* BL18 *SENJU and* BL22 *RADEN*. In this period, we accomplished a 40-day 500 kW beam-power supply for user experiments. However, the user operations were interrupted twice by cooling-water leakage from the neutron target vessel. The user operation was resumed on February 20th using the spare target vessel. The beam-power had to be reduced to 200 kW, though, because it had no protection from the pitting damage on the beam window.

Special programs to promote facility utilization, such as Trial Use and Elementary Strategy Initiative, proceeded successfully in 2015. Trial Use is a program promoting the use of neutrons by first-time or novice users from both the industrial and academic sectors. Elementary Strategy Initiative is an integrated strategic research program of the Japanese Government that promotes the development of innovative materials and alternative technologies in the research areas of permanent magnets, catalysis and batteries, and electronic and structural materials. Complementary Use is a program that encourages and facilitates the complementary and collaborative use of pulsed neutrons (J-PARC MLF), synchrotron radiation (SPring-8) and supercomputer (K computer).

I hope this Annual Report would serve as a useful information source for anyone wishing to know more about the current status of MLF, its recent scientific achievements, the technical R&D projects that support the science program, and the operational details of our facility.

On behalf of the team at CROSS-Tokai, I extend a warm welcome to all researchers who wish to use the Public Beamlines at J-PARC MLF.

Neutron Science and Technology Center, Comprehensive Research Organization for Science and Society
www.cross-tokai.jp

Contents

Preface

Research and Development Highlights

Neutron Source

Neutron Science

Muon Scinece

MLF Safety

MLF Operations in 2015

Organization Chart

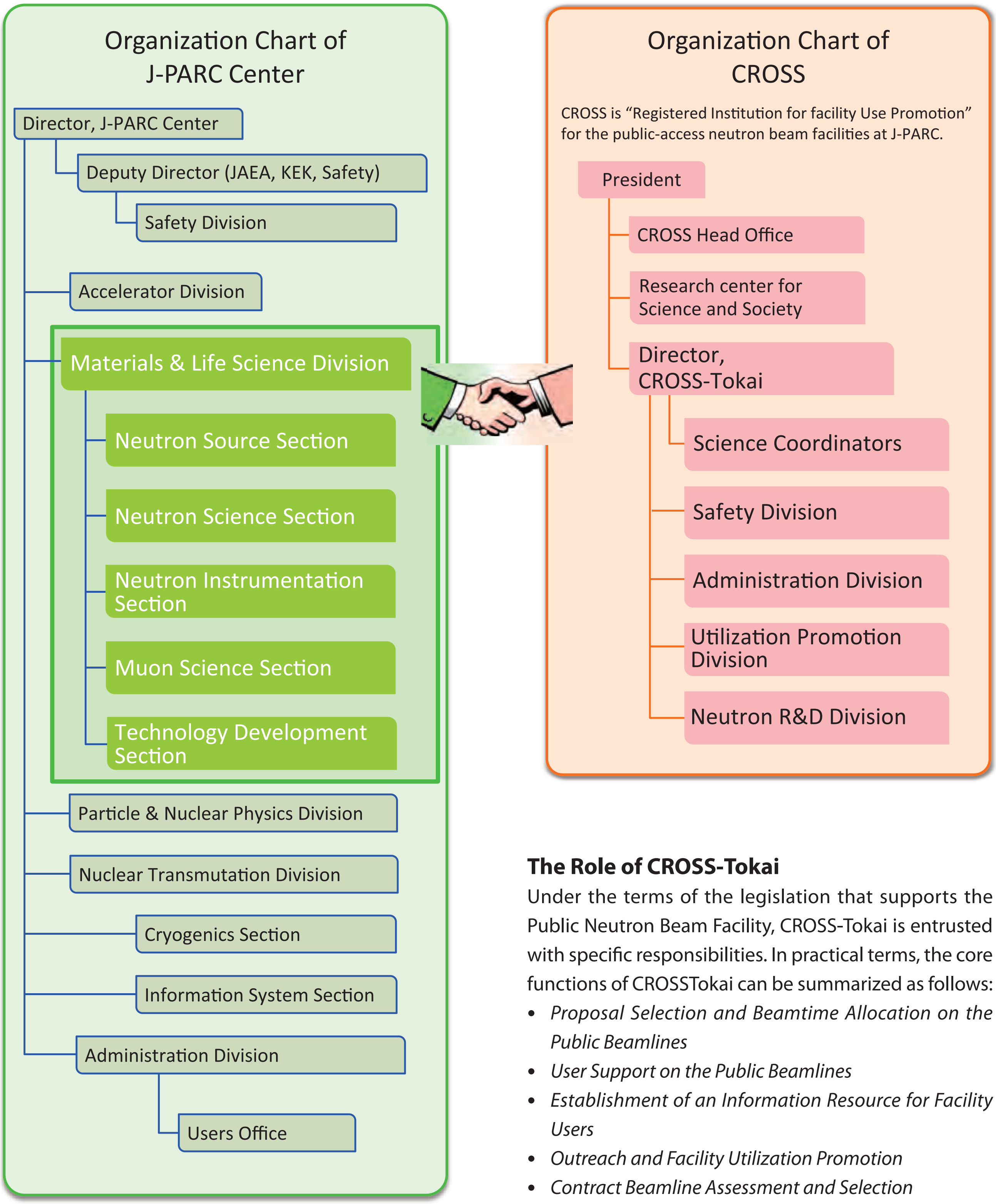

Organization Chart of J-PARC Center

- Director, J-PARC Center
  - Deputy Director (JAEA, KEK, Safety)
    - Safety Division
  - Accelerator Division
  - Materials & Life Science Division
    - Neutron Source Section
    - Neutron Science Section
    - Neutron Instrumentation Section
    - Muon Science Section
    - Technology Development Section
  - Particle & Nuclear Physics Division
  - Nuclear Transmutation Division
  - Cryogenics Section
  - Information System Section
  - Administration Division
    - Users Office

Organization Chart of CROSS

CROSS is “Registered Institution for facility Use Promotion” for the public-access neutron beam facilities at J-PARC.

- President
  - CROSS Head Office
  - Research center for Science and Society
  - Director, CROSS-Tokai
    - Science Coordinators
    - Safety Division
    - Administration Division
    - Utilization Promotion Division
    - Neutron R&D Division

The Role of CROSS-Tokai

Under the terms of the legislation that supports the Public Neutron Beam Facility, CROSS-Tokai is entrusted with specific responsibilities. In practical terms, the core functions of CROSSTokai can be summarized as follows:

- *Proposal Selection and Beamtime Allocation on the Public Beamlines*
- *User Support on the Public Beamlines*
- *Establishment of an Information Resource for Facility Users*
- *Outreach and Facility Utilization Promotion*
- *Contract Beamline Assessment and Selection*

J-PARC Map

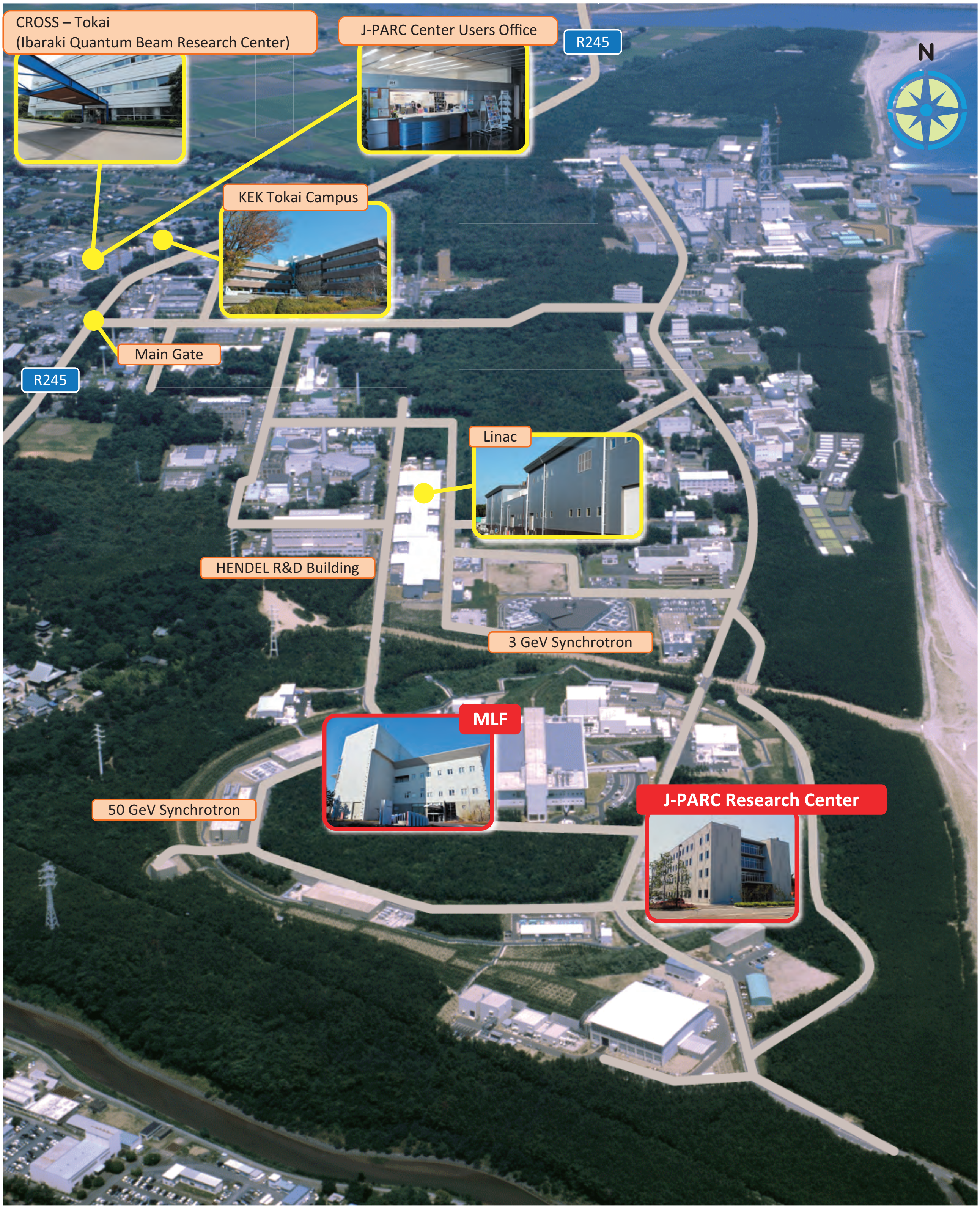
CROSS – Tokai
(Ibaraki Quantum Beam Research Center)
J-PARC Center Users Office
R245
N
KEK Tokai Campus
Main Gate
R245
Linac
HENDEL R&D Building
3 GeV Synchrotron
MLF
J-PARC Research Center
50 GeV Synchrotron

Muon and Neutron Instruments

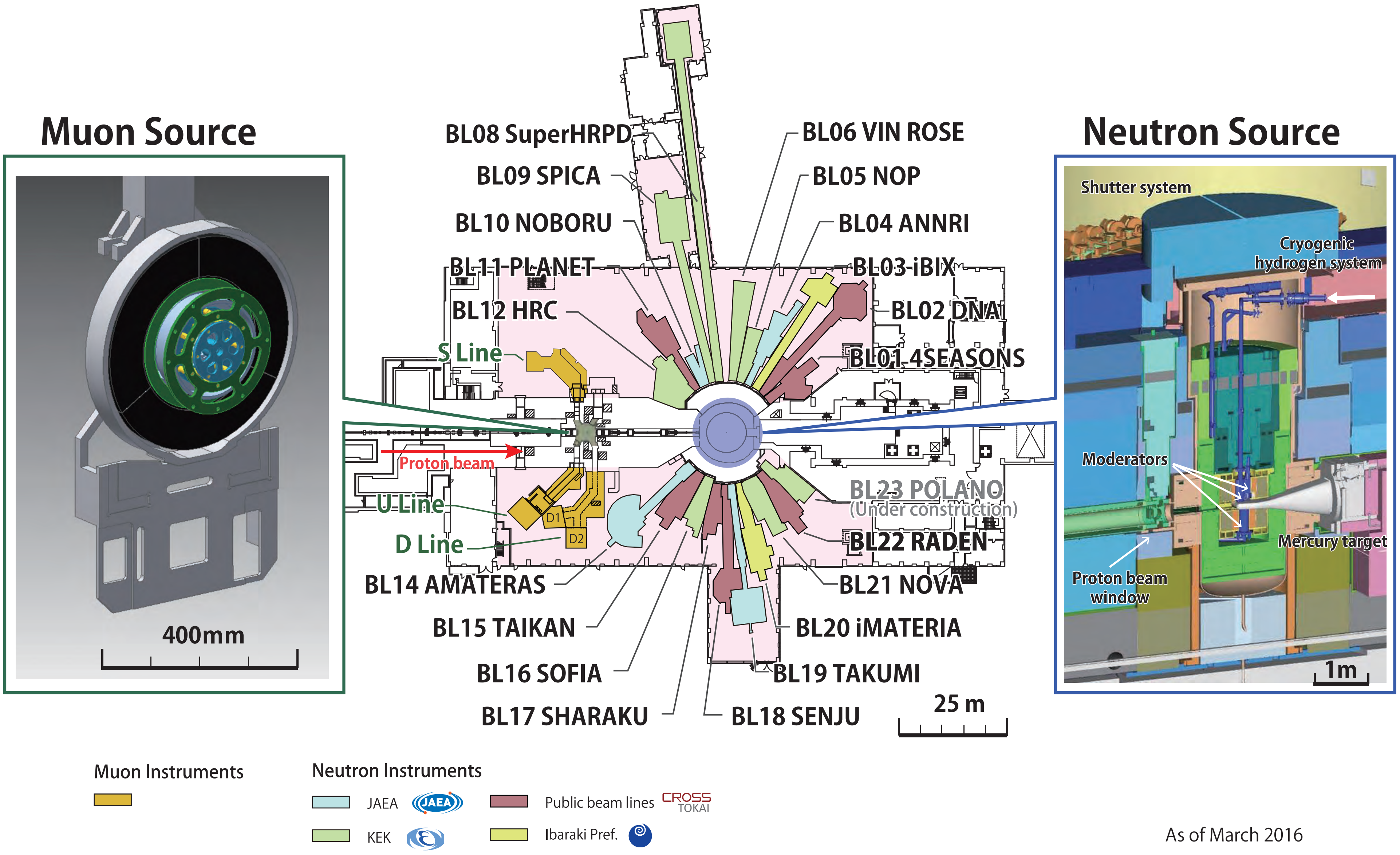

As of March 2016

Research and Development Highlights

Synthesis, Structure, and Pressure-Induced Polymerization of $Li_3Fe(CN)_6$ Accompanied with Enhanced Conductivity

1. Introduction

Pressure-induced polymerization (PIP) of alkynes and nitriles produces polymers with conjugated double bonds, which is a novel method to synthesize electrical conductive materials [1]. Metal-carbon network can be built using this method, with functional components, like metallic cations, embedded in the conductive matrix. However, the required pressure for polymerization of most metal cyanides and acetylides is usually tens of gigapascals [1b, 2, 3], which is too high for industrial processes. Thus, it is important to investigate the mechanism of the PIP and find low-pressure reaction routes leading to the formation of these promising materials.

A promising method is to use smaller cations to decrease the distance between the monomers. In this work, by using Li^+, we successfully compressed the cyanide ions to react at around 1 GPa and polymerize irreversibly above 5 GPa. Our crystallographic investigation suggests that the PIP of $Li_3Fe(CN)_6$ starts from the dimerization inside $Fe(CN)_6^{3-}$. This reaction can be realized on an industrial scale, and is a practical and potentially scalable synthetic approach to prepare carbon-based functional conductors.

2. Experimental section

$Li_3Fe(CN)_6$ was synthesized by the reaction between $Ag_3Fe(CN)_6$ and LiCl in aqueous solution. The yellow product [$Li_3Fe(CN)_6{\cdot}2H_2O$] crystallized from the solution was heated at ~130°C in a glovebox to obtain the anhydrous $Li_3Fe(CN)_6$. ^7Li and deuterated water were used in the synthesis of the sample for neutron experiments. X-ray diffraction patterns of $Li_3Fe(CN)_6$ were collected on a lab X-ray diffractometer (XRD) with a Bragg-Brentano geometry. Neutron diffraction patterns at ambient pressure were collected in a sealed vanadium can at beamline 3 (SNAP), Spallation Neutron Source, Oak Ridge National Lab (ORNL), and beamline 11 (PLANET) [4], Material and Life Science Experimental Facility, Japan Proton Accelerator Research Complex (J-PARC). In situ high-pressure neutron diffraction data were collected on the 6-axis press [5] at PLANET, J-PARC. The Raman data were collected on a laboratory-made spectrometer equipped with a second-harmonic Nd:YAG laser (operating at 532 nm) in a backscattering geometry for excitation and signal collection. In situ high-pressure XRD data were collected at 16-ID-B at Advanced Photon Source (APS), Argonne National Laboratory. In situ impedance spectroscopy was performed on an alternating current impedance spectroscopy system based on Zahner analyzer IM6 at the Center for Nanophase Materials Sciences, ORNL. The recovered polymerized $Li_3Fe(CN)_6$ was obtained by using the VX3 Paris–Edinburgh (PE) cell with sintered diamond anvils at SNAP [6], with precalibrated pressure. The samples are loaded in 2 mm quartz capillaries for the neutron total scattering experiment at Nanoscale Ordered Materials Diffractometer (NOMAD), SNS [7]. Data presented were reduced by the autoreduction program of NOMAD with $Q_{max} = 31.4$ Å^{-1} and convoluted by Lorch function.

3. Determination of Crystal Structure

The crystal structures of $Li_3Fe(CN)_6$ were determined ab initio by X-ray and neutron diffraction. The structural model of $Li_3Fe(CN)_6$ is shown in Fig. 1. $Fe(CN)_6^{3-}$ in

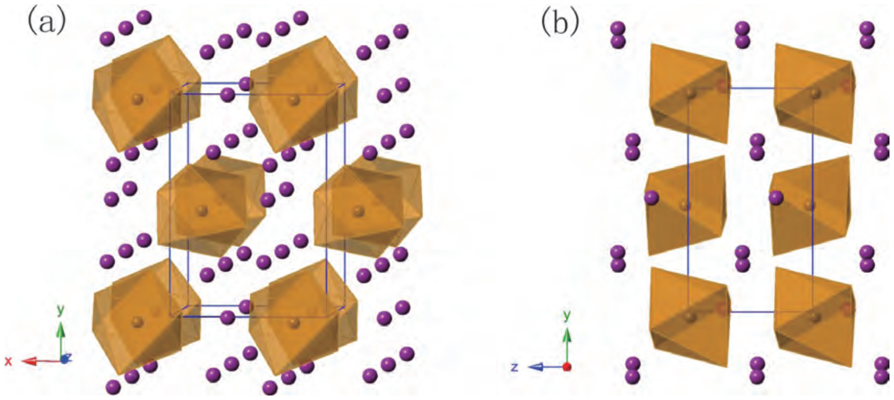

Figure 1. Crystal structure of $Li_3Fe(CN)_6$, viewed along (a) approximately [001] and (b) [100]. The brown octahedron stands for $Fe(CN)_6^{3-}$and the purple atom stands for Li^+; C and N are omitted for clarity.

$Li_3Fe(CN)_6$ forms close-packed layers arranged approximately perpendicularly to one another. Li^+ are located mainly between the $Fe(CN)_6^{3-}$ layers and are too small to completely separate $Fe(CN)_6^{3-}$. The nearest N-N distance between neighbored $Fe(CN)_6^{3-}$ in $Li_3Fe(CN)_6$ is around 3.2 Å, approximately the sum of van der Waals radii of nitrogen atom (3.1 Å) [8]. This indicates that in $Li_3Fe(CN)_6$ the N atoms of the neighboring $Fe(CN)_6^{3-}$ are almost touching each other directly. This short distance between $Fe(CN)_6^{3-}$ groups will facilitate significantly the inter group addition reactions.

4. Structural Transition under High Pressure

The crystal structure of $Li_3Fe(CN)_6$ under external pressure was studied by in situ neutron diffraction, and the structure model is shown in Fig. 2. The $Fe(CN)_6^{3-}$ complex anions are severely distorted, while their stacking remains nearly unchanged. This suggests that the Fe-C-N and the C-Fe-C connections are the easiest to be distorted against the electrostatic repulsion between $Fe(CN)_6^{3-}$. The distortion may promote reaction between the neighboring cyanide ions that coordinate to the same Fe^{3+}, as reported in our previous $K_3Fe(CN)_6$ paper [9].

To study the phase transitions above 1 GPa, an in situ synchrotron XRD experiment was performed with neon as the pressure medium. During the experiment, three phase transitions have been found at around 1, 5, and 10 GPa. The features of the XRD patterns were almost the same through these transitions, which suggests the crystal structure was not reconstructed, and the transitions were most likely induced by local reactions.

5. Reaction between Cyanides

The phase transitions are attributed to the reaction between cyanide anions, which can be identified by Raman spectroscopy. The intensity of the CN stretching mode, ν(CN), decreases above 1 GPa and remains unchanged up to 5 GPa, above which it disappears in the background. These two phase transitions are consistent with the transitions uncovered by diffraction experiments. The weakening of the ν(CN) peak above 1 GPa may be attributed to the reaction between two CN groups that coordinate to the same Fe(III), as suggested in the neutron diffraction results.

Strong evidence supporting the reaction between CN^- comes from neutron PDF analysis. G(r) patterns of $Li_3Fe(CN)_6$ recovered from high pressure are shown in Fig. 3. The peak at 1.1 Å corresponds to the C-N triple bond (Fig. 3a). Its intensity decreases above 5 GPa with increasing pressure up to above 10 GPa. A shoulder in the range 1.3–1.5 Å rises simultaneously, which corresponds to the formation of conjugated C=N bonds. Conjugated C=N bonds are also evidenced by the peak rising at around 2.4 Å. This is the distance between the atom and its next nearest neighbors in the sp^2-conjugated chain with bond angles $\alpha = 120°$ (Fig. 3b). This evidence clearly verifies that the cyanide anions react with each other and the reaction is partially irreversible.

The conductivity of $Li_3Fe(CN)_6$ was enhanced by ~10^3 fold when external pressure was applied. This is caused mainly by the approaching and bonding between the cyanide anions. The conductivity reaches a local maximum at around 5 GPa, which is attributed to the beginning of the second phase transition.

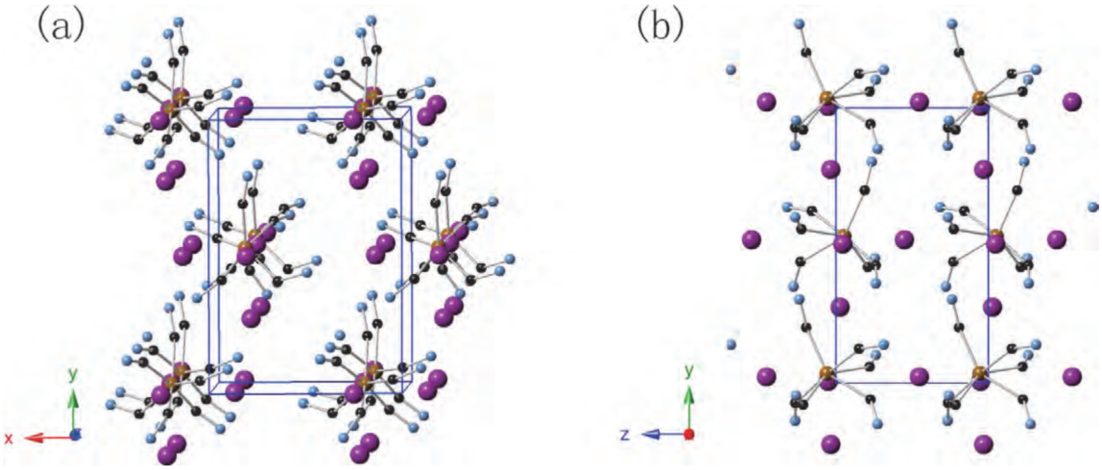

Figure 2. Crystal structure of $Li_3Fe(CN)_6$ at 0.8 GPa, viewed along (a) approximately [001] and (b) [100]. Brown, black, blue, and purple atoms represent Fe, C, N, and Li, respectively.

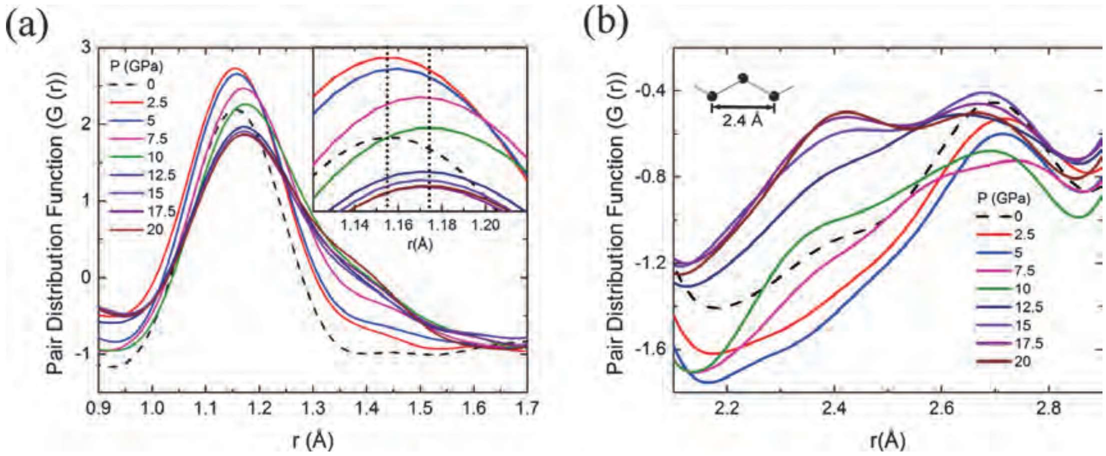

Figure 3. Neutron PDF patterns [G(r)] of $Li_3Fe(CN)_6$ recovered from high pressure. PDF plots with (a) r = 0.9–1.7 Å and (b) r = 1.9–2.9 Å are shown.

6. conclusion

In conclusion, we designed and synthesized anhydrous $Li_3Fe(CN)_6$, determined its crystal structure using neutron diffraction techniques, and investigated its PIP and phase behavior under external pressure up to ~20 GPa. The crystal structure of $Li_3Fe(CN)_6$ under external pressure was determined. $Fe(CN)_6^{3-}$ is highly distorted and two of the cyano groups coordinating on the same Fe(III) cation are expected to get bonded to each other. The PIP of the cyano groups is irreversible when they are compressed to above 5 GPa and is believed to be responsible for the enhancement of the conductivity.

Adapted with permission from ref 10. Copyright 2015 American Chemical Society.

References

[1] (a) Aoki, K.; Kakudate, Y.; *et al.*, Synth. Met. 1989, 28, D91-D98.
(b) Li, Y. L.; Luo, W.; *et al.*, Natl. Acad. Sci. U. S.A. 2013, 110, 9289-9294.

[2] Nylen, J.; Konar, S.; *et al.*, J. Chem. Phys. 2012, 137, No. 224507.

[3] (a) Kulkarni, A.; Doll, K.; *et al.*, J. Phys. Chem.B 2010, 114, 15573-15581.
(b) Heckathorn, J. W.; Kruger, M. B.; *et al.*, Phys. Rev. B: Condens. Matter Mater. Phys. 1999,60, 979-983.
(c) Chen, X. Q.; Fu, C. L.; Franchini, C. J. Phys.:Condens. Matter 2010, 22, No. 292201.

[4] Hattori, T.; Sano-Furukawa, A.; *et al.*, Nucl. Instrum. Methods Phys. Res., Sect.A 2015, 780, 55-67.

[5] Sano-Furukawa, A.; Hattori, T.; *et al.*, Rev. Sci. Instrum. 2014,85, No. 113905.

[6] Klotz, S.; Hamel, G.; Frelat, J. High Pressure Res. 2004, 24, 219-223.

[7] Neuefeind, J.; Feygenson, M.; *et al.*, K. Nucl. Instrum. Methods Phys. Res., Sect. B 2012, 287, 68-75.

[8] Bondi, A. J. Phys. Chem. 1964, 68, 441-451.

[9] Li, K.; Zheng, H.; *et al.*, J. Phys. Chem. C 2015,119, 22351-22356.

[10] Li, K.; Zheng, H.; *et al.*, Inorg. Chem. 2015, 54, 11276-11282.

K. Li[1,2], H. Zheng[1,2], T. Hattori[3], A. Sano-Furukawa[3], C. A. Tulk[4], J. Molaison[4], M. Feygenson[4], I. N. Ivanov[5], W. Yang[1,6], H. Mao[1,2], and J. Huang[1]

[1]*Center for High Pressure Science and Technology Advanced Research;* [2]*Geophysical Laboratory, Carnegie Institution of Washington;* [3]*Japan Proton Accelerator Research Complex Center, Japan Atomic Energy Agency;* [4]*Spallation Neutron Source and* [5]*Center for Nanophase Materials Sciences, Oak Ridge National Laboratory;* [6]*HPSynC, Geophysical Laboratory, Carnegie Institution of Washington*

Investigation of Microstructure by Energy-Resolved Neutron Imaging

1. Introduction

Recent developments of high resolution energy-resolved neutron imaging, enabled by the bright pulsed neutron beamlines (e.g. Noboru and Raden at J-PARC, IMAT at ISIS, FP5 at Los Alamos, VENUS and ODIN to be built at SNS and ESS, respectively) and fast neutron counting detectors (e.g. MCP/Timepix devices [1, 2]) provide unique opportunity to study microstructure within relatively thick metal samples in cases where they cannot be studied by conventional X-ray diffraction techniques. Indeed, cutting metal samples to thin slices, which is required for X-ray studies due to the opacity of metals, often affects the microstructure of the sample (e.g. releases residual strains [3, 4]). Neutrons can still interrogate thick metal samples. The energy-resolved imaging, a complementary method to neutron diffraction (which is a well-established technique nowadays), accomplishes this task by providing the entire map of some microstructure parameters with spatial resolution of ~100 μm, all from one measurement. The deficiency of transmission imaging should be pointed out here: only the integral characteristics through the sample thickness are obtained by this technique. However, in some cases that averaged information is sufficient, as demonstrated by the studies of weld cross sections and other samples reported previously [5-8].

2. Experimental setup

There are several methods of energy-resolved neutron imaging currently available, with energy resolution provided by some type of energy selection technique (e.g. velocity selector or double crystal monochromator used at continuous sources) or by neutron time of flight technique (TOF) by either chopping the beam by choppers or by taking advantage of the pulsed nature of spallation neutron sources. The energy resolution $\Delta E/E$ of velocity selectors and crystal monochromators are typically on the scale of 15% and 3%, respectively, and multiple measurements, scanning through various energies, are required. The time of flight method has been demonstrated to reach energy resolution better than ~0.1% at spallation sources, enabling various unique studies, where all energies are measured at the same time, in one experiment. The challenge of energy-resolved imaging with the TOF technique lies in the requirement to detect both position and time for every registered neutron with fluxes exceeding now 10^7 n/cm^2/s. Such high fluxes are necessary for high-resolution imaging studies, where multiple transmission spectra are measured within areas as small as 55 × 55 μm^2 [1, 2, 6-9], with as many as >250000 spectra measured at the same time.

Various neutron detection technologies were developed for energy-resolved neutron imaging over the past decade, each having its advantages and disadvantages (e.g. large active area, but low count rate capability, and vice versa). Unfortunately, there is no one device yet, which can meet all the requirements and compromises are always necessary in conducting each experiment.

In this study, a detector with Microchannel Plates and Timepix readout [1, 2] was installed at the Noboru (BL10) beamline facility in the direct beam at ~14 m from the neutron source. That detector allows for simultaneous acquisition of spectra in each 55 × 55 μm^2 pixel within the area of 28 × 28 mm^2 with time resolution as high as ~20 ns for epithermal neutrons and ~0.5 μs for thermal and cold neutrons. Neutron transmission spectra in a wide range of energies, spanning from ~30 keV to 1 meV, can be acquired by such a detector, allowing studies of crystallographic properties through Bragg scattering analysis in the thermal and cold ranges of energies, simultaneously with imaging of elemental composition and temperature through neutron resonance absorption, as demonstrated previously [6, 9, 10]. No T_0 chopper was used in our experiments. The detector was synchronized with the T_0 pulse from the source, measuring the time of arrival for each detected neutron relative to that trigger. Multiple acquisition shutters, separated by readout gaps of ~320 μs, were acquired for each neutron pulse in order to prevent event saturation in a single frame. This readout deadtime resulted in the presence of small gaps seen in the measured transmission spectra shown in Fig. 1.

In this report, only the measurement of microstructure within polycrystalline metal samples is described and the studies of microstructure within single crystal materials and mapping of elemental composition and temperature will be reported later elsewhere.

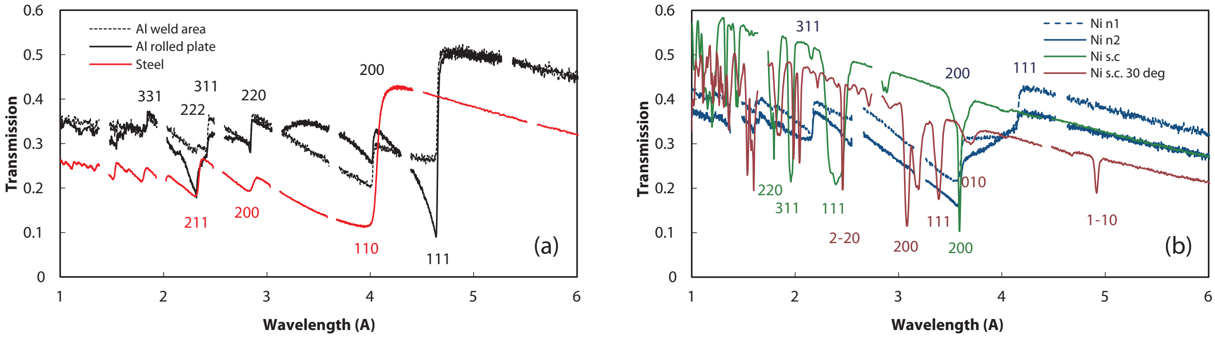

Figure 1. Neutron transmission spectra measured at BL10 for various polycrystalline metal samples, Fig. 1.a (~1 cm steel, ~10 cm Al and ~0.5 cm nickel) as well as single-crystal Ni alloy, Fig. 1.b (~0.5 cm). Each spectrum is obtained for a ~5 x 5 mm^2 area, although transmission spectrum (much noisier, only due to limited acquisition time) was measured for each 55 x 55 μm^2 pixel. The variation of transmission spectra between different areas of the same sample can be used for the reconstruction of microstructure parameters (e.g. residual strain as demonstrated in Fig. 2).

3. Results

The flight path length and trigger delay, required for the conversion of neutron time of flight to energy, were first calibrated with resonance absorption spectrum measured for an Indium-based alloy. Each image and each spectrum measured for samples were normalized by the "open beam" spectrum and images, which were obtained with no samples present in the beam. The acquisition time for the results reported here was on the scale of 1-2 hours.

The microstructure within relatively thick metal samples can be studied due to the presence of a sharp variation of neutron transmission at certain wavelengths, characteristic to a particular material, which is often referred to as Bragg edges (similar to Bragg peaks observed in the diffraction spectrum). The wavelength and the shape of these Bragg edges can be used for the reconstruction of certain microstructure parameters: for example, the residual strain within the sample can be reconstructed from the variation of wavelength of a particular Bragg, measured at different areas of the sample (up to a limit of a 55-μm pixel, providing sufficient statistics are acquired for the transmission spectra within each pixel); some texture-related variations of the microstructure within the sample can be reconstructed from the variation of edge shape and the spectrum between the edges; quantification of the different phases within the sample can be obtained from the height of respective Bragg edges, etc. Ideally, a full spectrum analysis, such as Rietveld refinement [11], should provide the most accurate and diverse information on the microstructure within the samples. However, the challenge of energy-resolved imaging is in the fact that such refinement has to be performed >10^5 times in order to provide the maps of microstructure distribution across the sample, which is not implemented in the present study. Instead, a fitting to a single Bragg edge is used here to recover the variation of residual strain within a weld sample. The images acquired within a narrow range of neutron energies (around specific Bragg edges) were employed in our study to visualize some microstructure variations within weld samples.

Typical spectra, measured for steel and Al samples, are shown in Fig. 1.a. A large difference in the measured spectra of the Al weld sample is observed for the areas within the weld (where friction stir welding produced material with small grains free of strong texture) and within the adjacent rolled plate area, exhibiting a strong texture variation through the sample thickness. Such transmission spectra are obtained in each pixel of our detector in one measurement, although the statistical variation of single pixel spectra is much larger compared to the curves shown for a ~5 × 5 mm^2 area in Fig. 1. That is why an accurate curve fitting for each small area of the sample is very important for the analysis of our data. The spectra of Fig. 1 also demonstrate that residual strain and some other microstructure parameters can be reconstructed for the assemblies, where these materials overlap (e.g. as performed in reference [8]). Indeed, the fact that Bragg edges occur at different wavelength allows analysis of certain parts of the assembly separately from the surrounding material if Bragg edges do not overlap in wavelengths.

A similar variation of transmission spectra due to the presence of texture within Ni samples is observed in Fig. 1.b, especially between (200) and (111) edges. This Figure also demonstrates the large difference in transmission spectra measured for a polycrystalline material versus single crystal samples of the same material, where dips instead of edges are observed in the spectra. These dips can be used for the quantification of crystal orientation (single grain orientation in case the

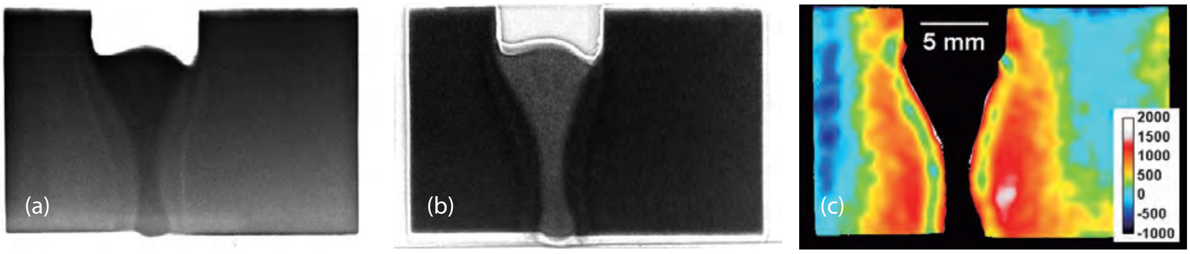

Figure 2. (a) Full spectrum neutron transmission image of a weld between two steel plates with a different filler material. (b) Same weld imaged at a narrow energy range around (110) Bragg edge. Heat affected zone in the welded plates is observed with a higher contrast compared to a white spectrum image (a). (c) The map of the residual strain reconstructed from (110) Bragg edge measured within each pixel of our dataset. An accurate fitting of a 5-parameter analytic function allows reconstruction of residual strain with sub-mm spatial resolution, across the entire sample measured in one experiment. The color legend represents the strain values measured in microstrain.

grains are large enough [12]), crystal mosaicity [13] and possibly strains within single crystal samples.

The residual strain within a steel weld sample, reconstructed from the measured transmission, is shown in Fig. 2, together with two transmission images, revealing some microstructure variations formed within the weld area. The location of the filler material is clearly seen in these transmission images, since the filler material in that weld had a different neutron attenuation coefficient due to changed composition. The heat-affected zone is also clearly seen in these images. However, in friction stir welds with the same materials present everywhere in the sample, no contrast can be observed in a white spectrum image [7], while energy resolved imaging helps to visualize the bulk variation of microstructure within the welds and other samples, which can be complementary to many other well established characterization techniques.

4. Future Plans

We plan to continue working on the neutron detection technology optimized specifically for high-resolution energy-resolved imaging. Multiple detector characteristics and the reconstruction of sample parameters can still be improved by optimization of existing detector hardware, firmware and data acquisition and data analysis software. Some new event-encoding electronics with event-driven Timepix3 readout may be very useful for such experiments, as no readout gaps will exist in the measured spectra. We also hope to increase the active area of the detector by tiling up larger arrays of these chips.

References

[1] A. S. Tremsin: Neutron News 23 35-38 (2012).
[2] A. S. Tremsin, J. V. Vallerga, J. B. McPhate, O. H. W. Siegmund: Nucl, Instr. Meth., A787 20-25 (2015).
[3] J. Altenkirch, A. Steuwer, M. Peel, D.G. Richards, P. J. Withers: Materials Science and Engineering, A488 16-24 (2008).
[4] J. Altenkirch, A. Steuwer, M. J. Peel, P. J. Withers: Powder Diffraction Suppl. 24 S1 S31-S36 (2009).
[5] J. R. Santisteban, L. Edwards, M. E. Fizpatrick, A. Steuwer, P. J. Withers: Appl. Phys., A74 S1433–S1436 (2002).
[6] A. S. Tremsin, S. Ganguly, S. Meco, G. R. Pardal, T. Shinohara, W. B. Feller: J. Appl. Crystallography, 49 1130-1140 (2016).
[7] A. S. Tremsin, W. Kockelmann, Shu-Yan Zhang, A. M. Korsunsky, T. Shinohara, E. H. Lehmann: J. Phys.: Conference Series, 746 012040 (2016).
[8] A. S. Tremsin, T. Y. Yau, W. Kockelmann, "Non-destructive examination of loads in regular and self-locking Spiralock® threads through energy-resolved neutron imaging", in print, Strain, 2016.
[9] A. S. Tremsin, T. Shinohara, T. Kai, M. Ooi, T. Kamiyama, Y. Kiyanagi, Y. Shiota, J. B. McPhate, J. V. Vallerga, O. H. W. Siegmund, W. B. Feller: Nucl, Instr. Meth., A746 47-58 (2014).
[10] A. S. Tremsin, W. Kockelmann, D. E. Pooley, W. B. Feller: Nucl, Instr. Meth., A803 15-23 (2015).
[11] H. M. Rietveld, J. Appl. Cryst., 2 65 (1969).
[12] W. Ludwig, S. Schmidt, E. M. Lauridsen, HF Poulsen: J. App. Crystal., 41 302-309 (2008).
[13] F. Malamud and J. R. Santisteban; J. Appl. Cryst., 49 348–365 (2016).

A. S. Tremsin[1], S. Ganguly[2], T. Shinohara[3], and K. Oikawa[3]
[1]*University of California at Berkeley;* [2]*Cranfield University;* [3]*Japan Atomic Energy Agency*

Impurity Effects in the Microscopic Elastic Properties of Polycrystalline Mg-Zn-Y Alloys with Sychronized Long-Period Stacking Order Phase

1. Introduction

In recent years, novel Mg-based alloys containing Zn and rare earth metal impurities have attracted much attention owing to their potential for widespread applications as light-weighted structure materials [1]. In contrast to pure Mg, the new Mg alloys exhibit non-flammable nature and high thermal stability.

To clarify the origin of these remarkable properties, extensive studies on the microscopic structure of the Mg alloys were performed using electron microscope and diffraction techniques [2], and it was found that a long period stacking ordered (LPSO) phase was formed. According to an atomic-resolution *Z*-contrast imaging of transmission electron microscope measurements [3] shown in Fig. 1, it was found that the Zn/Y impurities are enriched around the stacking faults as clusters. Egusa et al. [4] proposed a structural model of L1_2 clusters based on an *ab initio* molecular dynamics simulation.

Inelastic scattering is a powerful tool to prove the microscopic elastic properties in materials. We carried out a complementary study of inelastic neutron and X-ray scattering (INS and IXS) to clarify the impurity effects in the elastic properties on the excellent Mg LPSO alloys [5].

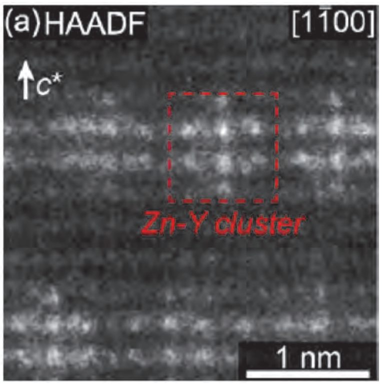

Figure 1. A TEM image of $Mg_{86}Zn_6Y_9$ alloy with the LPSO phase. Taken from [4].

2. Experimental procedure

The INS experiment was performed on the $Mg_{97}Zn_1Y_2$ polycrystal using the HRC spectrometer [6], installed at BL12/MLF/J-PARC. The incident neutron energy was chosen to be 200 meV, resulting in the energy resolution of about 6 meV. The *Q* resolution was set to be ± 0.5 nm^{-1}. The measured Q-ω ranges were 1-11 nm^{-1} and ± 40 meV, respectively, mostly limited to a triangle region due to the Q-ω relations of neutrons. The rod sample size was 29 mmϕ × 70 mm. A background measurement was carried out in the same experimental conditions, and an extremely low level of background was observed.

3. Results and discussion

The circles in Fig. 2 show the logarithmic plots of the INS spectra of $Mg_{97}Zn_1Y_2$ polycrystal at $Q = 4.0$, 6.0, and 8.0 nm^{-1}. The dashed curve indicates the resolution function of the present INS spectrometer. The upward and downward arrows, and the bar indicate longitudinal acoustic (LA), transverse acoustic (TA), and optic modes assigned by the IXS data of pure Mg and $Mg_{97}Zn_1Y_2$ polycrystals.

The triangles exhibit the IXS spectrum at 7.9 nm^{-1} for comparison with the INS data at $Q = 8.0$ nm^{-1}, which was broadened to make the width of the quasielastic peak coincide with the INS data. Distinct differences can be clearly realized in the peak magnitudes between the INS and IXS data. Namely, the LA mode, indicated by the upward arrow, is quite small in the INS spectrum, while it is very distinct even in the broadened IXS spectrum. On the other hand, the TA mode, indicated by the downward arrow, exhibits a broad peak in the INS spectrum, while that is unclear in the broadened IXS spectrum. Also, the quasielastic peak in the INS spectrum is much smaller than that in the broadened IXS spectrum.

We will discuss further the contributions of the impurity atoms to the inelastic spectra. Table 1 shows the atomic numbers, *Z*, neutron coherent and incoherent scattering lengths, b_{coh}, and b_{inc}, respectively, of the Mg, Zn, and Y elements. The atomic form factors, *f*, for the X-ray scattering rapidly decrease with an increasing *Q*. However, the ratios of *f* values between the elements are quite similar to the ratios of the *Z* values.

The b_{inc} values of all constituent elements are very small, compared with the b_{coh} values. Therefore, the INS spectra are dominated by the coherent scattering, and the contribution of the incoherent scattering is not the reason for the difference between the INS and IXS spectra.

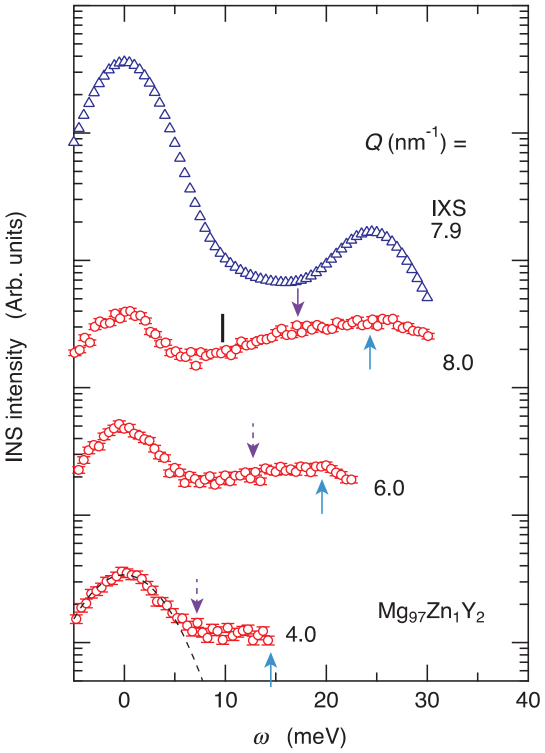

Figure 2. The circles show the INS spectra of $Mg_{97}Zn_1Y_2$ polycrystal at $Q = 4.0$, 6.0, and 8.0 nm^{-1}. The triangles exhibit the broadened IXS spectrum at 7.9 nm^{-1}. The upward and downward arrows, and bar indicate LA, TA, and optic modes assigned by the IXS data of pure Mg and $Mg_{97}Zn_1Y_2$ polycrystals. Taken from [5].

Table 1. The Z, b_{coh}, and b_{inc} values of Mg, Zn, and Y elements.

Elements	Z	b_{coh}	b_{inc}
Mg	12	5.375	~0
Zn	30	5.680	~0
Y	39	7.75	1.1

As of the multiple scattering in the INS data, the transmission of neutrons through the present sample is estimated to be about 75%, and most of the remaining 25% is coherent scattering. So, the multiple scattering effect may not explain the large difference of the IXS and INS spectra.

The remaining possible reason is the difference of scattering cross-sections of X-rays and neutrons. The f value of Mg is mostly 30-40% of those of impurities. On the other hand, the b_{coh} values for the neutron scattering are 70-95%. The cross-sections are proportional to the squares of the f and b_{coh} values. As a result, the cross-sections of the impurities are more than 5 times larger in IXS than in INS. By comparing between the IXS and INS spectra, it can be concluded that the LA excitations are highly related to the motions of impurity atoms, while the TA modes may concern more to those of host Mg atoms.

In addition, the magnitude of the quasielastic peaks in INS is much smaller than those in IXS. The quasielastic peaks in the Mg-LPSO alloys have originated from the scattering due to the stacking faults, and the impurity atoms are enriched in the stacking fault regions. Thus, the present experimental result is consistent with the synchronized LPSO views in these Mg alloys.

4. Conclusion

The INS and IXS experiments are performed on polycrystalline $Mg_{97}Zn_1Y_2$ alloy with synchronized LPSO phase to investigate the impurity effects in the microscopic elastic properties of the Mg LPSO alloy. By comparing with the INS data on the polycrystalline LPSO alloy, the contributions of the impurities to these excitation modes are discussed using the differences in the scattering cross-sections between neutrons and X-rays. The LA mode and quasielastic peak are closely related to the motions of impurity atoms, while the TA modes may concern more to those of the host Mg atoms.

This work was supported by a Grant-in-Aid for Scientific Research on Innovative Areas ‘Materials Science on Synchronized LPSO structure’ (No. 26109716) from the Japan Society for the Promotion of Science (JSPS). The INS experiments were performed at BL12 of MLF in J-PARC (Proposal No. 2015A0059).

References

[1] Y. Kawamura *et al.*, Mater. Trans. 42, 1172 (2001).
[2] K. Hagihara *et al.*, Acta Mater. 58, 6282 (2010).
[3] E. Abe *et al.*, Philos. Mag. Lett. 91, 690 (2011).
[4] D. Egusa and E. Abe, Acta Mater. **60**, 166 (2012).
[5] S. Hosokawa *et al.*, J. Alloys Compd. 695, 426 (2017).
[6] S. Itoh *et al.*, Nucl. Instrum. Met. Phys. Res. A 631, 90 (2011).

S. Hosokawa[1], M. Yamasaki[2,3], Y. Kawamura[2,3], K. Yosida[4], Y. Kawakita[5], and S. Itoh[6]
[1]*Department of Physics, Kumamoto University;* [2]*Magnesium Research Center, Kumamoto University;* [3]*Department of Materials Science, Kumamoto University;* [4]*Department of Chemistry, Fukuoka University;* [5]*J-PARK Center, JAEA;* [6]*Neutron Science Division, KEK*

High-Temperature Neutron Diffraction Study on CaWO$_4$-based Oxide Ion Conductor

1. Introduction

Oxide ion conductors have attracted significant interest for application in electrolytes of gas sensors, oxygen pumps or solid oxide fuel cells (SOFC). Several distinct structured oxides have been intensively studied, e.g. fluorite, perovskite, pyrochlore or apatite, while relatively fewer reports have been published about scheelite-type (Fig. 1) structured oxide ion conductors. When lead ions in PbWO$_4$ with scheelite-type structure are partly substituted by lanthanum ions to form oxide ion interstitials as Pb$_{1-x}$La$_x$WO$_{4+x/2}$, high oxide ion conduction occurs at elevated temperatures [1]. We have studied on this compounds in terms of electrochemical and structural point of view [1-3]. On the other hand, CaWO$_{4,}$ which as a mineral is called "scheelite", does not exhibit such an oxide ion conduction enhancement due to the lanthanum substitution.

Recently, we revealed that alkaline ion substituted solid solutions of Ca$_{1-x}$A$_x$WO$_{4-x/2}$ (A = K, Rb, Cs) also exhibit high oxide ion conduction at high temperatures [4]. In this system, the created oxide ion vacancies are supposed to contribute to the oxide ion diffusion and oxide ion conduction mechanism and should be similar to that of the PbWO$_4$-based system with oxide ion interstitials at high-temperatures. Nevertheless, some ambiguity in the conduction property still remains, i.e. CaWO$_4$-based oxide ion conductors exhibit a bend in slope of the Arrhenius plot around 500°C (Fig. 2), without showing thermal anomalies, and they still have a little higher activation energy than the La-substituted PbWO$_4$.

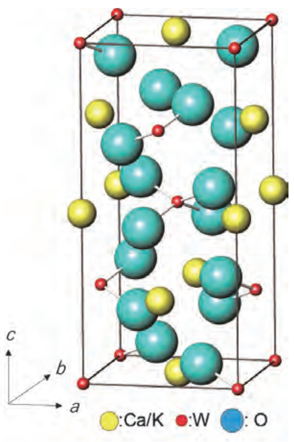

Figure 1. Schematic view of Ca$_{0.9}$K$_{0.2}$WO$_{3.9}$ with scheelite-type structure. Part of Ca site is substituted by K.

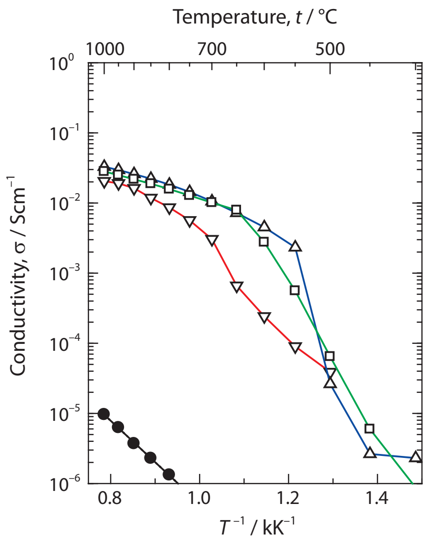

Figure 2. Arrhenius plots of conductivity for Ca$_{0.9}$A$_{0.1}$WO$_{3.95}$ (A = K (△), Rb (□), Cs (▽)).

We have previously measured the neutron diffraction experiment on the La-substituted PbWO$_4$ at room temperature [2] and also at high-temperature in 2015A0096. In the present study, we have carried out the neutron diffraction experiment on the K-substituted CaWO$_4$ at high temperatures to clarify the structural variation with the temperature, as well as the difference in conduction properties with the PbWO$_4$-based system.

2. Experimental

2.1 Sample preparation

Ca$_{1-x}$K$_x$WO$_{4-x/2}$ (x = 0.2) were prepared by the conventional solid state reaction method, started with the stoichiometric mixture of CaCO$_3$, K$_2$CO$_3$ and H$_2$WO$_4$. The calcining and sintering temperatures were selected as 800°C and 1000°C, respectively. The crystalline phases of the obtained samples were confirmed by powder X-ray diffraction (Rigaku, Ultima IV) with CuKα radiation (40 kV, 40 mA).

2.2 High-temperature neutron diffraction

About 5.5 g of the Ca$_{0.9}$K$_{0.2}$WO$_{3.9}$ sample pellets were put into a quartz tube with 0.5 mm in thickness to prevent the reaction, which was then installed into a vanadium cell. TOF neutron diffraction experiments are conducted using SHRPD in J-PARC with high-temperature furnace equipment. At first, the sample was heated up to 800°C, then the diffracted neutron data were collected at 800, 600, 400, 200 and 36°C in the cooling order. The diffraction patterns were obtained by detracting the contribution of the quartz tube as well as the vanadium cell and furnace.

The Rietveld refinements were made using Z-Rietveld assuming $I4_1/a$ symmetry. Ca(K) and W ions were placed on 4*b* and 4*a* sites, respectively and the O ion was on 16*f* with the nominal occupancy ($g = 0.9875$).

3. Results and discussion

Figure 3 shows the measured and the Rietveld refined neutron diffraction patterns of $Ca_{0.9}K_{0.2}WO_{3.9}$ at 800°C, where fairly good agreement was attained with R_{wp} = 8.39%. Even at 800°C, no apparent symmetry changes from the room temperature phase were found. Figure 4 shows the temperature variation of lattice parameters. Both *a* and *c* gradually grew with the temperature and no inflection was observed as the bend in Arrhenius plot in Fig. 2.

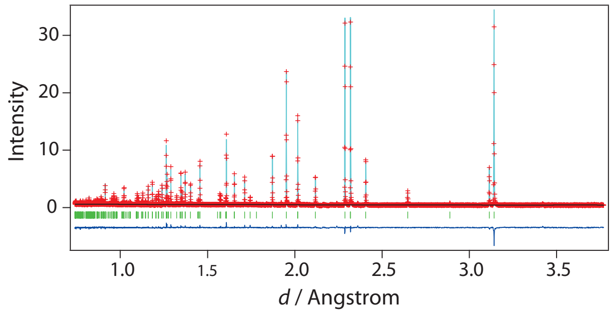

Figure 3. The Rietveld refined TOF neutron diffraction patterns of $Ca_{0.9}K_{0.2}WO_{3.9}$ based on measures taken at 800°C.

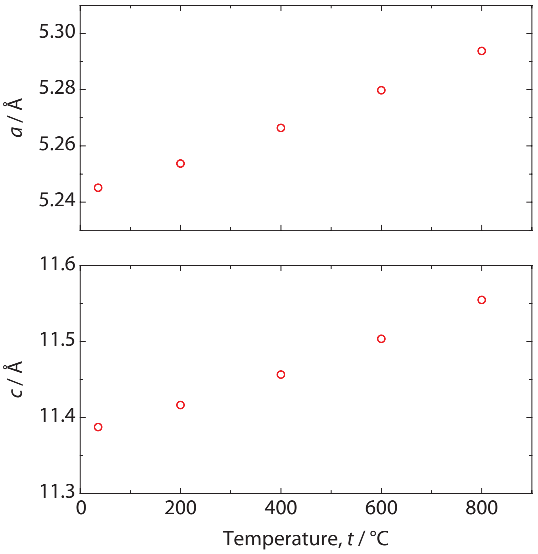

Figure 4. The Rietveld refined TOF neutron diffraction patterns of $Ca_{0.9}K_{0.2}WO_{3.9}$ based on the measures taken at 800°C.

The interatomic distance W-O, as represented in Fig. 5(a), showed rapid decrease with temperature below 500°C, while it thereafter gradually increased at high temperatures. Two types of O-W-O bond angles in WO_4 tetrahedra are also represented in Fig. 5(b) and (c). Angle $\phi_{A,}$ facing the center of the fluorite-related structure part, at first increased with temperature up to 600°C and then started to decrease. On the contrary, ϕ_B opening toward the side of the unit cell showed the opposite behavior. Namely, in the lower temperature region, the WO_4 tetrahedra development flattened with the increasing temperature. On the other hand, at a high temperature, they evolved along the *c*-axis when the oxide ion conduction became evident.

Accordingly, it can be seen that the average oxide ion positions are closely related to the oxide ion conduction. Unlike $Pb_{1-x}La_xWO_{4+x/2}$ system with oxide ion interstitials, the nuclear density of (regular) oxide ion estimated using Z-MEM code elongates toward the *c*-axis. Such a difference might be due to the existence of interstitials or the electronegativity difference between Pb (La) and Ca (K). Further consideration, including the Bond Valence model, should be made to clarify the

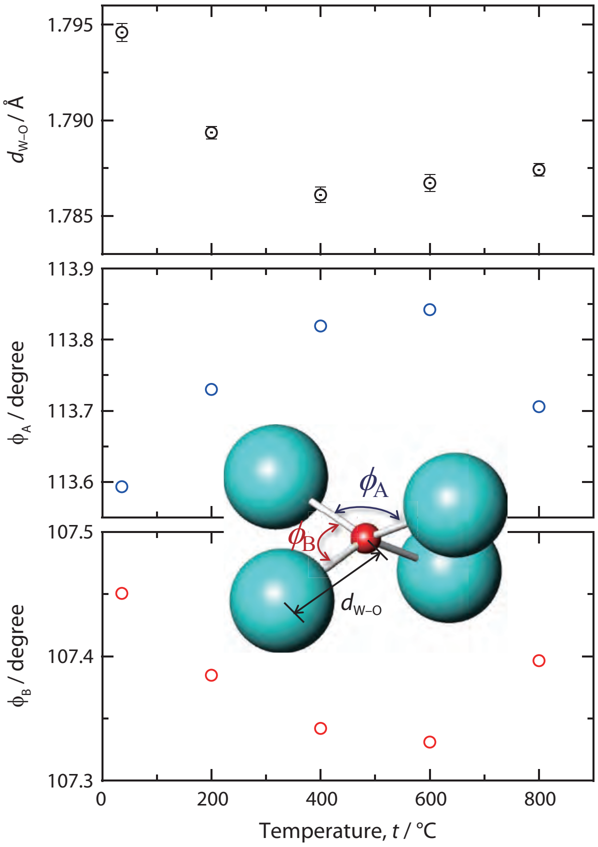

Figure 5. Temperature dependence of interatomic distance $d_{W\text{-}O}$, and bond angles ϕ_A and ϕ_B in WO_4 tetrahedra obtained by the Rietveld refinements.

precise oxide ion conduction mechanism in the scheelite-type structured oxide ion conductors. Moreover, we are also planning to perform a high-temperature neutron diffraction experiment on $Pb_{1-x}La_{2x/3}WO_4$, which does not possess the interstitials essentially, even though the $PbWO_4$-based system.

4. Conclusions

We have investigated the high-temperature structure of the $CaWO_4$-based oxide ion conductor with oxide ion vacancy by means of TOF-neutron diffraction. Accurate determination of the oxide ion position revealed that the temperature variation of the oxide ion position is altered at the high-oxide ion conduction region. The conduction mechanism is supposed to be different from the $PbWO_4$-based system with oxide ion interstitials from the oxide ion position and MEM estimation.

References

[1] T. Esaka, T. Minaai, H. Iwahara, Denki Kagaku, 59 343-344 (1991).

[2] S. Takai, S. Touda, K. Oikawa, K. Mori, S. Torii, T. Kamiyama, T. Esaka, Solid State Ionics, 148 123-133 (2002).

[3] S. Takai, T. Nakanishi, K. Oikawa, S. Torii, A. Hoshikawa, T. Kamiyama, T. Esaka, Solid State Ionics, 170 297-304 (2004).

[4] S. Takai, Y. Morishita, Y. Kondo, T. Yao, T. Yabutsuka, T. Esaka, J. Ceram. Soc. Jpn, 124 819-822 (2016).

S. Takai[1], S. Kaji[1], T. Yabutsuka[1], S. Lee[2], P. Miao[2], S. Torii[2], T. Kamiyama[2], and T. Yao[3,4]

[1]*Graduate School of Energy Science, Kyoto University;* [2]*Institute of Materials Structure Science, KEK;* [3]*National Institute of Technology, Kagawa College;* [4]*Institute of Advanced Energy Science, Kyoto University*

High-Resolution Powder Neutron Diffraction Unravels Magnetic Structure and Phase Transition Mechanism in MnO, CoO, and NiO

1. Introduction

C. G. Shull and his co-worker had carried out the first neutron diffraction for magnetic materials, i.e. transition metal monoxides MnO, FeO, CoO, and NiO in the Oak Ridge National Laboratory [1, 2]. They proved experimentally the antiferromagnetic spin alignment, which was proposed theoretically by Néel. Their pioneering works open new frontiers in the neutron science; and develop the way to answer on the questions 'where atoms are' and 'what atoms do'.

Because of this history, many textbooks of neutron scattering and condensed matter physics introduce neutron diffraction and antiferromagnetism using transition metal monoxides. For the general researcher in condensed matter physics and material science, this situation creates the misunderstanding that no issues remain in the study of crystal and magnetic structures of transition metal monoxides. Actually, the details of the crystal and magnetic structure have been discussed for more than half a century in complex situations, where the magnetic transition induces structural phase transition and ferroelastic domains simultaneously [3, 4]. For instance, each group of researchers has reported different scattered values for the CoO spin directions [4]. There is no information on the precise MnO and NiO spin direction inside the *R*-3*m* hexagonal plane. In addition, the renormalization group theory, based on the reported crystal and magnetic structure that expects all TMOs to show discontinuous phase transition, is inconsistent with the CoO and NiO experimental results.

2. Experiments

We obtained commercial powder samples MnO 99%, CoO 99.99%, and NiO 99.999% from Sigma Aldrich. Time-of-flight neutron powder diffraction was carried out in the super-high-resolution powder diffractometer (SuperHRPD, BL08 in MLF) with top-loading CCR and Vanadium furnace option [5, 6]. Narrowing the selected detector area allowed us to obtain higher-resolution diffraction data, while it decreased the diffraction intensity. To observe tiny monoclinic distortion in CoO, we selected the middle-part area of the backscattering bank. We employed the Z-Rietveld [7, 8] and Fullprof program [9] to analyze the crystal and magnetic structure using the total area of the backscattering bank. We also did group theoretical analysis to construct the group-subgroup family tree and study the phase transition mechanism.

3. Results and discussions

All MnO, CoO, and NiO are simple NaCl structures in paramagnetic phase. The spin parallel and anti-parallel spatial distribution gives rise to distinguished bond strength and length, the so-called 'exchangestriction'. On the other hand, the spin direction must be compatible with the crystal symmetry. For instance, spin direction, which is perpendicular to the 3-fold crystal symmetry, is not allowed by the 3-fold crystal symmetry. Therefore, this spin direction induces additional structural distortion, the so-called 'magnetostriction'. The well-known rhombohedral structure model of MnO and NiO couldn't satisfy the comparability between the 3-fold crystal symmetry and the spin direction, which is perpendicular to the 3-fold axis [3, 4].

Regarding exchangestriction and magnetostriction, we made a group-subgroup family tree that represents the transformation of crystal and magnetic structure in the cubic, rhombohedral, and monoclinic structure with their related physical interaction, as shown in Fig. 1. Exchangestriction and magnetostriction break the 4-fold and 3-fold symmetry respectively that induces common *C*2/*m* crystal structure and magnetic propagation vector $k_m = (0\ 1\ 0.5)$. In principle, there are only two $\Gamma_1^+ = (0, m_y, 0)$ and $\Gamma_2^+ = (m_x, 0, m_z)$ spin directions. The Γ_1^+ spin direction induces normal strain with respect to the mirror plane, while this spin direction is still inside the spin easy-plane given by dipolar magnetic anisotropy energy. On the other hand, the Γ_2^+ spin direction induces shear strain, which is parallel to the mirror plane, while the spin direction can deviate from the spin easy-plane given by dipolar magnetic anisotropy. If the orbital moment is quenched, the dipolar magnetic anisotropy with normal strain selects Γ_1^+ spin direction. If the orbital moment is unquenched, the spin-orbit-lattice coupling can compensate for the increasing of dipolar magnetic anisotropy energy and select Γ_2^+ spin direction. By simple comparison, all MnO, CoO, and NiO are described by common *C*2/*m* with $k_m = (0\ 1\ 0.5)$. The difference comes only from the Γ_1^+ and Γ_2^+ spin directions.

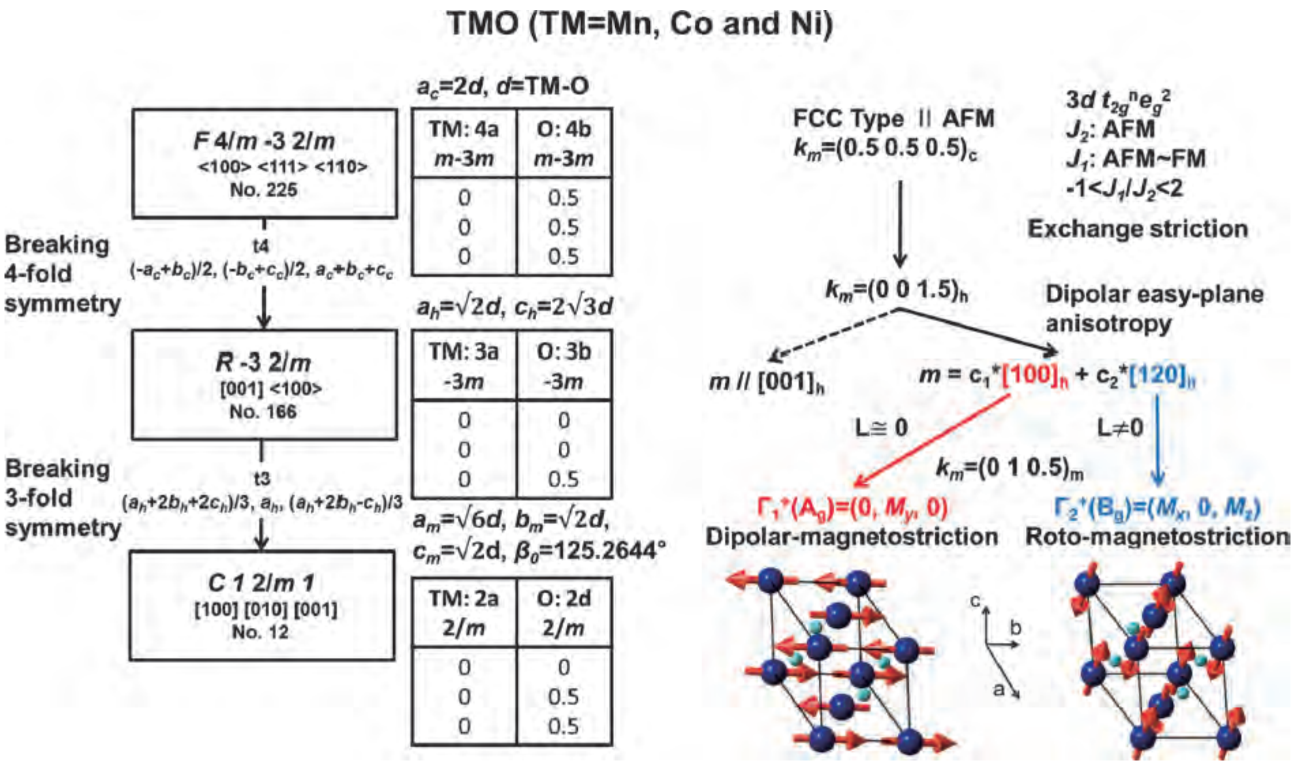

Figure 1. Group-subgroup family tree under exchangestriction and magnetostriction [4]. Spin spatial distribution and spin direction reduce the crystal structure from cubic to rhombohedral, and finally to a monoclinic structure. We derived atomic position, lattice constant, magnetic propagation vector, spin direction in each cubic, rhombohedral, and monoclinic structure by following the physical mechanism.

For CoO, we confirmed successfully a very tiny monoclinic peak splitting about 0.00025 Å, as shown in Fig. 2 [4]. It is consistent with the previous high-resolution synchrotron x-ray diffraction [10]. And then, we determined unambiguously the Γ_2^+ magnetic structure with precise spin directions. On the other hand, for MnO and NiO, the well-known rhombohedral distortion is clearly detectable. However, the further monoclinic distortions are too small to be detectable even with the world's best high-resolution diffractometer in existence. Fortunately, with our group-subgroup model and earlier experiments of references, we could assign Γ_1^+ and Γ_2^+ magnetic structure to MnO and NiO, respectively [3, 4].

We converted from the temperature dependence of the magnetic moment M and monoclinic angle β to order parameter vector diagram $\beta - M^n$ as shown in Fig. 3. The initial monoclinic angle β_0 is a paramagnetic phase. The increase of the ordered magnetic moment induces deviation in the monoclinic angle from β_0. The order parameter vector diagram shows two different cases by Γ_1^+ and Γ_2^+ spin directions. The orbital quenched case of MnO and orbital unquenched case of CoO and NiO choose the Γ_1^+ and Γ_2^+ spin directions, linear-quadratic $\sim\beta M^2$ and linear-cubic $\sim\beta M^3$ magnetoelastic couplings, and discontinuous and continuous phase transitions, respectively.

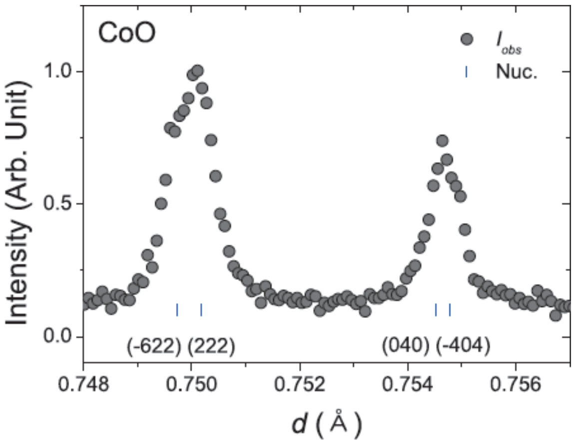

Figure 2. SuperHRPD observed successfully tiny monoclinic distortions [4]. The peaks position difference is about 0.00025 Å between d_{040} and d_{-404}. So far, such a small distortion has been considered practically negligible. However, any finite small distortion can induce a different symmetry of order parameter. In other words, it can affect the coupling type of order parameters and the mechanism of phase transition.

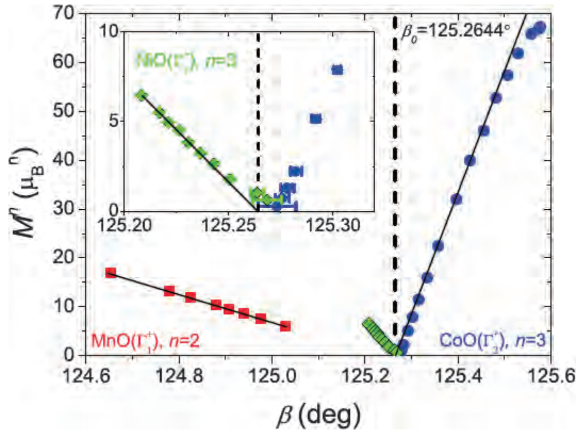

Figure 3. Order-parameter vector diagram in MnO, CoO and NiO [4]. β_0 is paramagnetic phase whereas $\beta = \beta_0 \pm \Delta\beta$ is antiferromagnetic phase. The Mn *d* orbital angular momentum is quenched, while Co and Ni ones are unquenched case. The orbital quenched case and unquenched case prefer Γ_1^+ and Γ_2^+ spin directions, respectively. Different Γ_1^+ and Γ_2^+ spin directions cause normal and shear strain, linear-quadratic $\sim\beta M^2$ and linear-cubic $\sim\beta M^3$ magnetoelastic coupling, discontinuous and continuous phase transition, respectively.

Traditionally, we used the time-reversal symmetry breaking to describe magnetic structure and phase transition. For the Landau theory of second-order magnetic phase transition, L. Landau expanded free energy in the polynomials of magnetic moments that must be invariant by time-reversal symmetry [11]. The charge density or crystal distortion are invariant while the magnetic moment, considered charge current from the classical viewpoint, is reversed by the time-reversal symmetry operation. So far, we expect that the even-power polynomials in magnetic moment will couples with structural distortions. However, CoO and NiO show experimentally linear-cubic magnetoelastic coupling forbidden by time-reversal symmetry. It seems that monoclinic distortion and magnetic moment are same irreducible representation which is not allowed by time-reversal symmetry. These experimental results provide the answer to the fundamental question whether time-reversal symmetry is suitable or not to describe the magnetic moment in condensed matter physics [4]. Further theoretical studies and other experimental examples will be necessary to expand our knowledge.

4. Conclusion

We elucidated the long-standing problems of the magnetic structure and phase transition mechanism for MnO, CoO, and NiO. Breaking the time-reversal symmetry couldn't explain the linear-cubic magnetoelastic coupling and continuous phase transition in CoO and NiO. These experimental results pose the general question what symmetry can be used to describe the magnetic moment in condensed matter physics. Our study shows that any tiny structural distortion and spin directions must not be ignored from a strict symmetric viewpoint. Currently, the SuperHRPD beamline displays the performance of the best high-resolution neutron powder diffractometer in the world. Just as a micrometer can see details inaccessible to bare eyes, it can investigate new physical phenomena or mechanisms, which we couldn't see before by using conventional resolution of the neutron diffractometer.

References

[1] C. G. Shull and J. S. Smart, Phys. Rev. 76, 1256 (1949).
[2] C. G. Shull *et al.*, Phys. Rev. 83, 333 (1951).
[3] S. Lee *et al.*, JPS Conf. Proc. 8, 034007 (2015).
[4] S. Lee *et al.*, Phys. Rev. B 93, 064429 (2016).
[5] S. Torii *et al.*, J. Phys. Soc. Jpn. 80, SB020 (2011).
[6] S. Torii *et al.*, J. Phys.: Conf. Ser. 502, 012052 (2014).
[7] R. Oishi *et al.*, Nucl. Instr. Meth. Phys. Res. A 600, 94 (2009).
[8] R. Oishi-Tomiyasu *et al.*, J. Appl. Cryst. 45, 299 (2012).
[9] J. Rodriguez-Carvajal, Phys. B Condens. Matter 192, 55 (1993).
[10] W. Jauch *et al.*, Phys. Rev. B 64, 052102 (2001).
[11] L. Landau, Zh. Eksp. Teor. Fiz. 7, 19 (1937).

S. Lee[1], Y. Ishikawa[1], P. Miao[1,2], S. Torii[1,3], T. Ishigaki[4], and T. Kamiyama[1,2,3]
[1]*Institute of Materials Structure Science, KEK;* [2]*Sokendai (The Graduate University for Advanced Studies);* [3]*J-PARC center, KEK;* [4]*Frontier Research Center for Applied Atomic Science, Ibaraki University*

Silver Photo-Diffusion into Amorphous Ge-Chalcogenide Films: *in situ* Neutron Reflectivity Measurement

1. Introduction

Interestingly, silver diffuses into amorphous chalcogenide (a-Ch) such as a-As_2S_3 and $GeSe_2$ when light illuminates Ag/ a-Ch double-layer film. This phenomenon is referred to as silver photo-diffusion, or, photo-doping [1, 2]. This effect has been used in several applications such as photo-lithography, the fabrication of relief images in optical elements and non-volatile memory devices [3]. This diffusion is unique, showing step-like silver-concentration changes in the depth direction with 'a diffusion front' and it was believed that the diffusion front progressed following the successive light exposure. Such diffusion model was built up from previous works, mainly by using Rutherford backscattering spectroscopy by *ex situ* way. However, the *in situ* measurement was difficult because the strong He ion beams induce silver diffusion. The use of strong X-ray beams also induces silver diffusion and the selection of proper probe beams has been a crucial subject to perform an *in situ* measurement, which should provide a correct answer to the kinetics. Recently, we performed an *in situ* neutron reflectivity measurement of Ag/Ge-Ch films and revealed their diversified kinetics [4-8]. Here we report the result of the neutron reflectivity measurement of $Ge_{33}S_{67}$/ Ag/ Si substrate film [7, 8].

2. Experimental

The neutron reflectivity measurement was carried out on *SHARAKU* (BL17) at the MLF [6]. In the measurement, the proton beam power was 300 kW. White light from a 300 W xenon lamp (MAX-303, ASAHI Spectra, Co., Ltd.) was used as an excitation light source. The experimental setup is shown in Figure 1 [6]. Neutron data were acquired using an event recording system, and arbitrarily time-sliced spectra were obtained from the full recorded data set.

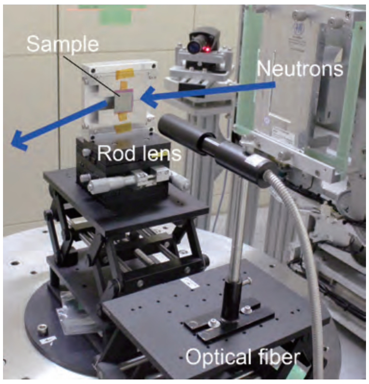

Figure 1. Experimental setup.

3. Results and Discussion

Figure 2 shows the time evolution of the neutron reflectivity of $Ge_{33}S_{67}$ 2000 Å/ Ag 500 Å/ Si substrate film under light exposure of Xe lamp and Figure 3 shows the time evolution of the scattering length density (SLD) profile, which is the result of the model fitting. As shown in Fig. 3, the Ag layer became thinner during the light exposure time and disappeared in about 17 min. The SLD of the Ch layer increased (1.9 -> 2.2) with the exposure time, but remained uniform over the layer. This means that the Ag ions spread over the layer, once they enter the Ch layer, as illustrated in Fig. 4. It seems that there is no potential barrier inside the Ch layer, but a potential barrier exists only at the Ag/ a-Ch interface. Such immediate diffusion is probably due to the ion-conductive nature of the Ch host under the light exposure. After successive light exposure for more than 27 min, the neutron reflectivity in the total reflection

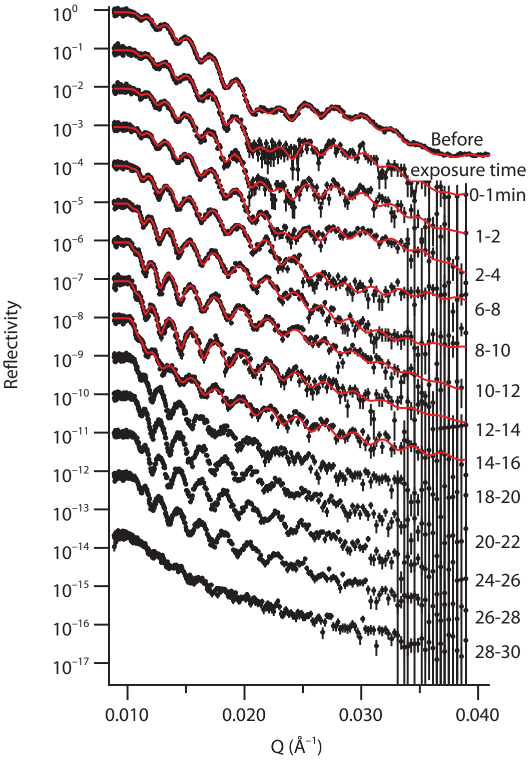

Figure 2. Time evolution of the neutron reflectivity of $Ge_{33}S_{67}$ 2000 Å/ Ag 500 Å/ Si.

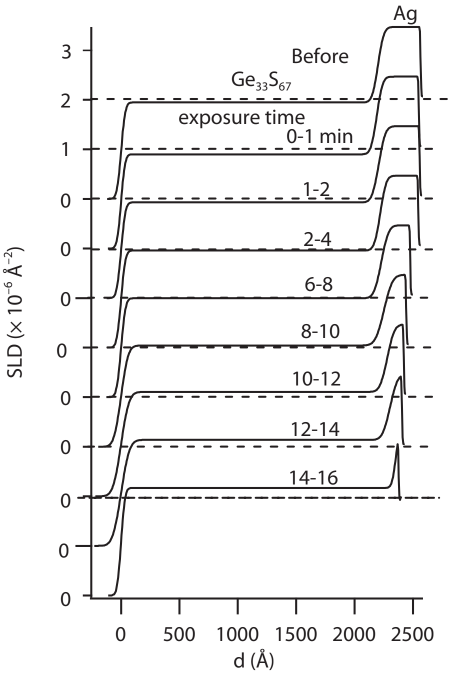

Figure 3. Time evolution of the SLD profile.

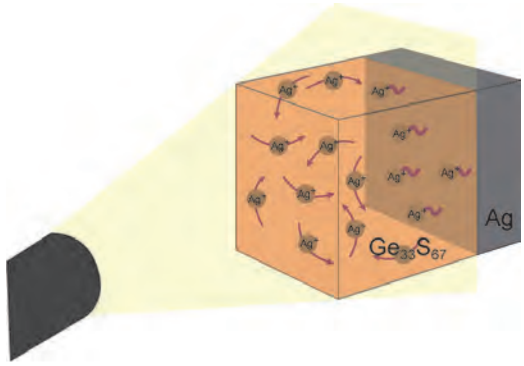

Figure 4. Schematic illustration of the diffusive nature of Ag ions under light exposure.

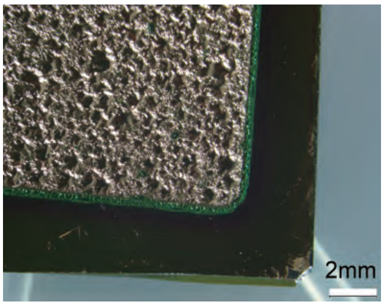

Figure 5. Optical microscope image of the surface after the light exposure.

region rapidly decreased and the fringes in the neutron reflectivity profile disappeared. Figure 5 shows the optical microscope image of the surface after the light exposure, suggesting macroscopic height-variations of the surface similar to mountains and valleys. We infer that a giant volume change or a change in the surface tension on the Si substrate was induced by the continuous light exposure and the change caused the macroscopic height-variations of the surface. In summary, the experimental result provided a profound insight into the photo-structural properties and functionalities of the $Ge_{33}S_{67}$/Ag/ Si film in terms of the ionic conductivity and self-organization under light exposure.

The neutron reflectivity measurements were performed on *SHARAKU* in J-PARC MLF under Project No. 2013B0159. We would like to thank N. Miyata, K. Akutsu, T. Ito, and S. Kasai (CROSS) for the technical support on the neutron reflectivity instrument and M. Ailavajhala for the sample preparation.

References

[1] M. T. Kostyshin, E. V. Mikhailovskaya, and P. F. Romanenko, Sov. Phys. (Solid State) **8**, 451 (1966).
[2] A. V. Kolobov and S. R. Elliott, Adv. Phys. **40**, 625 (1991).
[3] M. Mitkova and M. N. Kozicki, J. Non-Cryst. Solids **299-302**, 1023 (2002).
[4] Y. Sakaguchi *et al.*, Can. J. Phys. **92**, 654 (2014).
[5] Y. Sakaguchi *et al.*, J. Phys. Conf. Ser. **619**, 012046 (2015).
[6] Y. Sakaguchi *et al.*, JPS Conf. Proc. **8**, 031023 (2015).
[7] Y. Sakaguchi *et al.*, Phys. Status Solidi A **213**(7), 1894-1903 (2016).
[8] Y. Sakaguchi *et al.*, J. Appl. Phys. **120**, 055103 (2016).

Y. Sakaguchi[1], H. Asaoka[2], Y. Uozumi[2], Y. Kawakita[3], T. Hanashima[1], D. Yamazaki[4], K. Soyama[4], and M. Mitkova[5]
[1]*Neutron Science and Technology Center, CROSS-Tokai;* [2]*Advanced Science Research Center, JAEA;* [3]*Neutron Science Section, Materials and Life Science Division, J-PARC Center;* [4]*Neutron Instrumentation Section, Materials and Life Science Division, J-PARC Center;* [5]*Department of Electrical and Computer Engineering, Boise State University*

Operando Measurement of Solid Electrolyte Interphase Formation at Working Electrode of Li-ion Battery by Time-slicing Neutron Reflectometry

1. Introduction

In order to improve the safety and durability of the present lithium ion batteries (LIBs), we definitely need to understand the nature of a solid-electrolyte interphase (SEI) that is formed at the boundary between negative electrode material and electrolyte in LIBs [1]. Neutron reflectometry (NR) was employed for direct observation of the electrode/electrolyte interface of a LIB because neutrons can penetrate through the electrode and provide interference that reflects the interfacial structure [2-4]. The neutron scattering length density ρ, can be evaluated in the depth range between a few nanometers and a few hundred nanometers. Since ρ is related to the elemental composition and the density at the interface. Therefore, NR can be used to detect not only the SEI formation, but also the intercalation of Li^+ ions with an in situ method. Based on the *operando* NR of a model electrode with the SOFIA reflectometer in J-PARC/MLF [5, 6], we observed successfully for the first time the SEI growth process and the intercalation of Li^+ ions at an electrode during the charge reaction [7].

2. Experimental

Figure 1 shows a schematic of the electrochemical cell used for the present work. A carbon/titanium multilayer thin film on a 3-mm thick silicon substrate with an area of 30 × 30 mm was used as a model electrode and soaked with an electrolyte (see reference [7] for details). The electrochemical cell was mounted on the sample stage of the SOFIA reflectometer. The electrochemical potential at the carbon electrode, *E*, was controlled by an electrochemical analyzer with a scan rate of 1.0 mV/s in the potential range from 2.9 to 2.0 V (*vs.* Li/Li^+) and at 0.2 mV/s from 2.0 to 0.05 V during the NR measurement. The neutrons were introduced from the substrate side and the reflected neutrons were acquired every 5 minutes with an incident angle θ of 0.4° to obtain the reflectivity profile as a function of the momentum transfer normal to the basal plane Q_z; $Q_z = (4\pi \sin\theta)/\lambda$, by taking into account the wavelength of neutrons, λ, -based on the time-of-flight method.

3. Results and discussion

Figure 2 shows the reflectivity profiles as a function of *E* during the charge reaction. In contrast to the lack of change in the profile from the open circuit voltage (OCV; ca. 2.9 V) to 1.5 V, even with a decrease in *E*, the period and critical value of Q_z at the total reflection began to change at 1.5 V and the change was more pronounced at 0.6 V. This change was consistent with the

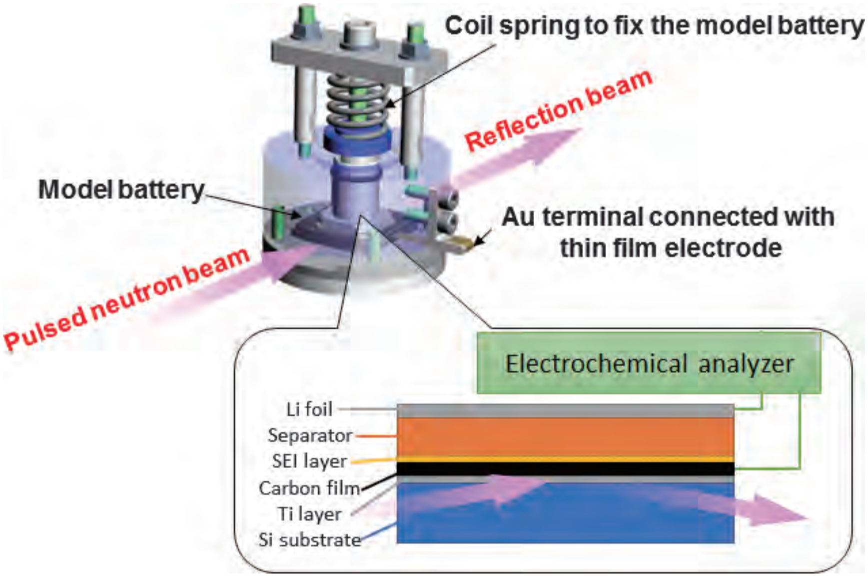

Figure 1. Schematic illustration of the electrochemical cell and cross-section of the model battery system for the *in situ* NR measurements [7].

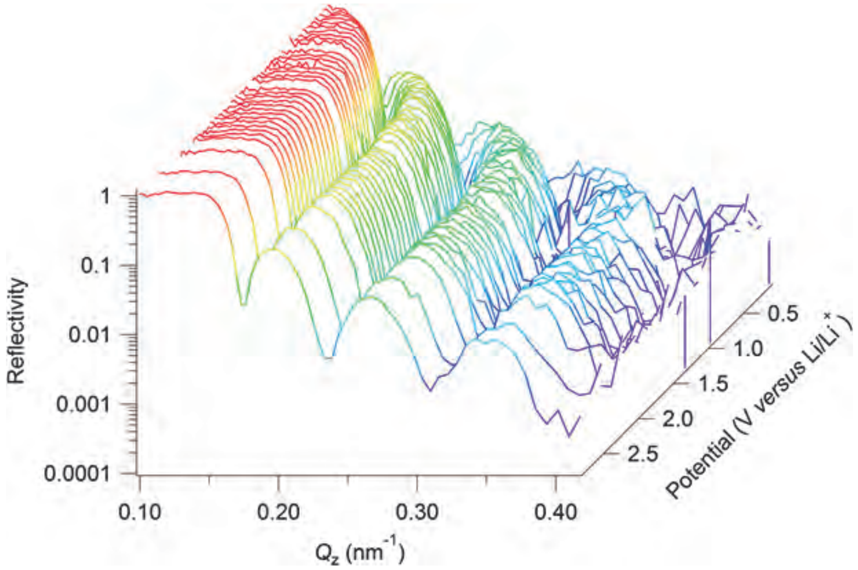

Figure 2. NR profiles as a function of *E* during the charging reaction obtained by the *operando* measurement [7].

voltammogram of the carbon electrode during the *in situ* NR experiment: no characteristic reaction occurred from OCV to 1.5 V (phase I), decomposition of the electrolyte and/or organic solvent occurred for the SEI formation from 1.5 V to 0.6 V (phase II), and the intercalation of Li ions occurred from 0.6 V to 0.05 V (phase III).

Figure 3 shows the dependence of ρ_C, ρ_I, d_C, and d_I obtained by the least-squares fitting based on a least-squares fitting with the Parratt formalism [8, 9]. Here, *d* indicates the thickness of a layer, and subscripts C and I indicate the carbon electrode and interfacial layer, respectively. The fitting result indicated the presence of an interfacial layer, even at the OCV, with $d_I = 17.0 \pm 1.7$ nm and $\rho_I = (2.50 \pm 0.20) \times 10^{-4}$ nm^{-2}. As a hydroxyl layer was detected by an *ex situ* X-ray Photoelectron Spectroscopy analysis on the surface of the carbon electrode after immersion in the electrolyte without charging, the interfacial layer is presumably attributed to an adsorption layer formed upon contact with the electrolyte before the SEI formation.

Furthermore, the values of d_I and ρ_I changed with a decrease in *E*, which indicated that an SEI started to form at the interface due to a decomposition reaction. According to the trend of d_I, the SEI gradually thickened with the charge reaction during phases I and II, and the rate of thickening was enhanced during phase III. On the other hand, ρ_I remained almost constant during phases I and II, while increasing during phase III up to $(3.26 \pm 0.72) \times 10^{-4}$ nm^{-2} at $E = 0.05$ V. ρ indicates the composition of the SEI; therefore, these results imply a change of the product by the charge reaction. The SEI formed in this system is reported to consist of the following components: polyvinylene carbonate (ρ = 2.84×10^{-4} nm^{-2}), Li_2CO_3 (3.48×10^{-4} nm^{-2}), lithium alkyl carbonate (2.75×10^{-4} nm^{-2}), polyethylene oxide (PEO; 8.22×10^{-5} nm^{-2}), $LiPF_6$ (2.21×10^{-4} nm^{-2}), and LiF (2.30×10^{-4} nm^{-2}). Therefore, the change in ρ implies a change of the product by the charge reaction, and Li_2CO_3, having the highest ρ value, is a strong candidate product that contributes to the increase in ρ_I during phase III.

Next, we focused on the intercalation of the Li$^+$ ions into the electrode during the charge reaction; d_C was 69.1 ± 0.3 nm at OCV, remained almost constant during phases I and II, and then increased monotonically up to 84.1 ± 0.8 nm at $E = 0.05$ V during phase III. The change in d_C is consistent with the volumetric change induced by the Li$^+$ intercalation into carbon, because the *c*-axis length of the Li$^+$-intercalated carbon is larger than that of carbon. On the other hand, Li has a negative coherent scattering length; therefore, the decrease in ρ_C also indicates intercalation. In fact, ρ_C at OCV, $(6.46 \pm 0.02) \times 10^{-4}$ nm^{-2}, remained constant during phase I, and decreased monotonically down to $(4.50 \pm 0.27) \times 10^{-4}$ nm^{-2} at $E = 0.05$ V during phases II and III. It should be noted here that the number of Li ions intercalated into the carbon electrode with one-electron transfer reaction during the charge reaction can be evaluated based on the changes in d_C and ρ_C. This means that the charge used for Li$^+$ intercalation can be evaluated by NR, the one and that used for SEI formation can be extracted by comparing with the total charge evaluated by voltammogram. This is a novel information only *operando* NR can provide, which is valuable for understanding the process of SEI formation during the charging.

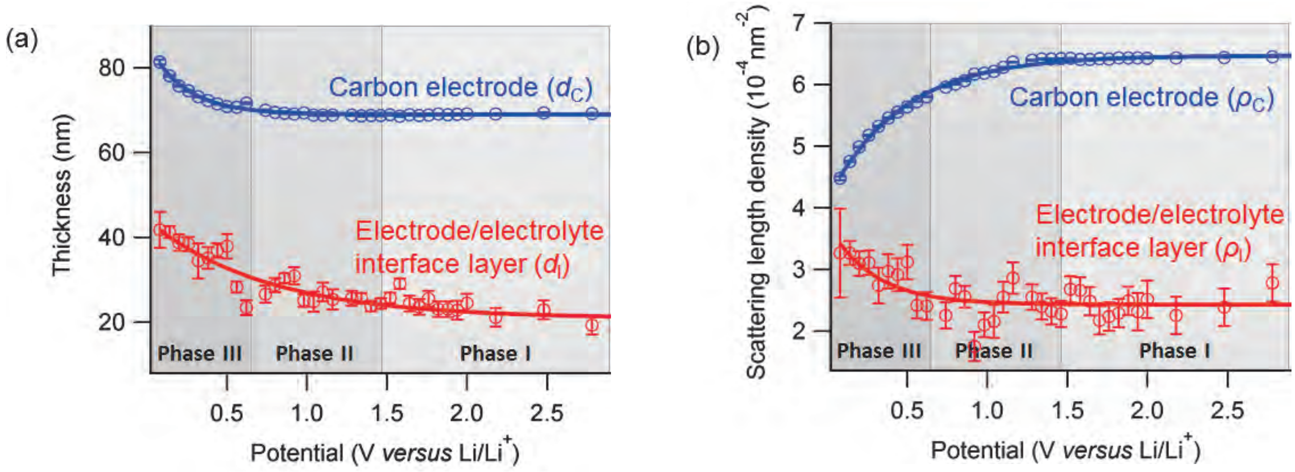

Figure 3. Evolution of the interfacial structure at the carbon electrode during electrochemical reaction: (a) thickness and (b) scattering length density of the electrode and interfacial layer as a function of *E* [7].

4. Conclusion

We have succeeded in the first *operando* measurement of SEI formation at the working electrode of a LIB using a combination of time-slicing NR. The results obtained clearly show the formation of a SEI layer at the carbon electrode and the intercalation of Li ions into the electrode. This method has the potential to be used to determine the chemical composition of an SEI and to evaluate the absolute amounts of charge used in the SEI formation and Li intercalation during an electrochemical reaction. We believe the *operando* NR technique opens a door to shed light on the "live" composition/decomposition process of SEIs under operation and deepens our understanding of the formation mechanism and its relationship with the performance of LIBs, which will lead to further improvement of the present LIBs and the development of advanced next-generation batteries.

Acknowledgements

JS was partially supported by a Kakenhi Grant-in-Aid (No. 23108003) from the Ministry of Education, Culture, Sports, Science, and Technology (MEXT) of Japan.

References

[1] M. Gauthier *et al., J. Phys. Chem. Lett.* 2015, **6**, 4653-4672.
[2] J. E. Owejan *et al., Chem. Mater.,* 2012, **24**, 2133-2140.
[3] J. F. Browning *et al., ACS Appl. Mater. Interfaces,* 2014, **6**, 18569-18576.
[4] M. Hirayama *et al., Electrochem. Comm.,* 2010, **78**, 413-415.
[5] N. L. Yamada *et al., Eur. Phys. J. Plus,* 2011, **126**, 1-13.
[6] K. Mitamura *et al., Polym. J.,* 2013, **45**, 100-108.
[7] H. Kawaura *et al., ACS Appl. Mater. Interfaces* 2016, **8**, 9540-9544.
[8] L. G. Parratt, *Phys. Rev.,* 1954, **95**, 359-369.
[9] A. Nelson, *J. Appl. Cryst.* 2006, **39**, 273-276.

H. Kawaura[1], M. Harada[1], Y. Kondo[1], H. Kondo[1], Y. Suganuma[1], N. Takahashi[1], J. Sugiyama[1], Y. Seno[1], and N. L. Yamada[2]
[1]*Toyota Central Research & Development Laboratories, Inc.;* [2]*Institute of Materials Structure Science, High Energy Accelerator Research Organization*

Unusual Dynamics of α-synuclein Amyloid Fibrils Detected by Quasielastic Neutron Scattering

1. Introduction

α-synuclein (αSyn) is a protein consisting of 140 amino acid residues, which is abundant in the presynaptic nerve terminals in the brain. Although its precise function is unknown, it is implicated in the pathogenesis of the Parkinson's disease (PD), a progressive neurodegenerative disorder. Filamentous aggregates of αSyn are often found to be a major component of the protein deposits in the brain of patients with PD. These aggregates (amyloid fibrils) and/or the intermediate structures toward the mature fibrils of αSyn are thought to be related to the pathogenesis of PD. Elucidating the mechanism of the fibril formation of αSyn is thus important for understanding the mechanism of the pathogenesis of PD.

The formation of amyloid fibrils generally involves partial unfolding of the proteins and the subsequent growth of the protofilaments and the mature fibrils. The involvement of the partial unfolding implies that the dynamics of the proteins plays an important role in the process of the fibril formation. Investigating the protein dynamics during the fibril formation is therefore important for elucidating the mechanism of this process. The purified αSyn from bacterial expression is monomeric but intrinsically disordered in solution and forms amyloid fibrils under various conditions. As a first step toward elucidating the mechanism of the fibril formation of αSyn, we investigated the dynamic behavior of the purified αSyn in the monomeric state and the fibril state. For this purpose, we employed quasielastic neutron scattering.

Neutron scattering provides a unique tool to directly measure the dynamics of proteins at ps-to-ns time scales and ångstrom length scales. In particular, incoherent quasielastic neutron scattering (QENS) provides information on the average motion of (the hydrogen atoms within) the entire protein. Here, we carried out the QENS experiments of the solution samples of αSyn in the monomeric and fibril states, and compared the dynamic properties of αSyn in these states [1]. It was found that αSyn in the fibril state shows unusual dynamic behavior.

2. Materials and methods

The solution sample of αSyn was prepared by purifying human wild-type αSyn, expressed in *E. coli*. The solution, containing 9.5 mg/ml αSyn, was prepared in D_2O. This sample represents the monomeric state. Fibrils of αSyn were prepared by incubating the solution sample in D_2O at 37°C under constant shaking. The sample representing the fibril state was prepared by pelleting this fibril solution. The pellets contained 46 mg/ml of the αSyn fibrils. The QENS experiments on these samples were carried out using the near-backscattering spectrometer, BL02 (*DNA*), at MLF/J-PARC. The measurements were done at several temperature points between 280 K and 300 K, at the energy resolution of 12 μeV.

3. Results

Figure 1 shows examples of the QENS spectra arising from αSyn in the monomeric and fibril states. The

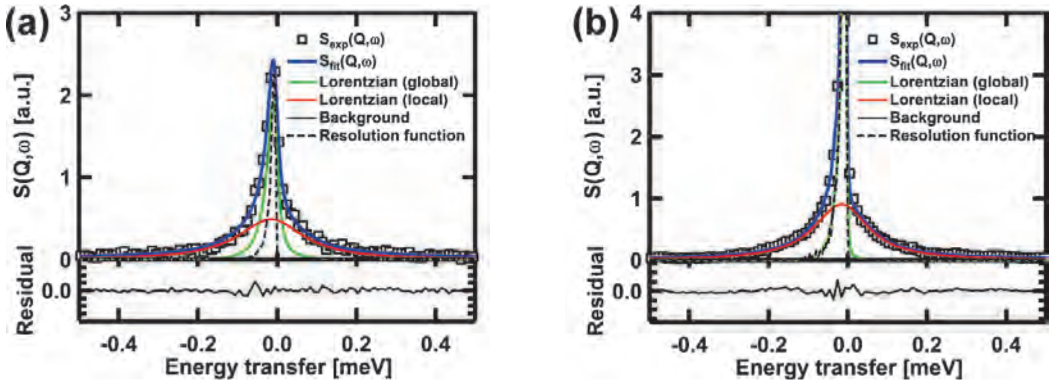

Figure 1. Examples of quasielastic neutron scattering spectra, S(Q,ω). The spectra of αSyn in (a) the monomeric state and (b) the fibril state, at Q = 1.225 $Å^{-1}$ and at 280 K, are shown along with the results of the fits using Eq. 1. In the upper panels, open squares denote the data, thick solid lines in blue denote the total fits, solid lines in green and red denote $L_{global}(Q,\omega)$ and $L_{local}(Q,\omega)$, respectively, thin solid lines in blue show the background, and dashed lines in black show the resolution functions. The lower panels show the residuals of the fits.

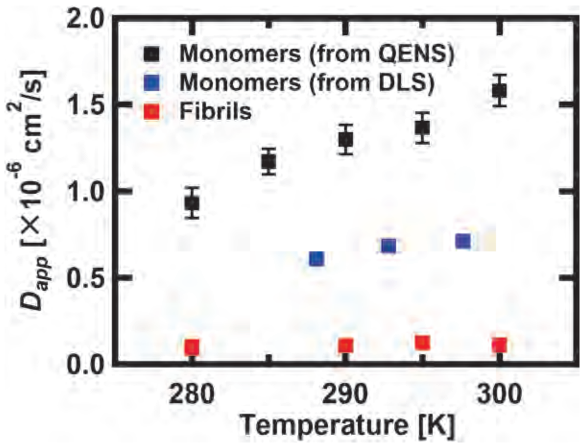

Figure 2. D_{app} of αSyn in the monomeric (■) and the fibril (🟥) states evaluated from the QENS spectra. The translational diffusion coefficients of αSyn in the monomeric state determined from the dynamic light scattering (🟦) are also shown.

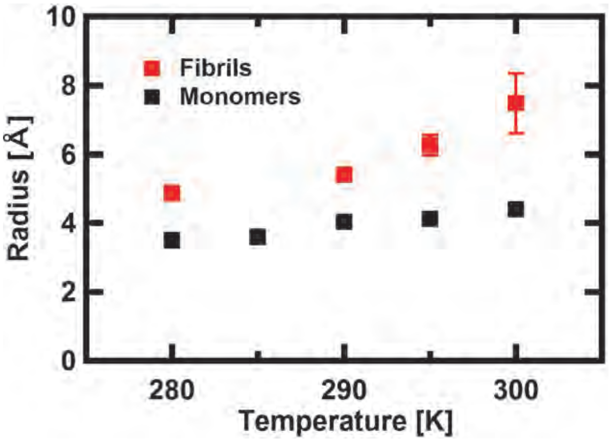

Figure 3. Radii of the confined spheres of αSyn in the monomeric (■) and the fibril (🟥) states, evaluated from the EISF curves.

spectra, S(Q,ω), can be fit with equation,

$$S(Q,\omega) = \{A_0(Q)\delta(\omega) + (1 - A_0(Q))L_{local}(Q,\omega)\} \otimes L_{global}(Q,\omega) \otimes RF(Q) + BG. \quad (1)$$

Here, Q is the momentum transfer, $\hbar\omega$ is the energy transfer, A_0(Q) is the elastic incoherent structure factor (EISF) that characterizes geometry of atomic motions, L_{local}(Q,ω) and L_{global}(Q,ω) are the Lorentzian functions that characterize the local motions within the protein and the global motions of the entire protein, respectively, and ⊗ denotes the convolution operation. By fitting the spectra with this phenomenological equation, the global motions and local motions can be separated.

The Q-dependence of the width of L_{global}(Q,ω) provides information on the diffusive motions of the entire molecules. Figure 2 shows the apparent diffusion coefficients (D_{app}) of αSyn in the monomeric and fibril states obtained from the analysis of these widths. It is shown clearly that diffusive global motions are observed in the monomeric state but largely suppressed in the fibril state. Note that D_{app} has significant differences with the translational diffusion coefficients evaluated from dynamic light scattering, suggesting that D_{app} obtained from QENS contains contributions from rotational diffusion and segmental motions within the protein.

The Q-dependence of the width of L_{local}(Q,ω) provides information on the rates of the local atomic motions within the protein. The residence times were found to be larger in the fibril state than in the monomeric state, indicating that the rates of the atomic motions within the protein are faster in the monomeric state than in the fibril state.

Information on the geometry of these local atomic motions can be obtained by analysis of the EISF curves. Figure 3 shows the radius of the confined sphere, in which the atoms undergo diffusive motions. Surprisingly, this radius was found to be larger in the fibril state than in the monomeric state. This is contrary to the expectation that aggregation reduces the motions of the molecules in the aggregates. This indicates that the amplitudes of the local motions are larger in the fibril state than in the monomeric state. This is interpreted to mean that a significant solvent space exists within the fibrils, which is attributable to the αSyn molecules within the fibrils having a distribution of conformations. The larger amplitudes of the local motions in the fibril state imply that the degree of the conformational freedom is larger in the fibril state than in the monomeric state, i.e., the fibril state is entropically favorable. This then implies that the fibril formation is entropically driven. The implication here is that once a potential barrier is overcome, the fibril formation proceeds naturally. The rate-limiting step of the fibril formation would then be the kinetics involved to overcome the potential barrier.

Reference

[1] S. Fujiwara *et al.*, PLOS ONE, 11 e015447 (2016).

S. Fujiwara[1], K. Araki[2], T. Matsuo[1], H. Yagi[3], T. Yamada[4], K. Shibata[5] and H. Mochizuki[2]

[1]*Quantum Beam Sci. Res. Dir., Natl. Inst. Quantum and Radiological Sci. Tech.;* [2]*Grad. School of Medicine, Osaka Univ.;* [3]*Tottori Univ.;* [4]*Neutron R&D Division, CROSS-Tokai;* [5]*Neutron Science Section, Materials and Life Science Division, J-PARC Center*

Uniaxial-Stress Control of Skyrmion Phase in MnSi

1. Introduction

Magnetic skyrmions are spin-swirling topological objects discovered in a long-wavelength helimagnet MnSi [1]. Figure 1(a) shows a schematic illustration of the spin arrangements in a magnetic skyrmion. Due to the two-dimensional soliton-like spin texture, the skyrmions acquire particle nature. Recent experimental studies have demonstrated that these magnetic particles can be created, deleted and transferred through a variety of external stimuli, for example, by flowing (spin-polarized) electric current [2, 3] or applying laser pulses [4]. Therefore, the skyrmions are expected to be applied in new spintronic and/or information storage devices, in which each skyrmion particle acts as a countable information carrier.

The magnetic skyrmions often form a two-dimensional triangular lattice in a plane perpendicular to the applied magnetic field, as shown in Fig. 1(b). Interestingly, recent ultrasound measurements on MnSi by Nii *et al*. revealed that the formation of the skyrmion lattice (SkL) is accompanied by anisotropic changes in elastic constants [5]. This suggests in turn that the SkL phase can be controlled by an application of anisotropic stress, which will be another methodology for manipulating skyrmions. Therefore, in the present study, we investigated the uniaxial-stress effects on the SkL phase in MnSi through small-angle neutron scattering (SANS) measurements using single-crystal samples at the TAIKAN instrument (BL15) in MLF of J-PARC.

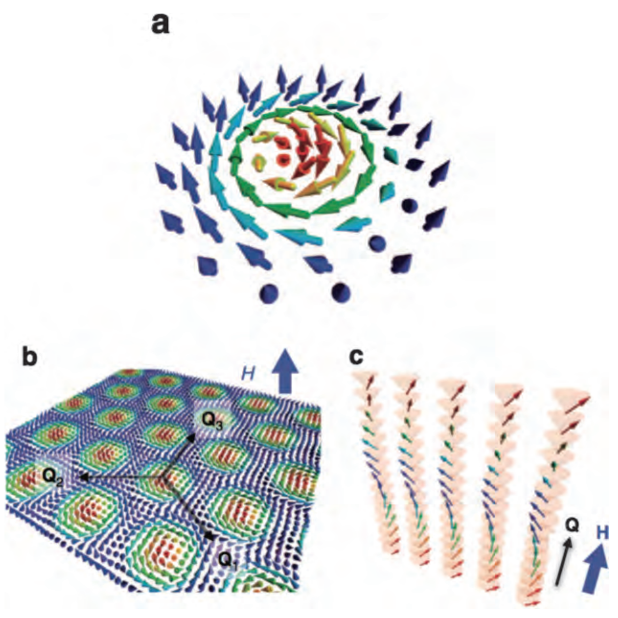

Figure 1. Schematic drawings of (a) single skyrmion, (b) triangular SkL and (c) conical magnetic order. (taken from Ref. [6] and modified to fit the present report.)

2. Preliminary magnetic susceptibility measurements under uniaxial stress

Prior to the SANS measurements, we performed AC magnetic susceptibility measurements under uniaxial stress in order to reveal how the magnetic phase diagram changes with the applied uniaxial stress. Figure 2(a) and 2(c) show contour mapping of the real part of the AC magnetic susceptibility on the *H*-*T* magnetic phase diagrams under zero uniaxial stress. Note that the difference in the color scale is due to different directions of the AC-magnetic fields; in Fig. 2(a) and 2(c), the AC fields were parallel and perpendicular to the DC magnetic field, respectively. In addition, the critical fields were also different because of the demagnetization effect arising from a difference in the shapes of the samples. Figure 2(b) and 2(d) show the magnetic phase diagram under uniaxial stress of 200 MPa applied parallel and perpendicular to the DC magnetic field, revealing that the parallel and perpendicular stresses squeeze and enlarge the SkL phase, respectively.

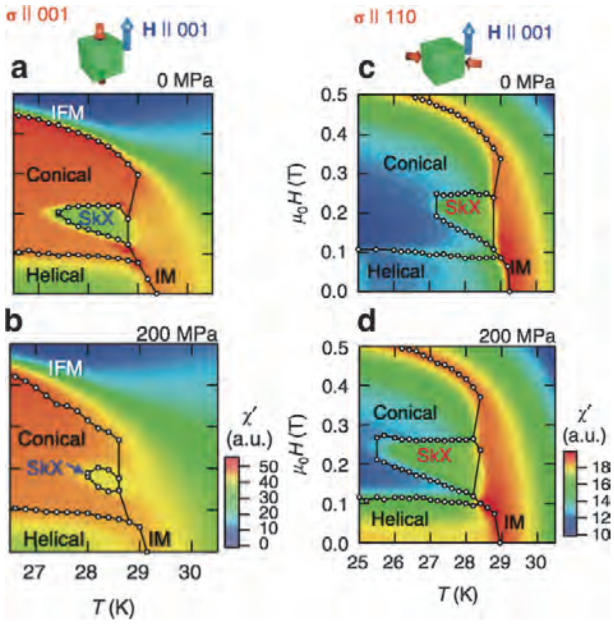

Figure 2. Contour maps of the real part of the AC magnetic susceptibility on the *H*-*T* magnetic phase diagrams. For (a) and (b), the AC and DC magnetic fields and uniaxial stress were parallel to each other. For (c) and (d), the uniaxial stress and the AC magnetic field were applied perpendicular to the DC magnetic field. (taken from Ref. [6], and modified to fit the present report.)

3. SANS measurements under uniaxial stress

To observe directly the uniaxial stress effects on the SkL phase, we performed SANS measurements under tunable uniaxial stresses. We prepared a bespoke uniaxial-stress insert, and loaded it into a vertical-field cryomagnet of MLF (see Ref. 6 for details). In Fig. 3(a), we schematically show the experimental setup. The uniaxial stress was applied along the q_z (vertical) direrction, which is parallel to the external DC magnetic field applied by a superconducting magnet. At 27.7 K and 0.19 T, the system was in the SkL phase under zero uniaxial stress. The triangular lattice of the skyrmions produces six magnetic Bragg spots on the q_x-q_y plane, and therefore we observed two of them on the scattering plane (q_y-q_z plane), as shown in Fig. 3(b). We increased the uniaxial stress without changing the temperature and the magnetic field, and measured the stress dependence of the SANS pattern. As a result, we found that the two magnetic reflections corresponding to the SkL phase disappeared with the stress' increase, and instead, two magnetic reflections appeared along the q_z direction, as shown in Fig. 3(b). These reflections are attributed to the conical magnetic order with magnetic modulation wave vector parallel to the magnetic field (see Fig. 1(c)). This demonstrates that the application of uniaxial stress indeed induces the phase transition from the SkL phase to the conical phase. Here, we emphasize that the critical stress of this transition is about 30 MPa, from which the mechanical energy to erase single skyrmion is roughly estimated to be 5×10^{-20} J. This value is significantly smaller than the energy cost for electric-current-induced skyrmion creation, 2.25×10^{-17} J, calculated in Ref. 7. This suggests that the application of uniaxial-stress can be another useful tool to manipulate skyrmions in magnetic materials.

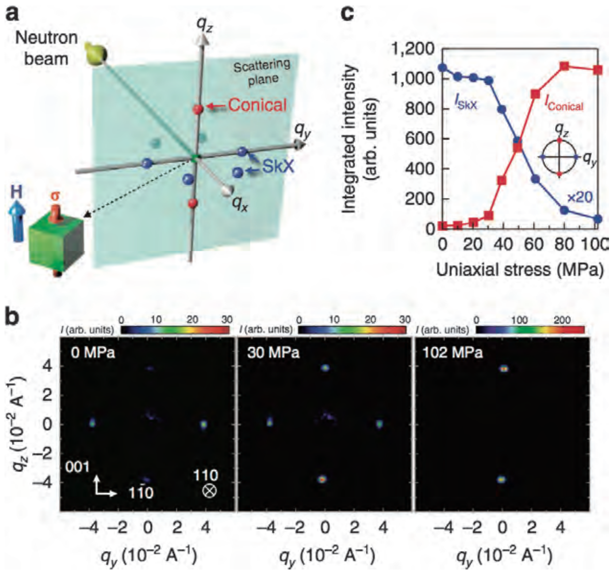

Figure 3. (a) A schematic showing the relationships among the incident neutron beam, the scattering plane, and the Bragg spots of the skyrmion and conical phases. (b) Typical SANS patterns measured at 27.7 K and 0.19 T with increasing uniaxial stress. (c) Uniaxial stress dependence of the intensities of the magnetic reflections of the skyrmion and conical orders. (taken from Ref. [6], and modified to fit the present report.)

Acknowledgements

We thank Y. Yamauchi and the members of the sample environment team in MLF of J-PARC for their technical support in the SANS measurements.

References

[1] S. Muhlbauer *et al.*, Science **323**, 915-919 (2009).
[2] F. Jonietz *et al.*, Science **330**, 1648-1651 (2010), X. Z. Yu *et al.*, Nat. Commun. **3**, 988 (2012).
[3] N. Romming *et al.*, Science **341**, 636 (2013).
[4] M. Finazzi *et al.*, Phys. Rev. Lett. **110**, 177205 (2013).
[5] Y. Nii *et al.*, Phys. Rev. Lett. **113**, 267203 (2014).
[6] Y. Nii, T. Nakajima *et al.*, Nat. Commun. **6**, 8539 (2015).
[7] W. Koshibae *et al.*, Jpn. J. Appl. Phys. **54**, 053001 (2015).

T. Nakajima[1], Y. Nii[1,*], A. Kikkawa[1], Y. Yamasaki[1,2], K. Ohishi[3], J. Suzuki[3], Y. Taguchi[1], Y. Iwasa[1,2], Y. Tokura[1,2], and T. Arima[1,4]
[1]*RIKEN Center for Emergent Matter Science (CEMS);* [2]*Department of Applied Physics and Quantum-Phase Electronics Center (QPEC), University of Tokyo;* [3]*Neutron Science and Technology Center, Comprehensive Research Organization for Science and Society (CROSS);* [4]*Department of Advanced Materials Science, University of Tokyo*
**Present address: Department of Basic Science, University of Tokyo*

Weyl Fermion in Spin Dynamics of $SrRuO_3$

1. Introduction

$SrRuO_3$ is a rare material exhibiting a ferromagnetic transition among 4d electron systems: it transitions to a ferromagnetic state at $T_C = 165$ K, takes a nearly-cubic perovskite type crystal structure, and shows a good electric conductivity at low temperatures. Normally, cubic ferromagnets, such as Fe, Ni, and so on, show very small magnetic anisotropy, and therefore, their spin wave gap is negligibly small. On the other hand, $SrRuO_3$ shows a large magnetic anisotropy and a finite spin wave gap is observed in it. Also, $SrRuO_3$ shows that an anomalous Hall resistivity is not proportional to the magnetization [1].

In ferromagnets, the repulsive Coulomb interaction between electrons results in an exchange splitting between bands with up- and down-spins, which produces spontaneous magnetization. The band crossing between an up-spin band and a different band with the opposite spin occurs due to the spin-orbit interaction, when the band overlaps of both spin components are finite. In this case, the effective Hamiltonian is described by $H = v(\mathbf{k}-\mathbf{k}_0)\boldsymbol{\sigma}$ with $\boldsymbol{k}$, $\boldsymbol{\sigma}$ and v being the momentum, Pauli spin matrices, and velocity, respectively. This is nothing but Weyl fermion and $\boldsymbol{k_0}$ is called Weyl point. In the ferromagnetic phase of $SrRuO_3$, a tight-binding model reveals that a number of Weyl points are produced in the first Brillouin zone [2]. The Weyl fermion produces the Berry phase, and the Berry curvature takes the form of the magnetic field of a monopole. The anomalous Hall conductivity σ_{xy} is described by the Berry curvature, and therefore, the fictitious magnetic field of the monopole is the origin of the anomalous Hall effect in $SrRuO_3$ [1]. We tried to observe spin waves in $SrRuO_3$ in order to detect the fictitious magnetic field as spin dynamics.

2. Neutron Brillouin scattering experiment

Because a large single crystal necessary for inelastic neutron scattering has not been synthesized for $SrRuO_3$, we performed neutron Brillouin scattering (NBS) experiments on HRC by using a polycrystalline sample [3]. NBS is the inelastic neutron scattering close to the forward direction. For observing ferromagnetic spin waves using a polycrystalline sample, the scattering intensity appears near (000) only and rapidly drops with increasing Q by the powder average. We can access the space near (000) using low-angle detectors and high-energy neutrons with high resolutions by approaching the kinematical constraint of the neutron scattering. HRC [4, 5], which has detectors at low angles down to 0.6°, provides such an opportunity for the present study.

Figure 1 shows the observed inelastic neutron scattering spectra with the background subtracted. Well-defined spin waves were observed at $T < T_C$, and it was confirmed that the inelastic neutron spectrum changes to that of the critical scattering at $T = T_C$. The observed peak positions of spin waves were well fitted to the dispersion relation of the ferromagnetic spin waves, $E(Q) = DQ^2 + E_g$. We determined the temperature (T) dependence of the stiffness constant D and the spin wave gap E_g, as shown in Fig. 2 (a) and (b).

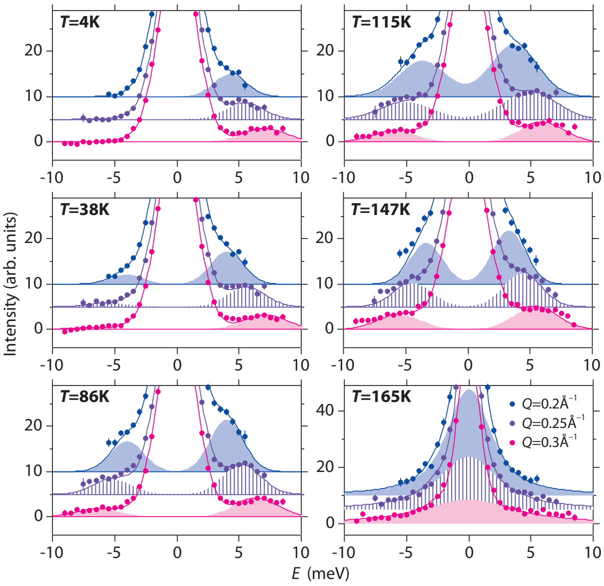

Figure 1. Observed spectra as a function of E (energy transfer) at several Q values for selected T. Spectra are shifted by a constant to aid the eye. The vertical bars represent statistical errors. The solid lines are curves fitted to the observed spectra, and the colored areas are magnetic components.

3. Results and summary

We found that $D(T)$ is proportional to the magnetization $M(T)$, which is a rather normal behavior. However, $E_g(T)$ was found to show a nonmonotonous T dependence, being well-fitted to the theoretical function $E_g(T) = a(M(T)/M_0)/[1+b(M(T)/M_0)(\sigma_{xy}(T)/\sigma_0)]$, where M_0 is the magnetization at zero temperature, $\sigma_0 = e^2/ha_0 = 9.9 \times 10^2\ \Omega^{-1}\mathrm{cm}^{-1}$ with $a_0 = 3.9$ Å (lattice constant of $SrRuO_3$), a and b are adjustable parameters (solid line in Fig. 2(b)). In this analysis, experimental data for $M(T)$ and $\sigma_{xy}(T)$

were used: $M(T)$ was determined by the T dependence of the magnetic Bragg intensity at (100) (Fig. 2(c)), and $\sigma_{xy}(T)$ was determined by the Hall effect measurement (Fig. 2(d)).

In the Hamiltonian of Weyl fermion $H = v(\mathbf{k}-\mathbf{k}_0)\boldsymbol{\sigma}$, one can relate the current operator j_a linearly to the spin operator σ_a ($a = x, y, z$) by replacing $\boldsymbol{k}$ with $\boldsymbol{k}+e\boldsymbol{A}$ and taking derivative of H with vector potential $\boldsymbol{A}$. By using this relation and the Kubo formula (conductivity is expressed as a current-current correlation), the generalized susceptibility for the band-crossing contribution, which is a spin-spin correlation, is proportional to σ_{xy}. Therefore, the Berry phase can be observed by inelastic neutron scattering through σ_{xy}.

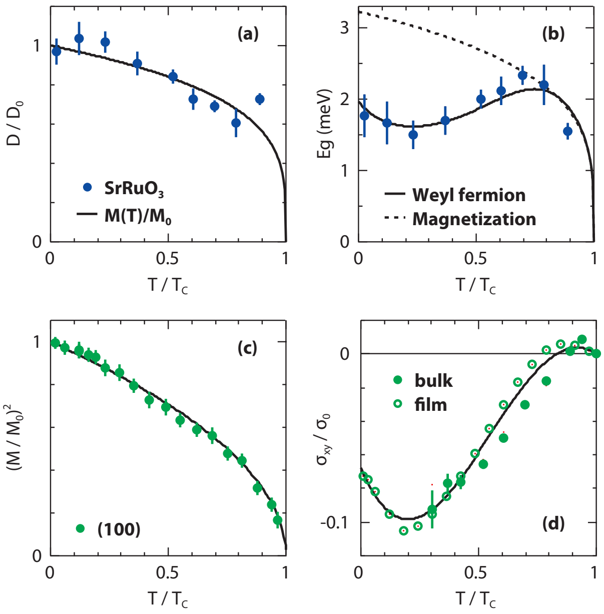

Figure 2. Stiffness constant D (a), spin wave gap E_g (b), intensity of magnetic Bragg scattering (c), and anomalous Hall conductivity σ_{xy} (d) in $SrRuO_3$ as a function of T/T_C. The vertical bars represent experimental errors.

Until this study was completed, Weyl fermions have been discussed in transport phenomena, in terms of spintronics. However, we showed here for the first time that the spin dynamics reflects directly Weyl fermions [3]. This result has revealed the novel connection between the transport and dynamical magnetic properties through the enhanced spin-orbit coupling effect.

References

[1] Z. Fang, N. Nagaosa, K. S. Takahashi, A. Asamitsu, R. Mathieu, T. Ogasawara, H. Yamada, M. Kawasaki, Y. Tokura, and K. Terakura, Science 302, 92 (2003).

[2] Y. Chen, D. L. Bergman, and A. A. Burkov, Phys. Rev. B 88, 125110 (2013).

[3] S. Itoh, Y. Endoh, T. Yokoo, S. Ibuka, J.-G. Park, Y. Kaneko, K. S. Takahashi, Y. Tokura, N. Nagaosa, Nature Communications 7, 11788 (2016).

[4] S. Itoh, T. Yokoo, S. Satoh, S. Yano, D. Kawano, J. Suzuki, and T. J. Sato, Nucl. Instr. Meth. Phys. Res. A 631, 90 (2011).

[5] S. Itoh, Y. Endoh, T. Yokoo, D. Kawana, Y. Kaneko, Y. Tokura, and M. Fujita, J. Phys. Soc. Jpn. 82, 043001 (2013).

S. Itoh[1,2], Y. Endoh[1,3], T. Yokoo[1,2], S. Ibuka[1,2], J.-G. Park[4,5], Y. Kaneko[3], K. S. Takahashi[3], Y. Tokura[3,6], and N. Nagaosa[3,6]

[1]*Institute of Materials Structure Science, KEK;* [2]*Neutron Science Section, Materials and Life Science Division, J-PARC Center;* [3]*RIKEN Center for Emergent Matter Science;* [4]*Institute for Basic Science;* [5]*Seoul National University;* [6]*Department of Applied Physics, The University of Tokyo*

Characterization of Ferromagnetic Order in $CePd_2P_2$

1. Introduction

A subject of significant interest in the *f*-electron systems is the competition between the Kondo effect and magnetic ordering, which frequently result in the occurrence of exotic quantum critical phenomena. In this context, a number of Ce compounds were investigated to clarify how the antiferromagnetic ordering competes with the Kondo effect, but a clear example of ferromagnetic (FM) ordering in a Ce compound is difficult to find. This is in striking contrast to the case of the uranium-based compounds, such as UGe_2, URhGe and UCoGe [1]. In order to explore the essential features of the FM quantum critical behavior and related phenomena, it would be intriguing to search for a new FM compound.

Recently, we found a new candidate for the Ce-based FM compound $CePd_2P_2$ [2]. Although this material was prepared by Jeitschko et al. in 1983, at that time, its detailed physical properties were not reported, except for the crystal structure [3]. Only recently, two groups independently examined the detailed magnetic properties of $CePd_2P_2$, and established the FM ordering with macroscopic measurements [4, 5]. Especially, Tran et al. reported an anomalous critical behavior and discussed a possible competition between the ferromagnetism and the Kondo effect in $CePd_2P_2$ [5].

We would like to note that $CePd_2P_2$ possesses several interesting features: e.g. (i) a large Curie temperature in spite of a large Ce-Ce distance, (ii) anomalous critical behavior, as reported in ref. [5], and more interestingly, (iii) it is a possible candidate for examining the FM quantum critical phenomena in a Ce-based compound. In the present study, we investigate the magnetic structure of $CePd_2P_2$ by neutron-scattering experiments, and examine the FM transition through the DC magnetization measurements in further detail [6]. In addition, we investigate the crystalline electric field (CEF) effect on the *4f* electron in $CePd_2P_2$ by probing the inelastic neutron scattering spectra.

2. Results and Discussion

To begin with, we confirmed the ferromagnetic ordering in $CePd_2P_2$ by the neutron-scattering experiment. Figure 1 exhibits neutron diffraction patterns measured at 3 K in the magnetically ordered phase (filled-blue circles) and at 40 K in the paramagnetic phase (filled-red circles). In order to extract magnetic signals, the intensity measured at 40 K was subtracted from that observed at 3 K, the residual intensity is depicted in Fig. 1 with open-blue rectangles. In a low-*Q* region, no Bragg peak was observed except for that at the fundamental Bragg positions. From this difference pattern, it is obvious that the magnetically ordered phase of $CePd_2P_2$ is a simple ferromagnetic order. Furthermore, the lack of a significant change of the intensity at the 002 position clearly indicates that an ordered moment is parallel to the *c*-axis. By analyzing the neutron scattering intensity at the 101 position, the magnitude of the ordered moment has been evaluated as ~ 1.3(3) μ_B per Ce ion at 3 K. A reduction in the ordered moment from the full moment (2.14 μ_B for $J = 5/2$) can be attributed to the CEF and/or the Kondo effect, as discussed in ref. [5].

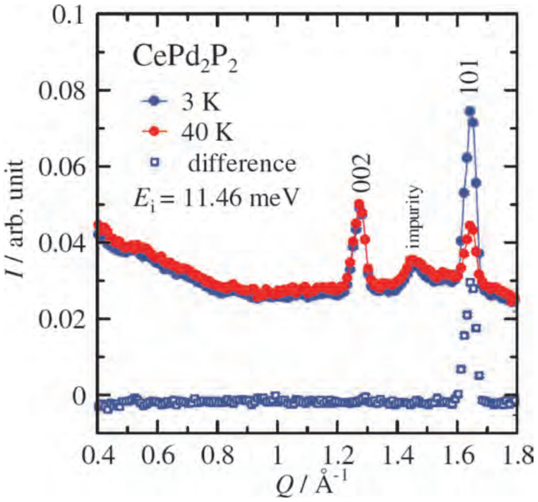

Figure 1. Neutron diffraction pattern at 3 and 40 K. The difference of the neutron-scattering intensity between 3 and 40 K is depicted with the open squares. The numbers on the peaks are the Miller indices.

In Fig. 2(a), we show the isothermal magnetization curves of $CePd_2P_2$ at 2 K. Here, the magnetization data labeled as "no-oriented" (circles) and "oriented" (triangles) in Fig. 2(a) were measured with an as-grown powder sample and a magnetically aligned powder sample, respectively. A clear hysteresis in the magnetization curves is also indicative of the FM ordering in $CePd_2P_2$ at low temperatures. The saturation magnetization is evaluated to be about 1 μ_B and 0.8 μ_B per Ce ion for oriented and no-oriented powder sample, respectively. The value of the oriented sample is in a reasonable agreement with the evaluated ordered moment from the neutron-scattering experiment (~ 1.3 μ_B). The slight discrepancy may be due to an imperfection of the field orientation of the powder sample. In any case,

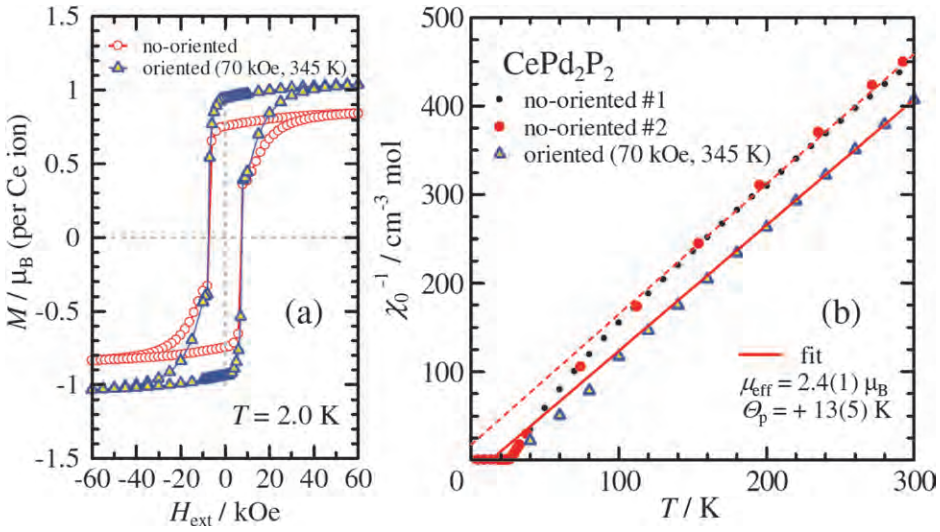

Figure 2. (a) Magnetic field dependence of the magnetization for CePd$_2$ P$_2$ measured at 2 K. (b) Reciprocal molar magnetic susceptibility of CePd$_2$ P$_2$ as a function of the temperature. Here χ_0^{-1} indicated by "oriented" (triangles) were measured with the powder sample, which was aligned in the magnetic field of 70 kOe at 345 K. The solid lines are results of a fit. The dash line is a guide to the eye.

the difference between the oriented and non-oriented powder sample is indicative of the magnetic anisotropy in CePd$_2$P$_2$ in the FM ordering state.

Next, we examine the magnetic properties in a paramagnetic region. Figure 2(b) shows the temperature dependence of the reciprocal magnetic susceptibility χ_0^{-1} of CePd$_2$P$_2$ for both "no-oriented" and "oriented" samples. As seen in Fig. 2(b), χ_0^{-1} of the oriented sample is smaller than that of the non-oriented sample. This difference in χ_0^{-1} in a paramagnetic state is also indicative of the magnetic anisotropy in CePd$_2$P$_2$ due to the CEF effect.

At high temperatures, χ_0 of the oriented sample shows Curie-Weiss behavior. From the result of a fit (red solid line), the effective magnetic moment and the paramagnetic Curie-Weiss temperature of CePd$_2$P$_2$ are evaluated as $\mu_{eff} = 2.4(1)$ μ_B /Ce and $\Theta_p = +13(5)$ K, respectively. The evaluated μ_{eff} is close to the free ion moment (2.54 μ_B) and consistent with the reported values [4, 5] within the experimental accuracy. On the other hand, Θ_p differs from their evaluated value ($\Theta_p^{Tran} = -2$ K [5]). This discrepancy in Θ_p can be attributed to a magnetic anisotropy owing to the CEF effect. In fact, a similar negative value of Θ_p was also obtained for χ_0^{-1} of our non-oriented sample. In contrast to their interpretation in ref. [5], the positive Θ_p of our oriented sample is in reasonable agreement with the ferromagnetic transition temperature of $T_C \sim 28$ K, and indicates strong FM correlations between the magnetic moments of Ce ions. Additionally, a deviation from the Curie-Weiss law at low temperatures could be attributed to the CEF effect and/or the development of ferromagnetic correlations.

Our neutron-scattering data indicate that the magnetic moments are parallel to the *c*-axis, so that the magnetic easy axis of CePd$_2$P$_2$ can be considered to be the *c*-axis. Considering the magnetic anisotropy observed in the magnetization measurement, a uniaxial (Ising-like) FM ordering is likely to be realized in CePd$_2$P$_2$.

Finally, we examine the inelastic neutron scattering spectra. Figure 3 shows the energy dependence of the *Q*-integrated inelastic neutron scattering intensity of CePd$_2$P$_2$ (blue-closed rectangles) and LaPd$_2$P$_2$ (red-open rectangles) measured at 3 K. To extract the contribution of the CEF excitations, the latter spectra is properly normalized and subtracted from that of CePd$_2$P$_2$ as a background. The residual is shown with the green-filled rectangles. In this Figure, one can observe a clear peak at around 35 meV, indicating the CEF excitation. The LS ground state of $J = 5/2$ for 4f^1 is lifted into the Γ_6, Γ_7^1 and Γ_7^2 doublets in the tetragonal CEF. The observed single-peak excitation spectra indicate that the excited two doublets have almost the same eigen energy, or, alternatively, the linear combination of Γ_7 states is possibly negligible in CePd$_2$P$_2$ [7]. In order to identify the CEF level scheme of CePd$_2$P$_2$, further experimental investigation is indispensable, in particular a magnetic measurement with a single-crystal sample is important.

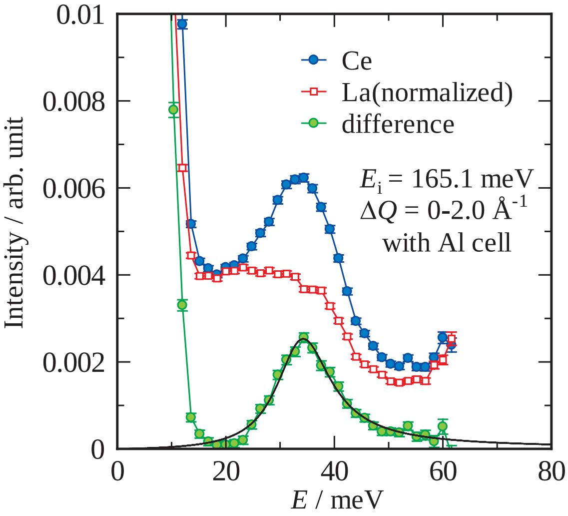

Figure 3. Energy dependence of the Q-integrated inelastic neutron scattering intensity of CePd$_2$P$_2$ (blue-closed rectangles) and LaPd$_2$P$_2$ (red-open rectangles) measured at 3 K. These data are integrated in a low-Q region [$Q = 0 \sim 2$ Å^{-1}]. The green-filled rectangles indicate the difference between those two sets of data. Here the data of LaPd$_2$P$_2$ is properly normalized and subtracted from the data of CePd$_2$P$_2$ as a background. To evaluate the CEF excitation levels of CePd$_2$P$_2$, we fitted the data with a Lorentzian curve, shown with solid lines.

3. Conclusion

We have performed a neutron scattering experiment to investigate the magnetic ordering in CePd$_2$P$_2$ and confirmed that an FM order is realized below T_C in CePd$_2$P$_2$. The ordered moment was evaluated to be ~ 1.3(3) μ_B per Ce ion at 3 K. The lack of a significant change in the neutron-scattering intensity at the 002 position indicates that the ordered moment is parallel to the c-axis. In particular, no evidence of the change in the magnetic structure was observed below T_C within the experimental accuracy.

In DC magnetization measurements with an as-grown powder sample and with a magnetically aligned powder sample, a clear magnetic anisotropy was observed in CePd$_2$P$_2$ in both the FM and paramagnetic phases. Considering the result of the neutron-scattering experiment, the magnetic easy axis can be considered to be the c-axis for CePd$_2$P$_2$. For the oriented sample, the saturation moment at 2 K of CePd$_2$P$_2$ is about 1 μ_B per Ce ion, and it is in reasonable agreement with the neutron-scattering data. From χ_0^{-1} of the oriented sample, the effective magnetic moment and the paramagnetic Curie-Weiss temperature of CePd$_2$P$_2$ are evaluated as μ_{eff} = 2.4(1) μ_B per Ce ion and Θ_p = +13(5) K, respectively. The positive value of Θ_p is in reasonable agreement with T_C of CePd$_2$P$_2$ and clearly indicates strong FM correlations between the magnetic moment of Ce ions.

A clear CEF excitation was observed at around 35 meV in the inelastic neutron scattering. The observed single-peak excitation indicates that the exited CEF states are almost quasi-quartet, or alternatively the linear combination of Γ_7 states is almost negligible for CePd$_2$P$_2$.

References

[1] As a review paper, e.g. D. Aoki, and J. Flouquet, J. Phys. Soc. Jpn 83 (2014) 061011.
[2] Konishi S., Ikeda Y., Araki S., Kobayashi C. T. 2013 presented at Japan Physical Society March meeting 27aPS33; Ikeda Y., Konishi S., Araki S., Kobayashi C. T., Yoshizawa H. 2014 presented at Japan Physical Society March meeting 28aPS27.
[3] Jeitschko W. and Hofmann K. W., J. Less-Common Metals 95 (1983) 317.
[4] Shang T *et al.*, J. Phys.: Condens. Matter 26 (2014) 045601.
[5] Tran H. V. and Bukowski Z., J. Phys.: Condens. Matter 26 (2014) 255602.
[6] Y. Ikeda, H Yoshizawa, S Konishi, S Araki, T. C. Kobayashi, T. Yokoo, and S. Ito J. Phys.: Conference Series 592 (2015) 012013.
[7] Because the Curie-Weiss behavior was observed at around 300 K, we expect that the energy scale of the second excited CEF state is at most as high as at room temperature. Therefore, no CEF excitations may be observed in a higher excitation range than those measured in this experiment.

Y. Ikeda[1,*], H Yoshizawa[1], S Konishi[2], S Araki[2], T. C. Kobayashi[2], T. Yokoo[3], and S. Ito[3]
[1]*Neutron Science Laboratory, The Institute for Solid State Physics, The University of Tokyo;* [2]*Graduate School of Natural Science and Technology, Okayama University;* [3]*Neutron Science Division, Institute of Materials Structure Science, High Energy Accelerator Research Organization*
**present address: Institute for Materials Research, Tohoku university*

Magnetic Excitations in Antiferromagnetic Alternating Spin-3/2 Chain Compounds *R*CrGeO$_5$

1. Introduction

We have studied the magnetism of the Cr^{3+} ions (spin 3/2) in *R*CrGeO$_5$ (R = Y or rare earth). Figure 1 shows its crystal structure [1]. The Cr^{3+} spins are expected to form an alternating spin-3/2 chain. We define the exchange interaction parameters J_1 and J_2 in Cr-Cr pairs with d_1 and d_2, respectively. The spin chains are separated from one another by GeO$_5$ square pyramids and R^{3+} ions.

We performed inelastic neutron scattering (INS) measurements on *R*CrGeO$_5$ (R = Y or ^{154}Sm) powder using the High Resolution Chopper (HRC) spectrometer at BL12 (Proposal Nos. 2012S01 and 2012B009). We confirmed that the spin system of Cr^{3+} was an antiferromagnetic (AF) alternating spin-3/2 chain [2]. The two compounds are the first spin-gap compounds with $S \geq 3/2$ except for spin cluster systems. We evaluated J_1 = 16.0 and J_2 = 2.3 meV for YCrGeO$_5$ and J_1 = 20.9 and J_2 = 1.1 meV for ^{154}Sm CrGeO$_5$.

The value of an exchange interaction is determined mainly by the Cr-Cr distance because a direct exchange interaction is dominant. Table 1 shows d_1 and d_2 values. The J_1 and J_2 values in YCrGeO$_5$ and ^{154}Sm CrGeO$_5$ are also written. The value of the exchange interaction decreases with increasing the Cr-Cr distance. We performed INS measurements on *R*CrGeO$_5$ (R = Ho, ^{166}Er or Nd) powder to investigate the Cr-Cr distance dependence on magnetism.

2. Experimental methods

Crystalline powder of *R*CrGeO$_5$ was synthesized using a solid-state-reaction method at 1,523 K in air with intermediate grindings [1]. We performed INS measurements using the High Resolution Chopper (HRC) spectrometer at BL12 (Proposal Nos. 2012B009 and 2015A0016) [3-5].

3. Results and discussion

Figure 2 and 3 show the INS intensity I(Q,ω) maps of *R*CrGeO$_5$ powder. Here, Q and ω are the magnitude of the scattering vector and the energy transfer, respectively. The energy of incident neutrons is E_i = 51.1 and 46.1 meV for Figs. 2 and 3, respectively. The bindings of Q and ω are 0.1 Å^{-1} and 0.25 meV, respectively. The intensity is normalized to compare data in different proton numbers and sample weights.

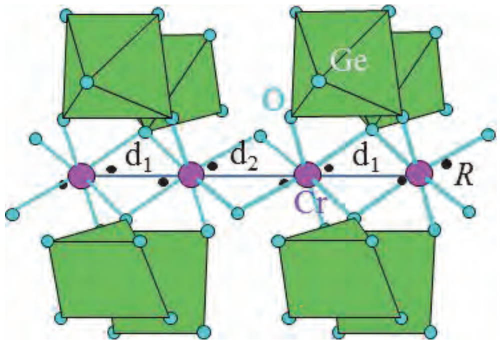

Figure 1. A part of the *R*CrGeO$_5$ structure showing two kinds of Cr-Cr distances in the chain of edge-sharing CrO$_6$ octahedra, GeO$_5$ square pyramids, and *R* atoms.

Table 1. Values of d_1, d_2 and d_2/d_1 in *R*CrGeO$_5$. We also show the J_1 and J_2 values in YCrGeO$_5$ and ^{154}Sm CrGeO$_5$.

	d_1 (Å)	d_2 (Å)	d_2/d_1	J_1 (meV)	J_2 (meV)
Y	2.811(4)	2.872(4)	1.022	16.0	2.3
Er	2.809(14)	2.873(14)	1.023		
Ho	2.813(12)	2.875(12)	1.022		
Sm	2.770(4)	2.952(4)	1.066	20.9	1.1
Nd	2.781(6)	2.964(6)	1.066		

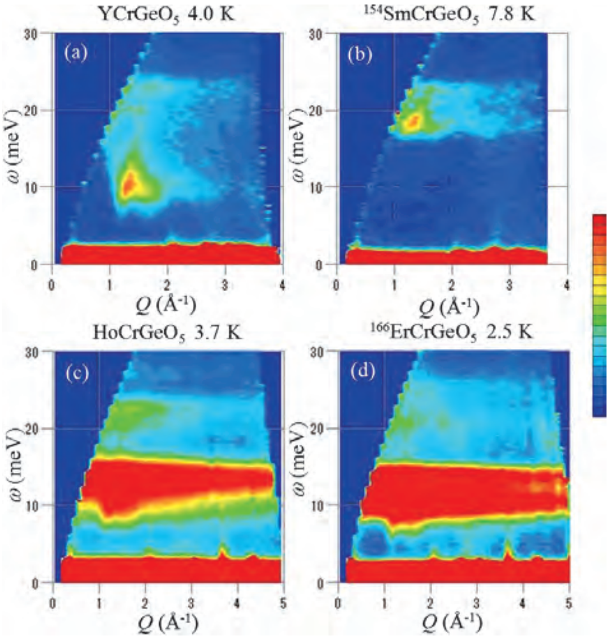

Figure 2. Maps of the neutron scattering intensity in the Q – ω plane. The energy of the incident neutrons E_i is 51.1 meV. The right vertical key shows the INS intensity in arbitrary units.

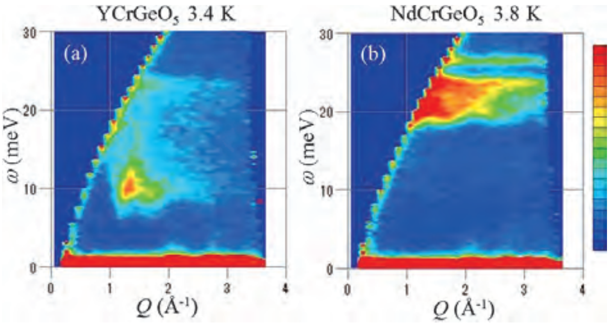

Figure 3. Maps of the neutron scattering intensity in the Q − ω plane. The energy of the incident neutrons E_i is 46.1 meV. The right vertical key shows the INS intensity in arbitrary units.

We can see magnetic excitations at $8 \leq \omega \leq 23$ meV in $YCrGeO_5$ and $18 \leq \omega \leq 23$ meV in $^{154}SmCrGeO_5$. As suggested, the magnetic excitations can be explained by the AF alternating spin-3/2 chain model.

We can see strong excitations at $10 \leq \omega \leq 15$ meV in $HoCrGeO_5$ and $9 \leq \omega \leq 15$ meV in $^{166}ErCrGeO_5$. The excitations remain even at high Q. Probably, crystal-field excitations of Ho and Er exist in the energy range. The *Q*-dependence of the INS intensity around $\omega = 10$ meV, however, shows a maximum around $Q = 1.3$ Å^{-1} (not shown) in both the compounds. The *Q*-dependence cannot be explained by the crystal-field excitations. We observed a maximum around $Q = 1.3$ Å^{-1} in $YCrGeO_5$. Therefore, the excitations at $10 \leq \omega \leq 15$ meV in $HoCrGeO_5$ and $9 \leq \omega \leq 15$ meV in $^{166}ErCrGeO_5$ include magnetic excitations of Cr. Weak excitations are seen up to 24 and 25 meV in $HoCrGeO_5$ and $^{166}ErCrGeO_5$, respectively, at small *Q*. The d_1 and d_2 values are almost the same in the three compounds. Probably, magnetic excitations of Cr exist in almost the same energy range in the three compounds.

We can see strong excitations at $20 \leq \omega \leq 25$ meV in $NdCrGeO_5$. The excitations remain even at a high *Q*. Probably, crystal-field excitations of Nd exist in the energy range. The *Q*-dependence of the INS intensity around $\omega = 20$ meV measured using neutrons with $E_i = 207$ meV shows a maximum around $Q = 1.3$ Å^{-1}. In addition, the d_1 and d_2 values in $NdCrGeO_5$ are close to those in $SmCrGeO_5$. Therefore, magnetic excitations of Cr must exist at $20 \leq \omega \leq 25$ meV.

4. Future Plans

We will evaluate the crystal-field excitations of Ho, Er, and Nd and subtract them from the observed excitations to obtain magnetic excitations of Cr. We will obtain INS intensity maps along the spin chain in $RCrGeO_5$ (*R* = Ho, ^{166}Er or Nd) using the conversion method [6] and evaluate the J_1 and J_2 values from comparison with the calculated results as performed in [2].

References

[1] R. V. Shpanchenko et. al., J. Solid State Chem. 181, 2433 (2008).
[2] M. Hase, et. al., Phys. Rev. B 90, 024416 (2014).
[3] S. Itoh, et. al., Nucl. Instr. Meth. Phys. Research A 631, 90 (2011).
[4] S. Yano, et. al., Nucl. Instr. Meth. Phys. Research A 654, 421 (2011).
[5] S. Itoh, et. al., Nucl. Instr. Meth. Phys. Research A 661, 58 (2012).
[6] K. Tomiyasu, et. al., Appl. Phys. Lett. 94, 092502 (2009).

M. Hase[1], S. Asai[2], M. Soda[2], T. Masuda[2], D. Kawana[2], T. Yokoo[3], S. Itoh[3], and M. Kohno[1]
[1]*National Institute for Materials Science (NIMS);* [2]*The Institute for Solid State Physics (ISSP), The Univ. Tokyo;* [3]*High Energy Accelerator Research Organization (KEK)*

Coherent Spin-Wave Excitations in a Correlated Metallic Antiferromagnet

1. Introduction

Topological materials have been a standout in the field of quantum matter ever since the discovery of the topological insulator [1]. However, their history reaches back to Quantum Hall insulators (QHIs) are their future seems ever more exciting with new systems surfacing every day. Weyl semimetals are characterized by pairs of magnetic monopoles (skyrmions/anti-skyrmions) in momentum space called Weyl nodes [2]. A distinguishing, but not necessarily unique, feature of WSMs is a surface “Fermi arc”—an incomplete line segment of filled states which connects a pair of bulk Weyl nodes via the 2D projection onto the surface. Such surface states have been observed by ARPES in a variety of materials following the initial discovery in the non-centrosymmetric TaAs [3], and have been proposed to exist in Mn_3Sn [4]. The anomalous Hall Effect observed in Mn_3Sn at high temperatures is may be explained if characterized as a WSM, but definitive evidence awaits [5].

Weyl semimetals present a unique case where the origin of the topological properties themselves is a particular pseudo-spin construction in k-space [6]. The potential for neutron scatter is paramount but relies on access to large ranges of momentum transfer, including the difficult to reach low-Q inelastic regime. The High Resolution Chopper spectrometer (HRC) is aptly designed to fill this tall order to separate the ordinary scattering from the potentially anomalous.

2. Magnetic dispersion in Mn_3Sn

We utilized a 200 meV incident energy conFiguration on the HRC at JPARC to map the full bandwidth of dispersive magnetic modes in the metallic Mn_3Sn. The 12 g sample used for this experiment was co-aligned into a $(3\ \mathrm{cm})^3$ volume using the forward scattering x-ray Laue facilities available at ISSP (see Fig. 1), enabling the use of the small angle detector bank typically used for powder samples. With the multi-rep conFiguration allowing 200 meV, 45 meV, and 19 meV the range of excitation energies covered in the first Brillouin zone was impressive.

The steep magnetic dispersion is clearly shown in Fig. 2 for modes traveling along a (120)-type axis of the hexagonal plane. For an itinerant system, these excitations are surprisingly coherent. A complimentary view of the hexagonal plane is shown Fig. 3. The presence of rings at the finite energy transfer of 45 meV indicates modes propagating in all basal directions. The slight asymmetry of the spin-wave velocities seen here also extends into the orthogonal direction. Past studies using a triple-axis spectrometer found the excitations along the (00L) direction to be consistent with a linear spin-wave theory [7]. On the basis of our measurements, a localized magnetic component does seem to be present for all independent crystal directions and an assessment of the degree to which this is captured by a linear model is underway.

Lastly, we made use of the small-angle scattering capabilities of HRC to access the 1st Brillouin zone, where the hexagonal symmetry of the magnetic scattering is also discernable. While the wide angle scattering seems the most reliable indicator of coherent excitations originating from magnetic moments with a relatively sharp form factor, it is the low-angles that will be most sensitive to deviations from this conventional case. With careful background subtraction and normalization to a vanadium standard, we hope this data can be used in conjunction with that from the other detector banks.

Figure 1. Co-aligned sample of Mn_3Sn (12 g). Alignment was performed using the forward scattering X-ray Laue apparatus in the Masuda Lab at ISSP.

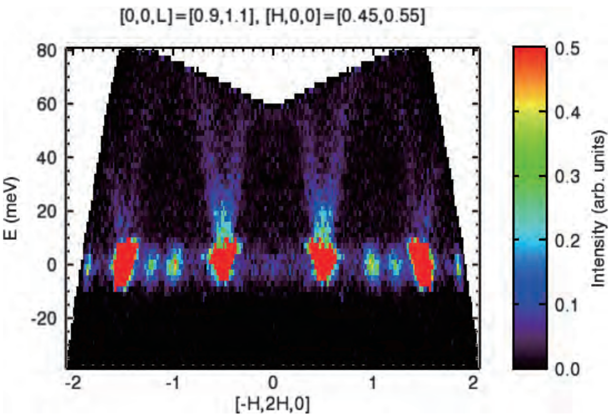

Figure 2. Magnetic dispersion of Mn_3Sn at 5 K.

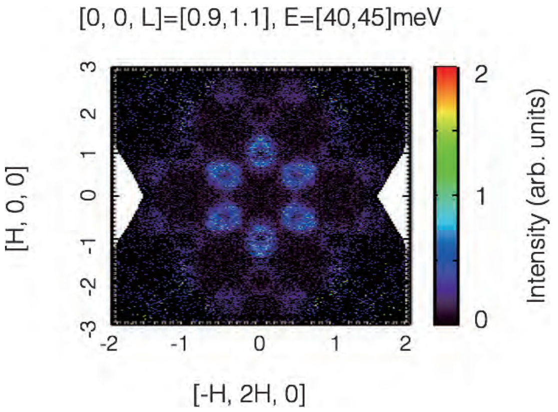

Figure 3. Dispersive rings for Mn_3Sn shown in the hexagonal plane. The aspect ratio has been chosen to respect the physical scattering angles.

4. Future Plans

The extensive dataset on Mn_3Sn gathered using the HRC should be sufficient to establish an accurate spin Hamiltonian. The first stage is to perform a global fit of a linear spin-wave theory consistent with the magnetic ground state. We will also combine the small and wide angle scattering data by careful normalization in an effort to establish whether a localized model is incomplete. If so, a follow-up experiment may well be warranted.

References

[1] M. Hasan and C. Kane, Rev. Mod. Phys. **82**, 3045 (2010).

[2] X. Wan, A. M. Turner, A. Vishwanath, and S. Y. Savrasov, Physical Review B 83, 205101 (2011).

[3] B. Q. Lv *et al.*, Physical Review X, 5(3):031013, July 2015.

[4] H. Yang *et al.*, https://arxiv.org/abs/1608.03404 (preprint).

[5] S. Nakatsuji, N. Kiyohara, and T. Higo. Nature, Oct. 2015.

[6] M. Bjerngaard, B. Galilo, and A. Turner. *Probing spin-momentum locking of Weyl nodes with neutron scattering*. Bulletin of the American Physical Society, Mar. 2016.

[7] J. W. Cable, N. Wakabayashi, and P. Radhakrishna, Physical Review B **48**, 6159 (1993).

G. G. Marcus[1], J. Kindervater[1], M. Ikhlas[1], N. Kiyohara[1], M. Soda[2,3], S. Nakatsuji[2], T. Masuda[2,3], and C. L. Broholm[1]

[1]*Institute for Quantum Matter, Department of Physics and Astronomy, Johns Hopkins University;* [2]*Institute for Solid State Physics, University of Tokyo;* [3]*Neutron Science Section, Materials and Life Science Division, J-PARC Center*

Magnetoelectric Coupling in the Honeycomb Antiferromagnet $Co_4Nb_2O_9$

1. Introduction

$Co_4Nb_2O_9$ is one of the magnetoelectric multiferroics. This material belongs to the $A_4B_2O_9$ (A = Co, Fe, Mn, and B = Nb, Ta), which have been studied since 1960's [1]. In $Co_4Nb_2O_9$, the Co(1) and Co(2) honeycomb layers alternately stack along the *c*-axis. Bertaut and coworkers analyzed its powder neutron diffraction patterns and reported that the Co^{2+} magnetic moments are ordered in a antiferromagnetically parallel way to the trigonal axis below $T_N = 27.4$ K, resulting in the magnetic space group P-3'c'1 with identical magnetic and crystallographic unit cells [1]. As a consequence, a linear ME effect is expected. In fact, the ME effect in polycrystalline $Co_4Nb_2O_9$ was first reported by Fischer *et al.* [2] and reinvestigated recently by Fang *et al.* [3], which revealed a large magnetoelectric coupling. In addition to the electric polarization induced by a magnetic field, they found out that $Co_4Nb_2O_9$ also exhibits a large modification in the magnetization by an electric field in the antiferromagnetic phase.

Motivated by these facts, we performed an investigation using single crystals of $Co_4Nb_2O_9$, necessary to elucidate intriguing ME properties in this material [4].

2. Experimental details

Single crystals of $Co_4Nb_2O_9$ were grown by the floating zone method. The crystallographic principal axes were determined by using x-ray Laue photographs. The magnetization was measured by using MPMS. The Laue photograph and magnetization measurement were performed at ISSP, University of Tokyo. The magnetic structure was determined by neutron diffraction of a single crystal (diameter of 0.5 cm and length ~1 cm) using the time-of-flight neutron diffractometer BL18 SENJU, installed at MLF, J-PARC. Intensities of 480 reflections (in condition $I > 3\sigma$) were collected at $T = 10$ K. The crystal and magnetic structures with atomic coordination, scale factor, extinction, and volume fraction parameters were refined using JANA 2006 [5] and visualized by VESTA [6].

3. Results

In the single-crystal neutron diffraction measurement, we observed an increase of 00l magnetic Bragg reflections with $l = 2n$ below T_N as shown in Fig. 1, which clearly indicates the ordering of the in-plane components of the Co^{2+} magnetic moments. It contradicts the early magnetic structure analysis by Bertaut *et al.* [1]. According to a symmetry analysis, if the trigonal symmetry is retained, the magnetic moments should be parallel to the trigonal axis, which is not consistent with the existence of 002 magnetic reflection and anisotropy in the magnetic susceptibility [4]. The magnetic structure can be described as antiferromagnetic monoclinic or triclinic space group as *C*2/*c*', *C*2'/*c*, or *P*-1'. We obtained the best agreement between experimental data and calculation for magnetic models, described by monoclinic magnetic space groups *C*2/*c*' with residual factor R = 8.38% (wR = 15.72%), as shown in Fig. 2. In this magnetic structure, the Co^{2+} magnetic moments are aligned perpendicularly to the [110] direction. In a honeycomb layer, the neighboring Co^{2+} moments are

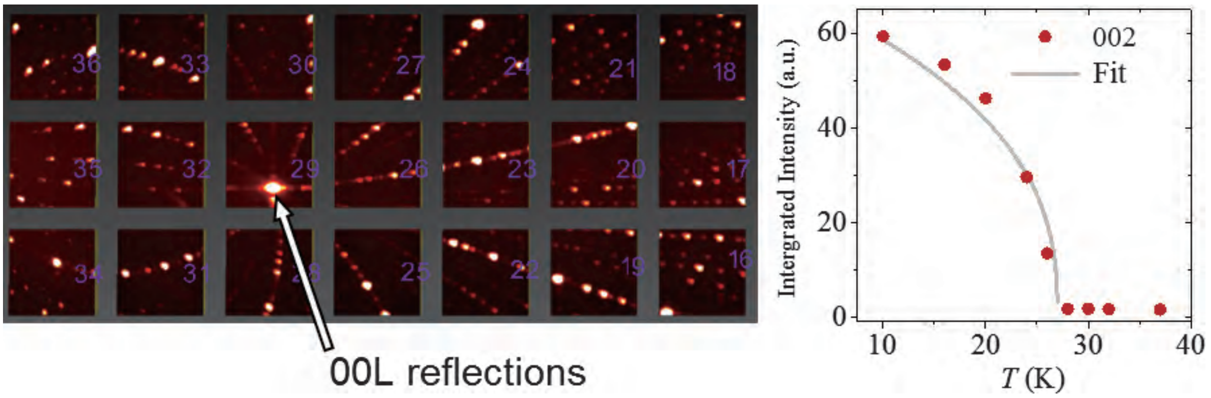

Figure 1. Laue pattern of $Co_4Nb_2O_9$ recorded at BL18, MLF/J-PARC, and temperature dependence of the integrated intensity of 002 magnetic Bragg reflection.

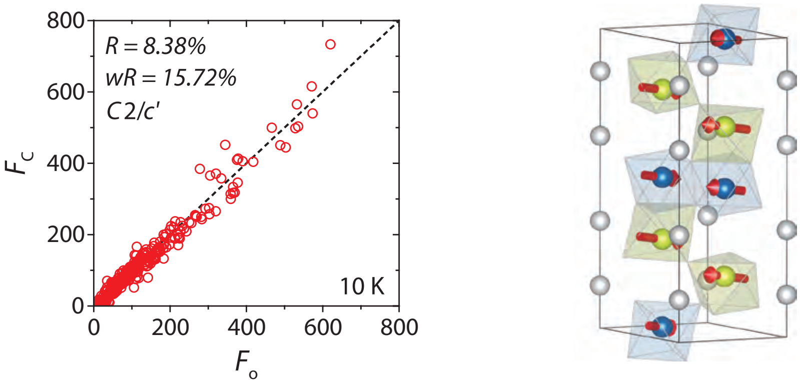

Figure 2. Comparison between observed and calculated intensities of the magnetic reflections, and a refined magnetic structure of $Co_4Nb_2O_9$.

arranged in opposite directions. The antiferromagnetic honeycomb layers stack along the trigonal axis without changing the spin orientation. The magnitudes of the magnetic moments of Co^{2+} at distinct crystallographic positions, denoted as Co(1) and Co(2), are 3.5 μ_B and 2.6 μ_B, respectively. Both magnetic moments are canted by around 20° away from the basal plane. From the result of the measurement of the magnetoelectric effect, this compound has non-zero off-diagonal terms of the linear magnetoelectric tensor. The magnetic structure is consistent with the anisotropy of the magnetoelectric effects [4].

4. Conclusion

We revised the magnetic structure of magneto-electric multiferroic $Co_4Nb_2O_9$ by using single crystal neutron diffraction. The in-plane components of the Co^{2+} magnetic moments are aligned antiferromagnetically, which induces off-diagonal terms of the linear magnetoelectric tensor.

References

[1] E. F. Bertaut *et al.*, J. Phys. Chem. Solids, 21, 234 (1961).
[2] E. Fischer *et al.*, Solid State Commun. 10, 1127 (1972).
[3] Y. Fang *et al.*, Sci. Rep. 4, 3860 (2014).
[4] N. D. Khanh *et al.*, Phys. Rev. B, 93, 075117 (2016).
[5] V. Petricek *et al.*, Z. Kristallogr. 229, 345 (2014).
[6] K. Momma and F. Izumi, J. Appl. Crystallogr. 44, 1272 (2011).

N. D. Khanh[1,2], N. Abe[1], H. Sagayama[3], A. Nakao[4], T. Hanashima[4], R. Kiyanagi[5], Y. Tokunaga[1], and T. Arima[1]
[1]*Department of Advanced Materials Science, University of Tokyo;* [2]*Department of Physics, Tohoku University;* [3]*Institute of Materials Structure Science, KEK;* [4]*Neutron R&D Division, CROSS-Tokai;* [5]*Materials and Life Science Division, J-PARC Center*

Spin Excitations in Hole-Overdoped Iron-Based Superconductivity

1. Introduction

Since the superconducting phase of iron pnictides lies beside the static antiferromagnetic (AFM) ordering phase, significant efforts have been focused on examining their spin dynamics. In order to clarify the role of magnetism for superconductivity in Fe-based superconductors, understanding the overall spin dynamics by using inelastic neutron scattering (INS) is indispensable.

INS studies on the spin fluctuations of non-doped $A\mathrm{Fe_2As_2}$ (A = Ba, Sr or Ca) over the entire Brillouin zone have clarified that the spin dispersion can be well described by the J_1-J_2 model. However, it is unclear whether the model, which is based on a localized spin picture, is valid because the carriers show an itinerant character. To establish a definitive model of magnetism in a wide hole-doping range, we report the overall spectra of spin fluctuations in hole-overdoped $\mathrm{Ba_{1-x}K_xFe_2As_2}$ obtained by the INS technique.

2. Experiments

Single crystals of $\mathrm{Ba_{0.5}K_{0.5}Fe_2As_2}$ (T_c = 36 K) and $\mathrm{KFe_2As_2}$ (T_c = 3.4 K) were grown by the KAs self-flux method [1].

The INS measurement was performed using the Fermi chopper spectrometer 4SEASONS in J-PARC [2]. We co-aligned 160 and 300 single crystals with $x = 0.5$ (~5 g) and $x = 1$ (~5 g), respectively. We employed the multi-E_i method with incident neutron energies of E_i = 31, 65, 110, 202, 409, 720 meV for $\mathrm{Ba_{0.5}K_{0.5}Fe_2As_2}$ and E_i = 30, 75, 149, 423 meV for $\mathrm{KFe_2As_2}$. The incident beam was parallel to the c-axis.

3. Results

We describe the (H, K) plane with orthorhombic notation, even though the superconducting $\mathrm{Ba_{1-x}K_xFe_2As_2}$ has a tetragonal crystal structure to facilitate comparison with non-doped $\mathrm{BaFe_2As_2}$. In $x = 0.5$, clear incommensurate peaks appeared around the (±1, 0) and (0, ±1) splitting along the longitudinal direction with a wave vector of ($\pm2\delta$, 0) and (0, $\pm2\delta$), respectively, where $\delta = 0.06$ at E = 13 meV. The ($1\pm2\delta$, 0) position corresponds to [$\pi(1\pm2\delta,0)$] in the ab plane and ($0.5\pm\delta$, $0.5\pm\delta$) in tetragonal notation. As the energy increases, spin excitations start to split along the transverse direction corresponding to ($\pm1\pm2\delta$, K) or (H, $\pm1\pm2\delta$) and reach the magnetic zone boundary with merging signals from the next zone boundaries. Figure 1(a) shows the dispersion cuts along the transverse direction (1, K) in $\mathrm{Ba_{0.5}K_{0.5}Fe_2As_2}$. A clear spin wave-like dispersion was observed up to E = 200 meV, similarly to the case of x = 0 and 0.33 [3].

In $x = 1$, on the other hand, the dispersive spin excitations reach the zone boundary around E = 80 meV, which is considerably lower than the energy for $x = 0.5$ (Fig.1(b)). Instead, a vertical dispersion with a chimney-like structure was observed from E = 80 meV up to 200 meV (Fig.1(c)). This chimney-like structure cannot be explained by the J_1-J_2 model, suggesting this structure has originated from itinerant character of electrons. In $x = 0.5$, signals of the chimney-like structure can also be found above E = 200 meV, but they are less clear than those in $x = 1$.

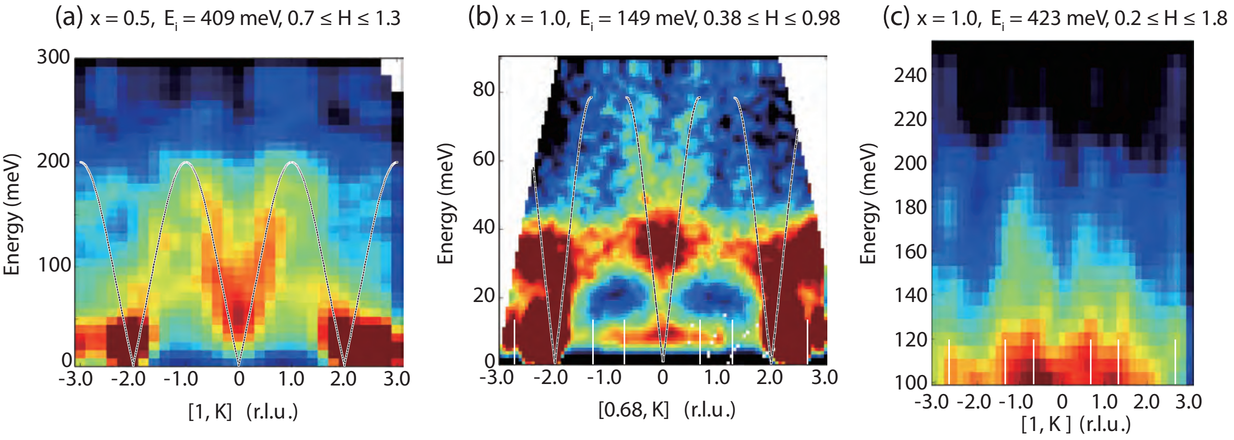
(a) $x = 0.5$, E_i = 409 meV, $0.7 \le H \le 1.3$
(b) $x = 1.0$, E_i = 149 meV, $0.38 \le H \le 0.98$
(c) $x = 1.0$, E_i = 423 meV, $0.2 \le H \le 1.8$

Figure 1. Dispersion cuts of (a) $\mathrm{Ba_{0.5}K_{0.5}Fe_2As_2}$ and (b) $\mathrm{KFe_2As_2}$ along the K direction, respectively. The solid lines are a guide to the eye. The vertical white-dashed lines depict the magnetic zone boundaries. (c) High-energy spin excitation of $\mathrm{KFe_2As_2}$ with E_i = 423 meV.

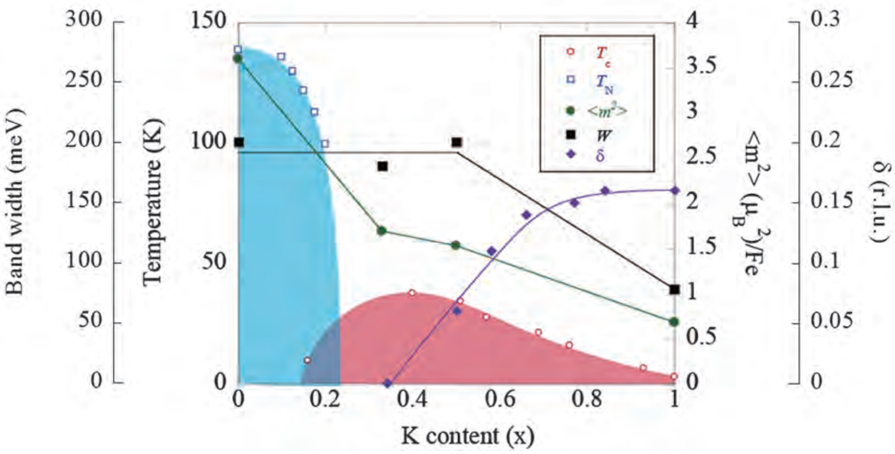

Figure 2. Phase diagram of $Ba_{1-x}K_xFe_2As_2$. Symbols denote T_c (open circles), The Néel temperature T_N (open squares), the total fluctuating magnetic moment $<m^2>$ (closed circles), bandwidth of the spin wave W (closed squares), and the incommensurability δ (closed diamonds).

4. Discussion

We summarize the phase diagram of this system in Fig. 2. The present observations demonstrate that the energy scale of the dispersive spin wave is robust upon hole doping up to $x = 0.5$, which is followed by a rapid decrease up to $x = 1$. The smaller band width of the spin wave leads to a less-effective magnetic exchange coupling J according to the Heisenberg model. The small value of J in KFe_2As_2 is consistent with the fact that its electronic interaction strength U is quite large.

The chimney-like structure can originate from particle-hole excitations, which define the itinerant character of the spin fluctuations. Note that the chimney-like structure resembles the spin excitations in the itinerant AF metals such as Cr [4]. The present results show that the bandwidth decreases and the chimney-like dispersion appears with hole doping. This is qualitatively consistent with DFT + DMFT calculations [5], which also supports the view that cause of the chimney-like dispersion could be the particle-hole excitations.

The suppression of T_c in hole-overdoped (Ba,K)Fe_2As_2 can rather be attributed to the reduction of J, which remains almost constant from the non-doped to the optimum-doped region and is followed by a rapid reduction in the overdoped region. The J dependence of the superconductivity has also been suggested in studies on spin resonance. Stronger magnetic correlation leads to a larger energy split between the resonance and the superconducting gap energy. In fact, the resonance energy in overdoped (Ba,K)Fe_2As_2 approaches the superconducting gap energy with doping up to $x = 0.77$ [6], which can result from the reduction of J. These results lead to the conclusion that there is a strong relationship between magnetism and superconductivity in $Ba_{1-x}K_xFe_2As_2$. This work has been published in Sci. Rep. [7].

References

[1] K. Kihou *et al.*, J. Phys. Soc. Jpn., 85 034718 (2016).
[2] R. Kajimoto *et al.*, J. Phys. Soc. Jpn., 80 SB025 (2011).
[3] M. Wang *et al.*, Nat. Commun., 4 2874 (2013).
[4] Y. Endoh *et al.*, J. Phys. Soc. Jpn., 75 111002 (2006).
[5] Z. P. Yin *et al.*, Nat. Phys., 10 845 (2014).
[6] C. H. Lee *et al.*, Sci. Rep., 6 23424 (2016).
[7] K. Horigane *et al.*, Sci. Rep., 6 33303 (2016).

K. Horigane[1], K. Kihou[2], K. Fujita[3], R. Kajimoto[4], K. Ikeuchi[5], S. Ji[6], J. Akimitsu[7], and C. H. Lee[2]

[1]*Graduate School of Natural Science and Technology, Okayama University;* [2]*National Institute of Advanced Industrial Science and Technology (AIST);* [3]*Aoyama Gakuin University;* [4]*J-PARC Center, Japan Atomic Energy Agency;* [5]*Neutron R&D Division, CROSS-Tokai;* [6]*Max Plank POSTECH Center for Complex Phase Materials;* [7]*Research Center of New Functional Materials for Energy Production, Storage, and Transport, Okayama University*

Tetra-Ortho-Tetra Type Phase Transitions and Inhomogeneous Magnetism in Sr_2VO_4

1. Introduction

Sr_2VO_4 is attracting renewed attention as a candidate compound for a d^1 Mott insulator showing novel spin-orbital magnetism. It has a tetragonal K_2NiF_4 structure with the space group *I*4/*mmm* at room temperature. The $V^{4+}(3d^1)$ is octahedrally coordinated with six ligand oxygen ions, where the octahedron is elongated along the *c* axis. The crystal field partially lifts the threefold degeneracy of the t_{2g} orbitals by splitting them into d_{xy} and d_{yz}/d_{zx} orbitals with d_{xy} having a higher energy. Thus, the single *d*-electron would occupy the unquenched d_{yz}/d_{zx} orbitals in case of a negligible spin-orbit interaction. However, it has been pointed out that the spin-orbit coupling may be large enough to split the d_{yz}/d_{zx} state into two Kramers doublets [1]. It was also suggested that a magnetic octupole order would be the ground state of Sr_2VO_4.

Recently, several groups successfully synthesized high quality polycrystalline samples. The magnetic susceptibility (χ) and heat capacity measurements confirmed that the compound successively undergoes three phase transitions at T_{c0} ~ 10 K, T_{c1} ~ 100 K, and T_{c2} ~ 130 K [2,3]. Regarding the magnetic properties, the χ showed a sudden drop just below T_{c1} and a clear hysteresis was observed in the magnetization measurement below T_{c0}. A previous muon spin relaxation (μSR) study reported an anomalous magnetic ordered state with residual magnetic fluctuation, which has been observed in several geometrically frustrated magnets, in the temperature (T) range of $1.8\ K \leq T \leq T_{c0}$ [4].

To gain a further insight into the three phase transitions in Sr_2VO_4, we performed synchrotron radiation x-ray diffraction (SR-XRD) and μSR experiments on polycrystalline sample [5]. We carried out the SR-XRD experiment at the BL-8A Photon Factory (KEK-PF) and a μSR measurement was made at the D1 instrument at J-PARC MUSE above 4.2 K. Then, we extended the μSR measurement down to 30 mK by using the dilution refrigerator furnished on the M15 beamline at TRIUMF, Canada.

2. Synchrotron radiation x-ray diffraction

Above T_{c2}, the SR-XRD patterns were successfully indexed by a tetragonal structure with the *I*4/*mmm* space group as reported in the previous study [2]. Figure 1 shows the T variation of the half width at half maximum (HWHM) for the selected diffraction peaks. In the T range of $T_{c1} \leq T \leq T_{c2}$, the HWHM of the 200 and 420 peaks increased with decreasing T, although we could not find any additional peaks in the SR-XRD patterns. On the other hand, the 110, 004, and 002 peaks did not exhibit broadening within the experimental accuracy. These results might be attributed to the existence of an orthorhombic phase for $T_{c1} \leq T \leq T_{c2}$. The absence of broadening in the 110 peak suggests no diagonal distortion along the <110> direction. It also excludes the coexistence of two tetragonal phases, which had been suggested in a previous study [2]. The enhancement in the HWHM for 420(200) peak is explained by the tiny splitting of the peak into 420(200) and 240(020) peaks due to the expansion and contraction of the two tetragonal *a* axes. We confirmed clear difference between tetragonal *I*4/*mmm* and orthorhombic *Immm* space groups in the reliability factor (R_{wp}) of the Le Bail analysis. For instance, $R_{wp} = 9.5\%$ for *I*4/*mmm* and $R_{wp} = 8.6\%$ for *Immm* at 114 K.

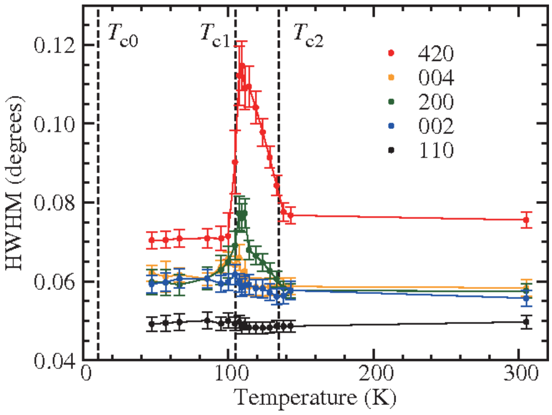

Figure 1. Temperature dependence of the half width at half maximum (HWHM) of the selected peaks for the SR-XRD patterns [5].

However, the HWHMs of the 420 and 200 peaks show sudden decrease just below T_{c1} and become identical to ones above T_{c2} within the experimental uncertainty, as shown in Fig. 1. We obtained similar values of R_{wp} with the *I*4/*mmm* and *Immm* structures, for instance, $R_{wp} = 9.7\%$ for *I*4/*mmm* and $R_{wp} = 9.4\%$ for *Immm* at 66 K. These results suggest that the intermediate orthorhombic phase appears in the $T_{c1} \leq T \leq T_{c2}$, whereas tetragonal phases appear in the $T_{c0} < T < T_{c1}$ and $T_{c2} < T$.

3. Muon spin relaxation

Figure 2(a) shows zero-field (ZF)-μSR spectra at 300 K and 80 K (i.e., above and below T_{c1}). There is no sign of an emergence of spontaneous internal magnetic field, such as oscillation and/or fast damping, below T_{c1}. This immediately leads us to the conclusion that no long-range magnetic order is present crossing T_{c1}.

We show μSR spectra at 30 mK measured at ZF and longitudinal-field (LF) of 100 mT in Fig. 2(b). As shown in Fig. 2(b), a rapid depolarization develops below T_{c0}. This data clearly demonstrates the absence of a conventional long-range magnetic order at the base T. The initial fast depolarization exhibits a gradual suppression when LF increases and is nearly quenched at LF = 100 mT. Surprisingly, the spectra exhibit a slow exponential decay over a long time even at 30 mK irrespective of LF, which may be attributed to a residual spin fluctuation. These features can be observed from the magnetic ordered state with widely distributed spontaneous local field (B_{loc}) at the muon site and slow persistent spin dynamics.

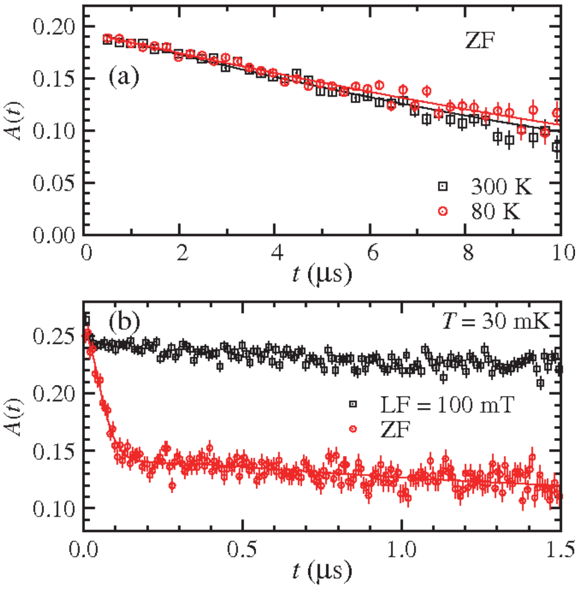

Figure 2. (a) Zero-field (ZF) μSR time spectra at 300 K and 80 K. (b) μSR spectra at 30 mK under ZF and longitudinal-field (LF) of 100 mT [5].

We adopted the Gaussian-broadened Gaussian (GbG) function as a recursive function for the curve fitting [6], which is appropriate for inhomogeneous magnetic ordered states with distributed B_{loc}. From the analysis, we estimated the mean spontaneous internal field at the muon site to be 12.1(7) mT. According to our Hartree potential calculation, the potential minima for a muon are located around the (0.50,0.24,0.69) position. Assuming randomly oriented 1μ_B V d-electron moments, we obtained the hyperfine coupling constant, ~52 mT/μ_B, at the relevant muon site. Thus, we roughly estimated the ordered moment at the V site to be ~0.2μ_B. This value is much smaller than the dipole moment for the $V^{4+}(3d^1)$ ion with quenching of the orbital moment, $\mu_{eff} \sim 1.7\mu_B$ for $S = 1/2$.

Finally, we briefly discuss the origin of the inhomogeneous magnetism. Imai et al. revealed that there is severe competition between many spin-orbital order patterns due to the coexistence of ferromagnetic and antiferromagnetic interactions and the associated effect of frustration in Sr_2VO_4 from their first-principal calculation [7]. We suggest that the observed broad B_{loc} distribution and persistent spin dynamics are signatures of the severe competition between the possible spin-orbital ordered patterns in Sr_2VO_4.

References

[1] G. Jackeli and G. Khaliullin, Phys. Rev. Lett. **103**, 067205(2009).
[2] H. D. Zhou *et al.*, Phys. Rev. Lett. **99**, 136403 (2007).
[3] R. Viennois *et al.*, J. Physics : Conf. Ser., **200**, 012219 (2010).
[4] J. Sugiyama *et al.*, Phys. Rev. B, **89**, 020402(R) (2014).
[5] I. Yamauchi *et al.*, Phys. Rev. B, **92**, 064408 (2015).
[6] D. R. Noakes and G. M. Kalvius, Phys. Rev. B, **56**, 2352 (1997).
[7] Y. Imai *et al.*, Phys. Rev. Lett., **95**, 176405 (2005).

I. Yamauchi[1,*], K. Nawa[2,3,], M. Hiraishi[1], M. Miyazaki[1,***], A. Koda[1,4], K. M. Kojima[1,4], R. Kadono[1,4], H. Nakao[4,5], R. Kumai[4,5], Y. Murakami[4,5], H. Ueda[2], K. Yoshimura[2], and M. Takigawa[3]**

[1]*Muon Science Laboratory and Condensed Matter Research Center, Institute of Materials Structure Science KEK;* [2]*Department of Chemistry Graduate School of Science, Kyoto University;* [3]*Institute for Solid State Physics, University of Tokyo;* [4]*The Graduate University for Advanced Studies (Sokendai);* [5]*Photon Factory and Condensed Matter Research Center, Institute of Materials Structure Science, KEK*

**Present address: Department of Physics, Graduate School of Science and Engineering, Saga University; **Present address: Institute of Multidisciplinary Research for Advanced Materials, Tohoku University; ***Present address: Graduate School of Engineering, Muroran Institute of Technology*

Lattice Dynamics and Crystal Fields in the Rare Earth Pyrochlores $R_2Ti_2O_7$ (R = Tb, Dy, Ho)

1. Introduction

The title compounds are rare earth pyrochlores, materials in which the magnetic rare earth ions form a pyrochlore lattice of corner sharing tetrahedrons (the titanium ions form a second interpenetrating pyrochlore lattice but are non-magnetic). The pyrochlore lattice is one of the most frustrated three-dimensional lattices known, and the three compounds have a long history in the study of highly frustrated magnetism [1]. With R = Dy, Ho, the materials are spin ices [2] with emergent magnetic monopole excitations [3], while with R = Tb, a non-frustrated counterpart to the spin ice state is expected, so the spin liquid state, which appears instead, is an on-going puzzle.

The crystal field scheme of a compound based on rare earth ions is very important, since it controls basic single ion properties, such as the size of the magnetic moment and anisotropy, as well as more complex ones, such as matrix elements for tunneling of the magnetic moments, all important quantities in spin ice physics. The phonon band structure is also important, since it allows us to understand properties, such as thermal expansion and the lattice heat capacity. Knowledge of both crystal field and phonons is essential for understanding interactions between crystal field and phonon transitions. Such interactions are strong in $Tb_2Ti_2O_7$, and may also contribute to spin-lattice relaxation processes of interest in the spin ices. Little is known about the lattice dynamics of rare earth pyrochlores, and the crystal field scheme of $Dy_2Ti_2O_7$ has not previously been determined experimentally due to the perceived difficulty of neutron scattering on samples containing natural isotopic abundance dysprosium. We planned to use the 4SEASONS spectrometer at J-PARC to rectify this situation by measuring both crystal field levels and phonon density of states in $Dy_2Ti_2O_7$ (we measured the other two compounds at ISIS using MERLIN).

2. Experimental

The properties of spin ices derive in part from their strongly anisotropic magnetic moments, which are due to a large crystal field splitting, with the first level in $Dy_2Ti_2O_7$ expected at ~30 meV. So, to measure the crystal field scheme, it was necessary to search for transitions from the ground state at low temperature, up to a reasonably high energy (e.g 100 meV) to ensure that all levels were located. However, it was also useful to seek transitions amongst excited states that appear at a higher temperature as the lowest ground state transitions are populated, but may themselves have quite small energies, if the excited states are not widely separated. 4SEASONS [4] is particularly suitable for this task because of the possibility to collect several incident energies at once by repetition rate multiplication [5]. Indeed, although we eventually measured with $E_i = 300$ meV to ensure we had really found all possible levels, in fact we could have used just the setting of $E_i = 153$ meV, which also allows to collect with $E_i = 55$, 28, and 17 meV, as eventually the highest level was at 93 meV. The simultaneously collected lower incident energies provide good resolution at lower energy levels. The problem of the absorption cross section of dysprosium was handled by ensuring that the sample thickness did not exceed 0.5 mm, the optimum thickness for our lowest incident energy. After subtracting the background of the aluminum sample can, we obtained clean data at 5 and 200 K, and a full set of transitions.

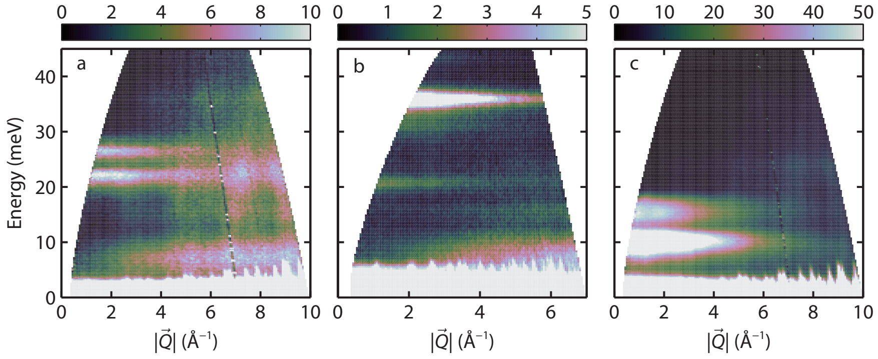

Figure 1. Crystal field transitions in $Ho_2Ti_2O_7$ (a), $Dy_2Ti_2O_7$ measured on 4 SEASONS (b), and $Tb_2Ti_2O_7$ (c).

3. Results

From the data [6], we extracted energies of the crystal field transitions [7] and phonon density of states [8]. In $Dy_2Ti_2O_7$, their wave-vector dependence exactly follows the magnetic form factor of Dy^{3+}, allowing their unambiguous identification. Only one was difficult to distinguish, but our crystal field calculations showed that it was very weak and likely overlapping another of the highest energy transitions. Although the composition of the ground state doublet was strongly dominated by $|m_j = +/-15/2>$ components, as expected, it was important to verify it experimentally. The first excited level at E~21 meV was somewhat lower than expected. We compared the phonon density of states with the other two compounds, for which we also performed density functional calculations [8]. In this way, we were able to assign the symmetries and energies of phonons in all three compounds, and to establish that the phonon energies undergo a minor softening as one moves to heavier rare earths. We expect this conclusion to apply quite generally across the series of rare earth titanate pyrochlores. We have been able to use our quantification of the lattice dynamics to understand anomalies in the temperature dependence of the lattice expansion of all three compounds [9], and our combined understanding of the crystal field and phonon levels to propose both a quantitative model for high temperature spin flipping in the spin ices by an Orbach mechanism [10] and a new example of a crystal field-phonon bound state in $Tb_2Ti_2O_7$ [7].

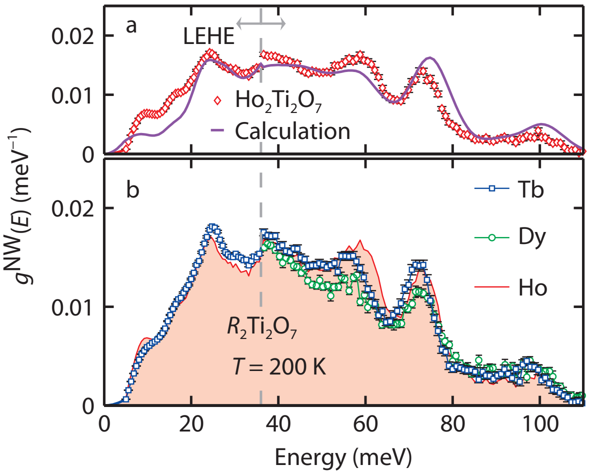

Figure 2. Phonon density of states in the $R_2Ti_2O_7$ pyrochlores (R = Tb, Ho, Dy) extracted from the powder inelastic neutron scattering data and compared with density functional calculations for $Ho_2Ti_2O_7$.

References

[1] J. S. Gardner, M. J. P. Gingras, and J. E. Greedan, Rev. Mod. Phys. **82**, 53 (2010).

[2] S. T. Bramwell and M. J. P. Gingras, Science **294**, 1495 (2001).

[3] C. Castelnovo, R. Moessner, and S. L. Sondhi, Nature **451**, 42 (2008).

[4] R. Kajimoto *et al.,* J. Phys. Soc. Jpn. **80,** SB025 (2011).

[5] M. Nakamura, R. Kajimoto, Y. Inamura, F. Mizuno, M. Fujita, T. Yokoo, and M. Arai, J. Phys. Soc. Jpn. **78,** 093002 (2009).

[6] Y. Inamura, T. Nakatani, J. Suzuki, and T. Otomo, J. Phys. Soc. Jpn. **82,** SA031 (2013).

[7] M. Ruminy, E. Pomjakushina, K. Iida, K. Kamazawa, D. T. Adroja, U. Stuhr, and T. Fennell, Phys. Rev. B **94**, 024430 (2016).

[8] M. Ruminy, M. N. Valdez, B. Wehinger, A. Bosak, D. T. Adroja, U. Stuhr, K. Iida, K. Kamazawa, E. Pomjakushina, D. Prabakharan, M. K. Haas, L. Bovo, D. Sheptyakov, A. Cervellino, R. J. Cava, M. Kenzelmann, N. A. Spaldin, and T. Fennell, Phys. Rev. B **93**, 214308 (2016).

[9] M. Ruminy, F. Groitl, T. Keller, and T. Fennell, Phys. Rev. B 94, 174406 (2016).

[10] M. Ruminy, S. Chi, S. Calder, and T. Fennell, submitted.

T. Fennell[1], M. Ruminy[1], K. Iida[2], and K. Kamazawa[2]

[1]*Laboratory for Neutron Scattering and Imaging, Paul Scherrer Institut;* [2]*Comprehensive Research Organization for Science and Society (CROSS)*

Neutron Diffraction up to 41.2 T- the New Record Established at the J-PARC NOBORU Beamline

1. Introduction

Through the combined efforts of scientists working at materials discovery and specialized high-field laboratories worldwide, a steady flux of novel materials displaying exotic phases and phase transitions at high magnetic fields is emerging. Typical material classes are superconductors, multiferroics, magnetoelectrics and quantum magnets. In many such cases, the identification of the magnetic propagation vector(s) is a significant step towards a full understanding the microscopic physical processes responsible for the occurrence of these phases. Short of a full determination of the magnetic structures at elevated fields, the propagation vector(s) provide strong constraints on theory.

For many years, neutron scattering experiments dedicated to understanding the response of materials subjected to magnetic fields were limited by the 15 T provided by commercially available Oxford Instruments cryomagnets. Laboratory equipment is, however, capable of measurements at far greater fields. Neutron scattering has therefore failed to make a large impact on the research on several topical materials where the intrinsic magnetic energy scales are such that the phenomena of interest (quantum phase transitions, magnetization plateaux, etc) occur beyond 15 T.

Recently, two developments have significantly boosted the range of magnetic fields achievable at neutron sources, thereby bringing within reach new quantum phases. One is the development, at the Helmholtz Center Berlin, of a Laue diffractometer (EXED) centered on a hybrid high-field magnet combining resistive and superconducting coils to reach a maximum DC field of 26 T [1, 2]. The second development, promising even larger magnetic fields is the introduction of pulsed-field technology. Compared to the hybrid magnet setup, the pulsed-field solution is significantly cheaper, and provides promising perspectives for further increases in the maximum field. It has been successfully demonstrated in combination with neutron, synchrotron x-ray and free electron laser x-ray diffraction [3-6].

2. Pulsed-field setup at NOBORU

At J-PARC MLF beamline 10 (NOBORU), a 500-kJ capacitor bank and a 50-T mini-solenoid pulsed magnet are installed. Until now, the system has been used to provide magnetic fields of up to 40 T with an 8 millisecond pulse width. The sample of interest is mounted inside the 12-mm mini-solenoid bore of a specially-built insert for a standard cryostat. The sample temperature can be controlled by the cryostat, while the magnet is immersed in a liquid nitrogen bath. By precisely timing the onset of the field pulse relative to the arrival of a "white" neutron beam at the sample position, it is possible to perform Laue diffraction experiments at cryogenic temperatures and very high fields. However, the much desired increase in field range comes at the expense of a significant reduction in the count rate achievable. This is caused by the need to cool the apparatus and sample after each field pulse. In the experiment described below, the typical cooling time between each 8-millisecond pulse was 18 minutes for magnetic fields in the range 30-41 T.

3. Results on $LiNiPO_4$

Here we present the results of our studies of the magnetoelectric Lithium orthophosphate $LiNiPO_4$ at NOBORU. In $LiNiPO_4$ application of a magnetic field along the crystallographic c-axis causes the development of an electrical polarization $\mathbf{P} = \alpha\mathbf{H}$ along the a-axis. The magnetoelectric coefficient α_{xz} is among the largest in transition metal compounds. Previous neutron diffraction experiments, extending to 17.3 T, have revealed a complex sequence of commensurate and incommensurate magnetic phases in $LiNiPO_4$ for fields along c, and have demonstrated how its magnetoelectricity is controlled by field-induced spin canting in the commensurate antiferromagnetic ground state.

Motivated by pulsed-field magnetization studies reaching 22 T [7], that we have extended and complemented by electric polarization measurements up to 55 T, we have engaged in a quest to determine the characteristic propagation vectors of the magnetic phases for fields larger than 17.3 T [8, 9]. The specific goal of the NOBORU experiment was to focus on the field range from 30 T to 41 T, where our bulk data indicate two phase transitions around 37 T and 39 T, the latter one separating a non-magnetoelectric phase, denoted phase VI, from a higher-field magnetoelectric phase, denoted phase VII. The results shown in Figure 1 demonstrate the power of the pulsed-field technique. For a single-crystalline sample with a mass of 370 mg and spin $S = 1$ Ni^{2+} ions, the characteristic propagation

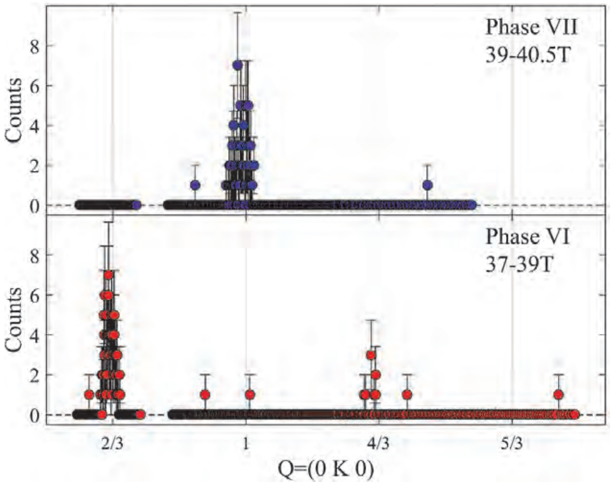

Figure 1. Pulsed-field neutron Laue diffraction data obtained on a 370-mg single crystal of magnetoelectric $LiNiPO_4$ with the field applied close to the c-axis [9]. The data are produced by collecting all neutron counts that correspond to a field at the sample position in the ranges 39-40.5 T (phase VII, upper panel) and 37-39 T (phase VI, lower panel).

vectors of the high-field phases can clearly be identified. Fits of the data indicate that the magnetic Bragg peaks in phases VI and VII occur at (0 2/3 0) and (0 1 0), within error. Both data sets correspond to about 300 field pulses or about 12 seconds of effective counting time at a beam power of 200 kW. The largest field applied in our experiment was 41.2 T. To the best of our knowledge, this is the highest magnetic field ever employed in a pulsed-field neutron diffraction experiment. Work is now ongoing to analyze the neutron diffraction data obtained at NOBORU, and to correlate them with the measured electric polarization in phase VII [9].

4. Conclusion and perspectives

In our experiment, we successfully employed the pulsed-field Laue diffraction technique. In the process, we reached a record-high magnetic field, 41.2 T, and managed to determine the magnetic propagation vectors of all magnetic phases of interest. The success of the experiment was due to a combination of factors such as the high-flux "white" beam of NOBORU, the reliability and endurance of the pulsed-field equipment and – importantly - suitable sample characteristics. All magnetic propagation vectors known in the Li-orthophosphate family, which apart from $LiNiPO_4$, includes Fe, Co and Mn sister compounds, lie along (010). Moreover, these peaks have substantial magnetic structure factors. This means that we could execute the technically challenging experiment with a substantial degree of confidence that the high-field phases of interest would also have propagation vectors of the form (0K0), and that they would be observable on the relevant timescale of 10 seconds.

The favorable circumstances offered by $LiNiPO_4$ will not be present in all compounds and all high-field phases. On the other hand, they are not unique either, as shown by previous publications, e.g. [3, 4]. Therefore, it seems certain that pulsed-field Laue diffraction will become an increasingly important part of the neutron scattering toolbox, and that many exciting high-field magnetic phases in a diverse range of material classes are now within reach. From a technical perspective, increases of the maximum field are feasible, and further improvements of the neutron instrumentation and beam power will guarantee the future success of pulsed-field Laue diffraction.

References

[1] P. Smeibidl, A. Tennant, H. Ehmler and M. Bird, J. Low. Temp. Phys **159**: 402-405 (2010).
[2] O. Prokhnenko *et al.*, Review of Scientific Instruments **86**, 033102 (2015).
[3] S. Yoshii *et al.*, Phys. Rev. Lett **103**, 077203 (2009).
[4] H. Nojiri *et al.*, Phys. Rev. Lett **106**, 237202 (2011).
[5] Z. Islam *et al.*, Synchrotron Radiation News, **25**:6, 5-9 (2012).
[6] S. Gerber *et al.*, Science **350**, 949-952 (2015).
[7] V. M. Khrustalyov, V. N. Savitski and N. F. Kharchenko, Czechoslovak Journal of Physics **54**, D27-D30 (2004).
[8] R. Toft-Petersen, E. Fogh *et al.*, submitted to Physical Review B.
[9] E. Fogh, T. Kihara *et al.*, work in progress.

E. Fogh[1], T. Kihara[2], R. Toft-Petersen[1], M. K. Sørensen[1], H. Suto[2], Y. Matsuda[2], Y. Narumi[2], K. Oikawa[3], H. Nojiri[2], and N. B. Christensen[1]
[1]*Department of Physics, Technical University of Denmark;* [2]*Institute for Materials Research, Tohoku University;* [3]*Neutron Science Section, J-PARC center*

Measurement of Neutron Capture Cross Section of ^{99}Tc

1. Introduction

Long-lived fission products (LLFPs) in nuclear spent fuel have been an issue to deal with in nuclear power industry. The currently-planned geological method of nuclear waste disposal has been disputed by the publicity. The proposed solution for this long-standing issue is nuclear transmutation, in which LLFPs are transmuted into shorter-lived or stable isotopes through neutron-induced reactions [1]. Among LLFPs, technetium-99 has the highest priority to transmute due to its high fission yield and radiotoxicity. The design of a nuclear transmutation system for ^{99}Tc requires reliable neutron nuclear data of ^{99}Tc in a wide range of neutron energy. This motivated us to perform our present work. We measured the neutron capture cross section of ^{99}Tc with the Accurate Neutron-Nucleus Reaction Measurement Instrument (ANNRI) [2, 3] in MLF of J-PARC. An intense neutron beam from the spallation neutron source of MLF allows us to study neutron-induced reactions with a small amount of a sample, such as radioactive materials. With the high-intensity neutron beam of MLF, the neutron capture cross section of ^{99}Tc was measured from the thermal to keV neutron energy region. In particular, an effort was made to expand the high-energy limit of measurement to over 100 keV.

2. Experiments

A sealed ^{99}Tc sample was used in the measurements. A metal ^{99}Tc pellet with a diameter of 6.3 mm was sealed in an aluminum container with an outer diameter of 9 mm. The radioactivity of the sample was 52 MBq. The ^{99}Tc sample was placed at a sample position with a flight path length of 27.9 m from the MLF spallation neutron source.

Neutron capture gamma-rays from the sample were detected with NaI(Tl) detectors. Figure 1 shows the layout of the ANNRI-NaI(Tl) detectors. Two NaI(Tl) detectors had been installed in ANNRI. One detector was located at a 90° angle with respect to the neutron beam axis. The other detector was at 125°. The NaI(Tl) detectors were shielded from background neutrons and gamma-rays with borated material, Pb and enriched-^{6}Li compound. In addition, the cosmic-ray background was reduced by the anti-coincidence technique with annular plastic detectors surrounding the NaI(Tl) detectors. In 2015, the background was reduced even more. A neutron shield, made of enriched ^{6}Li, was added to the beam duct. The NaI(Tl) detectors were shielded from scattering neutrons from the sample, which could reach the detectors and induce capture events of ^{127}I(n,γ)^{128}I in the detector material.

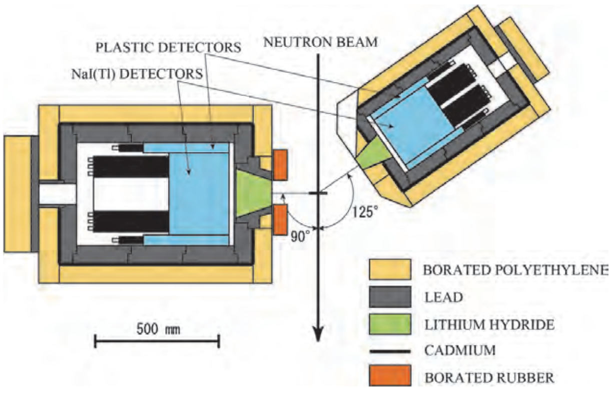

Figure 1. NaI(Tl) detectors of ANNRI.

Signals from the NaI(Tl) detectors were fed into a time digitizer FAST ComTec MPA4T [4]. The use of conventional analog modules was minimized because the analog modules were easily paralyzed by strong gamma-ray busts, called gamma flash, that are emitted from the neutron source when the pulsed proton beam hits the spallation target. Instead of pulse-height analysis with an analog amplifier, we used pulse-width analysis technique with the fast time digitizer [5].

In addition to the ^{99}Tc sample run, we conducted measurement runs with no sample, a dummy Al case, a graphite sample, a boron sample and a gold sample. The blank and dummy case runs were done for background estimations. The graphite run was used to estimate the background of scattering neutrons at the sample. The boron run was used to derive the incident neutron spectrum from 478 keV gamma-ray counts of the ^{10}B(n,$\alpha\gamma$)^{7}Li reaction. With the gold sample measurement, we checked the data reduction flow by comparing the derived cross section with the standard ^{197}Au(n,γ)^{198}Au cross section.

The proton beam power was approximately 200 kW. The pulsed proton beam was operated in the single-bunch mode. The single-bunch mode operation brought significant benefits to our present work. This allows us to analyze resolved resonances with a fine time resolution of 100 ns in a simple way. Otherwise, the double-bunch mode operation, which is normally adopted in the MLF beam operation, changes each resolved resonance into doublet peaks, requiring complicated resonance data analysis.

After background subtractions, the net TOF spectrum of ^{99}Tc was divided by the incident neutron TOF spectrum, providing relative cross section data. A saturated ^{99}Tc resonance at 5.6 eV was used to normalize the relative cross section to the absolute value.

3. Results

The preliminary results are shown in Fig. 2. The neutron capture cross section of ^{99}Tc was determined in the energy region from thermal to a few hundred keV. The fast signal processing technique, based on the pulse-width analysis method, successfully expanded the high-energy measurement limit of the NaI(Tl) system to over 100 keV.

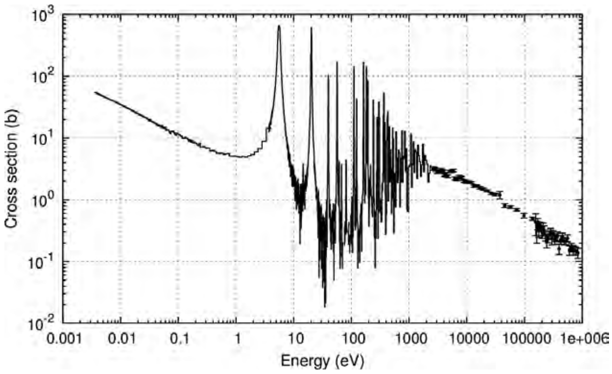

Figure 2. The neutron capture cross section of ^{99}Tc. Only statistical errors in the keV energy region are shown. Corrections for neutron self-shielding and multiple scattering have not been made.

4. Future Plans

We measured successfully the neutron capture cross section of ^{99}Tc using the NaI(Tl) detectors of ANNRI/MLF in the energy range from thermal to a few hundred keV. However, the results are still preliminary. Necessary corrections, such as self-shielding and multiple scattering, are underway. In addition, the pulse-height weighting technique [6] will be applied to obtain accurate cross section data. In the resolved resonance region from eV to a few keV, resonance parameters will be extracted.

After finalizing the data analysis, the present cross section data will contribute ^{99}Tc nuclear data evaluations in nuclear data libraries such as JENDL-4.0 [7] and ENDF/B-VII.1 [8].

Acknowledgements

The present study includes the result of "Research and Development for accuracy improvement of neutron nuclear data on minor actinides" entrusted to the Japan Atomic Energy Agency by the Ministry of Education, Culture, Sports, Science and Technology of Japan (MEXT).

References

[1] W. S. Yang *et al.*, Nucl. Sci. Eng. **146** 291 (2004).
[2] M. Igashira *et al.*, Nucl. Instr. Meth. Phys. Res. **A600** 332 (2009).
[3] Y. Kiyanagi *et al.*, J. Kor. Phys. Soc. **59** 1781 (2011).
[4] https://www.fastcomtec.com/products/mpa/mpa4t0/
[5] T. Katabuchi *et al.*, Nucl. Instr. Meth. Phys. Res. **A764** 369 (2014).
[6] R. L. Macklin and J. H. Gibbons, Phys. Rev. **159** 1007 (1967).
[7] K. Shibata *et al.*, J. Nucl. Sci. Technol. **48** 1 (2011).
[8] M. B. Chadwick *et al.*, Nucl. Data Sheets **112** 2887 (2011).

T. Katabuchi[1], M. Igashira[1], K. Terada[2], A. Kimura[2], S. Nakamura[2], T. Nakao[2], O. Iwamoto[2], N. Iwamoto[2], K. Mizuyama[2], H. Harada[2], J. Hori[3], and K. Kino[4]

[1]*Laboratory for Advanced Nuclear Energys, Tokyo Institute of Technology;* [2]*Japan Atomic Energy Agency;* [3]*Research Reactor Institute, Kyoto University;* [4]*Faculty of Engineering, Hokkaido University*

Measurement of Low-Energy Positive Muons from Metal Foil

1. Introduction

The goal of this experiment is to establish the muon deceleration method for the muon linac commissioning in the J-PARC E34 experiment [1]. The muon linac, which will be the first of its kind in the world, is also one of the key developments for the transmission muon microscope and future projects, such as the neutrino factory. In our project, the conventional surface muons (4 MeV) are decelerated and then injected into the muon linac. The initial stage of the muon linac [2] is a radio frequency quadrupole (RFQ), which has already been completed [3]. Muon deceleration is required to perform the muon linac commissioning as soon as the new muon beamline (H-line) is ready.

In the past, it has been observed that μ^+ with kinetic energy of sub keV are emitted from a thin Al foil with efficiency of 10^{-4} per incident muon [4]. The decelerated muons from the thin Al foil can be extracted and accelerated to the injection energy of the RFQ (5.6 keV) by the SOA lens. In the previous experiment, the phase space distributions of decelerated μ^+ were not measured. Because the RFQ acceleration efficiency depends on the phase space distributions of the injected beam, those should be measured. As a first step, in this experiment, we aim to demonstrate the muon deceleration with the thin Al foil and acceleration by the SOA lens.

2. Experimental method

The experimental layout is shown in Fig. 1. The muon beam at the MUSE D2 area is used with a momentum of 25 MeV/c. Some of the beam muons may marginally pass the thin Al foil with very small remaining energy. The decelerated μ^+ goes to electro-static acceleration and focusing (SOA lens). It acquires kinetic energy of 7 keV at the end of acceleration. Then, there is an electro-static deflector for energy and charge separation after a pair of electro-static quadrupoles. Finally, μ^+ reaches the detector installed downstream of the deflector, followed by a pair of quadrupoles. The detector is a microchannel plate (MCP) surrounded by a scintillator counter consisting of a plastic scintillator plate, wave length shifting fiber and SiPM.

The experimental apparatuses had been constructed (Fig. 2) in J-PARC MLF area 1 with support from the MLF Muon Section. Details about the construction and commissioning can be found in [5]. The detector system had been developed in a test bench and muon beam line, which has been described in [6].

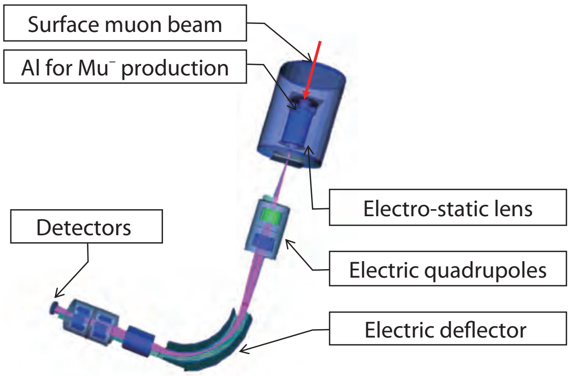

Figure 1. Layout of the experiment.

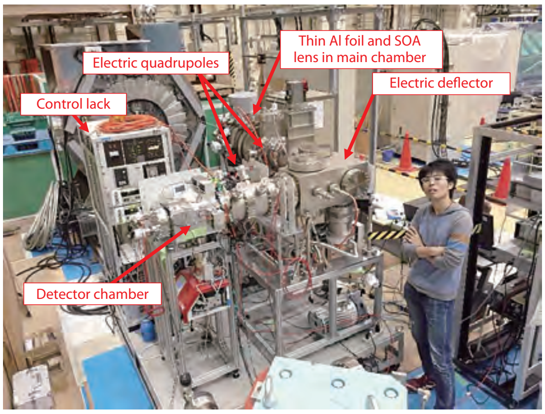

Figure 2. Photo of the experimental setup.

3. Results

Figure 3 shows timing distribution observed by the MCP detector. The signal event timing is evaluated to be about 900 nsec by the GEANT4 simulation and we observed successfully events at the expected timing. The events around 2700 nsec are considered to be protons knocked out from the foil surface by the injected muon beam.

Figure 4 shows charge distribution observed by the MCP detector. The red (green hatched) plot shows the distribution of the on-timing (off-timing) events. Those distributions are normalized by the number of events in the lower charge regions. Because the charge amount of the muon signal is estimated to be larger than that of the off-timing background, the difference of the distributions in the higher charge regions is thought to be

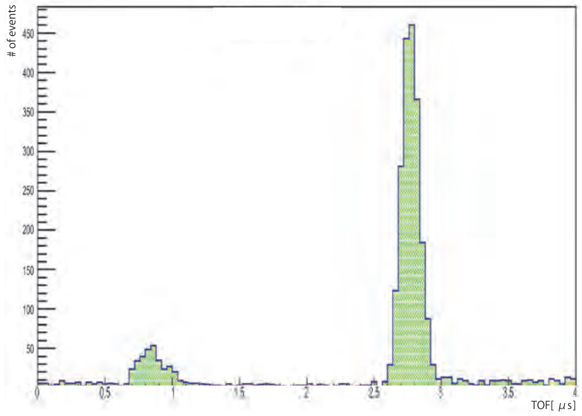

Figure 3. Timing distributions observed by the MCP detector.

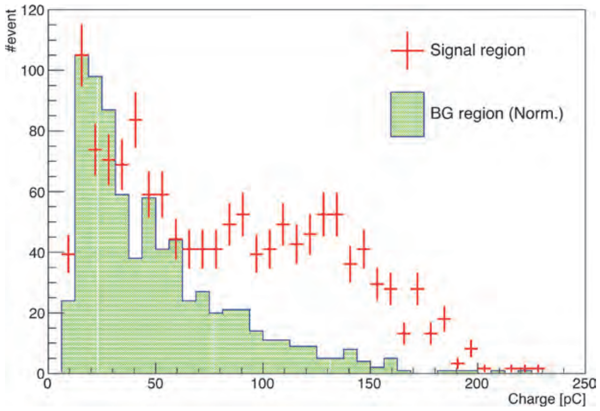

Figure 4. Charge distributions observed by the MCP detector.

due to the muon signal.

In conclusion, we demonstrated successfully muon deceleration with the thin Al foil and acceleration by the SOA lens. The transport efficiency of the SOA lens and a series of the electric apparatuses is being estimated by the GEANT4 simulation. Based on this study, the applied voltage to the electric apparatuses is tuned in order to measure the phase space distributions in next experiment.

4. Prospects

The expected beam rate after the RFQ acceleration at the H-line is estimated based on measured deceleration efficiency and expected phase space distributions

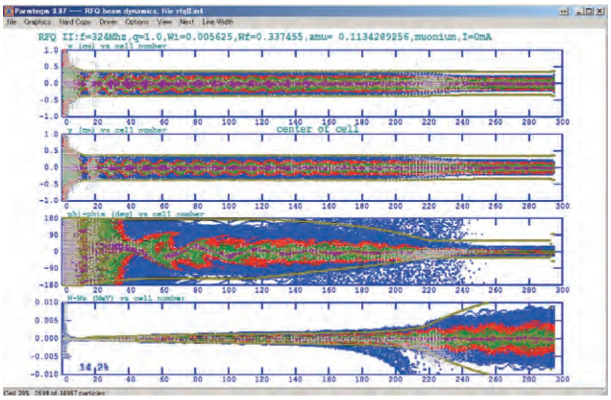

Figure 5. Muon beam evolutions in the RFQ simulated by PERMTEQM.

based on the MC simulation [4]. Figure 5 shows the expected muon beam evolution in the RFQ by PERMTEQM. The expected beam intensity after the RFQ is about a few Hz with 1 MW primary proton beam. In order to obtain more precise estimates, further measurements are necessary.

5. Acknowledgement

The authors are pleased to acknowledge the support from J-PARC MUSE facility by providing a stable beam during the experiment. We would like to thank J-PARC MUSE staffs for their support during the slow muon beamline assembly. This work was supported by JSPS KAKENHI Grant Numbers 15H03666.

References

[1] J-PARC E34 conceptual design report, 2011. (unpublished)

[2] M. Otani *et al.*, Phys. Rev. Accel. Beams, 19, 040101, 2016.

[3] Y. Kondo *et al.*, Proceedings of 6th International Particle Accelerator Conference, 2015, THPF045.

[4] Y. Kuang *et al.*, Phys. Rev. A 35, 3172 (1987), ibid. Phys. Rev. A 39, 6109 (1989).

[5] M. Otani *et al.*, PASJ2015 Proc. (Tsuruga, Japan, 2015), WEOM02.

[6] R. Kitamura *et al.*, JPS 71st Annual Meeting, 2016, 19aAH1.

M. Otani[1], T. Adachi[2], K. Bongho[3], Y. Fukao[1], Y. Ikedo[2], K. Ishida[4], M. Iwasaki[4], S. Kanda[5], N. Kawamura[2], Y. Kondo[6], T. Mibe[1], Y. Miyake[2], Y. Nagashima[7], K. Ninomiya[8], S. Okada[4], N. Saito[9], K. Shimomura[2], T. Suzuki[7], A. Yabuuchi[10], M. Yoshida[11], and R. Kitamura[5]

[1]Institute of Particle and Nuclear Studies, High Energy Accelerator Research Organization (KEK-IPNS); [2]Muon Science Laboratory, High Energy Accelerator Research Organization (KEK-IMSS); [3]Department of Physics, Soul University; [4]Advanced Meson Science Laboratory, Nishina Center for Accelerator-Based Science, RIKEN; [5]Department of Physics, the University of Tokyo; [6]Japan Atomic Energy Agency (JAEA); [7]Department of Physics, Tokyo University of Science; [8]Osaka University; [9]J-PARC Center; [10]Research Reactor Institute, Kyoto University; [11]Accelerator Laboratory, High Energy Accelerator Research Organization

Neutron Phase Imaging with Absorption Grating Fabricated by Imprinting Gd-Based Metallic Glass

1. Introduction

The conventional neutron radiography, that is, neutron imaging based on the neutron beam attenuation contrast, has been widely used in the field of non-destructive inspection. In some cases, however, the neutron absorption-contrast imaging is not sensitive enough to identify the small differences in elemental composition or density. The high penetration power of a neutron is not suitable for observing thin objects either.

Recent developments in that field included some neutron phase-contrast imaging techniques [1], which utilize the wave nature of neutrons and achieve higher sensitivity. We have started to develop the neutron phase imaging at BL22 RADEN [2] in J-PARC/MLF with the Talbot-Lau interferometer [3], which is a more powerful and stable device optical system compared to the crystal-based ones.

As shown in Fig. 1, the Talbot-Lau interferometer consists of three gratings. Periodic intensity patterns are formed behind the middle phase grating (G1) by the Fresnel diffraction due to G1. The analysis of a specific pattern with the most downstream absorption grating (G2), indicates the presence of a moiré fringe at the imaging detector. The changes in a neutron wave caused by the object are propagated into the moiré fringe. From the variations in mean intensity, phase, and amplitude of the moiré fringe, absorption-, differential-phase-, and visibility-constant-images are obtained at one-time measurement. The most upstream absorption grating (G0) prepares an array of line sources which enables the phase imaging with low coherent neutron beams.

The quality of G2 is the most important of the three to produce clear moiré fringes and achieve a fine spatial resolution. The fabrication of such G2s usually requires placing a neutron absorber into the grating grooves, which has a high-aspect ratio between its height and width. Recently, we adapted the imprinting method [4] of gadolinium-based metallic glass to fabricate G2, and performed the Talbot-Lau interferometry with the prototype G2.

2. Development of gratings

A set of gratings was designed for the neutron wavelength of 5 Å. The grating ruling patterns were fabricated on silicon wafers with 4-inch diameter and 525-μm thickness, applying the photolithography technique and Inductively Coupled Plasma (ICP) etching method. The pitch and aperture width of G2 is 180 μm and 48 μm, respectively. Silicone paste, including gadolinium oxide, was rubbed into its grooves as a neutron absorber. G1 is a $\pi/2$ phase grating for 5-Å-neutrons with 9.0-μm-pitch, 50% duty cycle, and 17-μm-high teeth. G2 is another absorption grating with 8.6-μm-pitch and 50% duty cycle. Since the groove width of G2 is finer than that of G0, the above method of absorber filling is not applicable to G2.

In the new method for G2, that is, the imprinting method, melted gadolinium-based metallic glass ($Gd_{60}Cu_{25}Al_{15}$) was pressed against the grating substrate. The metallic glass in the super cooled liquid state easily soaked into the grooves. Figure 2 shows the cross-section of a prototype G2 observed by a scanning electron microscope.

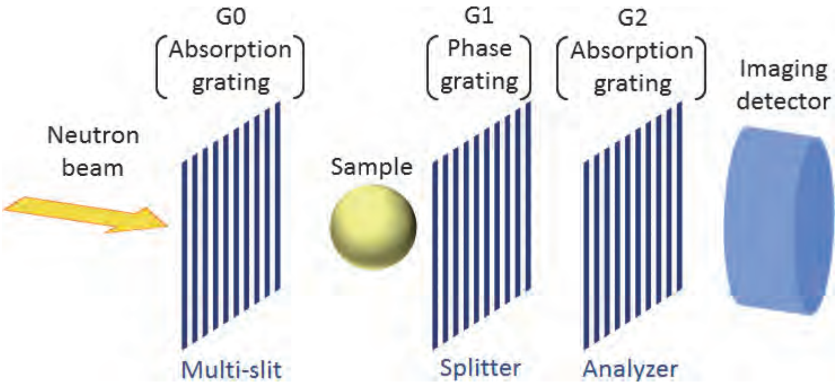

Figure 1. Schematic diagram of Talbot-Lau interferometer.

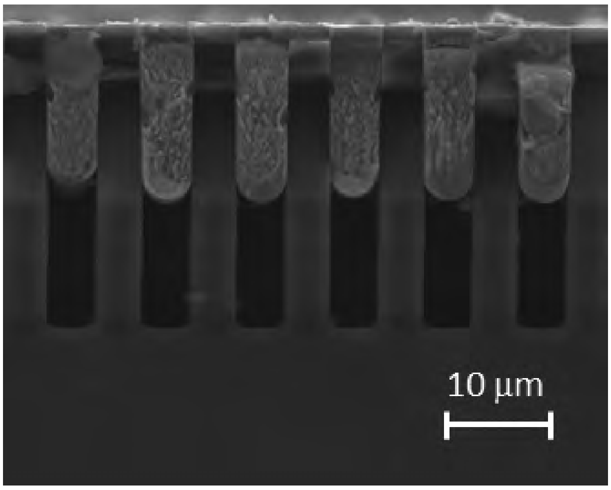

Figure 2. Cross-section of prototype G2 observed by SEM.

3. Experiment

The demonstration experiment was performed at the BL22 RADEN on J-PARC/MLF. Three gratings were aligned on an optical bench mounted on rubber vibration insulator. We were able to control the relative distances and angles of gratings by high accuracy pulsed-motor-driven stages. The distance between G0 and G1 was 1553 mm, and between G1 and G2 78 mm.

A combination of an electro-multiplying charge-coupled device (EM-CCD) camera and ZnS(Li) scintillator was used as a neutron imaging detector. This imager had a field of view of about 3.2 × 3.2 cm^2 (1004 × 1002 pixels) and spatial resolution of about 180 μm.

We performed absorption-, phase-, and visibility-contrast-imaging with the Talbot-Lau interferometer by using the central wavelength of 5 A ($\Delta\lambda/\lambda = 18\%$). The test sample was an aluminum rod with 5-mm diameter, located just in front of G1. The moiré fringes were analyzed with phase stepping method, where they were scanned by shifting the G2 position horizontally five times in the step of the fifth part of its pitch. The exposure time was 300 s at each G2 position.

4. Result

By using G2 with gadolinium-based metallic glass, we observed a moiré fringe with the high visibility of 68%. Figure 3 shows the resultant images of the Talbot-Lau interferometry. The shadow of the aluminum rod is not clear in the absorption-contrast image, whereas its edges are sharply enhanced in the differential-phase- and the visibility-contrast images.

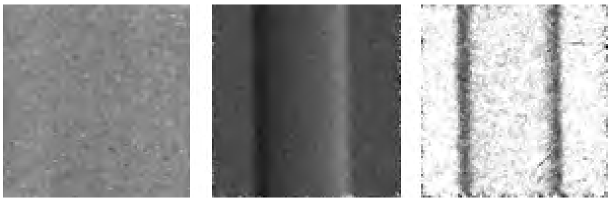

Figure 3. Resultant images of Talbot-Lau interferometry for aluminum rod. (Left) absorption-contrast imaging. (Middle) Differential-phase-contrast imaging. (Right) Visibility-contrast imaging.

5. Summary and prospects

The phase imaging with the Talbot-Lau interferometer was successfully demonstrated at the BL22 RADEN in J-PARC MLF. The G2, newly fabricated by the imprinting method, worked well, achieving a moiré fringe with high visibility.

We are going to apply the Talbot-Lau interferometry to pulsed beams for more precise measurement, and to polarized beams for magnetically sensitive measurement.

References

[1] I. S. Anderson *et al.*, “Neutron Imaging and Applications”, Chap. 8 (Springer Science+ Business Media, 2009).

[2] T. Shinohara *et al.*, J. Phys. Conf. Ser. 746, 012007 (2016).

[3] F. Pfeiffer *et al.*, Nat. Phys. 2, 258-261 (2006).

[4] M. Sadeghilaridjani *et al.*, Intermetallics 78, 55-63 (2016).

Y. Seki[1,6], T.Shinohara[1,6], J. D. Parker[2,6], K. Kato[3], W. Yashiro[4,6], A. Momose[4,6], and H. Kato[5]

[1]*Neutron Science Section, Materials and Life Science Division, J-PARC Center;* [2]*Neutron R&D Division CROSS-Tokai;* [3]*Department of Materials Science, Graduate School of Engineering, Tohoku University;* [4]*Institute of Multidisciplinary Research for Advanced Materials;* [5]*Institute for Materials Research, Tohoku University;* [6]*JST, ERATO, Momose Quantum Beam Phase Imaging Project*

Neutron Source

Progress of the Neutron Source Section

1. Failures in mercury target vessel

In April, 2015, the operational beam intensity for the neutron production target was ramped up to 500 kW, half of the rated intensity of 1 MW. During the operating time on April 30, dew point in the helium vessel, in which the neutron production mercury target was inserted, increased, suggesting a leak from the target vessel. Target vessel's triple-walled structure consists of a mercury vessel, inner and outer water shrouds, where the water shroud is bolted to the inner mercury vessel. The point of failure was located at a welded interface between the inner and outer water shrouds in the vicinity of a bolt on target vessel's bottom (see Figure 1). Our analysis confirmed that the diffusion bonding interface between the water shrouds was detached by welding thermal deformation in the fabrication process, followed by seal welding failure by the crack propagation induced by repeated thermal stress caused by beam trips.

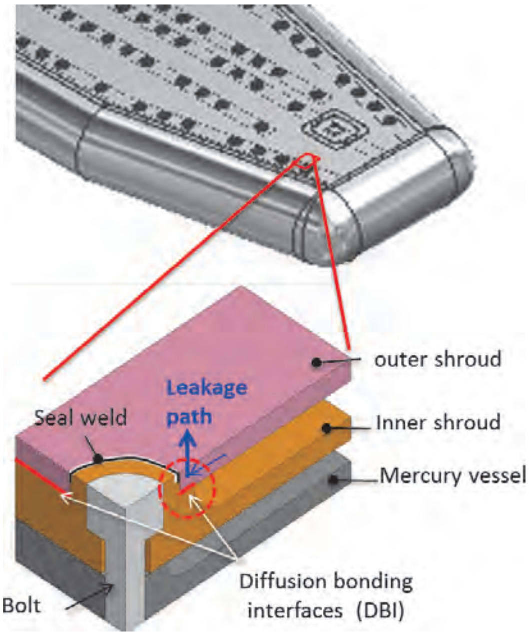

Figure 1. Schematic drawing of the specific location of the failure on the water shroud of the target vessel.

The regular target vessel replacement was scheduled for the 2015 summer shut down period. However, at the time of the incident, the fabrication of the next target vessel has not yet been completed. Because the structural design of the next target vessel was the same, we repaired the seal welding around all bolts to the full penetration welding before replacement. After the target replacement, user operation with the new target vessel was started from October 21.

After a 164-MWh operation at 500 kW on November 20, sensors, installed on the interstitial space between the mercury vessel and the water shroud, activated. Then we detected a pressure change in the cooling channel of the water shrouds. It indicated a failure in the inner water shrouds. Since it was difficult to inspect the inside of the target vessel at MLF, the specific failure location could not be identified. After reviewing the fabrication process and the analytical studies, we concluded that pressure wave induced stress might have expanded a crack at certain location, creating a leak path.

These problems forced us to re-design the target vessel to improve robustness. From this point of view, we changed the structure of the front part of the target vessel to eliminate welds and bolts in the high-stress region. We will also improve the inspection technique to detect fine cracks at the welds.

To ensure more reliable operation, we replaced the target vessel with an alternative with a mechanically robust structure. However, the replacement does not equip the gas micro-bubbles injection system, which is necessary for stable operation with an intensity higher than 300 kW. Therefore, we restarted the MLF user operation with a beam intensity of 200 kW from February 20, 2016.

2. New data related to pressure wave mitigation in the mercury target

In October, 2015, a part of the target front, the "beam window", was cut out to investigate the cavitation damage. It was the first observation of the target front structure with a double-walled build, aiming at reducing the damage by faster mercury flow in a narrow channel. With the replica method, we found the cavitation damage with a maximum size of about 25 μm in a belt along the horizontal mercury flow in a disk-shaped sample. (see Figure 2) The information was useful to understand the mechanism, causing cavitation damage in the narrow channel and the mitigation effect on the damage by the faster mercury flow.

New data on the pressure wave mitigation by the gas micro-bubbles injection was also taken for the 1-MW equivalent proton beam pulse with a laser-doppler vibrometer. The measured displacement velocity on the target vessel is shown in Figure 3. The maximum displacement velocity for the 1-MW case is equivalent to the velocity obtained for the 310 kW without gas micro-bubbles. This indicates that the pressure wave generated in mercury for the 1-MW operation could be mitigated to one-third by introducing a gas micro-bubbles injection.

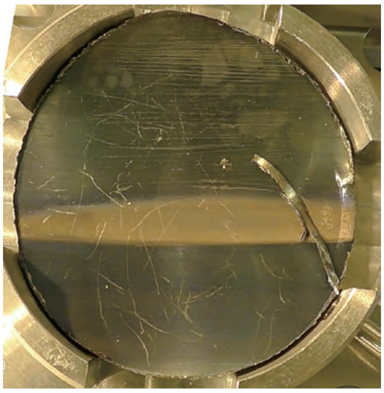

Figure 2. Photograph of the disk-shaped specimen cut out from the target front.

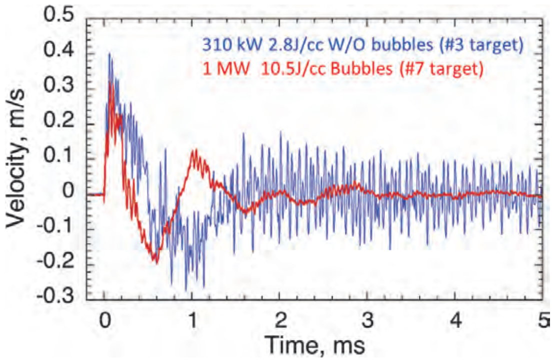

Figure 3. Displacement velocity on the mercury target vessel measured with a laser Doppler vibrometer. The red line represents the result for the 1-MW equivalent proton pulse injection on the target with gas micro-bubbles. The blue line stands for the 310-kW case without gas micro-bubbles.

3. Performance degradation of the helium refrigerator of the cryogenic hydrogen circulation system

In November, 2015, the performance of the helium refrigerator of the cryogenic hydrogen circulation system for the moderators deteriorated. We found out that water has accumulated in the heat exchanger of the helium refrigerator. We regenerated the charcoal, which might have been the source of the water contamination, and also conducted related purification during the shut-down period for the target replacement.

Unfortunately, the quality of the performance could not improve yet, due to another possible cause, such as oil contamination. The measure we took was to reduce the helium flow to suppress the source of contamination at the compressor of the refrigerator. We also introduced an operating scheme that stops the operation for purification for 6 days after a 3-week operating period. For the operating periods from February 20 to the end of March, 2016, the performance deterioration was at an acceptable level. We'll take every measure to solve this problem in the summer shut-down period in 2016.

4. Progress of spare components fabrication

2015 was the third year of a 6-year project to prepare moderators and a reflector. The fabrication of a coupled moderator and a reflector was completed and they were delivered to the J-PARC site. Currently, the fabrications of a de-couple moderator and a poisoned moderator are in progress. For these moderators, new material of Au-In-Cd alloy with a composition of 74.9:0.5:24.6 in at% will be installed.

H. Takada
Neutron Source Section, Materials and Life Science Division, J-PARC Center

Failure Cause Investigations and Design Improvements of the Mercury Target Vessel

1. Introduction

In 2015, we experienced twice failures of the mercury targets, caused by coolant water leak from the water shroud, when the facility was operating with a proton beam power of ca. 500 kW. The neutron source facility had to be shut down for the total period of about 5 months to investigate the reasons for those failures and to replace the mercury targets. So, thorough investigations of the failure mechanisms and the design improvements of the mercury target were carried out to prevent similar incidents.

Based on the investigation results so far, the cause of the failure is assumed to be the failure of bonding interface and welds initially generated in the course of fabrication. After the consecutive failures of the J-PARC mercury target, we improved the target design and paid special attention to the soundness of the welding lines. In this report, we will outline the water leak incidents and the new design of the mercury target.

2. Outline of the mercury target

Figure 1 shows the schematic view of the mercury target and its vertical cross-section. The mercury target is made of Type 316L stainless steel. The weight is 1.6 tons and the total length is 2 m. The front part, whose length is 1050 mm, has multi-walled structure, i.e. the double-walled water shroud covers the mercury vessel to confine the mercury contamination in the water shroud, if mercury leaks out of the mercury vessel. Mercury flows through the mercury vessel and coolant water flows through the water shroud to remove the heat load of spallation reactions in the mercury target. The intermediate space between the mercury vessel and the water shroud is filled with helium gas and three leak detectors are installed in the space. The design pressure of the mercury and the coolant water is 0.5 MPa and that of the helium gas is 0.2 MPa.

Figure 2 shows the structure of the mercury target. The water shroud consists of external and internal vessels. There are ribs on the internal vessel and its top surface is fixed together with the external vessel by diffusion bonding. The water shroud is bolted on the mercury vessel at 177 positions to endure an inner helium gas pressure of 0.2 MPa.

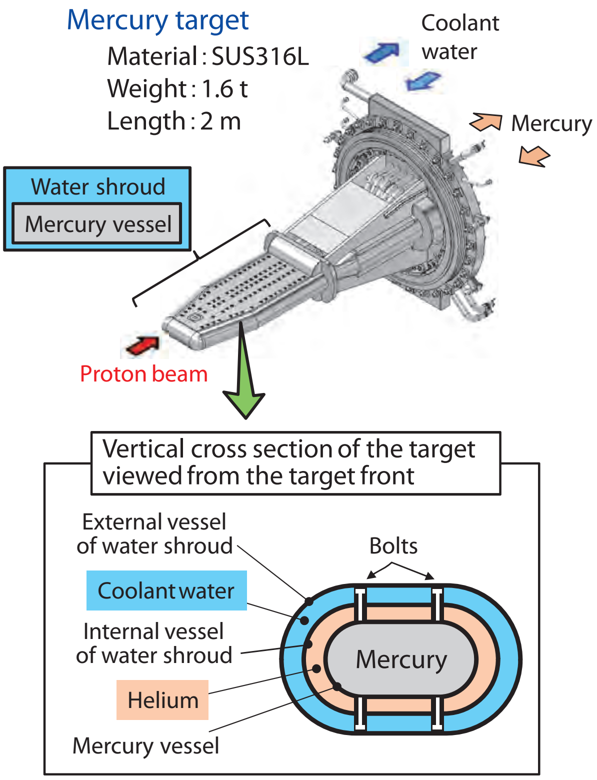

Figure 1. Schematic view of the mercury target.

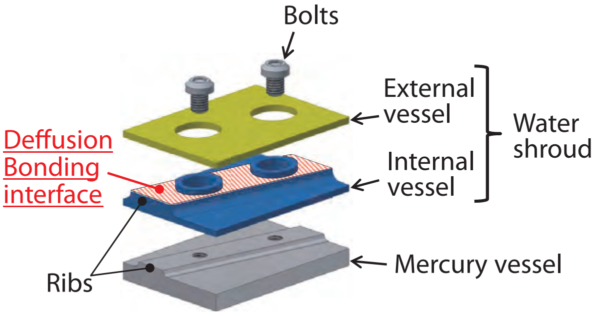

Figure 2. Structure of the mercury target.

3. Small water leakage trouble

On April 30, 2015, when the mercury target was operated with a proton beam power of 513 kW, the water leak detector in the drain pipe of the helium vessel detected a leak incident and the beam operation stopped. The coolant water of the water shroud was drained and the mercury target was moved to the maintenance area to investigate the failure. When the coolant channel of the water shroud was pressurized with helium gas to 0.16 MPa, the visual inspection revealed a water drop growing gradually on the bottom side of the mercury target. Next, the coolant channel was evacuated and the water drop shrank, which showed that the place where the water drop was found was the failure's location. The total proton energy injected into the mercury target was 670 MW.hour.

The failed mercury target was replaced with a new one, which was repaired based on the failure analyses of the failed target, during the maintenance period in the summer of 2015. The user beam operation resumed from October 27 with beam power of 505 kW, but the mercury target failed again on November 20. The total proton energy was only 170 MW.hour. Since the failure was a water leak into the helium layer this time, finding the failure's location, which was on the inside of the internal vessel, was extremely difficult. The efforts to find the problematic location and the investigations of what caused the failure are still going on.

In both incidents, the total amount of leaked water was estimated to be several liters at maximum.

4. Failure analyses of the mercury targets

Because the first failure was a water leak of the mercury target, the failure's location could be found easily by visual inspection. Figure 3 shows the structure of the mercury target at that spot, which is the vertical cross section of the cut-out model shown in Figure 2. A water drop was found at the welded interface between the external and internal vessels, where seal welding was used. Seal welding is TIG welding without groove and its depth is shallow, i.e. less than 1.5 mm. This type of welding does not ensure structural strength. The design of the water shroud relied on diffusion bonding to secure the structural strength of the water boundary and the seal welding was used only to fill up the interface line between the external and internal vessels. Based on the structure at the leak location, it was evident that the water leak path was formed by failures of both the diffusion bonding and the seal welding.

In the incident investigations, we found a suspicious procedure of fabrication to be the cause of the first failure. After the external and internal vessels were fixed together with diffusion bonding, the water shroud was bolted on the mercury vessel and then the bolt head was TIG welded to seal the helium layer. We suspected that large heat input by TIG welding of the bolt head caused the large thermal stress and failure of the diffusion bonding interface.

This assumption was verified by a partial mockup mode of the failure's location, fabricated with the same structure and procedure of the mercury target. An inspection by ultrasonic test showed failures of the diffusion bonding interface beside the bolts where the failure was assumed.

The phenomenon was also simulated by using FEM (Finite Element Method) code, LS-DYNA. In the simulation, the initial temperature of the bolt head was set at 1400°C, the melting point of stainless steel. Then the temperature was decreased to room temperature and the stress field generated by the material contraction was analyzed. Figure 4 shows the simulation result of stress component perpendicular to the diffusion bonding interface. It can be seen that tensile stress, far larger than the tensile strength (480 MPa) of stainless steel, was generated at the diffusion bonding interface. This large stress could have caused the failure of the diffusion bonding interface. The structure at the problem location after the TIG welding of the bolt head was assumed to be just like in Figure 5. The length of the diffusion bonding interface was only 2 mm at the failed location. After the beam operation started, the mercury target was exposed to repetitive temperature swings due to the frequent proton beam stops, which caused fatigue failure of the seal welding and the water leak path was completed.

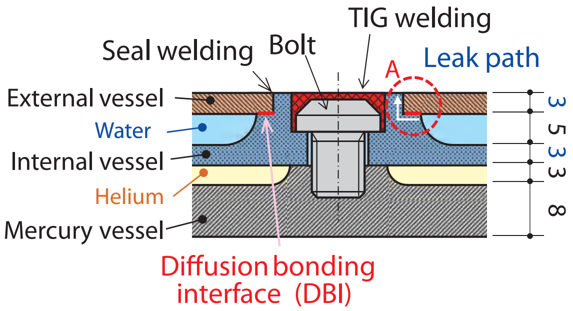

Figure 3. Cross section of the mercury target at the failed location.

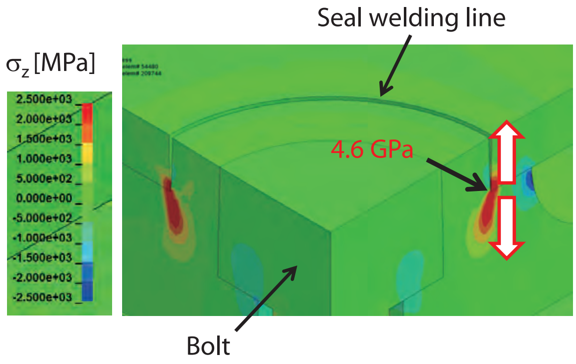

Figure 4. Simulation result of thermal stress around the failed location.

Though the reason of the second failure has not been clarified yet, one probable cause is the hot cracks in the TIG welding line, which were found in the mockup model of the internal wall of the water shroud. Mockup models of some places, which were suspected to be the cause of the second failure, were fabricated to investigate the soundness of the welding lines. After detail observations, tiny cracks were found at some places on the welding lines and the heat-affected zones. The details of the investigation results will be reported in the near future.

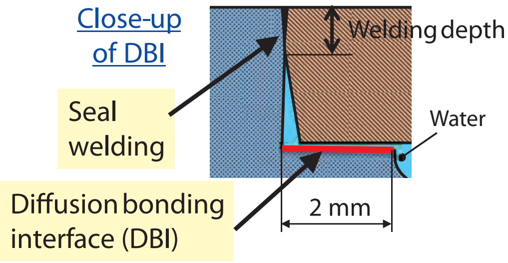

Figure 5. Structure of the water shroud after the DBI failure (Detail A of Figure 3).

5. Design improvements of the mercury target

Overall, the causes of these troubles are considered to be in the welding and bonding part in the high heat load area of the mercury target. In order to prevent such troubles in the next target design, diffusion bonding will not be used and the welding part will be minimized. Figure 6 shows the design improvements of the next mercury target. The water shroud in the front part of the mercury target, where the heat load is high during the beam operation, will be integrated with the mercury vessel. Parts of the mercury target will be fabricated by using wire-EDM and the welding line will be reduced more than 30%. Adopting the integrated design for the rear part would be difficult, but we will apply improvements to reduce the welding. Inspections to secure the good quality of the welds are also important. The fabrication of the new target will proceed with more rigorous inspections of the welds by Radiographic Test (RT) and Ultrasonic Test (UT). We have started the design and fabrication of the new mercury target to achieve the beam power of more than 500 kW.

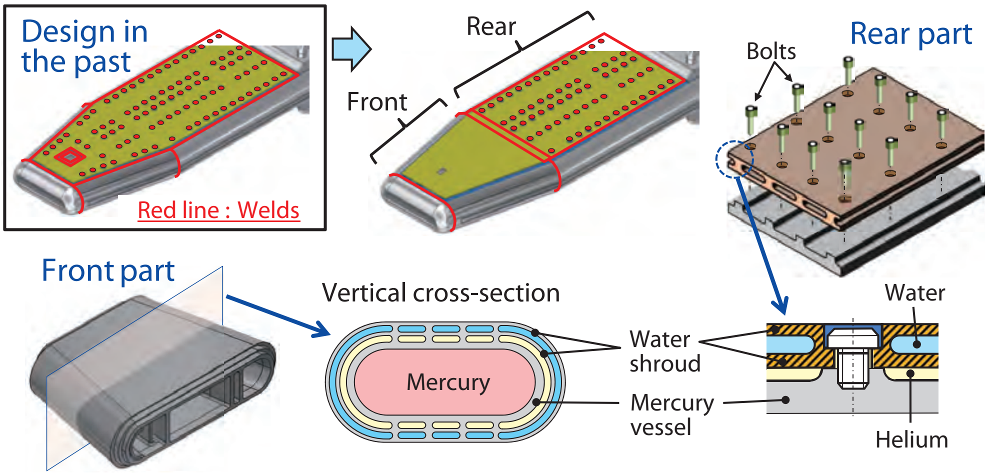

Figure 6. Improved design of the new mercury target.

K. Haga, H. Kogawa, T. Wakui, T. Naoe, and H. Takada
Neutron Source Section, Materials and Life Science Division, J-PARC Center

The Status of the Cryogenic Hydrogen System

1. Introduction

At MLF, a cryogenic hydrogen system provides cryogenic hydrogen to the moderators at supercritical pressure of 1.5 MPa, with para-hydrogen concentration of more than 99% and temperature lower than 20 K, generating high-performance pulsed cold neutron beams.

2. Performance deterioration of the refrigerator

The cryogenic hydrogen system consists of a helium refrigerator system and a hydrogen circulation system, as shown in Fig. 1. In the helium refrigerator system, helium gas flows from a compressor to oil separators, an activated charcoal, and a cold box, then returns to the compressor. The cold box has three heat exchangers, an adsorber (ADS) and a turbine.

The typical scheduled period of cryogenic hydrogen system's operation is approximately 3 months continuously for the neutron scattering experiments in MLF. This operation had performed well until December, 2014. However, since January, 2015, the pressure differences at heat exchangers No. 1 and No. 2 and the ADS increased rapidly much earlier than the previous operation, as shown in Fig. 2.

For a normal operation, the dew-point of the helium gas has been constant at about –80°C, and concentration of impurities, such as nitrogen, oxygen, methane and carbon oxide has been almost 0 ppm, respectively. After the operation from April to May, 2015, on the other hand, about 100 ppm of nitrogen concentration in helium gas was detected in the ADS. Furthermore, the dew-point at heat exchangers No. 1 and No. 2 was –45°C at room temperature. We thought that nitrogen and moisture from the charcoal of oil separator (OS-5) was the cause of the performance deterioration.

In the 2015 summer shut-down period, therefore, we replaced the charcoal of OS-5 to reset the impurities contained in the charcoal. After regenerating fresh charcoal by heated nitrogen gas, we restarted the refrigerator operation in October. However, from the first day, the pressure difference began to increase again, and 21 days later, the temperature at the outlet of heat exchanger No. 2 rose from 78.5 K to 81 K. This time, it affected the heat exchange balance between helium and hydrogen, leading to unfavorable hydrogen temperature rise in the hydrogen circulation system. Finally, in 3 weeks, the user operation was interrupted.

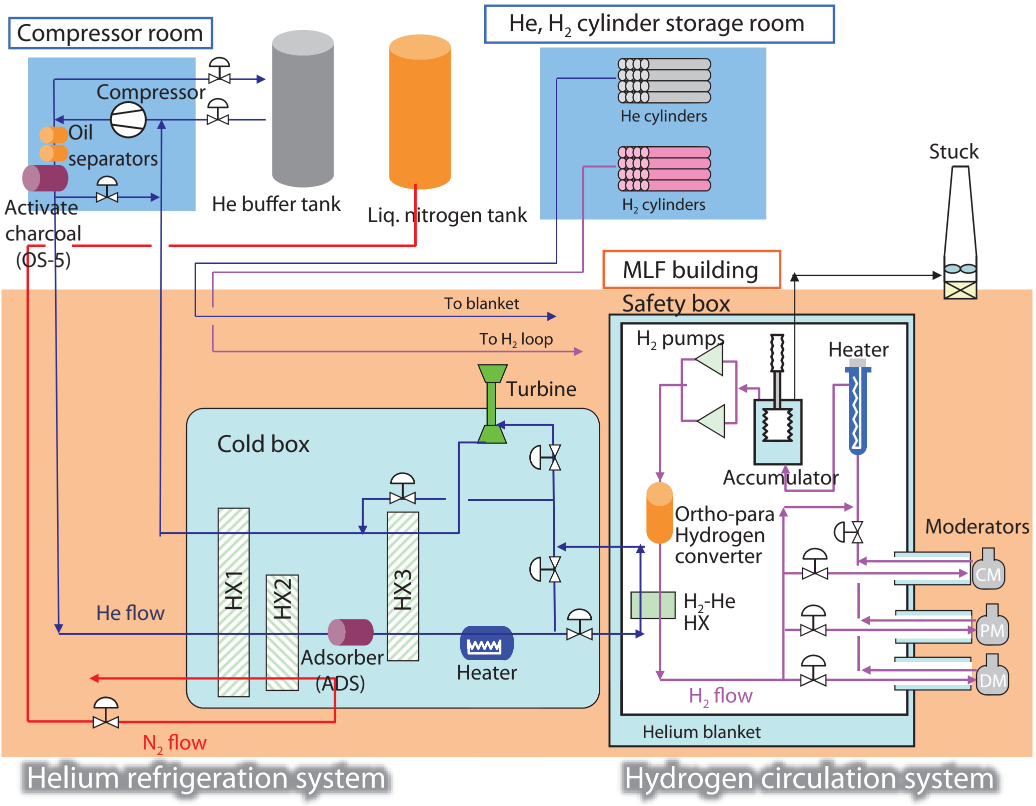

Figure 1. The cryogenic hydrogen system.

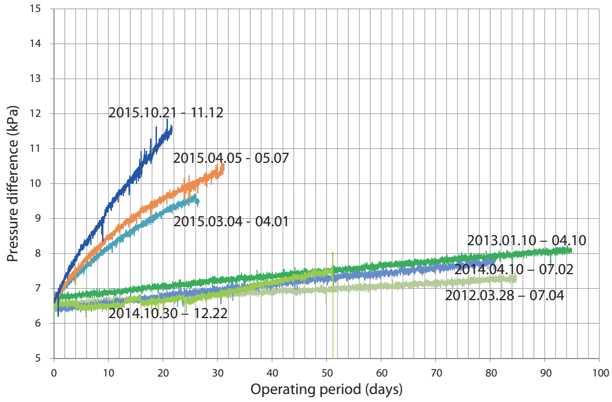

Figure 2(a). Pressure difference at heat exchangers No. 1 and No. 2.

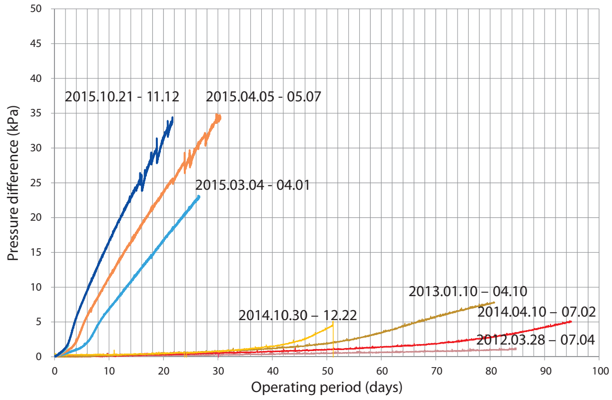

Figure 2(b). Pressure difference at the ADS.

In December, we regenerated again not only the charcoal of OS-5, but also the heat exchanger and the ADS to remove sufficiently the moisture. As soon as the test operation was started in January, the pressure difference at the heat exchangers and the ADS began to rise in the same or somewhat faster changing rate than during the previous operation. We analyzed the mass concentration of gases, sampled from the exchangers and the ADS, with a quadrupole mass spectro-analyzer and found that the water was undetectable. Another inspection of the inlet filter of the cold box detected reaction with oil when it was illuminated by black light. This suggested that oil contamination could be the suspected cause of the performance deterioration.

Any oil contamination removal treatment would require stopping the operation for several months, because such an irregular maintenance would take a long time to arrange. This was unacceptable in view of supplying users with stable neutron beams. Therefore, we have taken the following countermeasures. We reduced the helium flow in the compressor that uses a large amount of lubrication oil, in order to suppress the level of oil exhaust to the downstream. We observed previously that, after the impurities at the heat exchangers and the ADS were removed with helium for 5 to 6 days, the pressure difference dropped to its initial value, We changed the operation cycle, so that the 3-week refrigerator operation is followed by a 6-day maintenance, comprising of warm-up, purification and cool-down. As expected, this operation cycle worked well for the user operation started from February.

3. Future plans

In the 2016 summer maintenance period, we will take further necessary measures. For example, the ADS will be replaced with a new one because most of the pressure difference is generated there. The heat exchangers will be cleaned by Freon to remove the oil contamination. The activated charcoal of the oil separators will be replaced with a new charcoal to improve the performance. An inspection of the piping connecting the compressor and the cold box has also been planned. Until then, we will continue the intermittent 3-week operation followed by the 6-day maintenance.

T. Aso, H. Tatsumoto, S. Hasegawa, H. Muto, K. Aoyagi, and K. Nomura
Neutron Source Section, Materials and Life Science Division, J-PARC Center

Present Status of the Spare Moderator and the Reflector Fabrication

1. Introduction

Due to an accumulated-irradiation-damage, the structural material of the moderator and reflector, such as aluminum alloy, will reach its design value (20 DPA) around 2021. A fabrication of the spare moderator and reflector is moving ahead with a plan since 2013 toward these replacements. This year, the fabrication of a coupled moderator, reflector and reflector plug were just completed. The remaining two decoupled moderators will be fabricated in 2018. Here we report the fabrication status of the coupled moderator and the reflector.

2. Coupled moderator and reflector fabrication

In the spare moderator design, the invar joint with the lowest thermal expansion was adopted to improve the special fabrication, such as an asymmetrical setting at an elbow-shaped bend in the cryogenic (hydrogen) pipe due to thermal shrinkage of aluminum and SS316L, which was employed for the previous moderator design. The invar joints, such as invar-A6061 and invar-SS316L, were developed by the friction weld method [1] to be used in the cryogenic pipe and implemented in the coupled moderator. Many tests, such as appearance inspection, dimensional check, welding inspection, cooling test, etc., were performed until the coupled moderator fabrication was completed. Figure 1 shows the cooling test of the coupled moderator. It was conducted to evaluate the thermal load and thermal shrinkage of the hydrogen pipe by using nitrogen gas (100 ~ 140 K). It was confirmed that the measured thermal load, < 60 W, was roughly the same as the design value. The thermal shrinkage at a maximum position was also measured by X ray transmission under cold temperature, as shown in Fig. 1, resulting in a reasonable shrinkage, < 2 mm, as shown in Fig. 2. The adoption of invar alloy with lower thermal expansion than in the one previously used, facilitated the fabrication.

In the previous decoupled moderator and reflector, the Silver-Indium-Cadmium (Ag-In-Cd) decoupler was utilized to produce neutron beams with sharp pulse shape, newly, Gold (Au), instead of Ag, was selected to reduce dramatically the radioactivity of the used components without sacrificing the neutronic performance. The bonding between Au-In-Cd and aluminum alloy (A5083), which is a part of the structural material of the reflector, is required for the purpose of heat removal

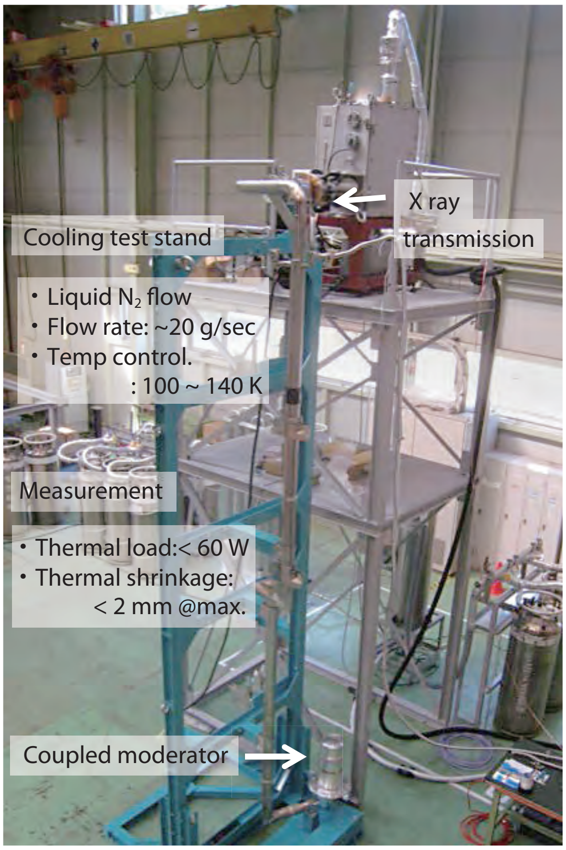

Figure 1. Cooling test of 2nd coupled moderator.

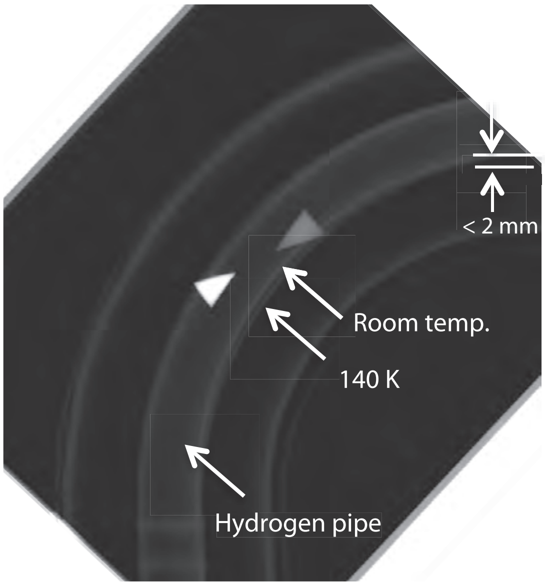

Figure 2. X ray transmission of hydrogen pipe.
Thermal shrinkage of hydrogen pipe was measured at 140 K, resulting in reasonable shrinkage, < 2 mm.

and thermal stress. The optimal bonding condition (100 MPa pressure, 535°C temperature and 1 hr holding time) was found for Au-In-Cd coin-shaped small test piece (3 cm in diam. × 2 mm in thick) by adopting a Hot Isostatic Pressing (HIP). However, there were critical engineering issues in terms of large sized bonding between Au-In-Cd and A5083 alloys to implement an actual reflector. We have investigated the HIPing process with respect to the surface condition, size and heat capacity of large-sized Au-In-Cd. Finally, we successfully implemented the Au-In-Cd decoupler into the actual reflector assembly. During the fabrication process, many inspection tests were also conducted to confirm the design, as shown in Fig. 3.

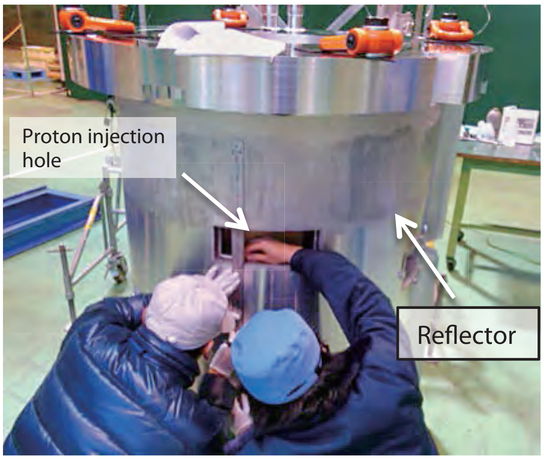

Figure 3. Dimensional check of reflector fabrication.

Acknowledgment

We thank for the cooperation of Metal Technology Co. Ltd. in fabricating the spare coupled moderator and in the reflector assembly. We also thank the NAT staff for their help with the Au-In-Cd material preparation.

References

[1] M.Harada *et al.*, Journal of Nucl. Mat. Vol. 398 (2010) pp. 93-99.

[2] M. Ooi *et al.*, Journal of Nucl. Mat. Vol. 450 issue 1-3 (2014) pp. 117-122.

M. Teshigawara, M. Harada, and M. Ooi
Materials and Life Science Division, J-PARC Center, JAEA

Modification of the Integral Control System for Sustainable Upgrade of Instruments

1. Introduction

A general control system (GCS) operates in MLF to supply safely and efficiently muon and neutron beams. The GCS comprises several subsystems, such as an integral control system (ICS) for controlling target systems, a personnel protection system (PPS) for preventing exposure of personnel to high radiation, shared servers, networks and a timing distribution system [1, 2]. Since the first proton beam injection in 2008, the GCS has been modified according to the annual upgrade of the target systems and the annual incremental upgrade to the user apparatuses [3, 4].

2. Modification of ICS in GCS

Figure 1 shows a conceptual structure of the ICS in the GCS. It consists of a monitor and operation (MO) system and a programmable logic controller (PLC) link system. The MO system comprises administrative control PCs (ACP), database servers, data storage servers, and so on. For sustainable long-term operation, an upgraded MO system based on experimental physics and industrial control system (EPICS) was built in 2013 [5, 6]. The upgraded MO system has operated in parallel with the previous MO system for over a year, and has been debugged. In 2015, the MO system was replaced completely with the upgraded one after shutting down the previous one.

The PLC system, shown in Fig. 1, includes PLCs, such as general control panels (GCP), remote input/output (I/O) panels, and local control panels (LCPs) for each equipment. These PLCs are connected through duplicate optical networks for PLC link, called the NETH. Station numbers (no.) and a shared memory area are allocated to these PLCs. The GCP-I, denoted by stations 1 and 2, manages the I/O panels and LCPs through the NETH main-loop. The I/O panels, shown as stations 3 and 5 in Fig. 1, have several stations under their NETH sub-loops. These sub-loops enable increment of instruments without increasing stations under the main-loop. In 2014, 34 stations under the main-loop and 6 stations under the sub-loops operated in the ICS.

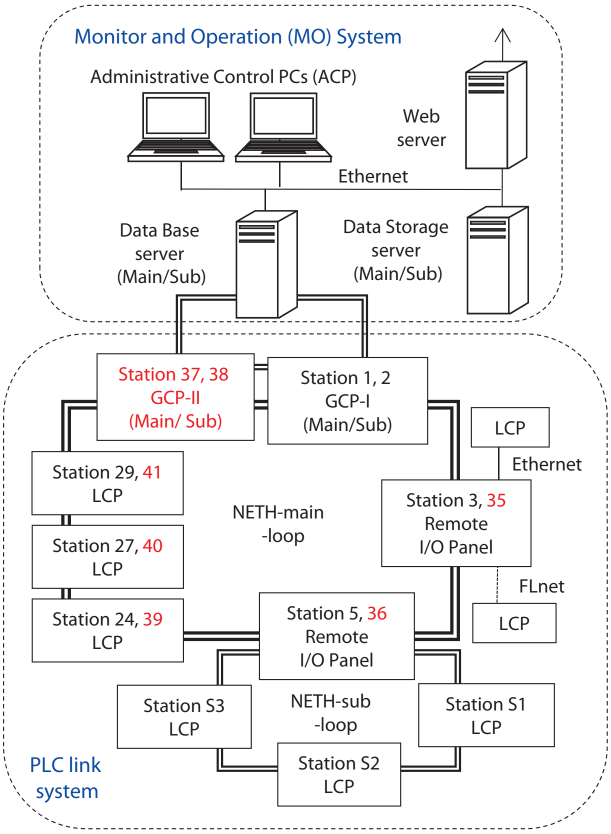

Figure 1. Conceptual structure of the integral control system (ICS) in the MLF general control system (GCS). The ICS consists of a MO system and a PLC link system. 41 stations under the main-loop and 6 stations under the sub-loops operate in the ICS. Stations 35 through 41 have been added anew in 2015.

Because data transmission through the NETH-loop is executed by transferring from the internal memory area of the PLC to the shared memory area of the NETH link, however, the amount of data transmitting through the main-loop is limited by the address number of the transferable internal memory. In addition, the amount of data transmitting between the main-loop and the sub-loops is limited by the address number of the shared memory allocated to the I/O panels. Therefore, frequent increments of instruments cause lack of address numbers of both the transferable internal memory and the shared memory allocated to the I/O panels. As a result, it has been difficult to create new stations both under the main-loop and the sub-loops for significant upgrades of instruments in the near future. For maintaining sustainable upgrades of instruments, the following modifications of the PLC link system were performed in 2015.

(1) The address number of the shared memory was increased significantly by expanding the transferable internal memory areas. Moreover, these

increased addresses were divided between stations 35 through 41, which were created anew under the NETH main-loop.

(2) Stations 35 and 36 were allocated to the existing I/O panels to enable increment of instruments under the sub-loops.

(3) Stations 37 and 38 were allocated to the GCP-II, which was added anew to the main loop. The GCP-II reduced the processing loads of the GCP-I by sharing station managements with it.

(4) Stations 39, 40 and 41 were allocated to the existing LCPs, which have managed muon S line instruments. These LCPs will also manage muon H line instruments, whose number will be increased soon.

3. Summary

The PLC link system of the ICS was modified to maintain sustainable long-term upgrades of instruments. Significant modification of a muon user PPS LCP to increase the user apparatuses of the muon H line, the upgrade of the MLF monitor LAN used by the monitoring camera system [7], and so on, have been also carried out in 2015.

References

[1] K. Sakai *et al.*, Nuclear Inst. and Meth. A600, (2009) 75.
[2] K. Sakai *et al.*, MLF Annual Report 2012, (2013) 75.
[3] K. Sakai *et al.*, JAEA Conf. 2015-002 (2015) 593.
[4] K. Sakai *et al.*, Progress in Nuclear Science and Technology Vol. 4, (2014) 264.
[5] K. Sakai *et al.*, MLF Annual Report 2013, (2014) 66.
[6] M. Ooi *et al.*, JPS Conf. Proc. 8, (2015) 036007.
[7] M. Ooi *et al.*, MLF Annual Report 2014, (2015) 67.

K. Sakai[1], M. Ooi[1], A. Watanabe[2], and Y. Kato[1]
[1]*Neutron Source Section, Materials and Life Science Division, J-PARC Center;* [2]*Accelerator Section III, Accelerator Division, J-PARC Center*

Neutron Science

Neutron Science Section

1. User Program

The user program of the 2015A period started on April 19 with 18 neutron instruments and commissioning activities for 2 beam lines with 500-kW power and was interrupted on April 30 due to a target vessel problem - cooling water leakage outside the vessel. The target was replaced in the summer, and we resumed the user program on October 27, but it was interrupted again on November 20 due to another problem with the neutron target – water leakage inside the vessel. The second target was replaced with the old model target, which was not equipped with any pitting mitigation system, such as a bubbler, a double inner wall and so on, so we resumed the user program on February 20 with 200-kW power.

In the general proposals for the 2015A period, 168 neutron proposals were approved and 33 proposals were reserved from the 281 proposals submitted by the MLF Advisory Board after the Neutron Science Proposal Review Committee. However, we decided to cancel the call for proposals for the 2015B period in order to accommodate the 2015A experiments. Moreover, we had to carry over a total of 70 experiment days from 2015 to the 2016A period.

2. Instruments

The layout of the neutron instruments at MLF as of the end of JFY 2015 is shown in Fig. 1.

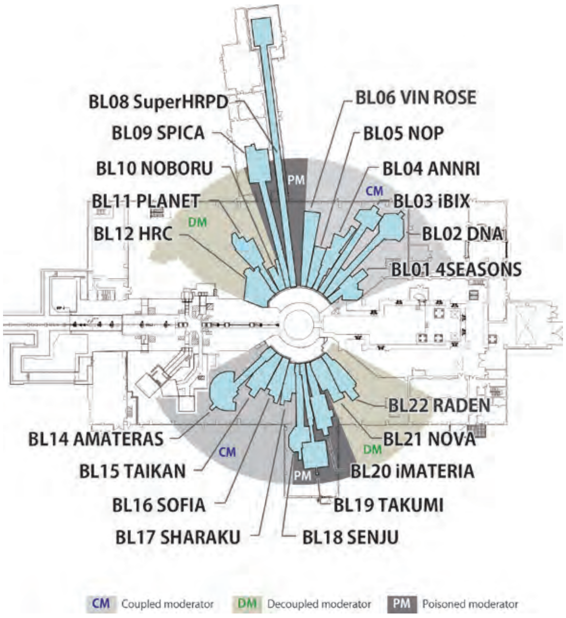

Figure 1. Layout of the neutron instruments at MLF as of JFY 2014. BL06 & 22 had proceeded to the commissioning and user program phases respectively in this fiscal year. BL23 remained under construction.

The upgrades of the operating instruments advanced by using grant-aids, such as the NEDO "Research & Development Initiative for Scientific Innovation of New Generation Batteries" (RISING) project. In the project, in-operando measurement of batteries was realized on SPICA at BL09. The Construction of the neutron spin echo (NSE) spectrometers VIN ROSE at BL06 was continued by Kyoto University and KEK. After refinement of the NSE signal in October, 2015, an effective 200 kHz TOF-MIEZE (Modulated IntEnsity by Zero Effort) signal was observed successfully (Fig. 2). POLANO at BL23, funded by the JFY2012 supplemental budgets of Tohoku University and KEK, is expected to accept the first neutron beam in FY2016. The first inelastic scattering experiment will be performed with ^{3}He spin filter and spin analyzer of Fe/Si supermirror system (Fig. 3).

The construction and part of the commissioning on the energy-resolved neutron imaging system, RADEN at BL22, have been finished and it was opened to the user program as a public beam line instrument from the 2015A period.

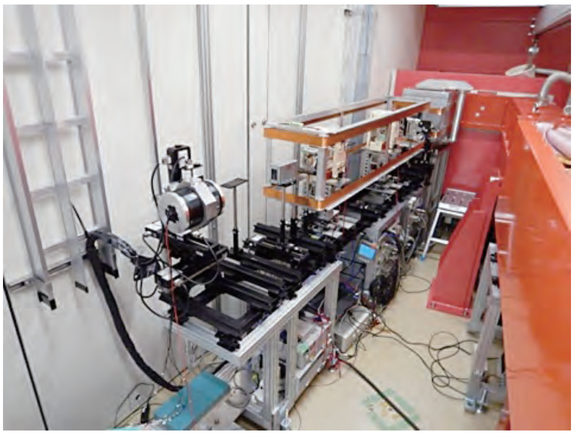

Figure 2. MIEZE spectrometer of VIN-ROSE.

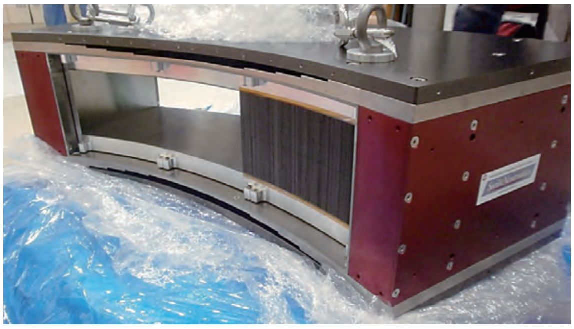

Figure 3. Spin analyzer system of POLANO.

3. International Activities

We hosted the Workshop on Neutron Wavelength-dependent imaging-7 (NEUWAVE-7), held from May 31 to June 3 at the Ibaraki Cultural Center in Mito. (Fig. 4) It was attended by 55 pariticipants from Japan, U.S., U.K., Denmark, Switzerland, Germany and other countries. We had 29 presetations on instruments and facilities reports, developments on intruments and methods, applications and so on. After this workshop, on June 4, we held the 2nd International Advisory Committee Meeting on RADEN(BL22) in Tokai, whith comittee members Dr. E. H. Lehmann (PSI), Dr. B. Schillinger (TUM), Dr. N. Kardjilov (HZB), Dr. W. Kockelmann (ISIS), Prof. Y. Saitoh (Kyoto U.) and Prof. T. Nakanishi (U. of Tokyo).

On July 30, we held the 1st Japan-Korea Joint Workshop on Polarized Neutron Reflectometry at the J-PARC Center. At this workshop, possible international collaboration between Korea and Japan was discussed. We had 18 participants (11 from Japan, 7 from Korea) and 10 presentations.

From December 2 to 5, we hosted the joint school of the 7th AONSA Neutron School and the 3rd MLF School (Fig. 5). The school was supported and sponsored by the Asia-Oceania Neutron Scattering Association (AONSA), the Japanese Society for Neutron Science (JSNS), the International Atomic Energy Agency (IAEA), the Society of Muon and Meson Science of Japan, the Comprehensive Research Organization for Science and Society, the University of Tokyo, the Institute for Solid State Physics, the Institute of Materials Structure Science, the High Energy Accelerator Research Organization, the Ibaraki Prefecture and the Australian Institute of Nuclear Science and Engineering. 41 young researchers and graduate students from Japan, Korea, Australia, Indonesia, India, China, Taiwan, Malaysia, United States and Iranparticipated in the school. Unfortunately, J-PARC had no neutrons or muons beams at the school, but the participants enjoyed cold-experiments on 11 neutron beam lines and one muon instrument, followed by comprehensive lectures on neutron and muon sciences.

4. Resultant outcomes

The research activities in neutron science at MLF resulted in more than 110 papers. The number includes articles in influential journals such as Nature Physics and Nature Communications.

The PLANET beam line group won the Technology Prize of the Japanese Society for Neutron Science for the development of the powder diffractometer specializing in high-pressure experiments, PLANET. Susumu Ikeda, a professor emeritus of KEK, received the Achievement Prize from the Japanese Society for Neutron Science for his contributions to the pulsed neutron scattering facility and observation of hydrogen in materials.

We distributed 5 press releases on scientific outcomes and technical development from our beam lines:
Just a touch of skyrmions: Skyrmions have been widely touted as providing the basis for new high-density memory devices because of their small size and relative stability. It was found that manipulation of skyrmions—tiny nanometer-sized magnetic vortices at the surface of magnetic materials— is possible by using mechanical energy. (October 13, 2015)
Comprehensive use of neutrons, X-rays and supercomputers for the development of tire rubber: Development of high-performance tire technology by Sumitomo Rubber Industries, Ltd. (ADVANCED 4D NANO DESIGN) was announced by the company. It was established that atomic scale structure and dynamics

Figure 4. Participants in the Workshop on Neutron Wavelength-dependent imaging-7 (NEUWAVE-7).

Figure 5. Group photo at the farewell party of the joint school of the 7th AONSA Neutron School and the 3rd MLF School.

of tires by neutrons, X-rays and computer simulations were used to improve inconsistent performances of the car tires, namely, fuel consumption, gripping and wear resistance. (November 12, 2015)

Diffusion process analysis of super ionic conductor towards all solid-state ion battery: The diffusion path of Li ion was revealed with the combinational technique of powder diffraction and quasi-inelastic measurements. The estimated diffusion distance of Li ion by structural modeling based on powder diffraction data is consistent with the one estimated by the momentum dependence of quasi-inelastic intensity. This technique will likely be applied to other super ionic materials. (January 20, 2016)

Hydride-ion conduction makes its first appearance: The first electrochemical reaction based on hydride ions in an oxide-based solid-state cell for potential next-generation batteries was demonstrated. It was examined how the structure of their oxyhydride compounds changed with composition and synthesis conditions. The characteristics of the electronic structure was also studied and suggested an ionic Li-H bond in the compound, namely the existence of H- in the oxides. (March 18, 2016)

Solid electrolytes open doors to solid-state batteries: Newly synthesized two-crystal materials show great promise as solid electrolytes. All-solid-state batteries built using the solid electrolytes exhibit excellent properties, including high power and high energy densities, and could be used in long-distance electric vehicles. By the powder diffraction technique, it has been shown how the lithium ions move fast in the structure of their compounds even at room temperature. (March 22, 2016)

K. Nakajima[1], Y. Kawakita[1], S. Itoh[1,2], and T. Otomo[1,2]

[1]*Neutron Science Section, Materials and Life Science Division, J-PARC Center;* [2]*Institute of Materials Structure Science, High Energy Accelerator Research Organization, KEK*

BL01: 4D-Space Access Neutron Spectrometer 4SEASONS

1. Introduction and Statistics

4SEASONS is a thermal neutron Fermi-chopper spectrometer for inelastic scattering measurements, and one of the Public Beamlines in MLF [1]. The momentum-energy region for this spectrometer occupies the middle of the momentum-energy space covered by all MLF spectrometers [2]. In the 2015A term, 18 General Use proposals, including 1 Urgent Proposal and 1 Trial Use Proposal, were applied for, and 12 of them were approved. 8 proposals were submitted by international users. The major research fields, reflected in the proposals, were strongly correlated electron systems and magnetism, which dominated 83% of the General Use proposals in 2015. In addition to the General Use proposals, 2 Strategic Use proposals for the Element-Strategy Project for electronic materials were submitted and approved. Unfortunately, more than half of the approved proposals had to be postponed for 2016, and the call-for-proposals for the 2015B term was canceled because of an unexpected long-term shutdown of MLF.

2. Detectors

The detector installation, which has been in progress through 2013 and 2014, continued in fiscal year 2015 and 13 new pieces were installed. Now, the maximum horizontal scattering angle is 90.7°. Although this value is still lower than the designed one, 130.5° [1], it is substantially larger than the initial value, 54.5°. We expect the increased scattering angle to make the experiments for lattice dynamics more feasible.

^{3}He detector is vulnerable to vibration, especially when the electric power is supplied. Our experience with the big earthquake in March 11, 2011, reminded us of the importance of the protection of the detectors against earthquakes. Accordingly, we introduced an interlock system to prevent detector damage caused by that type of disaster. It is connected to seismometers placed in the experimental halls. Once it detects an earthquake whose intensity is bigger than some specified value, it cuts the electric power supply to the detectors. The interlock system is expandable to adopt other input signals of incidents. We have connected the system to the vacuum gauge of the scattering chamber, so that it could also cut the power to the detectors in the case of an unexpectedly rapid vacuum break.

3. Preparing for Magnet

So far, no magnets are available on 4SEASONS, though the dimension of the sample environment attachment flange of the scattering chamber can accommodate the common-use 7-T magnet in MLF. Many iron components, surrounding the sample area, and the turbomolecular pumps with magnetic bearings, are attached just below the sample position, which makes it difficult to use magnets on the instrument. Because of that, we are investigating stray fields, taking into account the iron components with special consideration of the field intensity on the turbomolecular pumps. To validate our calculations, we operated the common-use magnet on 4SEASONS for the first time (Fig. 1), and measured the intensity of the magnetic field at several points around the magnet. Although the maximum applied field in this test operation was only 1 T, the observed values were consistent with the calculations. We are continuing the numerical calculations of the stray field to find an appropriate measure to protect the turbomolecular pumps against the field and estimate the maximum available field on the instrument.

Figure 1. The common-use magnet being installed on 4SEASONS by the technical supporting staffs of MLF.

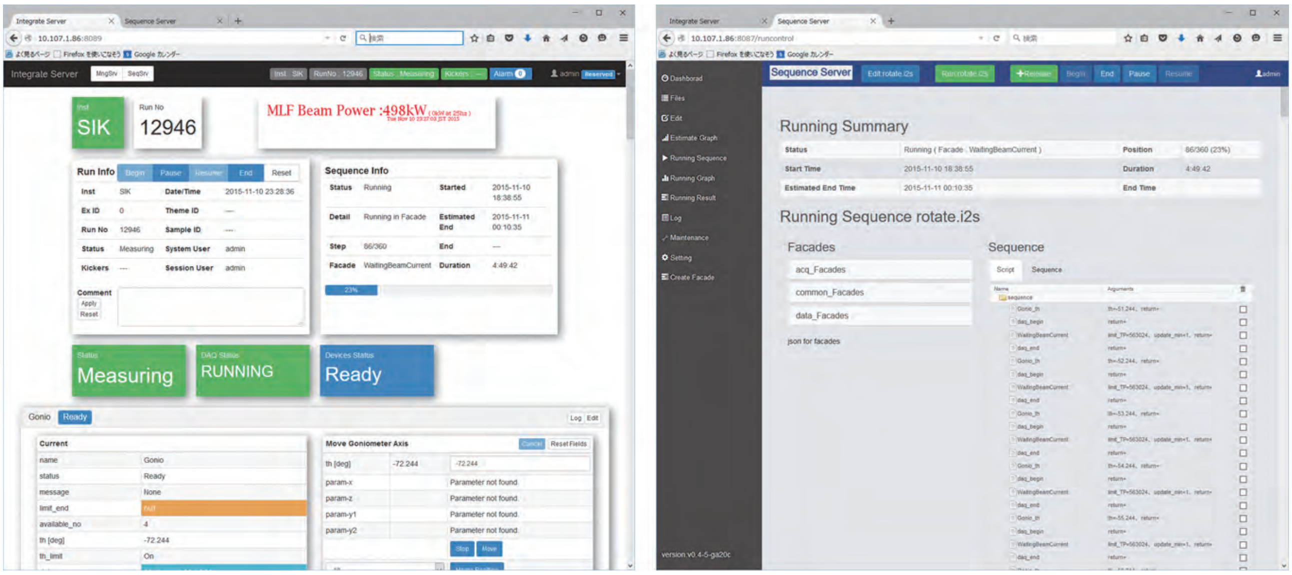

Figure 2. Web interfaces of the new instrument control system of 4SEASONS. (Left) Integrate Server to control the devices and run measurements. (Right) Sequence Server to manage measurement sequences.

4. Instrument Control System

Many of the instruments in MLF, including 4SEASONS, utilize instrument control systems based on the control software framework IROHA. Recently, a new control software framework, called IROHA2, has been developed to replace IROHA [3]. We developed a new instrument control system based on IROHA2, and made it available for user experiments. This new control system enabled us to control different devices uniformly and to introduce new devices easily. Furthermore, users can control the instrument intuitively and remotely using web-based user-interfaces (Fig. 2).

Figure 3. The extension floor under construction.

5. Extension Floor

Since 4SEASONS has the smallest dimension among the existing chopper spectrometers in MLF, it has a limited work area to operate the devices and to prepare for experiments. To expand the work area of the instrument, we constructed an extension floor between the shielding house and the wall of the experimental hall (Fig. 3). The extension floor is designed in a way to connect seamlessly to the roof of the shielding house.

References

[1] R. Kajimoto, M. Nakamura, Y. Inamura, F. Mi-zuno, K. Nakajima, S. Ohira-Kawamura, T. Yokoo, T. Nakatani, R. Maruyama, K. Soyama, K. Shibata, K. Suzuya, S. Sato, K. Aizawa, M. Arai, S. Wakimoto, M. Ishikado, S. Shamoto, M. Fujita, H. Hiraka, K. Ohoyama, K. Yamada, and C. H. Lee, J. Phys. Soc. Jpn. **80**, SB025 (2011).

[2] H. Seto, S. Itoh, T. Yokoo, H. Endo, K. Nakajima, K. Shibata, R. Kajimoto, S. Ohira-Kawamura, M. Nakamura, Y. Kawakita, H. Nakagawa, T. Yamada, BBA - General Subjects, doi:10.1016/j.bbagen.2016.04.025.

[3] T. Nakatani, Y. Inamura, T. Ito, and T. Otomo, JPS Conf. Proc. **8**, 036013 (2015).

R. Kajimoto[1], M. Nakamura[1], Y. Inamura[1], T. Nakatani[1], K. Kamazawa[2], K. Ikeuchi[2], K. Iida[2], M. Ishikado[2], and H. Kira[2]

[1]*Neutron Science Section, Materials and Life Science Division, J-PARC Center;* [2]*R&D Division, Neutron Science and Technology Center, CROSS*

BL02: Current Status of the Broadband Micro-eV Quasielastic and Inelastic Neutron Spectrometer DNA

1. Introduction and Specification

DNA, a time-of-flight (TOF) near-backscattering spectrometer (n-BSS), is a unique instrument among spallation pulsed neutron facilities over the world in terms of n-BSS equipped with a high-speed pulse-shaping disc-chopper [1]. Neutron beam from the coupled moderator which provides most intense but broadest pulse among all three moderators in MLF is handled flexibly in pulse width by this chopper with keeping intensity and making symmetrical pulse in a TOF spectrum. Si crystal analyzers with back-coated by neutron absorber extremely reduces unfavorable background scattering of the instrument so as to reach signal-to-noise ratio of ~10^5. Those factors gave big advantage to enlarge application fields to dynamical behaviors of atoms and spins in bio-molecules [2], soft-materials and strongly-correlated electron system in nanosecond timescale or in micro-eV energy region.

The overview of DNA is shown in Fig. 1(a). The pulse-shaping chopper, the first key device for DNA, is located relatively upstream in neutron guide at 7.75 m from the moderator since time for slit opening at this position becomes the origin of TOF analysis. The chopper disk has four slits with two types of different slit sizes (3 with 30 mm slit and 1 with 10 mm slit), which gives us adjustability of energy resolution as well as rotational speed change does. Another merit of the pulse shaping chopper is to realize scanning method over a wide energy-transfer range with keeping high energy resolution by changing phase of slit opening relative to pulse trigger.

The Si111 crystal analyzers, the second key device for DNA, installed in the vacuum vessel cover the scattering-angle ranges from −30 degrees to +150 degrees in the horizontal plane and from +21 degrees to −14 degrees in the vertical direction (Fig. 1(b)). The analyzer spherical surface is divided to the upper and the lower parts centering on different positions upward and downward by 102 mm of the scattering center (sample position), respectively. Neutrons scattered by

Table 1. Instrumental specifications of DNA.

Items	Specification
Neutron source (NS)	Coupled Liquid H2 Moderator
L1 (source-sample)	42 [m]
L2 (sample-analyzer)	~2.3 [m]
L3 (analyzer-detector)	~2.0 [m]
Pulse sharpening chopper (PS-chopper)	
Max speed: 300 Hz at ~7.5 m from NS	
(Present Max speed: 225 Hz by 4 slits on one disc)	
Crystal Analyzer	
Crystal and reflection index	Si(111) Si(311) in test
Bragg angle of analyzers	~87.5 [deg.]
Energy resolution	
	~2.4 [μeV]: Si(111) with 10 mm Slit @225 Hz ~3.5 [μeV]: Si(111) with 30 mm Slit @225 Hz ~14 [μeV]: Si(111) without PS-chopper ~12 [μeV]: Si(311) with 10 mm Slit @225 Hz.
Momentum range	$0.07 < Q < 1.86$ $[A^{-1}]$: Si(111) $1.0 < Q < 3.80$ $[A^{-1}]$: Si(311) in plan
Scan energy range:	
Si(111): −40 < E/μeV < 100: Single pulse scan around Ef	
−400 < E/μeV < 600: Multi pulse scan around Ef	
−500 < E/μeV <1500: without PS-chopper in second frame	
Si(311): −150 < E/μeV <300: Single pulse scan around Ef	
(the specifications by the end of March 2016)	

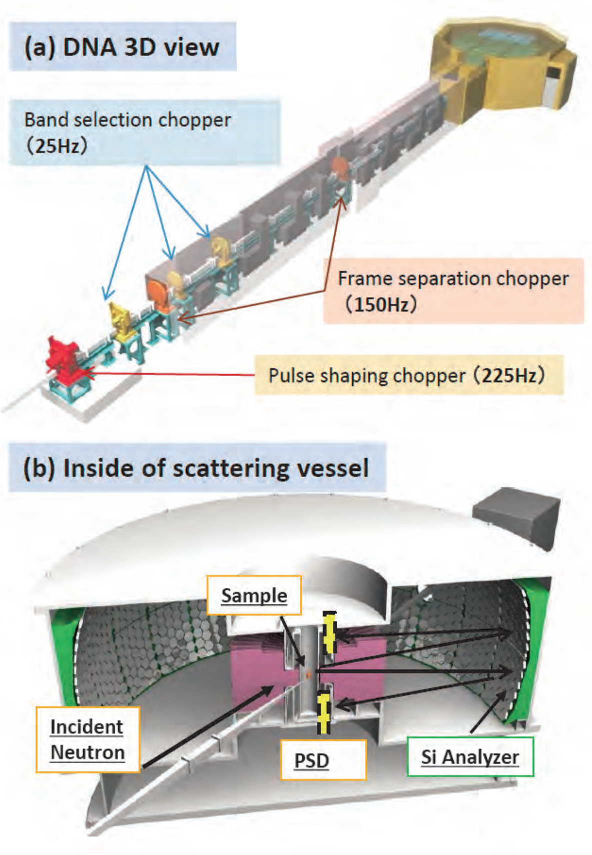

Figure 1. DNA 3D view (a) and inside of scattering vessel (b).

the sample are energy-analyzed with near back-scattering condition of at Bragg angle θ_B ~87.5 degree) and then countered by position-sensitive ^{3}He gas detectors (PSD) arranged on the same circumference of the scattering center upward and downward shifted (Fig. 1(b)). These arrangements of the analyzer units and the detectors enable us to angle-resolve scattered neutrons in horizontal and vertical directions two-dimensionally, and therefore, this spectrometer has a potential to conduct experiment even for single crystalline sample.

2. Application

The optimal combination of the major spectroscopic devices: pulse shaping chopper, Si crystal analyzer and so on, it became possible to measure the S (Q, E) with micro-eV high energy resolution, high beam intensity at the sample position and quite low instrumental background. Taking advantage of this feature, the sciences research field using *DNA* will be expanded not only for quasi- elastic neutron scattering but also for inelastic neutron scattering with very precise energy resolution.

References

[1] Kaoru SHIBATA, Nobuaki TAKAHASHI1, Yukinobu KAWAKITA, Masato MATSUURA, Takeshi YAMADA, Taiki TOMINAGA, Wataru KAMBARA, Makoto KOBAYASHI, Yasuhiro INAMURA, Takeshi NAKATANI, Kenji NAKAJIMA, and Masatoshi ARAI., JPS Conference Proceedings, 8, 036022 (2015).

[2] S. Fujiwara, T. Yamada, T. Matsuo, N. Takahashi, K. Kamazawa, Y. Kawakita, and K. Shibata: Journal of the Physical Society of Japan, 82, SA019 (2013).

K. Shibata[1], Y. Kawakita[1], M. Matuura[2], T. Tominaga[2], T. Yamada[2], K. Nakajima[1], W. Kambara[1], M. Kobayashi[2], Y. Inamura[1], T. Nakatani[1], and S. Kasai[2]

[1]*Neutron Science Section, Materials and Life Science Division, J-PARC Center;* [2]*Neutron R&D Division, CROSS-Tokai*

Current Status of IBARAKI Biological Crystal Diffractometer iBIX

1. Introduction

IBARAKI biological crystal diffractometer called iBIX was constructed at BL03, MLF, to perform high throughput single crystal neutron structure analysis mainly for biological macromolecules in various life processes (2008) [1]. To achieve a high performance, we developed successfully a new photon-counting two-dimensional detector system using scintillator sheets and wavelength-shifting (WLS) fiber arrays for the X/Y axes. In 2012, we upgraded the 14 existing detectors and installed 16 new detectors for the diffractometer of iBIX (Fig. 1). The total solid angle of detectors subtended by a sample and the average detector efficiency increased by 2 and 3 times, respectively [2]. The total measurement efficiency of the present diffractometer was on one order of magnitude from the previous one coupled with the increasing of the accelerator power. In the end of 2012, it became possible to use iBIX regularly to investigate biological macromolecules in user experiments. The final specifications of the iBIX are shown in Table 1.

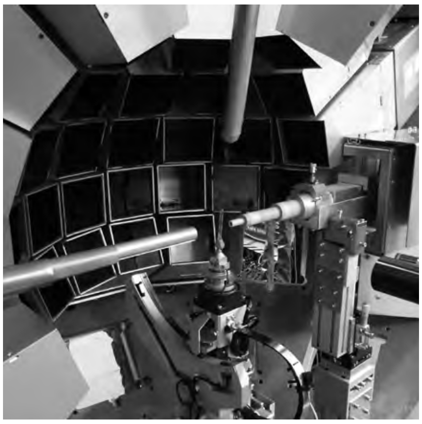

Figure 1. Inside of the iBIX Diffractometer.

Table 1. Specifications of iBIX.

Moderator	Coupled
Wavelength of incident neutron	0.7 ~ 4.0 Å (1st frame) 4.0 ~ 8.0 Å (2nd frame)
Neutron intensity (@1 MW)	0.7×10^6 n/s/mm^2
L_1	40 m
L_2	500 mm
Solid angle of detectors	19.5% for 4π
Detector covered region	+15.5 ~ +168.5 °
Detector size	133 × 133 mm
Detectors pixel size	0.52 × 0.52 mm
No. of detectors	30

2. Current status

In 2015, the accelerator power of J-PARC increased to 400 ~ 600 kW. We accomplished the following in collecting a full data set about biological macromolecules for neutron structure analysis by using iBIX. The maximum unit cell size was 110 × 110 × 70 Å. The average sample volume was about 2 ~ 3 mm^3, the average measurement time was about 7 ~ 10 days. If the accelerator power reaches 1 MW, the total measurement time or the sample size will be reduced by half.

At the beginning of 2015, we distributed two press releases on the scientific outcomes, which have made the most of the capabilities of the neutron diffraction experiment by using iBIX;

1) The neutron crystal structure of the PcyA-BV complex was determined at room temperature. It was observed that approximately half of the BV bound to PcyA was BVH+ , a state in which all four pyrrole nitrogen atoms were protonated (N-protonated), and both of the lactam structures of BV were preserved in wild-type PcyA. Those results will provide crucial information for elucidating the unique catalytic mechanisms of PcyA [3].
2) The neutron crystal structures of inveting cellulose unliganded and libanded PcCel45A were determined at room temperature. Those results indicate the key role of multiple tautomerizations of asparagine residues and peptide bonds, which are finally connected to the other catalytic residue via typical side-chain hydrogen bonds, in forming the "Newton's cradle"–like proton relay pathway of the catalytic cycle [4].

3. Development

In order to improve the quality of the integrated intensity of weak reflections, we developed a profile-fitting method for the peak integration of the data reduction software STARGazer. To determine the proper fitting functions, four asymmetric functions were evaluated using strong intensity peaks. The Gaussian function convolved with two back-to-back exponentials was selected as the most suitable fitting function for TOF diffraction data by iBIX. A profile-fitting algorithm for the integration method was developed and the integration component was implemented in STARGazer. The profile-fitting component was applied to the TOF diffraction data set of standard protein samples obtained by iBIX. From the results, the integrated intensities and model structure obtained by the profile-fitting method were more accurate than those of the summation-integration method, especially at higher resolution shells [5]. We already prepared its user manual and the distribution package of the data reduction software, including the profile-fitting component.

To respond to user's needs, we developed a new piece of equipment for sample environments, a cooling system for capillary-enclosed samples. The temperature of a capillary enclosed sample is maintained at around 0°C Both the peltier cooling system, mounted on the goniometer head, and the N_2 gas flow cooling system were used for sample cooling in order to prevent the condensation of dew inside the capillary. This equipment can be mounted on the three-axe goniometer. In 2016, we will attempt to test measurement with this equipment.

4. Future prospects

In the future, the accelerator power of J-PARC will be increased to 1 MW. iBIX should be available regularly for full-data set measurement of sample size of 1 mm^3. We will continue to develop the data reduction software and beamline instruments, in order to improve the accuracy of intensity data obtained from small samples. Furthermore, we will validate whether it is possible to conduct full-data measurement, its reduction and the structure analysis of the sample with a large unit cell (132 × 132 × 132 Å) by using iBIX.

We should be able to complete successfully the development of utility equipment for sample environments (heating, extension system for polymer sample, pulse laser system and cooling system for capillary-enclosed samples). And then, in 2016, we will start applying this equipment in user experiments.

References

[1] I. Tanaka, K. Kusaka, T. Hosoya, N. Niimura, T. Ohhara, K. Kurihara, T. Yamada, Y. Ohnishi, K. Tomoyori and T. Yokoyama, Acta Cryst. D66 (2010) 1194–1197.

[2] K. Kusaka, T. Hosoya, T. Yamada, K. Tomoyori, T. Ohhara, M. Katagiri, K. Kurihara, I. Tanaka and N. Niimura J. Synchrotron Rad. 20 (2013) 994-998.

[3] M. Unno, K. Ishikawa-Suto, K. Kusaka, T. Tamada, Y. Hagiwara, M. Sugishima, K. Wada, T. Yamada, K. Tomoyori, T. Hosoya, I. Tanaka, N. Niimura, R. Kuroki, K. Inaka, M. Ishihara, K. Fukuyama J. Synchrotron Rad. 20 (2013) 994-998.

[4] A. Nakamura, K. Igarashi, K. Kusaka, S. Fushinobu, Y. Higuchi, T. Ishida, T. Yamada, Ichiro Tanaka, S. Kaneko, K. Ohta, H. Tanaka, K. Inaka, N. Niimura, M. Samejima J Science Advances (2015) e1500263.

[5] K. Kusaka, T. Hosoya, T. Yamada, K. Tomoyori, T. Ohhara, M. Katagiri, K. Kurihara, I. Tanaka and N. Niimura J. Am. Chem. Soc., 137 (2015) 5452–5460.

[6] N. Yano1, T. Yamada1, T. Hosoya, T. Ohhara, Ichiro Tanaka and K. Kusaka Scientific report 6 (2016) in press.

K. Kusaka[1], T. Yamada[1], N. Yano[1], T. Hosoya[1], I. Tanaka[1], T. Ohhara[2], and M. Katagiri[1]

[1]*Frontier Research Center for Applied Atomic Sciences, Ibaraki University, Tokai;* [2]*J-PARC Center, JAEA*

Current Status of Accurate Neutron-Nucleus Reaction Measurement Instruments, ANNRI (BL04)

1. Introduction

In the J-PARC facility, the proton beam power intensity reached approximately 500 kW in 2015, which was moew than 20-fold increase, compared to the first 20-kW beam shot in 2009. Increasing the beam power of the facility allows its users to obtain a much larger amount of experimental data yields than before.

In the ANNRI facility, two different types of γ-ray detector systems are operated for the neutron capture cross-section measurement. One is a germanium detector system (Ge system), which has very fine γ-ray energy resolution, the other is an NaI detector system (NaI system) with the capability of measurement in a wide neutron-energy range. Since the current DAQ system for the Ge system was designed in 2009, its counting rate performance is almost saturated for the recent J-PARC proton beam power. In order to adapt well to the recently improved J-PARC performance, a new DAQ system has been developed.

In addition, a new Li-glass neutron detector system (Li-glass system) for the total cross-section measurement was installed recently. A new DAQ system for the Li-glass system must be developed, because the current DAQ system cannot be applied to the Li-glass detector signals as is.

2. New DAQ system specification

The new DAQ system is designed by TCP/IP protocol based client-and-server model in order to perform simultaneous measurements at two different locations. The role of the client-side application is to gather data from each ADC and send it to the server-side. The server-side application receives data from each client, build the event data sequence, and save them to the disk. Each client is controlled by a common signal issued from the server-side application.

As a consequence of the client-and-server model design, the DAQ system can accept additional detector systems flexibly, by just creating new clients and connecting them to the server side. Additionally, in the case of a new detector system being installed, only a new client application is necessary for its integration.

Signals from the J-PARC beam monitor were used to measure time-of-flight events. Trigger signals issued from the J-PARC facility were distributed to the ANNRI counting room and divided to the appropriate number of signals. As the trigger signal reaches the facility by several micro-seconds delay, compared to the fastest neutron event (the so-called "gamma-flash"), each trigger is delayed by about one acceleration cycle in order to acquire the gamma-flash events as well.

Figure 1 shows the schematic diagram of the J-PARC/MLF/ANNRI facility and the data flow of the DAQ system.

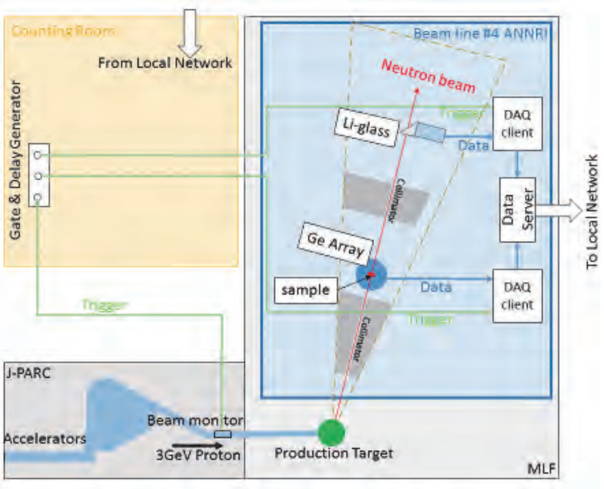

Figure 1. Schematic view of the J-PARC/MLF/ANNRI facility and the data flow of the DAQ system.

3. Total cross-section measurement system development

In order to measure the total neutron cross-section, two Li-glass scintillators with different characteristics were prepared. One was the ^{6}Li enriched type (>90%) scintillator (GS20) and the other was the ^{7}Li enriched type (>99.99%, GS30). Since the neutron detection by the Li-glass scintillator is followed by a ^{6}Li(n,α)t reaction, the enrichment of the ^{7}Li isotopes hinders the neutron detection efficiency. The low neutron detection efficiency of the GS30 scintillator allows its usage for estimating the amount of γ-ray background. Two different volumes, 1 × 50 × 50 mm and 10 × 100 × 100 mm, of glasses were prepared for each of the scintillators.

Figure 2 shows the pulse height spectrum registered by the GS20 scintillator. The 1-mm scintillator has better energy resolution than the 10-mm one because of its light-collection efficiency. For the neutron detection by using a Li-glass detector, the main background event is due to γ-rays. In order to remove the γ-ray effect,

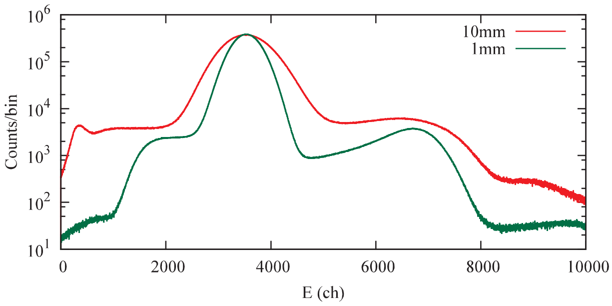

Figure 2. Pulse height spectrum of GS20-type neutron detectors. The green solid line represents the 1-mm-thick scintillator, and the red solid line the 10-mm-thick one.

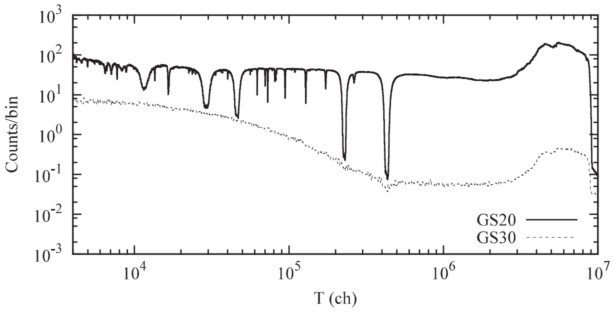

Figure 3. The γ-ray background estimation using the GS30 scintillator. The solid line shows the time-of-flight spectrum by the GS20 scintillator and the dashed line depicts the GS30 scintillator.

a GS30 scintillator was used. From the measurement in the same experimental setting for both GS20 and GS30, the γ-ray background amount is estimated by the GS30 spectrum. The amount of the γ-ray background was estimated using black resonance filter, located at the upstream side of the ANNRI beamline. Figure 3 shows an example of GS30 γ-ray background estimation. The black resonance locations are reproduced well by the GS30 spectrum.

4. Count rate performance

In the new DAQ system, two different types of ADCs are prepared. One is the CAEN [1] v1724 peak sensitive type ADC. The other is the CAEN v1720 charge integrate type ADC. In case of the v1720 ADC board, no self-trigger signal will be established while a gate signal is open. The dead time, caused by a trigger signal, will never be extended by the pile-up signal. By the way, the dead time, caused by the pile-up rejection logic, will be extended with probability proportional to the event rate. In the v1724 case, both dead time by trigger signal and pile-up rejection logic will be extended depending on the event rate. The counting efficiency of the DAQ system was determined by careful analysis of the different behavior.

Figure 4 shows the counting efficiency. The Figure on the left depicts the Ge detector with different shaping time settings. The Figure on the right shows the difference between 1-mm-thick and 10-mm-thick Li-glass. Typically, the system works with 50 kHz for Ge detectors and 100 kHz for Li-glass detectors.

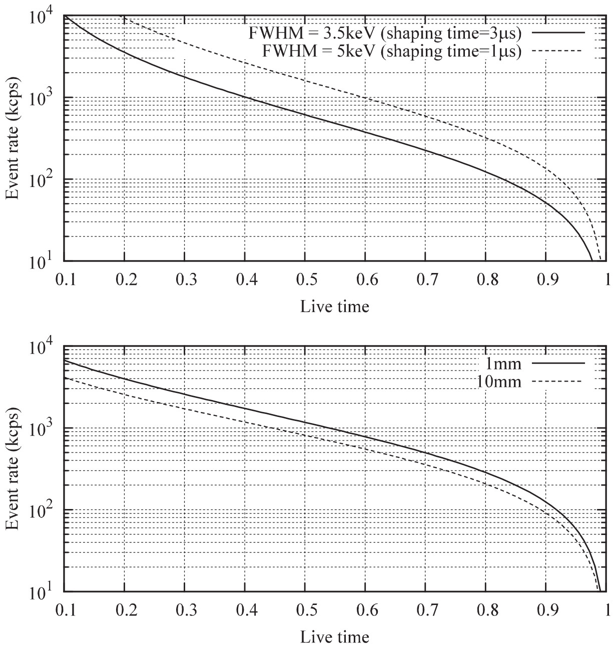

Figure 4. The counting efficiency of the DAQ system. The upper Figure shows the acceptable event rate of the Ge detectors with different shaping time. The lower Figure shows the difference of the counting rate capability of the 1-mm (solid line) and the 10-mm (dashed line) Li-glass scintillators.

The authors would like to thank the accelerator and technical staff at J-PARC for operating the accelerator and the neutron production target and for their other experimental support. The present study includes the result of "Research and Development for accuracy improvement of neutron nuclear data on minor actinides" entrusted to the Japan Atomic Energy Agency by the Ministry of Education, Culture, Sports, Science and Technology of Japan (MEXT).

Reference

[1] http://www.caen.it/

T. Nakao
Nuclear Data Center, Nuclear Science and Engineering Center, JAEA

Present Status of BL05 (NOP)

1. Introduction

BL05 (NOP) is a beamline to carry out fundamental physics experiments using neutrons. The beamline is divided at its upstream into three branches to conduct different experiments in a parallel way [1]. The present status of the ongoing experiments at BL05 (NOP) will be reported here.

2. Measurement of the neutron lifetime

A neutron decays into a proton, an electron, and an antineutrino. The lifetime is an important parameter for the unitarity of the CKM matrix or the primordial big bang nucleosynthesis. However, recently reported values for the neutron lifetime deviate significantly from the systematic errors. An experiment to measure the neutron lifetime with a pulsed beam is ongoing at BL05 (NOP). The lifetime is measured as the ratio of the electron events to the ^{3}He(n,p)^{3}H events caused by precisely doped ^{3}He gas using a time-projection chamber (TPC) [2].

Physics data have been collected for about 4 week by the TPC. Then the data were analyzed by using Monte Carlo simulation.

For cross check and demonstration of our TPC and gas handling system, we measured the reaction cross section of ^{14}N(n,p)^{14}C, which has been previously measured with an accuracy of 1.6% with scale factor of 1.54. Our preliminary result was 1.864(3) barn, whose accuracy was 0.3%, consistent with the mean value from previous measurements (Fig. 1).

3. Ultracold neutron production by Doppler shifter

Ultracold neutrons (UCNs), which have energy less than ~250 neV (velocity of 6.8 m/s), are utilized for various precision measurements in fundamental physics. A Doppler shifter is working to produce UCNs on the BL05 (NOP) beamline [3]. It reflects very cold neutrons (VCNs) with velocity of ~136 m/s with a moving mirror with 68 m/s and produces neutrons with velocity of less than 20 m/s. The UCN intensity is 160 cps at 1 MW.

A UCN storage have been demonstrated using a polished stainless steel vessel. The vessel has two valves to shut UCN up for storage and extraction. The measured UCN storage time was 270 sec at maximum (Fig. 2). An aluminum filter on the exit port at the Doppler shifter shortened the storage time to 180 sec, which could be interpreted that the low-energy UCNs below the Fermi potential of Al (54 neV) were cut, so that the higher energy of the UCNs increased the collisions at the wall.

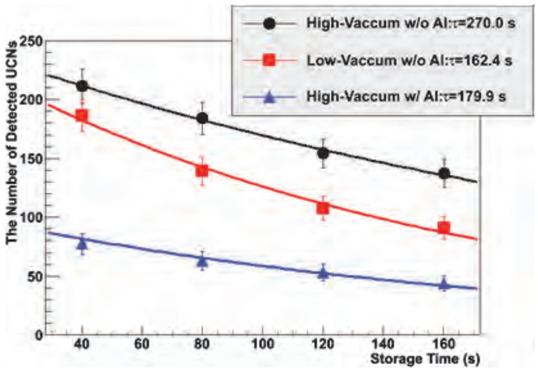

Figure 2. Storage time of UCNs in the stainless storage vessel [5]. The maximum storage time was 270 sec (black). Al filter on the exit of the Doppler shifter shortened the storage time to 180 sec (blue). The worsening of the vacuum (few Pa) also decreased the storage time to 162 sec.

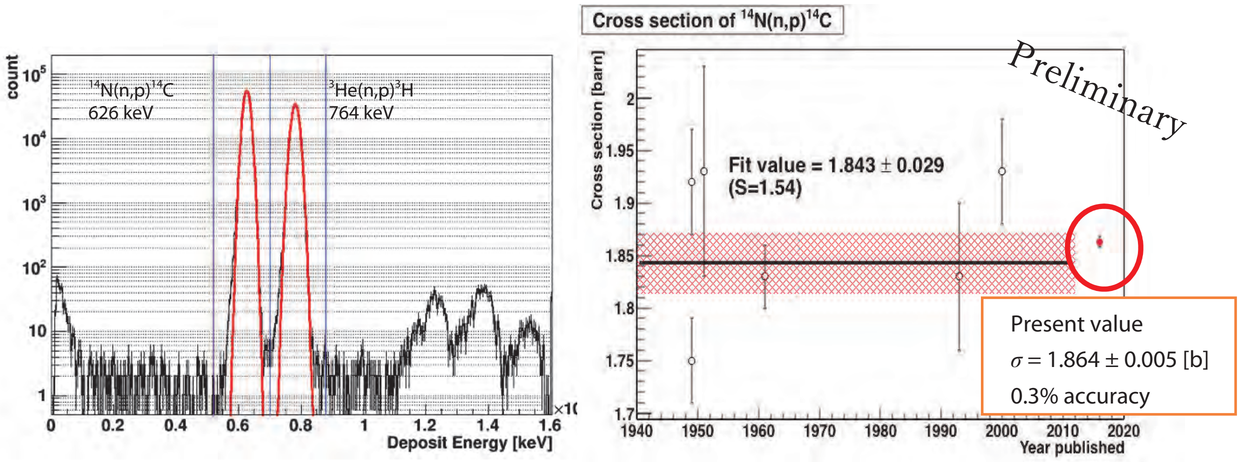

Figure 1. Energy spectrum of ^{14}N(n,p)^{14}C and ^{3}He(n,p)^{3}H reactions (left). Cross sections of ^{14}N(n,p)^{14}C, previous and present [4] (right). The present cross-section (preliminary) was consistent with the mean value of previous results.

4. Development of a sub-micron position sensitive neutron detector using nuclear emulsion

We have been developing a neutron detector with spatial resolution of less than 1 μm by loading ^{6}Li into fine-grained nuclear emulsion. By exposure to thermal neutrons, tracks from neutron capture events were observed. From their grain density, the spatial resolution was estimated. The detection efficiency was also measured at BL05 with cold neutrons, and we concluded that it was consistent with the expected value [6].

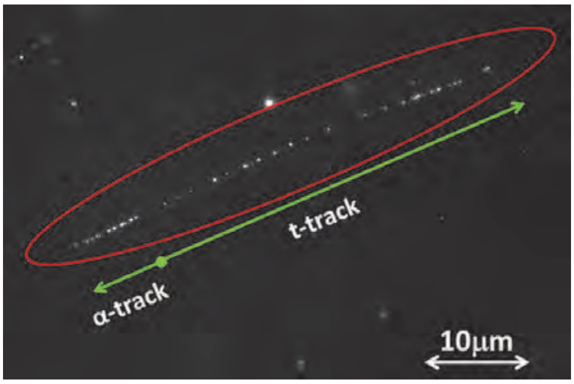

Figure 3. An example of a neutron absorption event by ^{6}Li observed under an optical microscope with an epi-illumination system (surrounded by a red ellipse). A pair of tracks of an alpha particle and a triton in back-to-back topology were recognized [6].

References

[1] K. Mishima, Neutron network news (Hamon), vol25, No2 (2015) 156-160.
[2] Y. Arimoto *et al.*, *Nuclear Instruments and Methods in Physics Research A*, 799 (2015) 187-196.
[3] S. Imajo *et al.*, *Progress of Theoretical and Experimental Physics* 2016.1 (2016) 013C02.
[4] R. Kitaraha *et al.*, JPS Autumn meeting, Miyazaki University (2016).
[5] R. Katayama *et al.*, JPS Autumn meeting, Osaka City University (2015).
[6] N. Naganawa *et al.*, "A neutron detector with spatial resolution of submicron using fine-grained nuclear emulsion" https://arxiv.org/abs/1612.04544

K. Mishima[1,2] on behalf of NOP collaboration
[1]*Neutron Science Section, Materials and Life Science Division, J-PARC Center;* [2]*Institute of Materials Structure Science, KEK*

BL06: Commissioning Status of VIllage of Neutron ResOnance Spin Echo Spectrometers (VIN ROSE)

1. Introduction

Kyoto University and KEK have been installing jointly two types of neutron spin echo (NSE) spectrometers with neutron resonance spin flippers (RSFs) at BL06, that is, a neutron resonance spin echo (NRSE) instrument and a modulated intensity by zero effort (MIEZE) instrument.

Today, the NSE technique is an essential spectroscopic technique, which has achieved the highest energy resolution with neutrons as a probe [1]. NSE with RSFs is a rather new approach [2]. Furthermore, the combination of NSE and a pulsed neutron source makes possible to scan a wide spatiotemporal space very efficiently. The beamline has been named "VIN ROSE" (VIllage of Neutron ResOnance Spin Echo spectrometers) and it will spawn a new field of spectroscopic methods [3].

(a)

2. Commissioning Status at BL06

The project has been started in FY2011, and the first neutron beam has been accepted in FY2014. The first MIEZE signal was observed in the end of FY2014. Figure 1 shows a recent photo (a) and the schematic top view of BL06 (b).

A highlight of the progress achieved in FY2015 was the quantitative analysis of the time-of-flight MIEZE signal. Because the combination of time-of-flight and MIEZE (TOF-MIEZE) is a novel approach, its detailed verification is still ongoing. In the case of continuous neutron sources, the geometric restriction for MIEZE is very tight, that is, a very accurate setting for the distances between the source, flippers, and the detector is required. On the other hand, this requirement can be relaxed by the TOF-MIEZE method, which was investigated both theoretically and experimentally by using BL06 [4]. In Fig. 2, the measured TOF-MIEZE signal and the corresponding 200-kHz power spectrum is exhibited, where the position of the second spin flipper was displaced by 80 mm. The corresponding power spectrum shows a slight deviation from 200 kHz, while the clear TOF-MIEZE signal is observed at that condition. Further theoretical evaluation is now in progress, which is urgently needed for quantitative conversions from MIEZE signals to intermediate scattering functions.

3. Summary

The current status of BL06 VIN ROSE was briefly described. The main progress in FY2015 was the quantitative verification of TOF-MIEZE. This result is essential to evaluate quantitatively the intermediate scattering

(b)

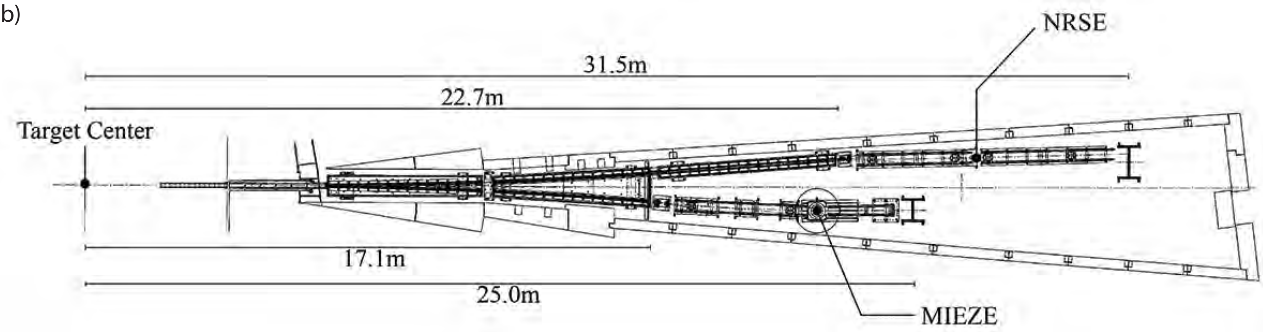

Figure 1. Current picture of BL06 (a), and a schematic top view of MIEZE and NRSE beamline at BL06 (b).

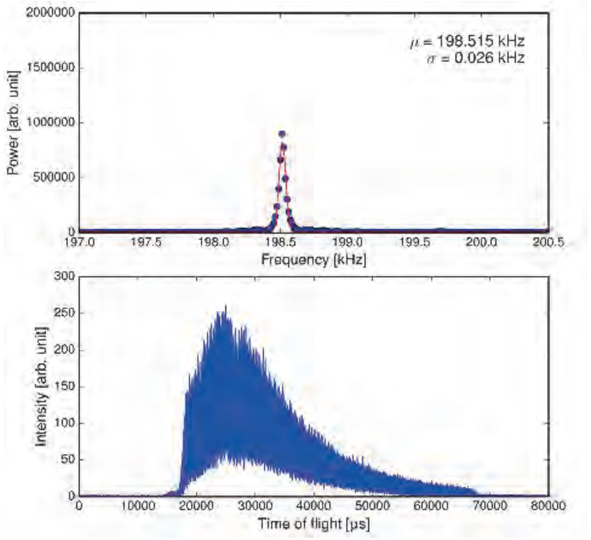

Figure 2. Bottom: experimentally observed TOF-MIEZE signal with effective 200 kHz and 80 mm displacement of the second flipper. Top: corresponding power spectrum by Fourier transformation.

functions. The other advancements are as follows: a 500-kHz MIEZE signal was tested and its feasibility was proved, and prototypes of two-dimensional elliptic mirrors for the NRSE spectrometer were developed and tested at the beamline. Based on these fundamental developments, experiments with some standard samples will be planed for FY2016.

References

[1] F. Mezei ed., Neutron Spin Echo, Lecture Notes in Physics, (Springer, Berlin) 128 (1982).

[2] R. Gähler and R. Golub, J. Phys. France, 49, (1988) 1195-1202.

[3] M. Hino, T. Oda, M. Kitaguch, N. L. Yamada, H. Sagehashi, Y. Kawabata, H. Seto, *Physics Procedia* **42**, (2013) 136.

[4] T. Oda, Doctor Thesis, Kyoto University, (2016).

H. Endo[1,2], M. Hino[3], T. Oda[3], N. L. Yamada[1,2], H. Seto[1,2], and Y. Kawabata[3]
[1]Neutron Science Section, Materials and Life Science Division, J-PARC center; [2]Institute of Materials Structure Science, KEK; [3]Kyoto University Research Reactor Institute

Current Status of the Super High Resolution Powder Diffractometer, SuperHRPD

1. Introduction

SuperHRPD has the world's highest resolution among the TOF neutron powder diffractometers of the same type. In fiscal year 2015, an unscheduled long shutdown due to neutron source problems resulted in shortage of beam time. Four general proposals and a part of the S-type project of 2014S05 were carried out during that limited beam time. The beam time, available for developmental study of the instrument, was insufficient.

2. Updated resolution using powder samples

In FY2014, we installed a new detector system using an 8-mm diameter Position Sensitive Detector (PSD) at all backward banks. The overall resolution of the powder sample improved from $\Delta d/d = 0.1\%$ to 0.08%, and reached resolution $\Delta d/d = 0.04\%$ using limited high angle detectors [1]. In FY2015, with the enhancement of the beam power, we tried to collect data in a more limited detector area (Fig. 1). We divided the backward detector area along the Debye ring, and the area of the different scattering angle 2θ was defined as the a8 from a1. In addition, we defined the horizontal part of the highest scattering angle area as a1′. The NIST standard silicon powder (SRM640d) was measured using a 6 mm in diameter standard sample holder at beam power of 400 kW, and it took 14 hours to obtain the results from this measurement. Figure 2 shows the TOF resolution dependence in each detector area (a1~a8 & a1′). All plotted data points of the resolution were calculated by

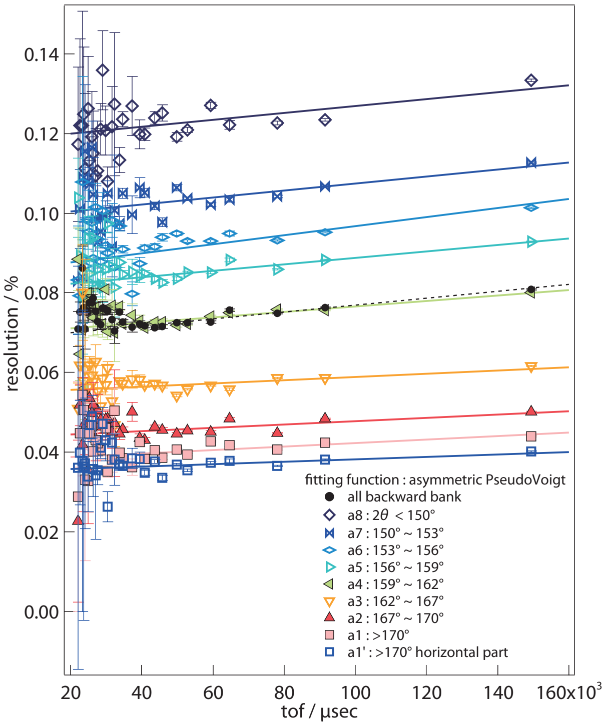

Figure 2. Resolution variation in each detector area. a8 - a1 and a1′ correspond to the divided area of the backward bank detector shown in Fig. 1.

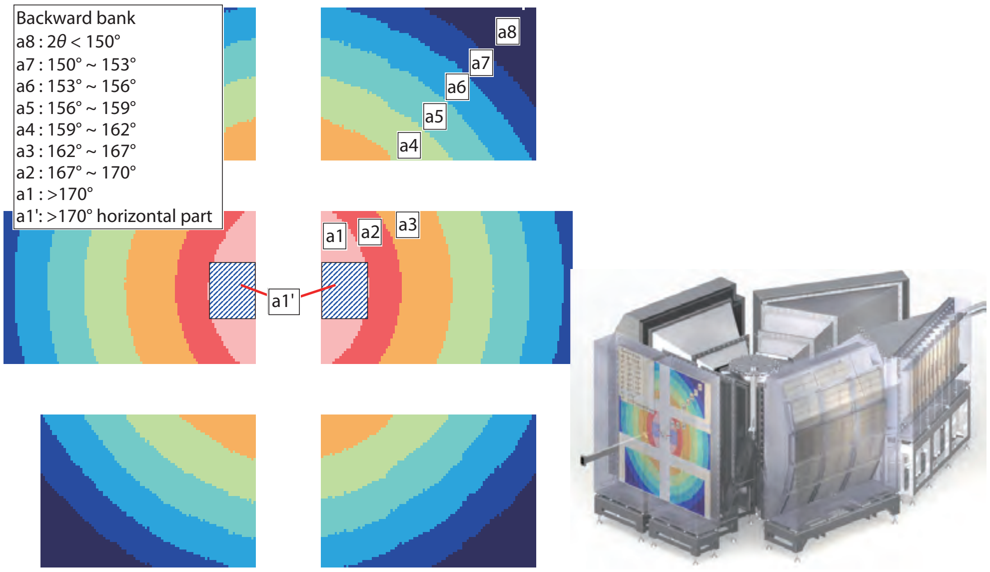

Figure 1. SuperHRPD backward bank detector. We divided the detector area along the Debye ring. The parts shown by hatching are the newly specified area (a1′).

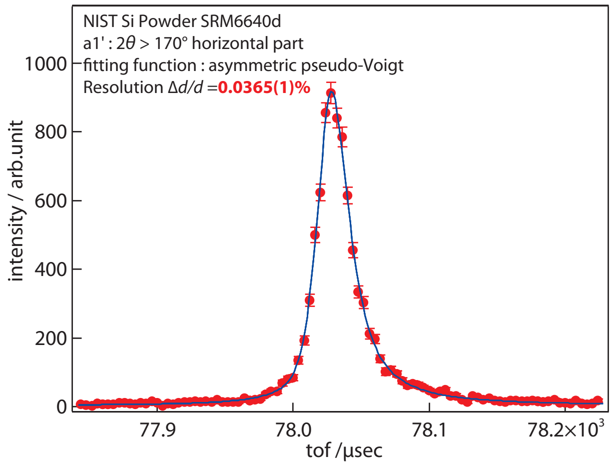

Figure 3. Diffraction peak of the horizontal part of the highest scattering angle area (a1'). We achieved 0.0365(1)% resolution in Δ*d*/*d*.

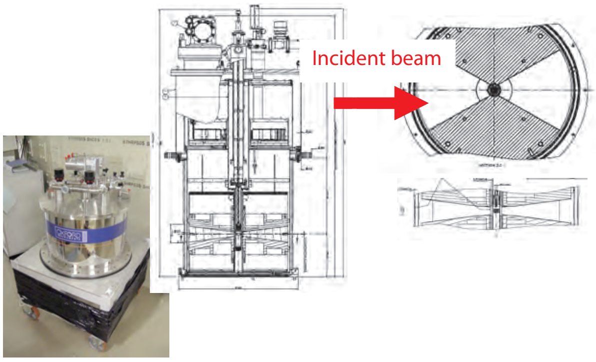

Figure 4. 14-Tesla magnet photo and drawings. The window design created specifically for high-resolution experiments; 1) Open to the high- and low-angle bank side. 2) Large azimuth angle as wide as possible.

fitting of Bragg peaks in a diffraction pattern observed in each detector area using the asymmetric pseudo-Voigt function. It was possible to achieve a resolution of less than 0.1%, except for the a7 and a8 areas, where 2θ was smaller than 153°. With the data obtained by adding all backward detectors (black circle and dashed line), the achieved resolution was less than 0.08%. In the newly defined a1' area (blue square), it achieved less than 0.04%. Figure 3 shows a peak fitting result of the a1' area. The function used for fitting is the asymmetric pseudo-Voigt, as described above. As the Figure indicates, a very sharp peak in the left-right symmetry was obtained. The resolution indicates $\Delta d/d = 0.0365(1)\%$, this value is equivalent to the one evaluated using a single crystal silicon in June, 2008 [2]. This result shows that it is possible to carry out experiments with the best possible resolution for a powder sample by using a limited detector area.

3. Current status of the 14-Tesla Magnet

We purchased a 14-Tesla magnet from Oxford Instruments PLC. A feature of this magnet is a window design created specifically for high-resolution experiments. The high-angle side window is aiming for observation of very small structure distortion with high resolution, the low-angle side is for observation of the magnetic scattering peaks, by consistently maintaining a large azimuth angle, it is possible to detect efficiently the scattered neutrons (Fig. 4).

In the beginning of this fiscal year, we carried out off-site excitation test outside of MLF and were able to confirm the occurrence of a stable maximum magnetic field of 14 Tesla. Thereafter, the magnet was transported to the MLF SuperHRPD building, where it was assembled and adjusted. Recently, the vacuum leak test was completed, and now we are working urgently to prepare the magnet for commissioning on-site.

4. Future Plans

Further in this study, we plan to complete the initial stage of the development research of SuperHRPD, and reach a stage of expanded and stable scientific research.

References

[1] S. Torii, P. Miao, S. Lee, M. Yonemura and T. Kamiyama, MLF Annual Report 2014, 88-89 (2014).

[2] S. Torii, M. Yonemura, Surya Panca Putra Y T, J. Zhang, P. Miao, T. Muroya, R. Tomiyasu, T. Morishima, S. Satoh, H. Sagehashi, Y. Noda and T. Kamiyama, J. Phys. Soc. Jpn. 80 (2011) SB020.

S. Torii[1,2], P. Miao[1,2], S. Lee[1,2], Y. Ishikawa[1,2], M. Yonemura[1,2], and T. Kamiyama[1,2]
[1]*Neutron Science Section, Materials and Life Science Division, J-PARC center;* [2]*Institute of Materials Structure Science, KEK*

Battery Studies on the Special Environment Neutron Powder Diffractometer using Operando Techniques

1. Introduction

The "*in situ*" techniques have been the world's standard to investigate reactions or structure changes, while preserving the reaction systems or sample environments. On the other hand, the "*operando*" method is used for the same type of targets, but it results in destruction of samples, especially in operative conditions. SPICA has been developing as a dedicated diffractometer for battery studies using *operando* measurements. Elucidating reaction mechanisms occurring in practical operations is crucial for the future development of battery technologies.

In 2010, the design and construction of SPICA began with a grant from foundation supported by RISING (Research & Development Institute for Scientific Innovation of New Generation Batteries). The construction of the main components of SPICA has been almost completed. Some testing measurements were carried out on SPICA. In 2015, the *operando* diffraction and imaging of commercial batteries were measured. From the diffraction data, structure changes, depending on charge rate, were observed. The lithium-ions' distribution and concentration were successfully determined by Rietveld analysis. The observations under high current drain revealed inhomogeneous reactions, a structural relaxation after discharge, and a shift in the lithium concentration ranges with cycling in the electrode matrix.

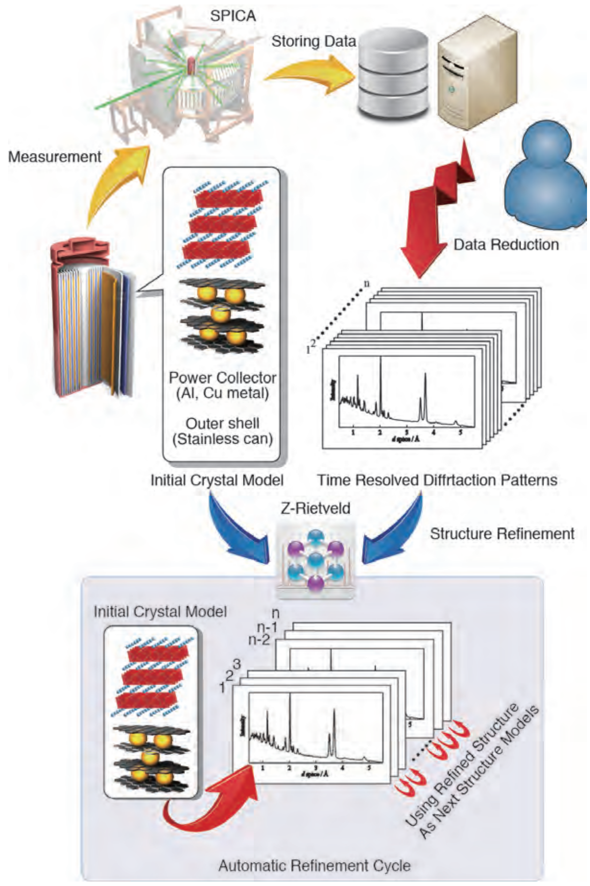

Figure 1. Scheme of automatic structure refinements for a dataset of *operando* measurements.

2. Developing of SPICA and analysis methods for *operando* measurements

Figure 1 shows a typical procedure of *operando* measurements, followed by structural analysis. After the *operando* measurements, some data reduction processes are necessary to analyze diffraction data by the Rietveld method. Therefore, data reduction software was created for *operando* measurements. In MLF, all detected scattered neutrons were stored as the event data. In the *operando* measurements, all scattered neutrons are recorded in a computer storage at once. From the event data, an amount of diffraction data, which depend on the integrated time for each time-resolved diffraction pattern, is needed. Manyo-lib were enhanced to create effectively a data set. As a result, the data reduction speed increased more than 10 times.

After the data reduction process, structure determination using the Rietveld method was necessary. The huge number of diffraction patterns is generated from *operando* measurements. Structure determination was not important for the users because the understanding the structural changes is more valuable for their work. Therefore, an automatic structure analysis process has been developed by improving "Z-Rietveld". Z-Rietveld can handle a data set, which includes multi-diffraction patterns from an *operando* measurement and refinement structures cyclically. In this structure refinements cycles, In the sequential refinement process, the refined crystal structure is used to be as the new crystal structure model to refine the next diffraction pattern.

3. *Operando* measurements and refinements of 18650-type lithium-ion battery

Figure 2(A) depicts the powder neutron diffractometer, SPICA, and Figure 2(B) shows a typical operando measurement geometric condition. A 18650-type commercial lithium-ion battery was put on the sample position of the SPICA diffractometer. The diffraction data were collected under a constant current drain condition. The 18650-type lithium-ions battery has cylindrical shape and contains 5 components, a cathode electrode, anode electrode, polymer separators, electrolyte and a body of the cell, as shown in Figures 2(C) and 2(D).

The typical refinement result of the *operando* multiple data set was shown in Figure 3. It contains all the diffraction peaks from the battery components, i.e. Li_x(Ni, Mn, Co)O_2 (NMC) as the cathode, graphite (C) as anode, Al, Cu as a current corrector and a battery cell (Fe). The structure refinements were carried out by the program, Z-Rietveld. The good agreement factor, R_{wp} and the goodness of fit factor, S of the refinemenst were obtained. This indicated that the automatic refinement provided reasonable structural parameters for the individual phases of the experimental diffraction data during battery operation. The lattice parameters, the ratio of the phases present in the cell, and the structural parameters of each phase were automatically refined by the automatic Rietveld refinement routine developed by a powder-diffraction group in J-PARC.

The *operando* diffraction data set for the automatic refinement verifications by Z-Rietveld was collected using the 0.1 C rate. The lithium composition in both the cathode and the anode was directly determined by the Z-Rietveld for the region, where stage 1 and 2 phases coexist in the anode. Figure 4 shows the composition changes of both electrodes as a function of the capacity of the lithium battery. The lithium compositions at both electrodes were lineally changed. They were consistent with the lithium content changes by electrochemical measurements. Therefore, these results of structure refinements indicate that 1) the automatic refinement verifications by Z-Rietveld work well and 2) the direct measurement of the lithium content is possible during battery operation. This information of quantitative lithium concentration analysis will provide basic battery reaction data to clarify the deterioration mechanism during cycling and under high-temperature operation and storage conditions.

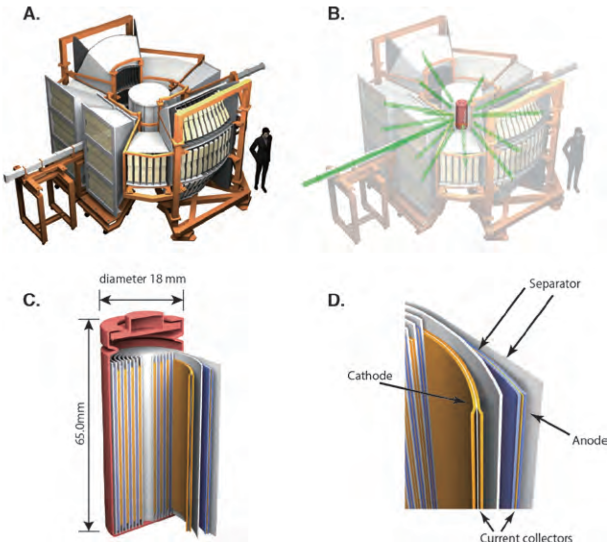

Figure 2. Illustration of the diffractometer, SPICA (A) and the schematic view of the *operando* experiments (B). Outline drawing of the cylindrical 18650-type commercial battery cell (C) and the inside of the cell.

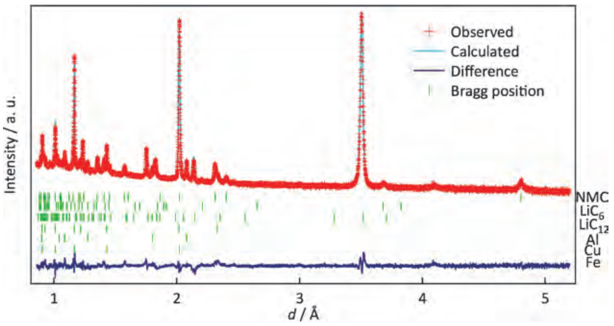

Figure 3. Rietveld-refined neutron diffraction pattern. Example of the Rietveld-refinement pattern after the automatic refinement process. Green dashes indicate the positions of Bragg reflections for the battery components.

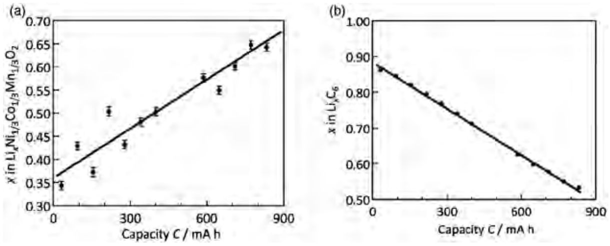

Figure 4. Lithium-composition changes for cathode (a) and anode (b) materials as a function of the capacity of the lithium cell.

Acknowledgement

This work was supported by the RISING project. The neutron scattering experiment was approved by the Neutron Scattering Program Advisory Committee of IMSS, KEK (Proposal No. 2009S10, 2014S10).

M. Yonemura[1,2], Y. Ishikawa[1], S. Torii[1], and T. Kamiyama[1,2]
[1]*Institute of Materials Structure Science, KEK;* [2]*Sokendai (The Graduate University for Advanced Studies)*

BL10: NOBORU

In FY 2015, most of the general use proposals at BL10 were postponed for the next year, because of the target incidents at MLF on April 30 and November 20, 2015.

This year, we performed the periodical measurements for neutron intensity, neutron spectra and pulse shape at BL10 with a proton beam power up to 0.5 MW. Fig. 1 shows the thermal and cold neutron reaction rates measured by the Au foil activation method by the same settings in April, 2015, October, 2015, and March, 2016, as a function of the proton beam power. The neutron reaction rate of the Au foil corresponds to the neutron intensity. An Au foil was located at 12.8 m from the moderator's surface. To derive the thermal and cold neutron intensity, irradiation with/without a 1 cm^2 Cd collimator was performed. We confirmed that the neutron intensity was almost proportional to the proton beam power up to 0.5 MW.

The pulse shapes of the cold neutrons, ca. $E_n <$ 10 meV, are very sensitive to the para-H_2 content of the moderator. A two-dimensionally aligned mica crystal has been used to measure the pulse shape of cold neutrons since 2008. This year, a standard powder sample, NIST SRM660 (La^{11}B$_6$), was also measured in the same experimental setting. The powder diffraction has an advantage when used for the reproducible measurement for the pulse shape of the thermal and cold neutrons. The powder sample contained in a cylindrical vanadium cell, 5 mm in diameter and 40 mm in height, was set on a sample position of NOBORU, 14.0 m from the decoupled moderator (DM). A zero-dimensional 1/2-inch ^{3}He counter was set at 1.0 m from the sample at $2\theta =$ 170°. In spite of a small solid angle of the single counter, an adequate counting statistics for the pulse shape estimation was obtained in a one-day measurement at 500 kW. The measured pulse shapes agreed well with the simulated ones, as shown in Fig. 2. The estimated full-width at half-maximum of the latest data, plotted as a filled triangle in Fig. 3, shows good agreement with the expected pulse width (= $\Delta t_{1/2}$(cal.)) as well as the previous pulse shape measurements. The result supports the 100% para-H_2 condition in the JSNS moderator, which is realized at beam power of at least 500 kW.

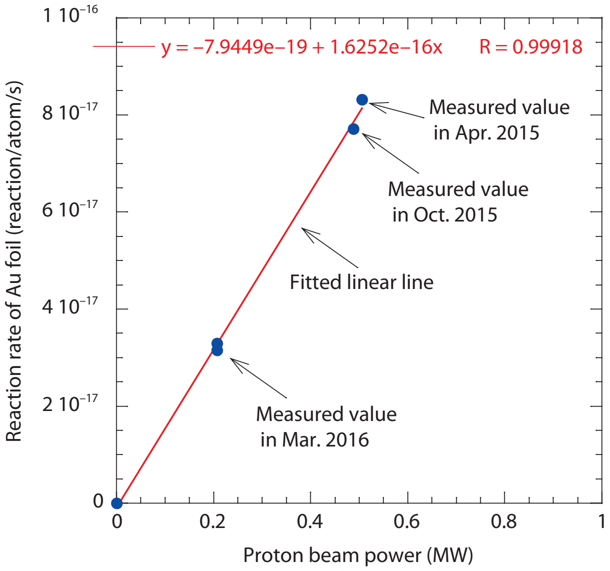

Figure 1. Measured neutron reaction rates of Au foil in April, 2015, October, 2015 and March, 2016.

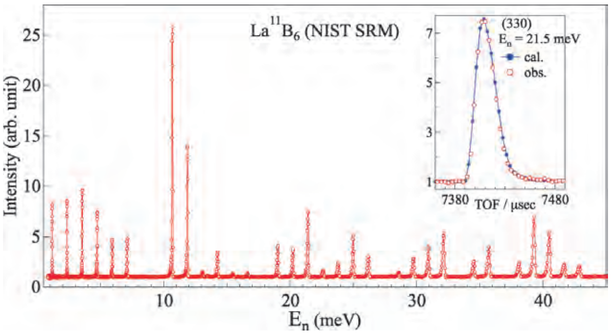

Figure 2. Powder diffraction pattern of La^{11}B$_6$ at 500 kW.

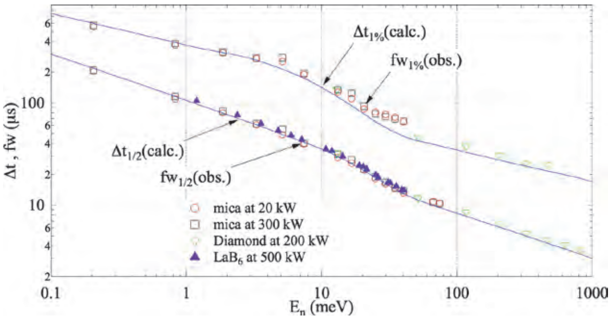

Figure 3. Pulse width at half and 1% maximum of the observed peaks and the calculated ones of DM of JSNS.

K. Oikawa and M. Harada
Neutron Science Section, Materials and Life Science Division, J-PARC center

Recent Developments in BL11 PLANET

1. Introduction

This year, we worked on the following developments:

(i) Reducing the background by shielding incident beam optics.

(ii) Increasing the scattering intensity by applying neutron transparent anvils for the experiments using the 6-axis press.

Here, we introduce the results of these developments.

2. Reducing the background by shielding incident beam optics

In the experiments using Paris-Edinburgh press, a focusing mirror is normally employed to increase the beam flux at the sample position, in which the focusing mirror, made of supermirrors with mirror index of m = 4 and length of 1.2 m, is placed in front of the sample. This mirror increases the neutron flux by a factor of about 2.3 for neutrons with wavelength of $\lambda = 1.5$ Å and larger. This mirror is effective in detecting weak sample peaks located at relatively large d-spacing, but that also increases the intensity of the background. Then, reduction of the background is urgently needed to maximize the benefit.

Analysis of the 2-dimentional pattern, taken by two detector banks, revealed that the background is generated by the incident mirror itself, as well as gaps between the mirror and other components installed at the upstream. To reduce the background, shielding of B_4C rubber with 5 mm thickness was attached on the surface of the tube holding the mirror (Fig. 1), and the gap of the optical devices was covered by cadmium plates with thickness of 0.5 mm.

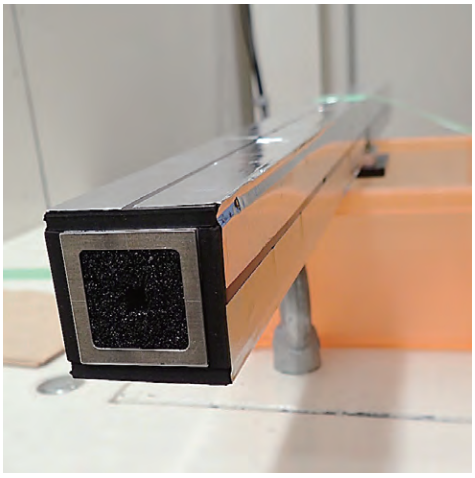

Figure 1. Tube holding the focusing mirror, on which the B_4C rubber is attached.

Figure 2 and 3 show the 2-dimensinal pattern and 1-dimensional pattern constructed from it, respectively. By adding the above-mentioned shielding, the parenthetic scattering in the 2-dimensional patterns was found to be successfully eliminated. Correspondingly, the background in the 1-dimensional pattern was significantly reduced. These findings suggest that the shielding has worked effectively.

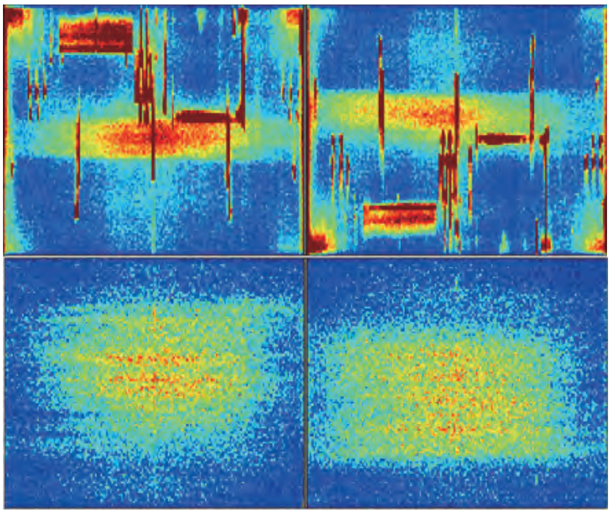

Figure 2. Comparison of the 2-dimenional patterns without (upper) and with (lower) shielding of B_4C rubber (left: North bank, right :South bank).

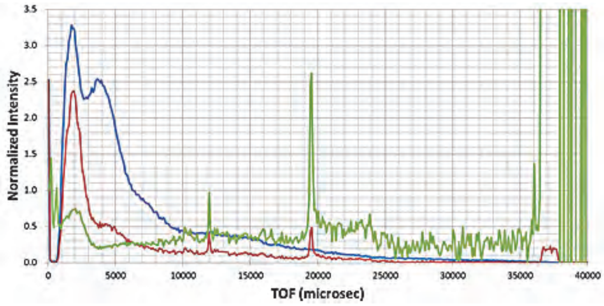

Figure 3. Comparison of the 1-dimenional patterns with (red) and without (blue) shielding of B_4C rubber. The ratio is also shown by a green line.

3. Increasing the scattering intensity with the use of neutron transparent anvils

In the data collection at high-pressure and high-temperature condition, a 6-axis press equipped with 6-6 compression system [1] is normally used. It uses anvils made of tungsten carbide (WC) with small neutron transparency. In that case, the incident beam is introduced into the sample through the gap between the anvils and the scattered neutrons are detected through other gaps (Fig. 4). Since the gap is drastically reduced at high pressures (typically to c.a. 0.8 mm at 7.5 GPa), the window for neutron detection is significantly limited and the scattering intensity from the sample is decreased correspondingly. To avoid such decrease, we faced the challenge to collect the neutrons through the anvils, not through the gap, by using the neutron transparent anvils.

As an anvil material, yttrium toughened zirconia (ZrO_2) (Tohoku ceramic, TCZ-ZM) was selected, based on ref. [2]. The photo of both kinds of anvils is shown in Fig. 5

In the on-beam test, anvils with shape identical to the original one (with height of the anvil 21 mm and size of the anvil top 10 mm) was used for ease of comparison. Fig. 6 compares the load dependence of intensity along the position-sensitive detector (PSD) between WC and ZrO_2 anvils. The scattering intensity taken with ZrO_2 was found to remain unchanged regardless of the applied load, while the one taken with WC anvils significantly decreased.

The pixel dependence indicates that the neutron eventually passes though the ZrO_2 anvils, since the distribution is widely spread and the width is not affected by the gap. Correspondingly, the Bragg peak of the sample (NaCl 220) didn't show significant decrease in its intensity (Fig. 7). Compared to the WC anvils, the integral intensity of the Bragg peak was found to increase by a factor of 1.5 at 1.3 GPa.

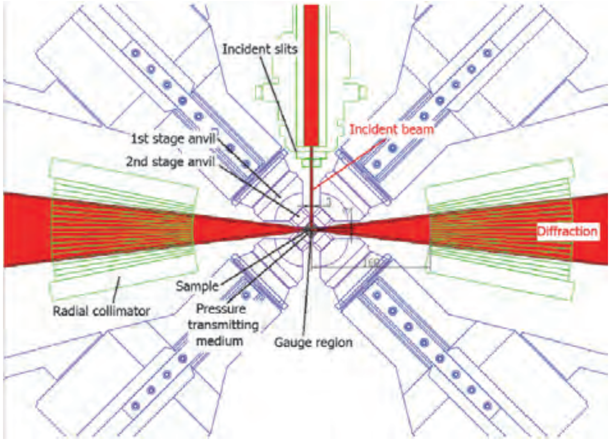

Figure 4. Diffraction geometry in the experiments using a 6-axis press. The figure is reprinted from Nucl. Instrum. Methods Phys. Res. A780, 55 (2015) with permission from Elsevier.

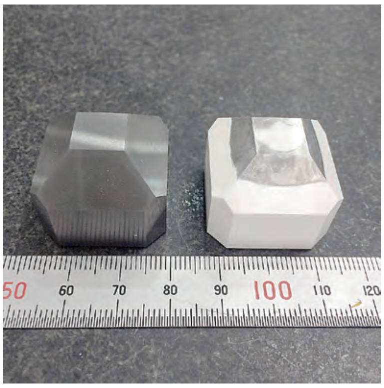

Figure 5. Comparison of the WC (left) and the ZrO_2 anvils (right). The top of the ZrO_2 is blackened after use since the pressure transmitting medium, made of aluminum sticks to the surface.

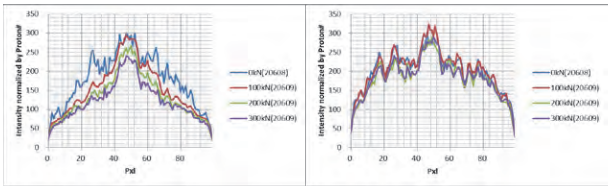

Figure 6. Comparison of the load dependence of intensity along the position-sensitive detector (PSD) between the WC (left) and the ZrO_2 anvils (right).

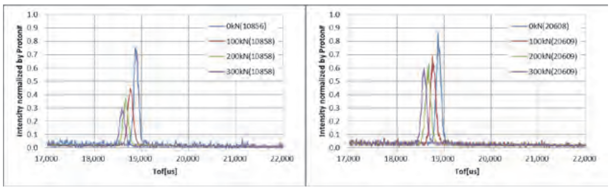

Figure 7. Comparison of the load dependence of intensity of NaCl220 peak between the WC (left) and the ZrO_2 anvils (right).

References

[1] N. Nishiyama *et al.*, High Press. Res., 28, 307 (2008).
[2] K. Komatsu *et al.*, High Press. Res., 34, 494 (2014).

T. Hattori[1], A. Sano-Furukawa[1], K. Funakoshi[2], J. Abe[2], and S. Machida[2]
[1]*Neutron Science Section, Materials and Life Science Division, J-PARC Center;* [2]*Neutron R&D Division CROSS-Tokai*

High Resolution Chopper Spectrometer at BL12

1. Introduction

The High Resolution Chopper Spectrometer (HRC) is being operated at BL12 to study the dynamics in condensed matters with high resolutions using relatively high energy neutrons. A research project using the HRC is being conducted to observe a wide range of correlated electron systems. In FY2014, we entered the 2nd phase of our project, where we will improve the performance of the HRC in the following points: (1) detector system at low angles for high-energy experiments, (2) Fermi choppers for higher resolution and lower background, (3) sample environments, (4) completing the installation of detectors at high angles, and (5) computational environment for easy operation of experiments.

2. Instrumentation in FY2015

The lowest temperature of 0.6 K was confirmed for the ^{3}He circulation type refrigerator. To achieve such low temperatures, a large number of radiation shieldings made of aluminum are mounted surrounding the sample. The scattering from the shieldings produces huge background noise. Fig. 1(a) shows ring-like scatterings from the shielding, which is comparable to or larger than the spots of the Bragg scattering from a single crystal sample. The ring-like scatterings were significantly reduced by operating the oscillating radial collimator (ORC), as shown in Fig. 1(b). Also, in the inelastic spectra, the huge phonons from the shieldings were greatly reduced by ORC (Fig. 1(c) and (d)). Thus, now this refrigerator can be used for inelastic neutron scattering experiments.

The control and analysis software programs, named YUI and HANA, respectively, developed individually for HRC, have been almost completed. In YUI, new tools, such as sample environment devices, were introduced and the automatic controls of devices in connection with the operation of DAQ were improved. In HANA, the following improvements were performed.

For the plot of $S(Q,\omega)$ for a single crystal sample, a striped pattern appeared along Q_a dependent on the step width of Q_b, as shown in Fig. 2(a). This was caused by the difference in the numbers of detectors contributed to each pixel. By applying to this plot the detector number normalization function, which was already applied to the plot for a powder sample, the striped pattern disappeared, as shown in Fig. 2(b). For the plot of $S(Q,\omega)$ for a powder sample, a jaggy pattern appeared when the step width of Q was smaller than the instrumental resolution. By applying to this plot the smoothing function for detector width, which was already applied to the plot for a single crystal sample, the jaggy pattern disappeared. Fig. 2(c) shows the intensity of the inhomogeneity caused by the inhomogeneous detector efficiency or the difference of the solid angles of detectors viewing the sample. This inhomogeneity disappeared by correcting the detector efficiency, as shown in Fig. 2(d). Also, the mask function was introduced to remove detector areas unwanted for the analysis.

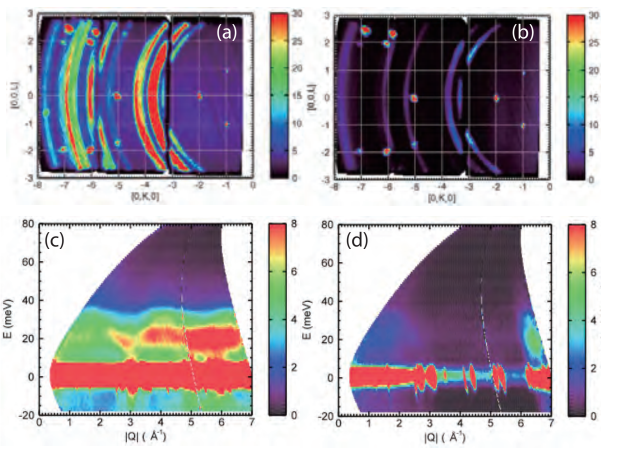

Figure 1. Effect of the oscillating radial collimaotor (ORC). Elastic scattering without ORC (a) and with ORC (b), inelastic scattering without ORC (c) and with ORC (d).

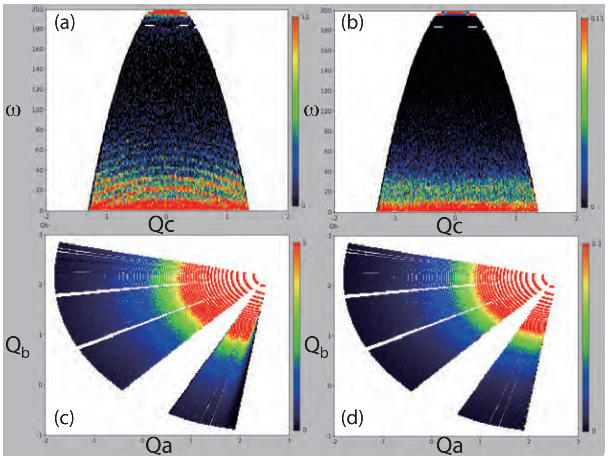

Figure 2. Improvement of HANA. $S(Q,\omega)$ plot for a single crystal sample without (a) and with (b) the detector number normalization function, without (c) and with (d) correcting the detector efficiency.

In the initial construction, we installed 128 pieces of 2.8 m detectors to cover scattering angles of ϕ = 3° − 42°. Later, more than 128 pieces could be purchased, which made it possible to cover ϕ = –31° − 62° in January, 2014. Some detectors in the later installation showed an inhomogeneous counting efficiency in the positional dependence. The maker discovered a defect in the detector structure of 88 detectors and re-manufactured all of them. We installed them again in January, 2015, however, the inhomogeneity was not improved. Engineers of the maker inspected and tuned them on HRC in September. Finally, they found that 6 pieces required repair, we installed living detectors to cover continuous ϕ. We checked the counting on beams in October. Although several detectors still showed inhomogeneity, which could be corrected in the analysis, we started experiments.

Below, we will describe other instrumentations. Following the success of the neutron Brillouin scattering (NBS) on HRC, new detectors for low angles and a vacuum flange to mount these detectors were approved. The detectors were mounted in pairs along the scattering beam to increase the counting rate. Some B_4C liners mounted on the inside surface of the vacuum scattering chamber blocked the scattering neutrons from the sample from reaching the detectors. Those liners were replaced by thinner ones to improve the neutron counts (but the problem could not be resolved completely). The vacuum system for the vacuum scattering chamber can be operated with a simple procedure on the control panel. Since there were some failures in controlling the cryopump, the original controller for the cryopump was removed and the cryopump was operated directly form the control panel. The regular maintenance for the cryopump was performed. The T0 chopper was designed for 4000 hours of running time at 100 Hz operation. The first machine was removed from the beam line in 2013, and the second machine is currently being operated. The maintenance, which consists of replacement of components damaged during the operation and the continuous running for realizing a smooth rotation of the mechanical bearings, was performed for the first time within a period of 4 months. This experience was very informative for planning the future maintenance. Electric noise, picked up with detector cables, produces a huge amount of unwanted event data. The detector cables were shielded to reduce the noise. We mounted the superconducting magnet and confirmed the maximum magnetic field of 10 T on HRC. After several experiments in February, 2015, a leak occurred between the liquid helium vessel and its vacuum surrounding, and repairs were started.

3. Scientific Results

On HRC, high resolution experiments in conventional energy momentum space and neutron Brillouin scattering experiments can be performed, and of the opportunities in sub-eV neutron spectroscopy are also explored. We obtained good results, which have been described in this report. One of the remarkable results was a study of spin waves in a metallic ferromagnet $SrRuO_3$ [1], which was obtained by the success of NBS on HRC. We found that the spin wave gap nonmonotonously depends on the temperature and can be described as a function of the anomalous Hall conductivity. In $SrRuO_3$, a band crossing due to spin orbit interaction produces the Berry phase and acts as a magnetic monopole in the momentum space. This is the origin of the anomalous Hall effect in $SrRuO_3$. Our experiment showed for the first time that monopoles in the momentum space could be detected by inelastic neutron scattering, in other words, the Berry phase is observable in inelastic neutron scattering. The details of these findings are described in a separate report.

Reference

[1] S. Itoh *et al.*, Nat. Commun. 7, 11788 (2016).

S. Itoh[1,2], T. Yokoo[1,2], T. Masuda[3], H. Yoshizawa[3], M. Soda[3], Y. Ikeda[3*], S. Ibuka[1,2], M. Yoshida[3], T. Hawai[1,2], T. Asami[3], R. Sugiura[3], D. Kawana[3], Y. Kawamura[3], T. Shinozaki[3], Y. Ihata[4]

[1]*Institute of Materials Structure Science, KEK;* [2]*Neutron Science Section, J-PARC Center;* [3]*The Institute for Solid State Physics, The University of Tokyo;* [4]*Technology Development Section, J-PARC Center*

**Present address: Tohoku University*

BL14 AMATERAS

1. Introduction

FY2015 was the seventh year of operation of AMATERAS, a cold-neutron disk-chopper spectrometer. We continued the user program, which was temporarily interrupted due to problems at the neutron target. We also contributed to international collaborations (experiments in the framework of the Korea-Japan collaboration program in neutron science and participation in the 7th AONSA Neutron School). In this fiscal year, we encountered mechanical problems of the equipment of AMATERAS, one of which was serious. The good news was that we had a new technical out-sourcing staff, Mr. Daisuke Wakai who succeeded the former staff Ms. Kaori Kamoshida.

2. User program, international activities & out-comes

In FY2015, the user program at MLF was seriously interrupted due to problems at the neutron target. In the 2015A period, we scheduled 12 general proposals (three of them were carried-over subjects from 2014B), four project research proposals (one of them was a carried-over subject from 2014B) and two elementary strategy initiative proposals (one of them was a carried-over subject from 2014B). We completed nine subjects and partially did five subjects. The remaining subjects will be carried out in FY2016.

AMATERAS joined the 7th AONSA Neutron School/ the 3rd MLF School held in December. Two students participated and studied quasi-elastic neutron scattering (QENS) experiment and data analysis for ionic liquid. They learned how to prepare a liquid sample with proper quantity and thickness in a double cylindrical container and set it to a cryostat (Fig. 1). Since there was no neutron beam, they analyzed QENS data previously measured by the instrument group. From a curve fitting with a jump diffusion model, they reduced the diffusion constant at several temperatures and the activation energy of the diffusion mode. We hope that the neutron experiment will become one of the tools to be used in their future research activities.

In this fiscal year, AMATERAS had a guest from the Korea Atomic Energy Research Institute (KAERI), Dr. Ji-Yong So, in the framework of the Korea-Japan collaboration program in neutron science. He is the person in charge of a cold-neutron disk-chopper spectrometer, DC-TOF at HANARO at KAERI and stayed at MLF for two months to learn the actual operation of instruments and the user-program at AMATERAS. He also carried out measurements on quasielastic scattering from block copolymers and inelastic scattering of phonons in steels to compare the performance between AMATERAS and DC-TOF.

Figure 1. (Top) Two students of the 7th AONSA Neutron School/the 3rd MLF School and staff members of AMATERAS. From the left, Mr. D. Wakai (J-PARC), Dr. B. Li (J-PARC), Dr. T. Kikuchi (J-PARC), Dr. A. B. Khan (Jamia Millia Islamia Univ.), Prof. X. Li (Univ. Tokyo), Dr. Y. Kawakita (J-PARC). (Bottom) Students instructed on sample mounting by Dr. Kawakita.

On November 12, 2015, Sumitomo Rubber Co., Ltd., issued a press release titled "ADVANCED 4D NANO DESIGN — New technology of developing rubbers for high-performance tires in combination with SPring-8•J-PARC•KEI," [1], part of that investigation was done on AMATERAS. Seven scientific papers (reviewed) on the results from AMATERAS were published in 2015. Also, two academic dissertations were completed in March, 2016, partially using results from AMATERAS.

3. Instrumental activities

We have updated each component of AMATERAS in FY2015, as follows. Firstly, the guide mirrors at the final

Figure 2. Replacement of supermirror of the final section of AMATERAS beam-transport.

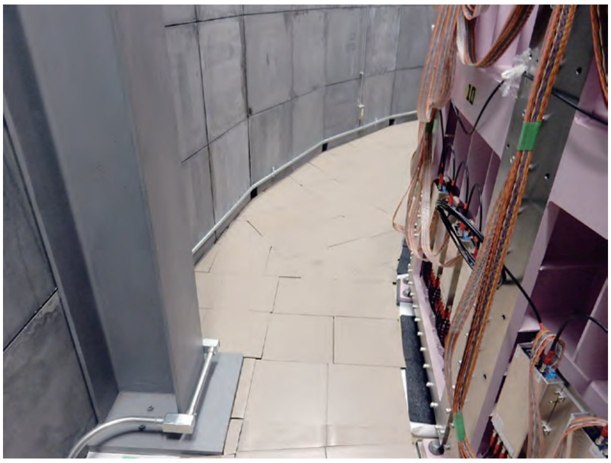

Figure 3. The floor is covered with tiles of B_4C (1 cm thickness). The upper surface of tiles are covered with flooring material.

section were replaced to new ones with higher *m*-values (Fig. 2). Their alignment was investigated after the replacement, and it was found that the displacement of each mirror was settled within 1 mm compared to the results in 2013. Secondly, we added utilities, such as electric distribution board, cooling water and helium recovery lines, to increase the capacity for operation of various sample environment accessories for users' experiments. Thirdly, we made efforts to reduce the background by placing B_4C tiles on the floor under the vacuum scattering chamber (Fig. 3). The tiles absorb neutrons, some of which come from the floor, resulting in reduction of the time-independent background. This background was eventually reduced by ~12% in the whole area covered by PSD's, especially by ~25% at the lower area. We should also note that we just launched refurbishment of the vane between the detector banks in the vacuum chamber. Because the vacuum chamber is pressed vertically when it is evacuated, the vane is slightly bent, which causes useless pixels in the data. A newly designed and attempted method was to keep pulling the vane vertically, even when the chamber was evacuated. Since this refurbishment was quite effective, we will continue it in FY2016. Moreover, we also made other minor updates, such as installation of IROHA2, which is a common software framework for the instrument control in MLF, and a control system for the radial collimator.

In FY2015, which is the seventh year since the operation of AMATERAS has been started, some problems, related to aging, are becoming obvious at several components. Anomalous vibration was found at a high-speed disk-chopper, so we decided to restrict temporarily its operation at the maximum speed. In a high-voltage power supply, unconventional fluctuation of the voltage was detected when ramping up the voltage. Furthermore, one of the compressors operating the cryopump system also broke, though two others are still working. We are planning to fix all of them the next fiscal year.

Reference

[1] see http://j-parc.jp/ja/topics/2015/Press151112.html (in Japanese).

K. Nakajima, S. Ohira-Kawamura, Y. Kawakita, and T. Kikuchi
Neutron Science Section, Materials and Life Science Division, J-PARC center

Upgrading TAIKAN

1. Introduction

The small and wide angle neutron scattering instrument TAIKAN (BL15) has been developed and upgraded to analyze microstructures or hierarchical structures of substances in various scientific fields precisely and efficiently with a 1MW spallation neutron source in J-PARC [1]. In FY2015, it was upgraded further to perform measurement in a horizontal magnetic field and low-*q* measurement.

2. Upgrading for measurement in a horizontal magnetic field

A cryogen free split-pair superconducting magnet (horizontal field magnet) with wide aperture angle of 90° was developed for wide angle neutron scattering measurement of magnetic and superconducting materials (Fig. 1). The magnet has been used to apply magnetic field up to 4 Tesla to a sample and cool the sample down to 1.6 K from RT.

3. Upgrading for low-*q* measurement

A focusing-geometry SANS method has been adopted for the measurement in a q range of 0.0005 – 0.005 A^{-1}. For the method, an ultra-small-angle detector is used. Figure 2 shows the scattering profile of mesoporous silica measured by TAIKAN with the new scintillation detector with an active size of 127 mm in diameter and spatial resolution of about 0.5 mm. The profile shows that q_{min} can be extended down to 0.0008 A^{-1} with the detector.

4. Future prospect

The focusing-geometry SANS system of TAIKAN is completed in combination with magnetic beam focusing devices: a quadrupole magnet, two sextupole magnets, and three radio-frequency gradient spin flippers. After the completion of the combination, q_{min} will be extended down to 0.0005 A^{-1}, the targeted value of TAIKAN.

Figure 1. A 4 Tesla split-pair superconducting magnet.

Reference

[1] S. Takata, J. Suzuki, T. Shinohara, T. Oku, T. Tominaga, K. Ohishi, H. Iwase, T. Nakatani, Y. Inamura, T. Ito, K. Suzuya, K. Aizawa, M. Arai, T. Otomo and M. Sugiyama, JPS Conf. Proc. 8, 036020 (2015).

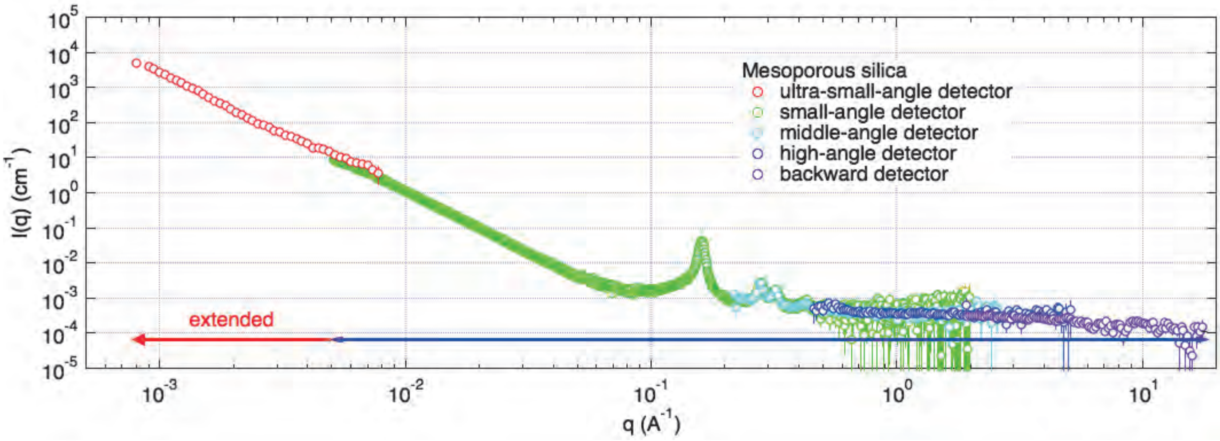

Figure 2. Scattering profile of mesoporous silica measured by TAIKAN, to which a new ultra-small-angle detector was installed.

J. Suzuki[1], S. Takata[2], K. Ohishi[1], H. Iwase[1], T. Morikawa[1], Y. Kawamura[1], and M. Sahara[1]

[1]*R&D Division, CROSS-Tokai;* [2]*Neutron Science Section, Materials and Life Science Division, J-PARC Center*

Sample changers for High-Throughput Measurement at the SOFIA Reflectometer

1. Introduction

Neutron reflectometry (NR) is very useful for investigations of structures of surfaces and buried interfaces composed of soft materials. SOFIA is a horizontal-type neutron reflectometer constructed at Beamline 16 (BL16) of the Materials and Life Science Experimental Facility (MLF) of the Japan Proton Accelerator Research Complex (J-PARC) [1, 2]. Due to the high-flux beam of the J-PARC, the exposure time for one measurement is drastically shortened in compared to those at the JRR-3 research reactor and the KENS spallation source. Table 1 shows the list of typical samples, sample size (and beam size), accessible *Q* range, and exposure time for full *Q*-range measurement at the SOFIA reflectometer with the proton power of 500 kW. Even though the beam power is still half of the planned value, 1 MW, the required time is over 10 times less than the time required at the JRR-3 and KENS. On the other hand, time loss caused by changing samples, and/or temperature becomes more prominent with the decrease of the time required for counting neutrons. This means that a sample changer is a key factor for high throughput measurements in order to take a full advantage of the high flux beam.

2. Sample changer for ambient temperature

So far, the SOFIA has been equipped with a sample stage with a motor for horizontal movement, which enables us to change samples remotely. Here, the number of samples to be measured at a time is limited by the motion range of the stage. As the range is 300 mm, seven samples can be measured at a time for 2-inch (50.8-mm) substrates in diameter. This means that the total time for the measurement is expected to be less than 4 hours, if the substrates are coated with deuterated polymers. The time for the measurement is too quick for an overnight run. Hence, a modification on the sample stage was made to increase the number of samples for one measurement run.

Figure 1 shows a photograph of samples mounted on the new sample stage. As the motion range in horizontal direction is limited due to the interference with the surrounding components, a vertical translation stage with a long-motion range, 110 mm, was introduced. This enables us to add stages above the samples and mount more samples on the additional stages. If the thickness of the stage is 10 mm and the gaps between the stages are 20 mm, four stages can be used at a maximum, that is, fourfold samples can be measured at one experiment run.

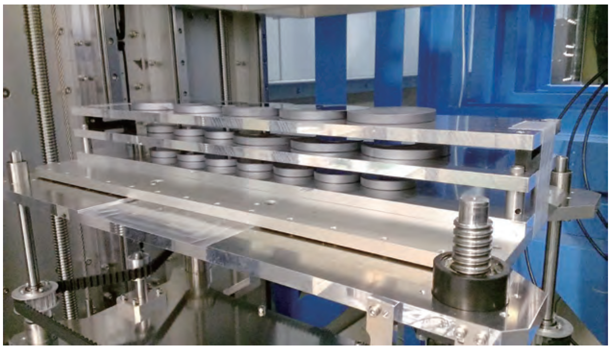

Figure 1. Photograph of samples mounted on the new sample stage.

Table 1. List of typical samples, sample size (and beam size), accessible *Q* range, and exposure time required for full *Q* range measurement at the SOFIA reflectometer with proton power of 500 kW.

Sample interface	Sample size (Beam size)	Q range	Exposure time
air/Si	50.8 mmØ (30×40 mm^2)	< 2 nm^{-1}	3/4 hour
air/protonated polymer/Si	50.8 mmØ (30×40 mm^2)	< 2 nm^{-1}	1 hour
air/deuterated polymer/Si	50.8 mmØ (30×40 mm^2)	< 4 nm^{-1}	1/2 hour
air/D_2O	25 mL (40×40 mm^2)	< 2 nm^{-1}	1/4 hour
air/no reflection water	25 mL (40×40 mm^2)	< 1 nm^{-1}	3 hours
Si/D_2O	76.2 mmØ (30×50 mm^2)	< 2 nm^{-1}	1 hour
Si/protonated polymer/D_2O	76.2 mmØ (30×50 mm^2)	< 2 nm^{-1}	1 hour
Si/deuterated polymer/H_2O	76.2 mmØ (30×50 mm^2)	< 2 nm^{-1}	1 hour

In addition, an auto sample adjustment routine was implemented in the measurement program of the SOFIA. This routine adjusts precisely the position and incident angle of the sample surface to the neutrons, which is required before a neutron reflectivity measurement. It frees us from the necessity to adjust samples and can extend further the total measurement time for one experiment run by performing the auto adjustment before the reflectivity measurement.

3. Temperature controlled stages

To control efficiently sample's temperature, two sample stages were newly developed: one is for high temperature (from room temperature to 250°C) and the other is for low temperature (from 0°C to 100°C). The high-temperature stage consists of two evacuable chambers and a silicon block with a rubber heater is installed in each chamber (Fig. 2). The size of the silicon block is 153 mm in the direction of the horizontal translation, on which three 2-inch substrates can be mounted. The purpose of this stage is to keep the two silicon blocks thermally isolated, so that the temperature can be controlled independently. This means that we can change the temperature of a silicon block during a measurement for a sample on the other block, which avoids the time loss when the temperature changes. Similarly, the low temperature stage consists of two cupper blocks with peltier elements in a chamber with a water circulation path (Fig. 3). The temperature of the two blocks can be controlled independently, and dry gas flow can be introduced in the chamber to avoid the condensation of water vapor on the sample. The size of the cupper block is 192 mm in the direction of the horizontal translation, on which three 2-inch substrates can be mounted.

The temperature of the stages can be controlled by the measurement program of the SOFIA. By repeating the measurement and temperature control alternately, a sequence of temperature variation experiments can be performed without the time loss when the temperature changes automatically.

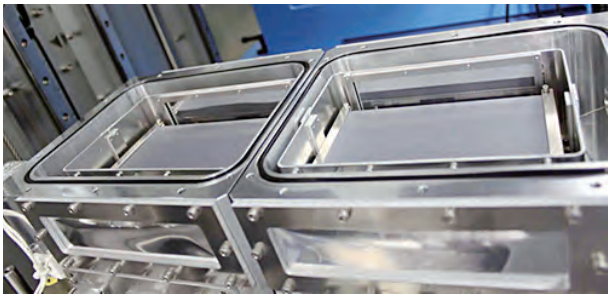

Figure 2. Photograph of the temperature-controlled stage for high temperature.

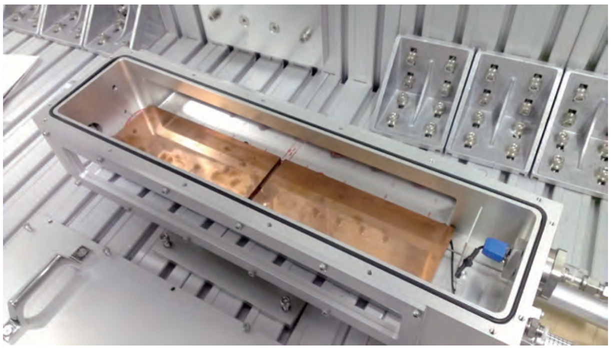

Figure 3. Photograph of the temperature-controlled stage for low temperature.

4. Conclusion

For high throughput measurements, the vertical translation stage and temperature stages were developed. The former resulted in an increase in the number of samples and total measurement time for one measurement run in combination with the software of the SOFIA. The latter can complete the sequence of the temperature variation experiments also in combination with the software. We should note that the extension of one measurement run can make time for sample preparation, data reduction, and/or taking a rest. We believe the development here makes the experiment at the SOFIA more efficient and productive.

References

[1] N. L. Yamada *et al.*, *Euro. Phys. J. Plus*, **44** (2011) 9424.
[2] K. Mitamura *et al.*, *Polymer J.*, **45** (2013) 100.

N. L. Yamada[1, 2]
[1]*Neutron Science Section, Materials and Life Science Division, J-PARC center;* [2]*Institute of Materials Structure Science, KEK*

BL17: Polarized Neutron Reflectometer SHARAKU using 2-D MWPC with Indivisual Readout System

1. Introduction

Polarized neutron reflectometry is one of the powerful methods to investigate various phenomena on the surfaces and interfaces of a variety of films with layered structures, such as magnetic multilayers, polymer films, and biological membranes. The polarized neutron reflectometer SHARAKU [1], named after the famous Japanese ukiyo-e artist, was constructed at BL17 of MLF in J-PARC and we have continued to utilize it in the user program in 2015 [2-5]. SHARAKU has suitable options for the measurement of specular reflectivity, off-specular reflectivity, grazing incidence diffraction (GID), and grazing incidence small-angle neutron scattering (GISANS). In order to enable these measurements, the instrument is equipped with a zero-dimensional (0-d) He-3 detector and a two-dimensional (2-d) position-sensitive neutron detection system [6]; it consists of a multi-wire proportional chamber (MWPC) with helium-3 gas and its own data reduction software. In this report, we describe the specifications of the two-dimensional MWPC system at BL17 and its applications to neutron specular and off-specular reflection measurements.

2. Demonstration of the MWPC system

Figure 1 shows a view of the SHARAKU reflectometer with the 0-d detector and Fig. 2 shows a setup of the 2-d MWPC installed at a distance of 2500 mm from the sample position (L1 + L2 = 18 m). The MWPC [2] has a neutron sensitive area of 128 × 128 mm^2. It consists of a 256-channel detector element (x: 128 lines, y: 128 lines), each wire's signal is read out by amplifier-shaper-discriminator (ASD) individually to meet the demands for fast counting response and high spatial resolution for measurements at intense pulsed neutron sources. The full width at half maximum (FWHM) of the spatial error is 1.8 mm.

Figure 3 shows a neutron transmission image of B$_4$C slits located between the vacuum chamber and MWPC. The inset intensity profiles, which are integrated along the X or Y axis, are nearly flat and the neutron distribution data is used to produce uniformity correction data.

Figure 4 shows the reflectivity profiles of a Nickel thin film with a thickness of 200 nm, coated on a silicon substrate measured by using the 0-d counter and MWPC. By using both detectors, we could obtain equal specular reflectivities down to 10^{-5}. In this measurement mode, the 2-d MWPC works similar to the 0-d detector, and the detected counts are integrated over the specular reflection area.

As shown in Fig. 5, a non-polarized intensity map of off-specular reflection has been measured for a Ni/Ti multilayer with d = 10 nm and 20 bilayers at beam power of 300 kW. In this measurement, we focused on the small q-region between $0.1 < q_z < 0.8$ nm^{-1} and $0.001 < q_x < 0.01$ nm^{-1}, and the direct beam and specular beam were protected by using B$_4$C slits to decrease the neutron background. In order to get credible results, we measured the reflections in the same q-region by using thr 0-d detector and obtained almost equal off-specular reflection profiles.

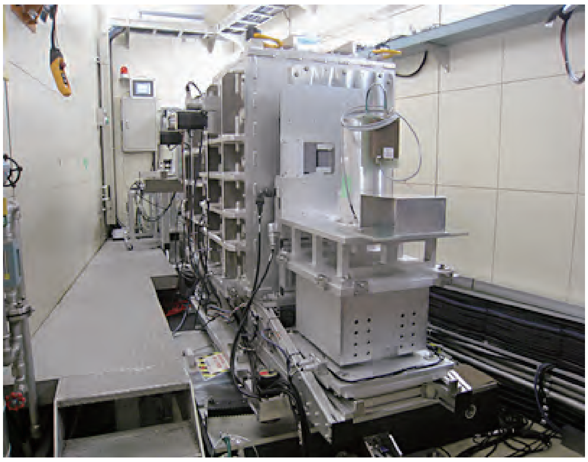

Figure 1. SHARAKU with 0-d detector.

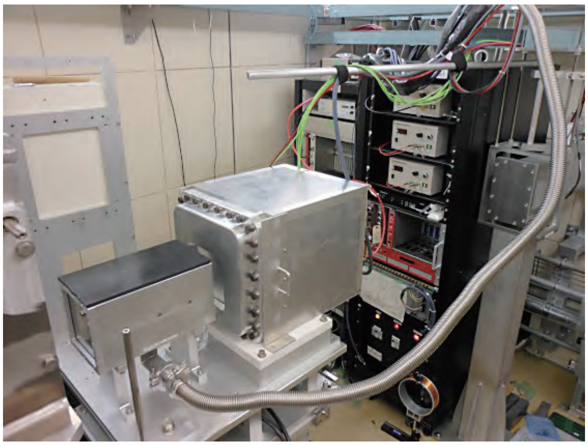

Figure 2. MWPC setup.

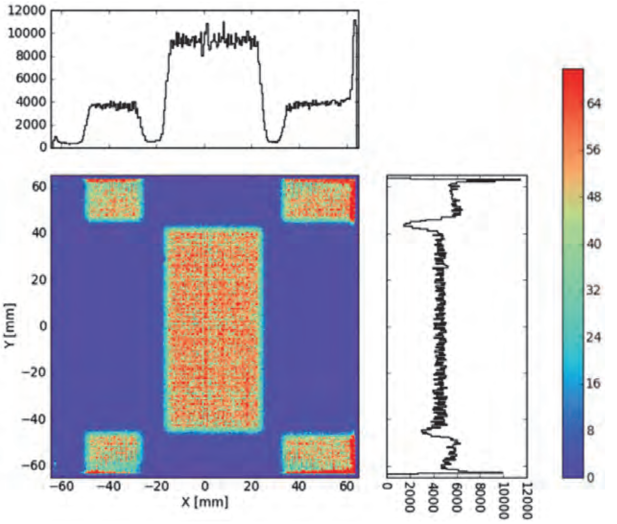

Figure 3. A neutron transmission image of B_4C slits (S9) detected by the 2-D MWPC with a neutron sensitive area of 128 × 128 mm^2.

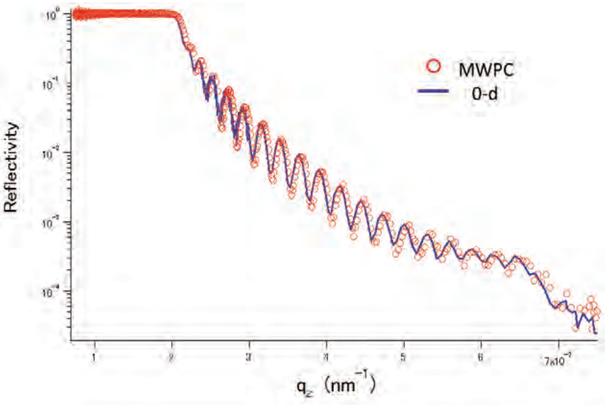

Figure 4. Neutron reflectivity profiles of Nickel thin film with a thickness of 200 nm detected by the 0-d detector and MWPC.

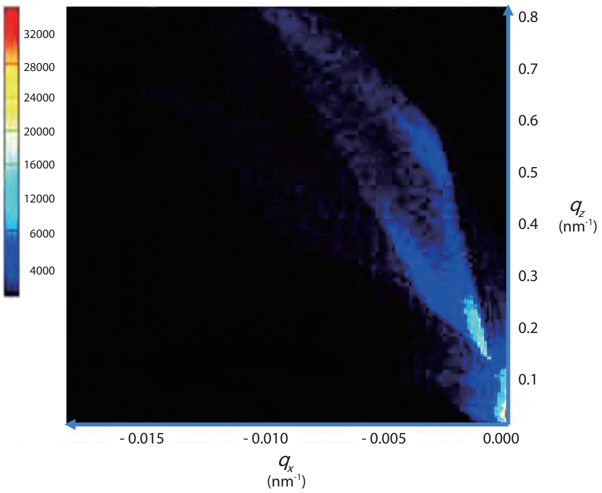

Figure 5. Off-specular intensity map from Ni/Ti multilayer with d = 10 nm and 20 bilayers.

3. Conclusions

In order to enable surface scattering measurements on off-specular reflectivity, grazing incidence diffraction (GID), and grazing incidence small-angle neutron scattering (GISANS), the 2-d MWPC with individual read out system has been installed and a commissioning test has been conducted. The function of the 0-d detector measurement worked well, and weak diffuse scattering has been observed in the low q-region.

References

[1] M. Takeda *et al.*, Chinese J. Phys. **50** (2012).
[2] K. Amemiya *et al.*, JPS Conference Proceedings 8 34004 (2015).
[3] T. Ueno *et al.*, JPS Conference Proceedings 8 034008 (2015).
[4] Y Sakaguchi *et al.*, Journal of Physics; Conference Series 619 012046 (2015).
[5] K. Akutsu *et al.*, Proceedings of the 12th Annual Meeting of Particle Accelerator Society of Japan 72-76 (2015).
[6] K. Toh *et al.,* J. of Instrumentation, Vol.9 (2014).

K. Soyama[1], D. Yamazaki[2], N. Miyata[3], K. Akutsu[3], S Kasai[3], T. Hanashima[3], J. Suzuki[3], and M. Kubota[4]
[1]*Materials and Life Science Division, J-PARC Center;* [2]*Neutron Instrumentation Section, Materials and Life Science Division, J-PARC Center;* [3]*Neutron R&D Division, CROSS-Tokai;* [4]*Materials and Life Science Division, Quantum Beam Science Directorate, JAEA*

SENJU 2015

1. Introduction

SENJU is a TOF single-crystal neutron diffractometer designed for precise crystal and magnetic structure analyses under multiple extreme environments, such as low-temperature, high-pressure and high-magnetic field, and also designed for taking diffraction intensities of small single crystals with less than 1.0 mm^3 down to 0.1 mm^3 in volume [1]. Just after the launch of SENJU in 2012, continuous commissioning and upgrading have been carried out.

In 2015, we developed an anvil-type high pressure cell and performed the first measurement of magnetic reflection under high pressure at SENJU. We also upgraded the software for device control, IROHA, and for data processing, STARGazer for SENJU.

2. Observation of magnetic reflections under high-pressure

Measurement of the magnetic neutron reflections under high pressure condition is a powerful experimental tool to understand the relationship between magnetic property and structural change by pressure at atomic level. Thus, we have developed high pressure sample cells for SENJU. In the previous report [2], we showed a piston-cylinder type high pressure cell. In FY2015, we developed another type of high pressure cell, self-clamped opposed type hybrid anvil (HA) cell [3], for SENJU (Fig. 1). The HA cell consists of a pair of tungsten carbide and single crystal sapphire anvils; it can reach higher pressure than a piston-cylinder cell. By using this HA cell, we carried out the magnetic reflection measurement under high pressure. A CeSb single crystal (0.9 × 0.9 × 0.33 mm^3) was set in the HA cell and pressurized up to 2 GPa. The cell was cooled down to 2.7 K by using a closed-cycle refrigerator. The pressure was determined by the ruby fluorescence method. As shown in Fig. 2, we successfully observed distinct pressure induced magnetic reflections from the type-IA anti-ferromagnetic phase of CeSb. This was the first example of observation of magnetic reflection under high pressure and low temperature in SENJU.

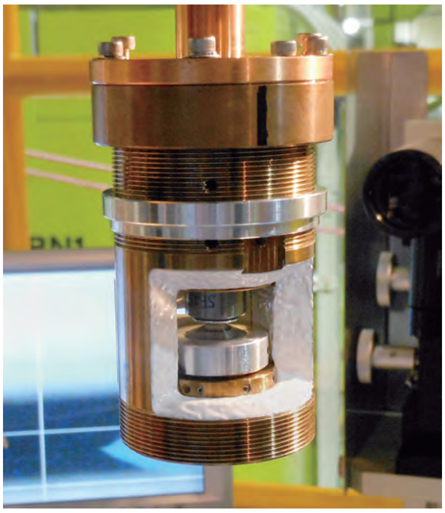

Figure 1. Photograph of the HA cell.

3. Upgrading of the device control software: from IROHA to IROHA2

IROHA is MLF standard software to control detectors, sample environment devices and neutron optical devices. Recently, IROHA was upgraded to a new version with browser-based user interface, IROHA2 [4]. In FY2015, we started to use IROHA2 instead of IROHA as device control software of SENJU. IROHA2 made easier the remote monitoring of the measurement status of SENJU, e.g. from J-PARC Research Building or IQBRC Building. New device control middleware for T_0 and disc choppers designed for IROHA2 was also installed. Consequently, the choppers of SENJU were placed under the control of the SENJU control cabin and automatic shifting from the 1st frame to the 2nd frame became possible. The commissioning of IROHA2 continued during the summer shutdown period and we began to use it from November, 2015.

4. Upgrading of the data processing software: STARGazer for SENJU

Software for data processing, i.e., making a reflection (HKLF) file from raw data, and data visualization is one of the essential components of a single-crystal diffractometer. For SENJU, a program called "STARGazer for SENJU" is used for data processing and visualization.

In FY2015, an update of STARGazer for SENJU was introduced, with the following developments:

1. Automatic exclusion of powder rings in the peak search process.
2. Automatic intensity integration of satellite reflections in the peak-integration process.

The first one was developed to improve the reliability of the peak search process. The diffraction images measured by SENJU usually contain the powder pattern of aluminum that comes from the ra-diation shields of a cryostat and/or sample mounting pin. When the sample

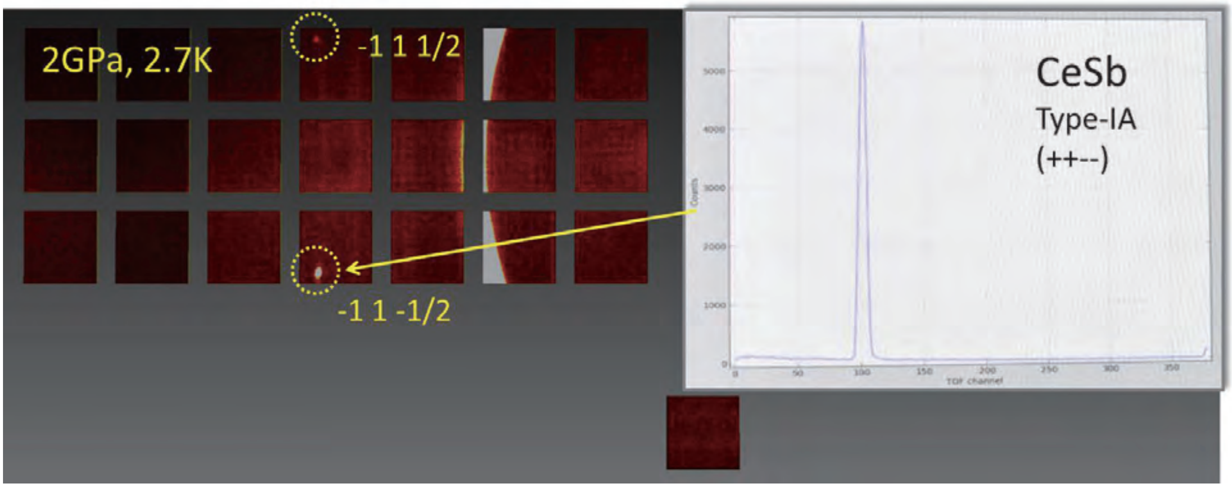

Figure 2. Pressure-induced magnetic reflections from a CeSb crystal at 2 GPa and 2.7 K observed by SENJU (2nd frame).

size is small and the intensities of the Bragg reflections are weak, the powder pattern seriously decreases the reliability of the peak search process and makes the UB-matrix determination difficult. The new function automatically estimates the peak widths of both the X and Y directions and removes the peaks when the width of the Y direction is much broader than that of the X direction.

The second one was developed to process satellite reflections, which have non-integral indexes effectively caused by modulated structures. In the function, users can input indexes of more than one modulation vector in the peak integration process. The function then calculates and outputs the integrated intensities of the corresponding satellite reflections, not only the first-order reflections but also the high-order ones. This new function should help to determine intricately modulated structures or slight change of magnetic structure by phase transition more accurately.

References

[1] T. Ohhara *et al.*, J. Appl. Cryst., 49 120 (2016).
[2] T. Ohhara *et al.*, MLF Annual Report 2013, 106 (2013).
[3] T. Osakabe *et al.*, J. Phys. Soc. Jpn. 79, 034711 (2010).
[4] T. Nakatani, Y. Inamura and K. Moriyama, Proc. 7th MLF Symposium (2016).

T. Ohhara[1], R. Kiyanagi[1], A. Nakao[2], T. Hanashima[2], K. Munakata[2], T. Moyoshi[2], and T. Kuroda[2]
[1]*Neutron Science Sectioin, Materials and Life Science Division, J-PARC center;* [2]*Neutron Science and Technology Center, CROSS-Tokai*

Engineering Sciences in TAKUMI

1. Introduction

TAKUMI is a neutron diffractometer (ND) for various studies in materials engineering. TAKUMI functioned almost flawlessly during JFY2015, but unfortunately many experiments had to be stopped or not conducted at all, due to the unexpected stoppage of the beam operation caused by a problem with the neutron source. Some enhancements, related to new devices and methodology, have been performed using the limited beam time. The details are as follows.

2. Enhancements during JFY2015

2.1 Supplementation of the 90° scattering detector bank

TAKUMI has a pair of 90° scattering detector banks, and each of them was designed with an angular area of ±15° horizontally and ±20° vertically [1]. Seven modules of scintillator detectors of ENGIN-X type with 360 horizontal-channels were designed to be added to each bank. However, only five modules were installed in each bank during the construction due to the limited budget. Two modules were purchased and installed within two years since JFY2014, and the current appearance of TAKUMI is shown in Fig. 1. The commissioning of the detectors is under progress and will continue in JFY2016.

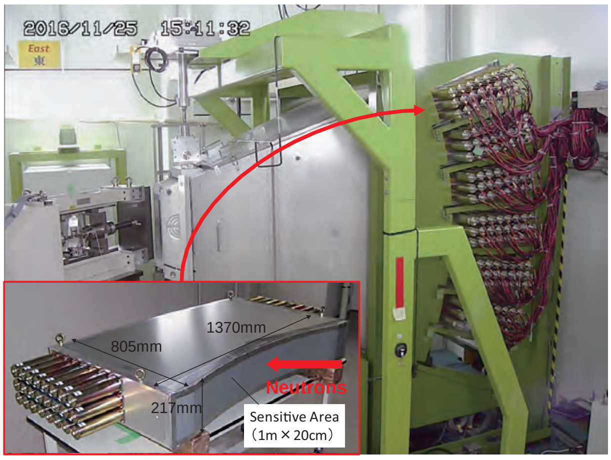

Figure 1. The current appearance of TAKUMI with 6 modules of scintillator detectors in each bank.

2.2 Thermec-mastor installation & commissioning

A new sample environmental device for simulating thermo-mechanical processes of materials (thermec-mastor) has been installed in a collaboration between a research group in Kyoto University and TAKUMI, within a scheme of Elements Strategy Initiative for Structural Materials supported by the Ministry of Education, Culture, Sports, Science and Technology, Japan. This new device is designed to heat the specimens by induction heating and cool them by gas injection. The highest rates for heating and cooling are about 30°C s^{-1}. It can also apply compressive deformation with the highest rate of 100 mm s^{-1}. The first neutron diffraction data on steels was conducted at the 300 kW accelerator operation. Diffraction patterns extracted with the interval time of about 1 s could be used to determine the occurrence of phase transformation during thermo-mechanical processes [2]. The accelerator operation will be 1 MW in near future, so that shorter time resolution would be achievable. Hence, the in-situ neutron diffraction experiment using this new device is believed to simulate current industrial steel processing (thermo-mechanically controlled processing). An example of the experiment is shown in Fig. 2.

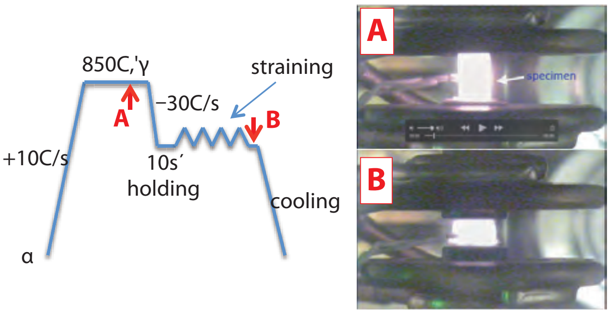

Figure 2. An example of a thermo-mechanical program and appearances of the specimen during the process.

2.3 Profile analysis

The information of elastic strain (lattice strain), dislocation density, dislocation character and crystalline size is very important to understand the relation between microstructures and mechanical properties, however, the dislocation and crystallite size information did not receive enough attention because of the ND limitations and the difficulties in the analysis. TAKUMI adopted an advanced analysis method, the convolutional multiple whole profile (CMWP) fitting [3] that made it possible to perform profile analyses to extract dislocation and crystallite size information from its diffraction patterns. From a demonstration of tensile deformation of martensite steel, the dislocation densities were interestingly kept almost unchanged, though the tensile stress increased with increasing the plastic strain, while significant increase of the correlation between the dislocations was observed [4]. An example of CMWP fitted diffraction pattern of martensite steel is shown in Fig. 3.

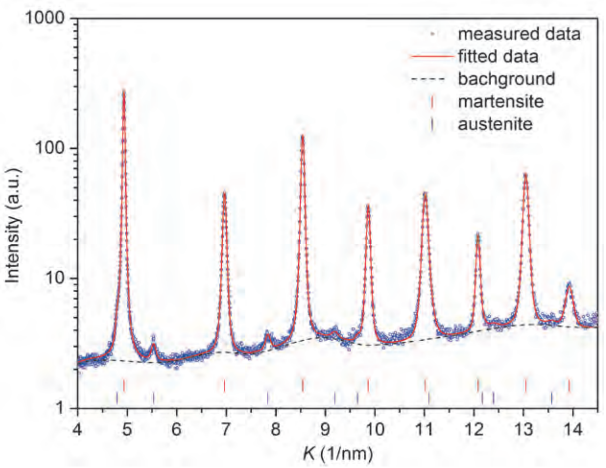

Figure 3. An example of CMWP fitted diffraction pattern of martensite steel.

2.4 *Stroboscopic measurement*

In-situ measurements during cyclic tests or operations like high frequency fatigue, cyclic electric field of piezo sensor, etc. need sub-second acquisition time. However, the short collecting time for a specific condition within a cycle provides data with poor quality. Meanwhile, summing neutron data obtained in a cycle will be meaningless, because the different conditions will be averaged to zero. A stroboscopic measurement and a condition filtering data reduction have been developed in TAKUMI, and preliminary tests with a fatigue test of steel and a cyclic electric field of a piezoelectric materials in a stacked-type actuator have been done. The principle of condition filtering data reduction for stroboscopic measurement is shown schematically in Fig. 4. By using this method, the diffraction patterns at specific conditions during cyclic tests can be extracted with sufficiently good statistics. From the cyclic electric field test of a piezoelectric materials in a stacked-type actuator, crystal plane dependences of the lattice strain due to the inverse piezoelectric effect and the hysteresis loop in both the lattice strain and domain switching were observed [5].

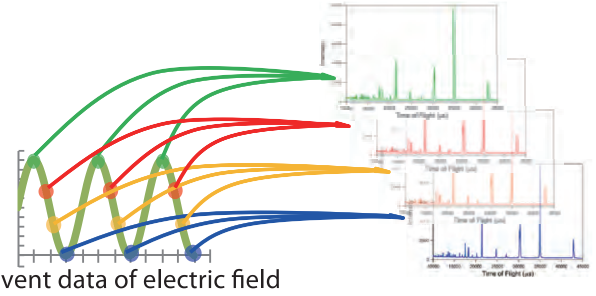

Figure 4. A schematic illustration showing the principle of condition filtering data reduction for stroboscopic measurement.

3. Summary

Some enhancements were completed at TAKUMI using the limited beam time in JFY2015. Successfully done were the supplementation of the 90° scattering detector banks, thermec-mastor installation and commissioning, profile analysis, and stroboscopic measurement. Some of them have also been used by TAKUMI users in their experiments.

References

[1] S. Harjo *et al.*, Mater. Sci. Forum, 524-525 199 (2006).

[2] A. Shibata *et al.*, CAMP-ISIJ, 28 341 (2015).

[3] G. Ribarik & T. Ungar, Mater. Sci. Eng. A528 112 (2010).

[4] T. Kawasaki *et al.*, JPS Conf. Proc., 8 031009 (2015).

[5] T. Kawasaki *et al.*, Acta Cryst., A71 s349 (2015).

S. Harjo[1], T. Kawasaki[1], K. Aizawa[1,2], T. Ito[3], and K. Sakasai[4]

[1]*Neutron Science Section, Materials and Life Science Division, J-PARC center;* [2]*Technology Development Section, Materials and Life Science Division, J-PARC center;* [3]*Neutron R&D Division, CROSS-Tokai;* [4]*Neutron Device Section, Materials and Life Science Division, J-PARC Center*

The Current Status of the Versatile Neutron Diffractometer, iMATERIA

1. Introduction

Ibaraki prefecture, local government of Japan's area where the J-PARC sites are located, has decided to build a versatile neutron diffractometer (IBARAKI Materials Design Diffractometer, iMATERIA [1]) to promote industrial applications for the neutron beam in J-PARC. iMATERIA is planned to be a high-throughput diffractometer that could be used by materials engineers and scientists in their materials development work like the chemical analytical instruments.

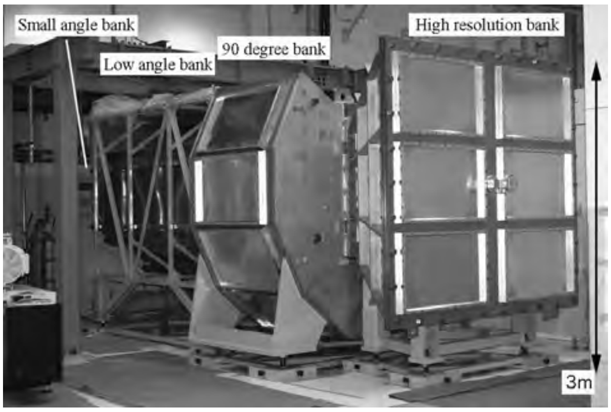

Figure 1. IBARAKI Materials Design Diffractometer, iMATERIA without detector for each bank and instrument shielding. The high-resolution bank, special environment bank (90° bank), and low angle bank, can be seen from right to left. The small-angle detector bank, which is not shown in the picture, is situated in the low-angle vacuum chamber (left hand side of the picture).

The applications of neutron diffraction in materials science are (1) to do structural analyses of newly developed materials, (2) to clarify the correlation between structures and properties (functions), and (3) to clarify the relation between structural changes and improvements of functions, especially for practical materials. To achieve those purposes, a diffractometer with super high resolution is not required. The matching among intermediate resolution around $\Delta d/d = 0.15\%$, high intensity and wide *d* coverage is more important.

This diffractometer is designed to look at a decoupled-poisoned liquid hydrogen moderator (36 mm, off-centered) (BL20), and to have the incident flight path (L1) of 26.5 m with three wavelength selection disk-choppers and straight neutron guides with a total length of 14.0 m. The instrumental parameters are listed in Table 1. There are four detector banks, including a low-angle and small-angle scattering detector bank. The angular coverage of each detector bank is also shown in Table 1. The rotation speeds for the disk-choppers are the same with a pulse repetition rate of 25 Hz for the most applications (SF mode). In this case, the diffractometer covers $0.18 < d$ (Å) < 2.5 with $\Delta d/d = 0.16\%$ and covers $2.5 < d$ (Å) < 800 at three detector banks of 90 degree, low angle and small angle with gradually changing resolution. When the speed of the wavelength selection disk-choppers is reduced to 12.5 Hz (DF mode), we can access a wider *d*-range, $0.18 < d$ (Å) < 5 with $\Delta d/d = 0.16\%$, and $5 < d$ (Å) < 800 with gradually changing resolution with doubled measurement time from SF mode.

Table 1. Instrumental parameters of iMATERIA. L2 is the scattered flight path. The *d*-range (*q*-range) for each bank is the maximum value for 2-measurement mode.

L1	26.5 m	
Guide length		Total 14 m (3 section)
Position of Disk choppers		7.5 m (double)
		11.25 m (single)
		18.75 m (single)
High	2θ	$150° \le 2\theta \le 175$
Resolution	L2	2.0 – 2.3 m
Bank	*d*-range	$0.09 \le d(\text{Å}) \le 5.0°$
Special	2θ	$80° \le 2\theta \le 100°$
Environment	L2	1.5 m
Bank	*d*-range	$0.127 \le d(\text{Å}) \le 7.2$
Low	2θ	$10° \le 2\theta \le 40°$
Angle	L2	1.2 – 4.5 m
Bank	*d*-range	$0.37 \le d(\text{Å}) \le 58$
Small	2θ	$0.7° \le 2\theta \le 5°$
Angle	L2	4.5 m
Bank	*d*-range	$0.007 \le q(\text{Å}^{-1}) \le 0.6$

2. Current status

All of the four banks, high-resolution bank (BS bank), special environment bank (90 degree bank), low-angle bank and small-angle bank are operational. It takes about 5 minutes (DF mode) to obtain a 'Rietveld-quality' data in the high-resolution bank at 500 kW beam power for about 1 g of standard oxide samples.

Figure 2 shows a typical Rietveld refinement pattern for $LiCoO_2$ sample, cathode material for LIB, at the high-resolution (BS) bank by the multi-bank analysis function of Z-Rietveld [2]. It takes 20 min at DF mode to collect the available Rietveld data, due to the high neutron absorption cross section for natural Li ($\sigma_s^{Nat} = 70$ barn).

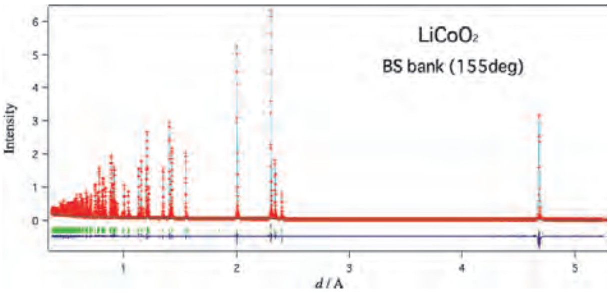

Figure 2. Rietveld refinement pattern for $LiCoO_2$ at the high-resolution bank of iMATERIA.

3. Sample Environments

The automatic sample changer is the most important sample environment for high-throughput experiments. Our automatic sample changer [3] consists of sample storage, elevating system of two lines, two sets of pre-vacuum chambers and a sample sorting system. We can handle more than 600 samples continuously at room temperature without breaking the vacuum of the sample chamber.

The V-furnace (~900°C), the crio-furnace (4 K) and the 1 K crio are ready for experiments. The gas furnace (~900°C) will also be in operation soon.

5. Rapid Measurement Scheme for Texture

The crystallographic texture measurement system was optimized by applying Rietveld texture analysis [4]. The optimized measurement scheme made it possible to do quantitative texture measurements in several minutes. 132 spectra corresponding to different sample directions were simultaneously measured and the data were analyzed by MAUD software [5]. Figure 3 shows the $\phi_2 = 45°$ sections of the orientation distributions in Euler space for ferrite and austenite phases in a rolled sheet of NAS64 duplex stainless steel. The results listed under "5 × 36" were obtained by the conventional measurement scheme requiring measurement of 36 spectra at 5 different sample geometries. The newly suggested scheme, "1 × 132", is the measurement of 132 spectra at a single sample geometry. The results by both schema show good similarity, which indicate the validity of the new scheme without sample rotation. The result of an EBSD measurement for the same sample also matched well the above results.

This rapid measurement scheme needs to both a high resolution and a wide range of scattering angle, *i.e.* the features of iMATERIA. Since the new scheme can determine the bulk average texture with a single neutron exposure for 3 ~ 5 minutes (using single frame mode @500 kW), it is an optimal method for in-situ texture measurement. The achievement described above has been attracting researchers from metallurgy and other related industries, who are newcomers to the field of neutron sciences.

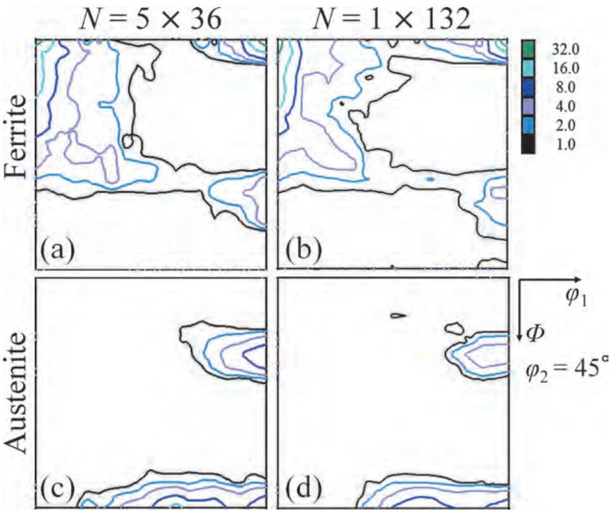

Figure 3. $\varphi_2 = 45°$ sections of the orientation distributions in Euler space for (a), (c) ferrite and (b), (d) austenite phases in a rolled sheet of NAS64 duplex stainless steel [4]. The descriptions of schemes "5 × 36" and "1 × 132" can be found in the text.

References

[1] T. Ishigaki *et al.*, Nucl. Instr. Meth. Phys. Res. A 600 (2009) 189-191.

[2] R. Oishi *et al.*, Nucl. Instr. Meth. Phys. Res. A 600 (2009) 94-96.

[3] A. Hoshikawa *et al.*, J. Phys.: Conf. Ser. 251 (2010) 012083.

[4] Y. Onuki *et al.*, J. Appl. Cryst. 49 (2016) 1579-1584.

[5] Wenk, H. –R. *et al.*, Powder Diffr. 25 (2010) 283-296.

T. Ishigaki, A. Hoshikwa, Y. Yoshida, T. Matsukawa, and Y. Onuki
Frontier Research Center for Applied Nuclear Sciences, Ibaraki University

Status of the High Intensity Total Diffractometer (BL21, NOVA)

1. Introduction

Total scattering is a technique to analyze non-crystalline structure in materials with atomic Pair Distribution Function (PDF). NOVA was designed to perform total scattering and is the most intense powder diffractometer with reasonable resolution ($\Delta d/d$ ~ 0.5%) in J-PARC. It is easy to adapt NOVA to a very wide field: liquids, glass, local disordered crystalline, magnetic structure of long lattice constant, and so on. The observation of the hydrogen position in materials is one of the most important scientific themes of NOVA.

2. Development of a cell for hydrogen gas atmosphere

For the hydrogen gas atmosphere measurement (~ 10 MPa), single-crystal sapphire cell was used but the signal-to-noise ratio at high-Q range is fatal for PDF measurements. It is necessary to use material with small coherent cross-section, such as vanadium. However, vanadium is known as a hydrogen-absorbing metal. To realize the vanadium cell for hydrogen gas atmosphere, two measures were taken: thermal treatment to prevent hydrogen absorption at the surface and a double-wall structure to relax the strain caused by lattice expansion of the sample in a hydrogen absorption process.

3. Auto-sample changers

For effective measurements with intense neutron flux NOVA, the auto-sample changers are essential: a temperature-controlled (20 K ~ 500 K) auto-sample exchanger, which can load 18 samples, and an ambient temperature auto-sample exchanger, which can load 40 samples, were introduced in the end of FY 2014. In FY 2015, refinement of sample exchanging mechanism as well as safety verification and software drivers for the automatic operation of sample changers were combined with neutron scattering data acquisition.

Acknowledgement

Operation and developments of NOVA was performed under the S1-type program (2014S06) approved by the Neutron Scattering Program Advisory Committee of IMSS, KEK. The development of the cell was supported by Photon and Quantum Basic Research Coordinated Development Program from the Ministry of Education, Culture, Sports, Science and Technology, Japan.

T. Otomo[1,2], K. Ikeda[1,2], T. Honda[1,2], H. Ohshita[1,2], N. Kaneko[1,2], T. Seya[1,2], and K. Suzuya[2]

[1]*Institute of Materials Structure Science, KEK;* [2]*Neutron Science Section, Materials and Life Science Division, J-PARC Center*

Current Status of the Energy-Resolved Neutron Imaging System "RADEN"

1. Introduction

A pulsed-neutron instrument, named Energy-Resolved Neutron Imaging System "RADEN", has been constructed at the beam line of BL22 in the Materials and Life Science Experimental Facility (MLF) of J-PARC [1]. The primary purpose of this instrument is to perform energy-resolved neutron imaging experiments through effective utilization of the pulsed nature of the neutron beam, making it the world's first instrument dedicated to pulsed neutron imaging experiments. After the first neutron beam transport in Nov. 2014, commissioning study using neutron beam has started. From the 2015 period, RADEN started to accept user proposals. About half of the beam time in FY2015 was used by the instrument group for a commissioning study of the instrument, 1/4 was allocated to the project use and the rest was utilized by users.

2. Technical development at RADEN

Together with the commissioning study, the RADEN instrument members continued the technical development on neutron imaging. At first, the CCD camera type detector was converted into a much brighter system by using a high-reflectivity single mirror (Fig. 1). This improvement shortened the distance between the CCD camera and the scintillator screen, and now we can focus on a small area of the scintillator and easily secure 100 μm spatial resolution. Then, the polarization analysis system for the magnetic field imaging experiment was improved to obtain uniform polarization distribution in the beam (Fig. 2). Based on the numerical simulation of the magnetic field and conservation of the neutron spin direction along the neutron trajectory, we evaluated the expected performance of the system and confirmed it experimentally [2]. As a result of the experiments, neutron polarization of over 90% was obtained at the range of neutron wavelength longer than 3 Å. The polarization distribution image confirmed that the standard deviation along the vertical direction was 2.0% in contrast with the one along the horizontal direction of 0.3%. This indicated that the magnetic field connection was good enough to preserve the neutron spin direction. In addition, a new neutron imaging technique using interference of neutron beams, named neutron phase imaging, has been developing using pulsed neutrons [3]. The key of this technique is preparing the precise absorption grating to construct a Talbot-lau interforometer. We fabricated absorption grating by using the imprinting technique of metallic glass [4], and this grating finally allowed us to observe very high visibility of moire pattern around 60% at the wavelength of 5 Å.

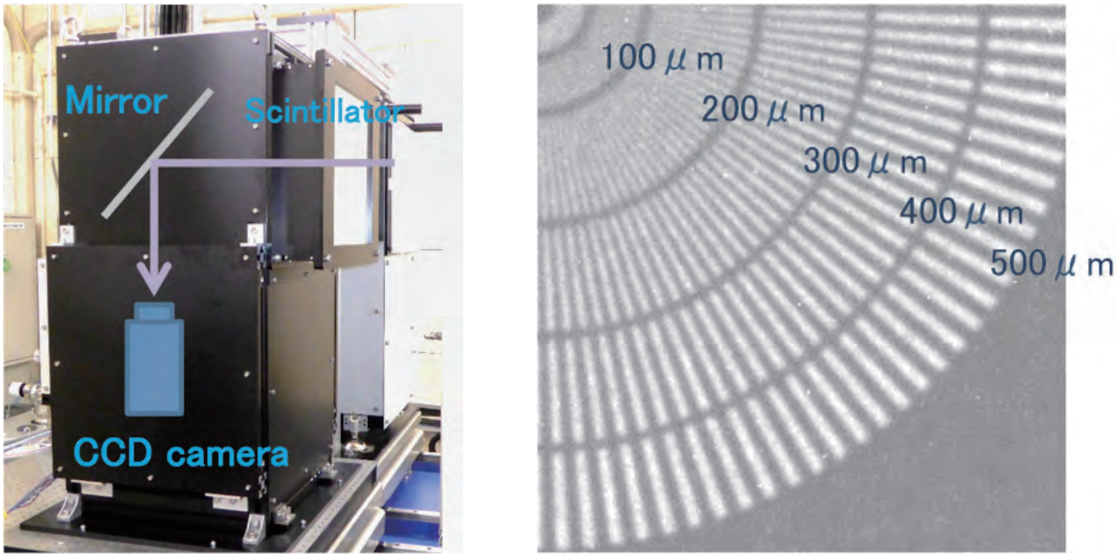

Figure 1. New CCD camera type detector system using single mirror (left) and obtained image using test chart (right).

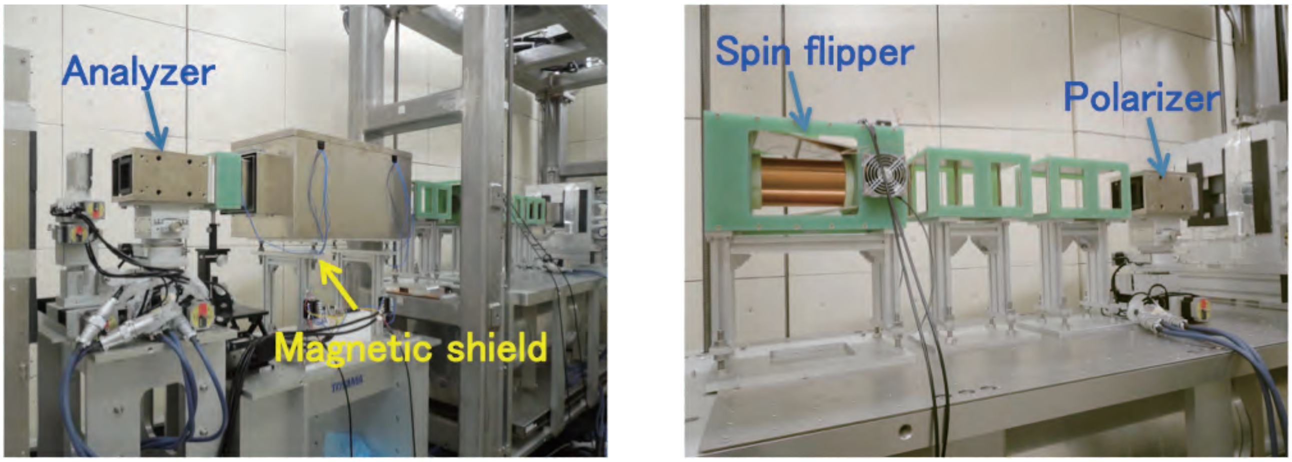

Figure 2. Polarization analysis system of RADEN.

3. User programs and project use

RADEN started to accept general user programs and trial use proposals from FY2015, and 7 of the 10 submitted proposals were approved. About half of them were regarding the Bragg edge imaging technique. The field of proposals covered material science, industrial application, and metal archaeology. Two proposals were conducted as project use. Within this proposal, magnetic field imaging of a model electric motor was performed and succeeded to visualize polarization change due to the change in the magnetic field inside the motor. In addition, Bragg edge imaging of a bent steel sample revealed the spatial distribution of the microstructure of the sample, such as texture variations, crystallite size, and phase [5]. Each quantity was compared with the one obtained by neutron diffraction experiment and that confirmed its value's validity.

4. Summary

RADEN started user programs together with the commissioning study from FY2015. Several energy-resolved neutron imaging experiments, such as magnetic-filed imaging of a model motor and Bragg edge imaging of a steel sample, were performed in the user program. Technical developments of the CCD camera type detector and the polarization analysis system were performed, and their performance was improved. In addition, for the first time, a new imaging technique using neutron interferometry was conducted with pulsed neutrons.

Acknowledgement

This work was partially supported by JST ERATO Momose Quantum Beam Phase Imaging Project and by Photon and Quantum Basic Research Coordinated Development Program from the Ministry of Education, Culture, Sports, Science and Technology, Japan.

References

[1] T. Shinohara *et al.*, J. Phys: Conf. Series 746 012007 (2016).
[2] K. Hiroi *et al.*, JAEA-Technology 2016-021 (2016).
[3] ERTO Momose Quantum Beam Phase Imaging Project.
[4] W. Yashiro *et al.*, Jpn. J. Appl. Phys. 55 048003 (2016).
[5] Y. Su *et al.*, Mater. Sci. Eng. A675 19-31 (2016).

T. Shinohara[1,3], T. Kai[1], K. Oikawa[1], T. Nakatani[1], M. Segawa[1], K. Hiroi[1], Y. Su[1], H. Hayashida[2], J. D. Parker[2,3], Y. Matsumoto[2], S. Zhang[2], W. Ueno[1,3], Y. Seki[1,3], and Y. Kiyanagi[4]

[1]*Neutron Science Section, Materials and Life Science Division, J-PARC Center;* [2]*Neutron R&D Division, CROSS-Tokai;* [3]*JST, ERATO, Momose Quantum Beam Phase Imaging Project;* [4]*Nagoya University*

Status of Polarized Neutron Spectrometer POLANO (BL23)

1. Introduction

POLANO is a chopper type spectrometer with a polarization analysis capability, now under construction at the Materials and Life Science Experimental Facility (MLF), J-PARC. In 2012, the full-scale construction began under a joint project between KEK and Tohoku University [1-4]. The construction and development of devices have been underway in the year 2015. After the construction is completed, we will assess the radiation, then, POLANO will be approved as a proper neutron beam line and the commissioning will start.

Our principal concept for designing POLANO is to achieve higher-energy polarization analysis of inelastic scattering beyond a reactor-based neutron source. We target the energy range over $E_f = 40$ meV using the combination of SEOP for a polarizer and bender supermirror as an analyzer of $m = 5$ to 5.5. In the second phase, we will focus on a realization of even higher energy experiments (0 meV $< \Delta E <$ 100 meV) with a wide solid-angle SEOP/MEOP analyzer. In order to achieve a high-flux polarized neutron experiment, we plan to adopt the cross correlation method. R&D of the correlation chopper is now underway. In this article, we report the current status of the construction and design of the POLANO spectrometer.

2. Beyond the reactor neutron source

As mentioned above, POLANO is targeting relatively high-energy polarization analysis, which had not been realized so far. The energy range up to 100 meV contains many significant scientific topics, particularly in the field of the so-called strongly correlated electron systems. In the light of recent discoveries in material science, many of the observed complex phenomena are largely caused by entangled physical degrees of freedom of spins, charges, orbitals, and even lattice vibration. Although the polarized neutron technique has been developed and used for many years, the application of the time-of-flight (TOF) method has only started in the recent years. In particular, with regard to the inelastic spectrometer, the polarized neutron technique finds limited practical use in wide scattering angle instruments. By combining the polarized neutron technique and the TOF method (pulsed neutron technique), we are going to put in practice the high-energy polarization analysis in POLANO. The schematic beam line design is depicted in Fig. 1.

3. Status of the POLANO beam line

Converging $4Q_c$ guide tubes optimized for 110 meV neutron energy are aligned in the beam line (Fig. 2). These tubes can efficiently transport neutrons at sample position. Several devices are placed in the intersection of the beam line. In particular, choppers are one of the key devices ensuring the success of the inelastic neutron scattering experiments. POLANO utilizes four different types of choppers. The T0 chopper can eliminate gamma flash and fast neutrons. Disk choppers (slow-rotating band choppers and fast-rotating correlation choppers) are used for the cross-correlation method. The correlation chopper has been newly developed. The Fermi chopper is for selecting incoming (incident) neutron energy rotating at 600 Hz. These choppers, except the correlation chopper, have been installed in the beam line.

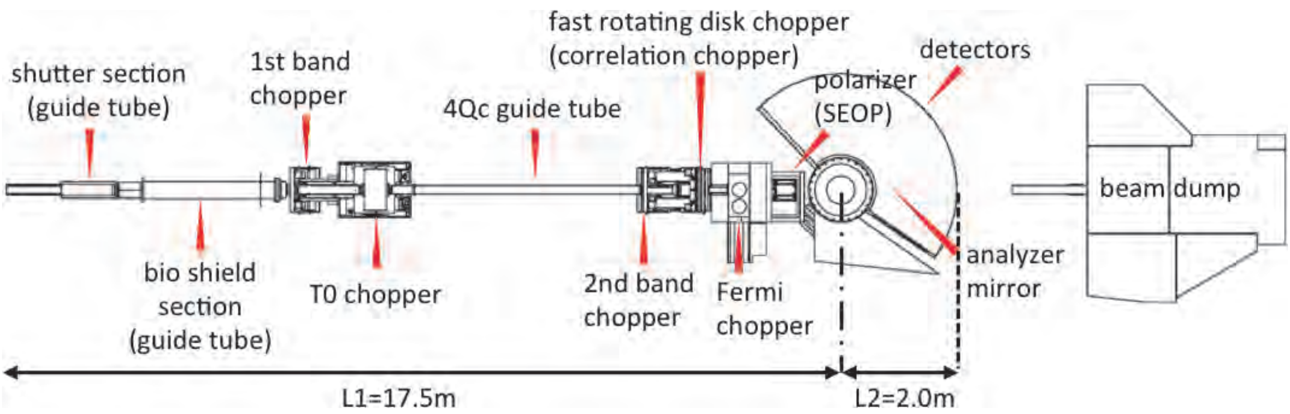

Figure 1. Schematic drawing of the POLANO beam line with several devices' arrangement.

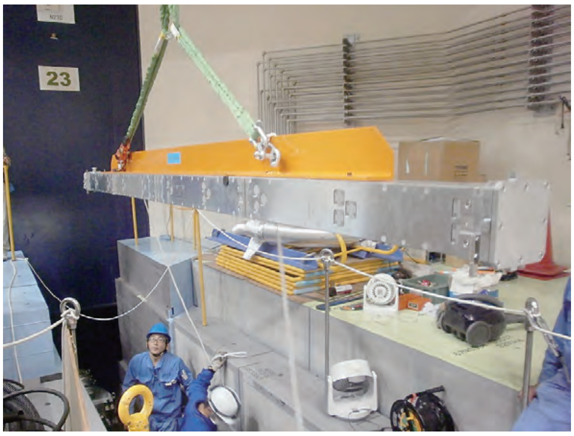

Figure 2. Installing operation of the 4 m super mirror guide tube in the beam line.

Figure 3. Installed position-sensitive detector array.

Since a large vacuum chamber and a get-lost-tube had already been placed, we proceeded with the installation of detectors at the back of the vacuum chamber. Figure 3 shows the installed position-sensitive detectors (PSD) at a detector bank (back of the vacuum chamber). The PSD with 60 cm effective length, 3/4″ diameter, 10 atm of ^{3}He gas pressure, and SKYN2 feedthrough developed in MLF and 32 PSD that we adopted, have been positioned in a detector bank covering the scattering angle of about 20°. In the vertical direction, there are three layers of PSD arrays. In the horizontal (central) layer, all the scheduled PSD are installed (from –20° to 120°).

Beyond the construction operation, we continue our efforts to develop new devices and technology for neutron science. One of those developing items is helium spin filter for polarization of neutron spins [5]. And the others are magnetic environment and devices for the polarization experiment [6], a new high-speed rotating disk chopper [7], dynamical nuclear polarization (DNP) technique, data acquisition and analysis system, and so forth.

4. Future plans

Within the next few years POLANO has to start user programs for scientific research. Therefore, the construction will be completed and radiological assessment will be finished and approved in 2016.

References

[1] T. Yokoo *et al.*, J. Phys. Soc. Jpn., 82 SA035 (2013).

[2] T. Yokoo *et al.*, J. Phys. Conf. Series 502 012045 (2014).

[3] K. Ohoyama *et al.*, J. Phys. Conf. Series 502 012051 (2014).

[4] T. Yokoo *et al.*, EPJ. Web of Conferences 83 03018 (2015).

[5] T. Ino *et al.*, J-PARC Annual Report 2015 vol. 2 pp.109-110.

[6] M. Ohkawara *et al.*, J-PARC Annual Report 2015 vol. 2 pp.106-108.

[7] T. Yokoo *et al.*, J-PARC Annual Report 2015 vol. 2 pp.111-112.

T. Yokoo[1,2], M. Fujita[3], S. Itoh[1,2], N. Kaneko[1,2], S. Sugai[1,2], M. Ohkawara[3], T. Ino[1,2], Y. Nambu[3], and M. Sakaguchi[1,2]

[1]*Neutron Science Section, Materials and Life Science Division, J-PARC Center;* [2]*Institute of Materials Structure Science, KEK;* [3]*Institute for Materials Research, Tohoku University*

Magnetic Devices and Environment for Polarization Experiments at POLANO

1. Introduction

The polarization neutron spectrometer POLANO, now under construction at BL23 of MLF, will be an indispensable instrument for investigations of magnets and strongly correlated electron systems under a collaboration between KEK and Tohoku University. For accurate polarized neutron scattering experiments, control of magnetic fields along the neutron pass is quite important to keep the polarization. Figure 1 shows a typical alignment of the magnetic-field devices of POLANO. Neutrons go through the devices from the left of the Figure to the right. The system consists of a solenoid coil for a ^{3}He polarizer, a vertical guide magnet with permanent magnets, a Helmholtz coil with additional three coils, which generate horizontal magnetic fields in an arbitrary direction, which is called 3D Helmholtz coil in this report, a fan-shaped guide magnet that generates magnetic fields between the sample position and the polarization analyzer, and the supermirror analyzer.

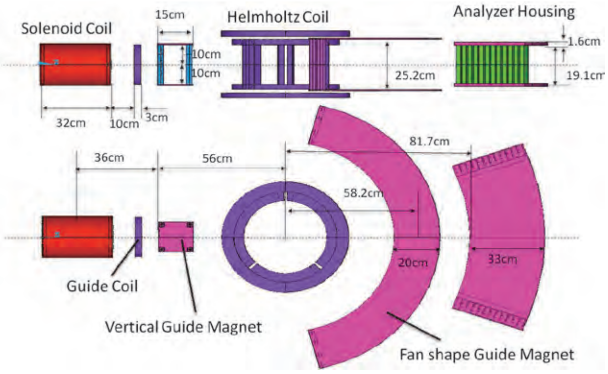

Figure 1. A typical alignment of the magnetic field devices at BL23. The beam goes through from the left to the right.

For spectrometers in reactor facilities, the magnetic-field devices are optimized in each polarized neutron experiment. However, it is difficult to optimize magnetic fields in spectrometers at J-PARC because of limited access space in the vacuum chambers. Therefore, optimization of magnetic fields devices by calculations and observations by off-beam mode is necessary. We have calculated the optimized alignments of magnetic-field devices by finite elements method software, ANSYS and FEMTET. Moreover, to confirm the calculations, we have prepared a test bench, which consists of a vertical guide magnet, a 3D Helmholtz coil, and a fan-shaped guide magnet [1].

Recently, we revised the designs of the fan-shaped guide magnet and the 3D Helmholtz coil to minimize the dead angles of the neutron beam. In this report, we will explain the new magnetic-field devices and the results of calculation and observation on the test bench of the magnetic fields.

2. Design of a 3D Helmholtz coil

We have two 3D Helmholtz coils for POLANO, which control the direction of the magnetic field at the sample position. The first 3D Helmholtz coil, which is called Coil-a in this report, is shown in Fig. 2(a). The covered angle of each horizontal magnetic field coil is the same as the one shown in Fig. 2(a). The vertical parts of the horizontal magnetic field coil (black) form dark angles shown as red parts in Fig. 2. To reduce these dark angles, we produced a new coil (Coil-b), on which the covered angle of horizontal magnetic field coils were not the same; the angle between the two pillars is 135°, 135° an 90°; this makes the dark angle relatively small, as shown in Fig. 2(b). The diameter of Coil-b is 660 mm, which is smaller than that of Coil-a (690 mm). The inner diameter of the both coils is 360 mm.

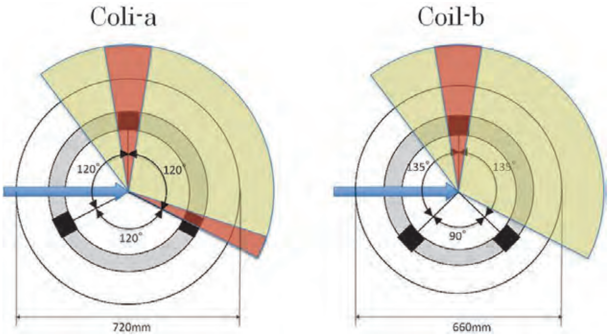

Figure 2. Upper figure of the two 3D Helmholtz coils. The gray part indicates horizontal magnetic field coils. Depicted in black are the vertical parts of the horizontal coils, which make a dark angle. The dark angle is shown in yellow. The arrows indicate the direction of the neutron beams.

Figure 3 shows the Coil-b on the test bench. To confirm the effect of the change of the coil design to magnetic fields, we measured magnetic field distribution along the beam pass in the test bench using 3D gaussmeter to obtain the magnitude of the magnetic field.

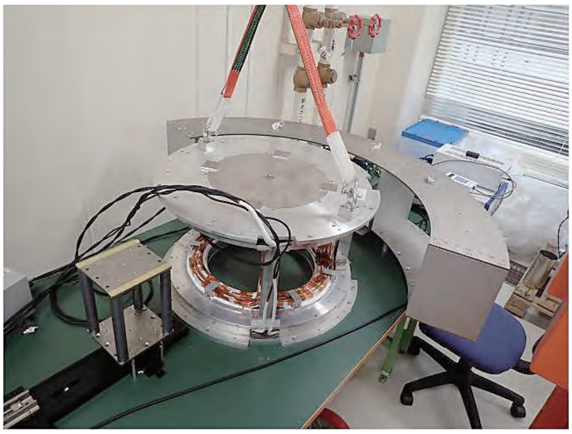

Figure 3. A picture of the test bench for measurement of magnetic fields. In this picture, Coil-b is installed.

Figure 4 shows the position dependence of the magnitude of the magnetic field. The direction of the magnetic field at the sample position was vertical, the current of the 3D Helmholtz coils was 10 A. The horizontal axis is the position from the right edge of the vertical guide magnet. We measured the magnetic fields at the beam center. The red and blue lines in Fig. 4 show the observed magnitude of the magnetic fields using Coil-a and Coil-b, respectively. As shown in Fig. 4, the magnetic field using Coil-b is smaller than that using Coil-a at the minimum at about 100 mm in the gap between the vertical guide magnet and the 3D Helmholtz coils, and at 750 mm at the gap between the 3D Helmholtz coils and the fan-shaped vertical guide magnet. This is due to the change of the outer diameter of the 3D Helmholtz coils. Based on the calculations of depolarization along the beam pass, the polarization can be kept when the magnitude of the magnetic field is larger than 15 G up to E = 100 meV. Thus, the depolarization at the bottom at 100 mm can be neglected for Coil-b. Though the magnetic field at the bottom at 750 mm is close to 15 G, the magnetic fields in this region will be increased by the leak magnetic fields from the polarization analyzer, in which magnetic field of 400 G is generated at the center of the polarizer. The calculation using ANSYS indicates that the enhancement of the magnetic fields at 750 mm by the polarization analyzer is estimated to be about 15 G. Thus, the depolarization at the bottom at 750 mm can be neglected in POLANO. These results indicate that Coil-b can be used in POLANO.

3. Effect of the design change of the fan-shaped guide magnet

The fan-shaped guide magnets are a device to connect magnetic fields between the 3D Helmholtz coil and the polarization analyzer, which consists of two fan-shaped iron plates and neodymium magnets. The neodymium magnets are set at the both ends of the iron plates. Since the first fan-shaped magnet has a slight dark angle by the neodymium magnets and the aluminum plate, which supports the two iron plates, the design was revised recently to reduce the dark angle. In the revised version of the fan-shaped magnet, the shape of the edge of the iron plates and the position of the neodymium magnets have been changed, as shown in Fig. 5. Moreover, in the revised version, the two fan-shaped iron plates are supported at a scattering angle of 90°. The dark angle of the revised version by the support wall is at the same angle of that by the 3D Helmholtz coil to minimize the dark angle.

By calculations using FEMTET, we confirmed the difference of the magnetic fields generated by the original and the revised fan-shaped magnet. Only the fan-shaped magnets were included in the calculations. Figure 6 shows the results of the calculations of the generated magnetic fields by the original (blue) and the revised (red) fan-shaped magnets. The origin of the

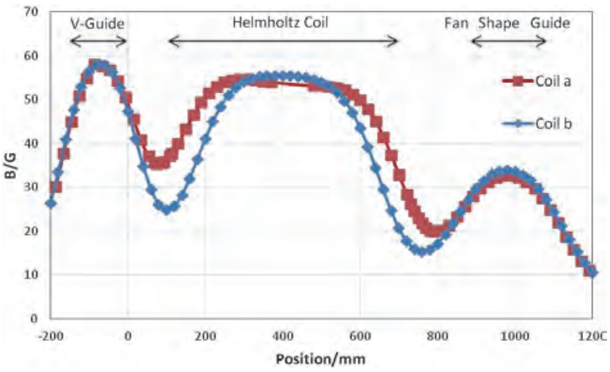

Figure 4. Observed magnitude of the magnetic fields in the test bench with Coil-a (red) and Coil-b (blue).

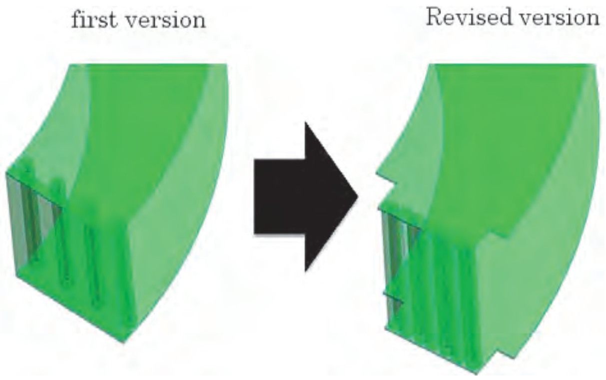

Figure 5. Revision of the fan-shaped guide magnet.

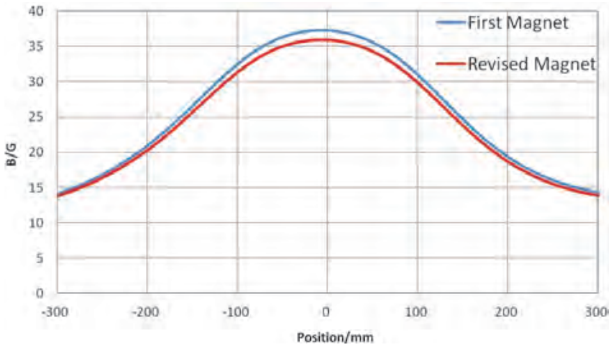

Figure 6. The calculated magnetic fields in the fan-shaped guide magnet. The red and blue lines indicate the magnetic fields of the original and revised designs, respectively.

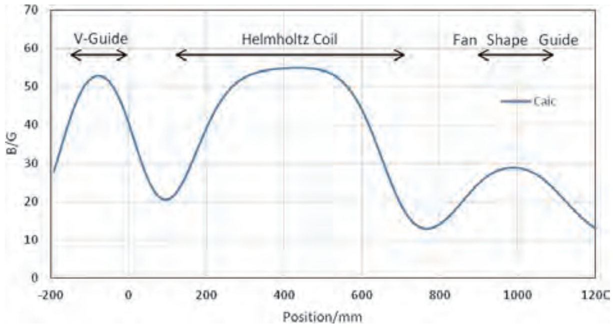

Figure 7. The calculated magnetic fields distribution from the vertical guide magnet to the revised fan-shaped guide magnet.

horizontal axis in Fig. 6 is the center of the iron plate. The calculation was made at the beam center.

As shown in Fig. 6, the largest difference of the magnetic field is at most 1.4 G, which is much smaller than the magnitude of the magnetic field at the maximum, meaning that the effect on the magnetic fields by the revision is negligible.

We also confirmed the effect of the revision on the magnetic field distribution in the test bench using FEMTET. In the calculation, the vertical guide magnet, Coil-b, and the revised fan-shaped magnet were included. The current of Coil-b is 10 A. Figure 7 shows the result of the calculation. There is a minimum at 750 mm between Coil-b and the revised fan-shaped guide magnet. Though the minimum magnetic field at 750 mm is smaller than 15 G, the magnetic field is enhanced by the leak fields from the polarization analyzer, as it was explained earlier. Thus, the depolarization at the bottom around 750 mm can be negligible.

Reference

[1] K. Ohoyama, T. Yokoo, S. Itoh, M.Sakaguchi, M.Ohkawara, Y.Nambu, T. Ino, N.Kaneko, MLF ANNUAL REPORT 2014, 55-57.

M. Ohkawara[1], K. Ohoyama[2], T. Yokoo[3,4], S. Itoh[3,4], M. Sakaguchi[3,4], M. Fjita[1], Y. Nambu[1], T. Ino[3,4], and N. Kaneko[3,4]

[1]*Institute for Materials Research, Tohoku University;* [2]*Ibaraki University;* [3]*Neutron Science Section, Materials and Life Science Division, J-PARC Center;* [4]*Institute of Materials Structure Science, KEK*

Development of an *in-situ* Polarized ^{3}He Neutron Spin Filter in POLANO

1. Introduction

A ^{3}He neutron spin filter (NSF) is one of the essential devices in POLANO for polarization of the incident neutron beam. It is required to be operated *in-situ* to provide a stable neutron polarization, and the spin-exchange optical pumping (SEOP) method is employed to polarize the ^{3}He gas. We have designed a compact whole-in-one ^{3}He NSF system that fits well in the limited space between the disk choppers and the sample chamber. The conceptual design of the NSF system has been fixed and it is now under construction. In the early stage of the commissioning of POLANO in FY2016, the ^{3}He NSF is going to be installed, and the test run will begin.

2. Conceptual design of the ^{3}He NSF on POLANO

The necessary elements for an in-situ polarized ^{3}He NSF are (1) a ^{3}He cell, (2) a homogeneous magnetic field with neutron guide fields, (3) a high-power laser with optical components for the optical pumping of Rb, (4) a heater to achieve the appropriate vapor densities of RB and K, and (5) adiabatic fast passage (AFP) spin flipping of polarized ^{3}He. A schematic view of the ^{3}He NSF on POLANO is shown in Fig. 1.

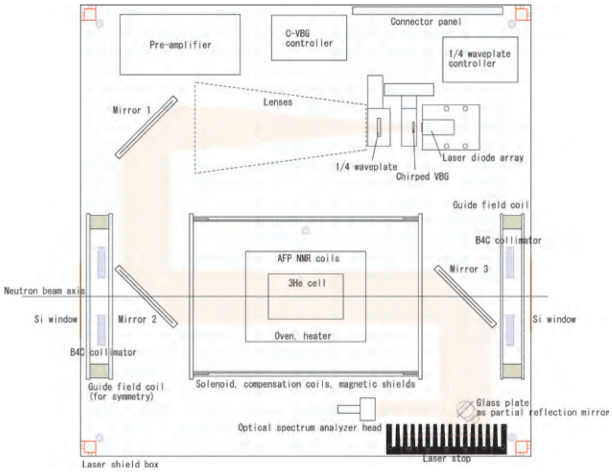

Figure 1. Schematic view of the ^{3}He NSF on POLANO. All essential elements are packed in a laser shield box with a size of 60 cm by 60 cm by 25 cm.

2.1 ^{3}He cell

We are preparing cylindrical cells made of GE180 aluminosilicate glass with a diameter of 60 mm and length of 60 to 100 mm. The cells are filled with ^{3}He gas at 2 to 3.5 atm, and their effective ^{3}He thickness ranges from 10 to 35 atm-cm for polarizing neutrons with energies of 10 – 100 meV. They are so-called K-Rb alkali hybrid SEOP cells where K and Rb are filled in appropriate mixing ratio for efficient optical pumping [1]. The ^{3}He gas pressure inside the cells increases as high as ~7 atm at the operating temperature of 250°C. Research on fabricating glass cells that can tolerate such high pressures is in progress.

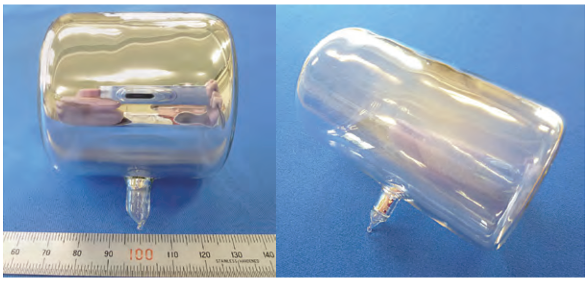

Figure 2. ^{3}He cells, Iori (left) and Kiyoshi (right). Both are with diameters of 60 mm; the lengths are 60 mm and 100 mm, respectively.

2.2 Magnetic field

A solenoid and compensation coils at both solenoid edges with Permalloy magnetic shield were designed and constructed together with additional two identical solenoids, each arranged upstream and downstream (Fig. 3). The downstream solenoid provides the spin guide field for polarized neutrons, and the upstream solenoid is placed in a symmetric position to ensure a homogeneous magnetic field at the ^{3}He cell position.

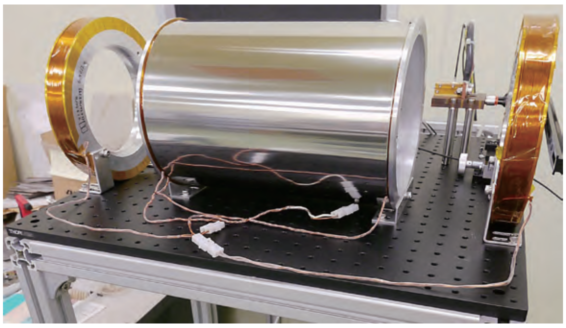

Figure 3. A magnetically shielded solenoid (center) and additional two identical solenoids. The downstream solenoid (right) provides an axial magnetic field with a strength of > 2 mT to keep the neutron polarization, and the upstream solenoid (left) provides a symmetric magnetic field for the ^{3}He cell.

2.3 Polyimide heater

In SEOP, hot air blowers (compressed air blow-ers) are commonly used to keep ^{3}He cells at an elevated temperature because they do not interfere with the homogeneous magnetic field, while the conventional electric heaters produce unnecessary magnetic fields. However, due to the limited space for the ^{3}He NSF, non-magnetic polyimide heaters that can be used up to 300°C are being developed. Specially arranged non-magnetic heater element sandwiched by two thin polyimide films is designed not to produce unwanted magnetic fields for the ^{3}He cell.

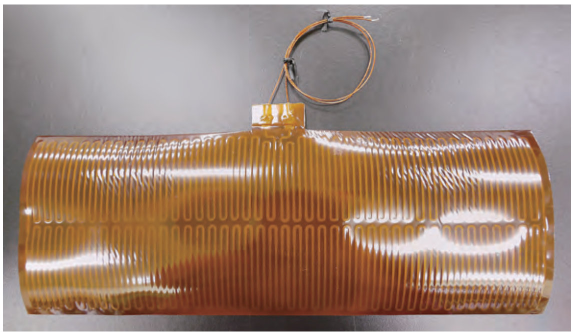

Figure 4. A prototype polyimide heater. This flexible heater is designed to wrap the cylindrical oven made of aluminum. The heating power is 270 W, and the maximum temperature is 300°C.

2.4 AFP NMR spin flip

Neutron spin flipping is essential in polarized neutron scattering, and neutron spin flip devices are commonly used. In ^{3}He NSF, however, polarized ^{3}He nuclei can be reversed by the adiabatic fast passage (AFP) method [2], instead of neutron spins. Such an AFP flipping technique is equipped in the ^{3}He NSF system on POLANO [3]. A uniform RF magnetic field is produced by a cosine-theta coil arranged inside the aluminum oven for AFP (Fig. 5).

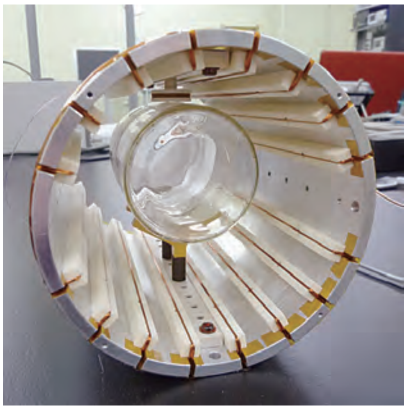

Figure 5. The AFP drive coil is arranged inside the aluminum oven to provide a uniform RF field for AFP spin flips.

3. Safety and future upgrading

The controllers for the in-situ polarized ^{3}He NSF system will be equipped with various safety mechanisms, such as interlocks for the laser and the heater, to meet the J-PARC safety standards. The ^{3}He NSF will be continuously operated for a long period, and the durability of the system is another key issue.

Although the goal at the first stage is to operate the ^{3}He NSF safely and steadily, the system will be upgraded in three directions. They are to increase the polarization of ^{3}He, to enlarge the cell size to cover a wider beam profile, and to increase the effective ^{3}He thickness for polarizing higher energy neutrons. Preparation of high quality ^{3}He cells is the key for these improvements.

References

[1] E. Babcock, I. A. Nelson, S. Kadlecek, and T. G. Walker, Phys. Rev. A 71, 013414 (2005).

[2] A. Abragam, The Principles of Nuclear Magnetism, Oxford University Press (1961).

[3] T. Ino *et al.*, J. Phys.: Conf. Ser. 340, 012006 (2012).

T. Ino[1,2], M. Ohkawara[3], T. Yokoo[1,2], Y. Nambu[3], M. Fujita[3], K. Ohoyama[4], S. Itoh[1,2], H. Kira[5], H. Hayashida[5], K. Kakurai[5], K. Sakai[6,7], and T. Oku[6]

[1]Institute of Materials Structure Science, KEK; [2]Neutron Science Section, Materials and Life Science Division, J-PARC Center; [3]Institute for Materials Research, Tohoku University; [4]Ibaraki University; [5]CROSS-Tokai; [6]Technology Development Science Section, Materials and Life Science Division, J-PARC Center; [7]Neutron Source Section, Materials and Life Science Division, J-PARC Center

Development of Choppers in POLANO

1. Introduction

POLANO is the chopper type spectrometer with polarization analysis capability, now under construction at the Materials and Life Science Experimental Facility (MLF), J-PARC [1-4]. Not to mention the chopper spectrometers for almost all pulse neutron instruments, the "chopper" is one of the most significant devices. The roles of the chopper are shaping the neutron pulse, eliminating unwilling neutrons, determining the band width of the neutron wave length, choosing the neutron velocity, and so forth. The following choppers are particularly useful for the POLANO experiment, namely T0 chopper, slow rotating disk chopper, and Fermi chopper. A time-distance diagram of an individual chopper is shown in Fig. 1.

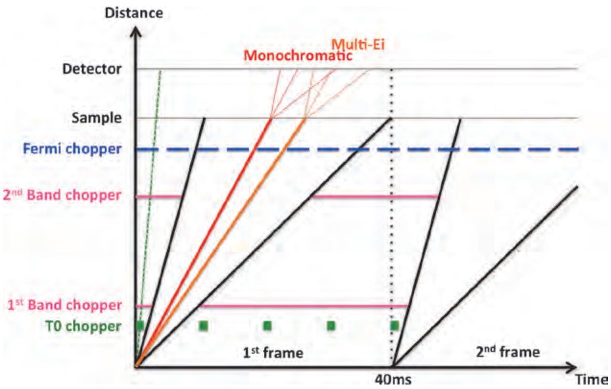

Figure 1. Time-distance diagram showing the opening and closing sequence of several types of choppers.

2. T0 chopper

The T0 chopper is a nimonic chopper to eliminate gamma flash and fast neutrons in the very early time ($t \sim 0$) of the pulses. When the blade center is initially positioned on the beamline, it takes $t_0 = (w+\Delta w)/(2\pi Rf)$ for the blade to be removed from the beam cross-section, where w is the width of the neutron beamline, $w+2\Delta w$ is the width of the chopper blade, R is the rotational radius of the chopper blade, and f is the rotational frequency. If this T0 chopper is located at a distance L from the neutron source, neutrons with energies less than $E_0 = (1/2)m_N(L/t_0)^2$ are transmitted through the T0 chopper and utilized on the spectrometer, and the intensities of high energy neutrons, i.e., neutrons with energies larger than E_0, are reduced, where m_N is the neutron mass. The blade that rotates and obstructs unwilling neutrons is normally made of massive material, so it is heavy. Its weight is almost 130 kg and it is fabricated from combination material, which includes Inconel X-750 and stainless steel. Experiments at POLANO are somewhat with higher energycomparing to standard inelastic scattering experiments (a range of sub-eV in the future), up to 100 Hz rotational speed is realized similar to the one that is developed for HRC [5]. The jitter of maximum 5 μs corresponds to the 1 mm blade clearance and can be well controlled. Chopper housing also made of stainless steel (SUS304) is equipped with "one-touch operation" for cooling water, vacuum line, and electricity. The manufactured POLANO T0 chopper is shown in Fig. 2(a).

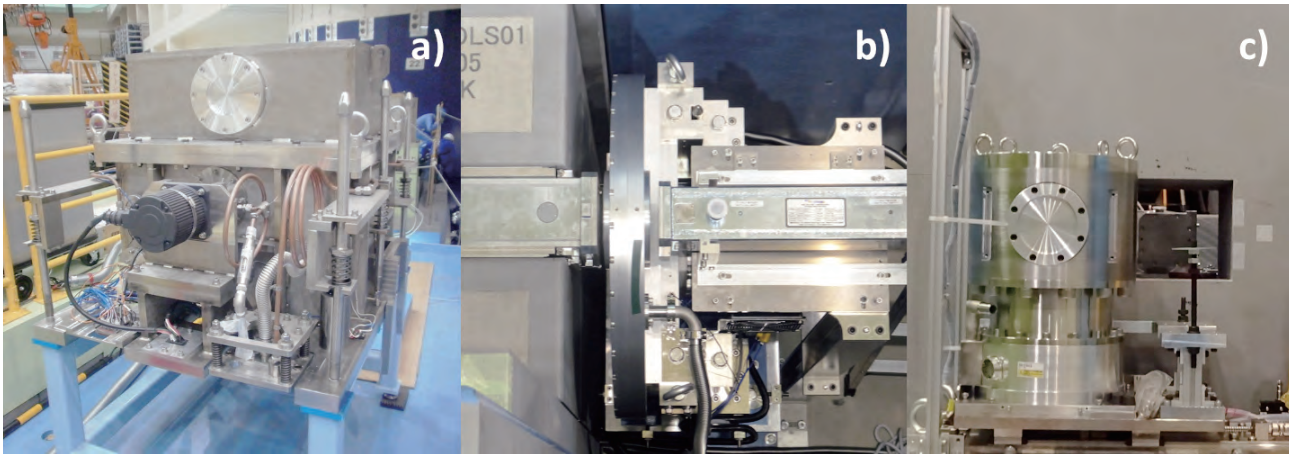

Figure 2. A suite of choppers developed for POLANO. a) T0 chopper, b) slow-rotating disk chopper (installed in beamline with neutron guide tubes), c) Fermi chopper.

3. Disk chopper

We are using two types of disk chopper. One is a slowly-rotating (25 Hz) disk chopper, which can define the time window (band width) of incoming neutron pulses, as you can see in Fig. 1. A pair of choppers is placed in the beam line. Each chopper has a rotating disk with diameter ϕ716.4 mm. At the beam cross-section, enriched B_4C and epoxy resin are coated as a neutron absorber in order to obstruct the neutron beam. The set chopper in the beam line with neutron guide mirrors is depicted in Fig. 2(b).

The other type of disk chopper is a fast-rotating chopper utilized for the cross correlation method. This type of chopper, with quite a different structure, has been developed recently. Two big difficulties complicate the design of a disk that rotates with fast speed. With a large disk like a class of 1 m diameter, the forth at the edge of the disk will be over a few thousand MPa to begin with. This forth can easily break a metal plate or even strong carbon fibers. Secondly, the disk must have 2^N-1 open and close sequences (slits and slots). In our case, $N = 8$, there are 255 sequences in total. This complicated disk structure yields stress concentration all over the place. So now we are testing equipment with low spec model. The diameter of the disk (spindle) is ϕ768 mm, and its weight is almost 100 kg.

4. Fermi chopper

The Fermi chopper is used as a neutron velocity selector to monochromatize incoming neutron energy (wave length). At a pulsed neutron source, the Fermi chopper is used for neutrons over a wide energy range up to the eV region. It consists of a slit package rotating in synchronization with the production timing of pulsed neutrons. The Fermi chopper opens when it rotates to a position with the slit direction parallel to the incident neutron beam, and neutrons pass through the slit; the slit-opening time (chopper-opening time, Δt_{ch}) determines the energy resolution of the chopper spectrometer.

Unlike the other choppers, the Fermi chopper must have quite fast rotational speed to obtain reasonable energy resolution. In case of HRC, its speed is 600 Hz maximum. We have already spent long time and efforts to develop the Fermi chopper [6], and now we have a very reliable and satisfactory chopper for the POLANO experiments. Figure 2(c) shows the Fermi chopper for POLANO. This is a HRC type of chopper rotating at 600 Hz, which is controlled with less than 0.5 μs phase accuracy. The slit called sloppy-type yields around 2.5% energy resolution energy resolution with respecting to incident neutron energy Ei.

References

[1] T. Yokoo *et al.*, J. Phys. Soc. Jpn., 82 SA035 (2013).
[2] T. Yokoo *et al.*, J. Phys. Conf. Series 502 012045 (2014).
[3] K. Ohoyama *et al.*, J. Phys. Conf. Series 502 012051 (2014).
[4] T. Yokoo *et al.*, EPJ Web of Conferences 83 03018 (2015).
[5] S. Itoh *et al.*, NIMA 661 86 (2012).
[6] S. Itoh *et al.*, NIMA 661 58 (2012).

T. Yokoo[1,2], S. Itoh[1,2], M. Fujita[3], and N. Kaneko[1,2]
[1]*Neutron Science Section, Materials and Life Science Division, J-PARC Center;* [2]*Institute of Materials Structure Science, KEK;* [3]*Institute for Materials Research, Tohoku University*

Sample Environment at MLF

1. Introduction

The SE team is in charge of preparation, maintenance and development of the beamline (BL)-common SE equipment, and provides assistance to users concerning the operation of the equipment. The team has 12 members: 7 from JAEA and 5 from CROSS, and is divided into sub-teams of cryogenics and magnets, high temperature, high pressure, soft-matter, etc. A pulsed magnet system, a low-temperature and high-pressure equipment and hydrogen equipment are under development.

The status and activities of the SE team in JFY2015 are summarized in this report.

2. Cryogenics and magnets

There are three pieces of BL-common equipment managed by the SE cryogenic and magnet sub-team: a vertical-field superconducting magnet (Fig. 1(a)), a ^{3}He-^{4}He dilution refrigerator (DR) insert (Fig. 1(b)) and a bottom-loading ^{3}He cryostat (Fig. 1(c)). We operated the superconducting magnet at BL15 and BL18 for users' experiments in JFY2015. The two other cryostats are under commissioning. After the test operation of the DR insert was carried out by setting it into the superconducting magnet, we confirmed that the system achieved 50 mK as the base temperature without a sample. We have also performed commissioning of the ^{3}He cryostat, to find out how to operate the system in the temperature range from 0.3 to 300 K. In this fiscal year, a top-loading ^{4}He cryostat was newly added to our BL-common equipment (Fig. 1(d)). This cryostat is a wet system and can be used with the DR insert. These three cryostats, including the new ^{4}He cryostat, are going to be opened for the users' experiments in 2016B after further commissioning.

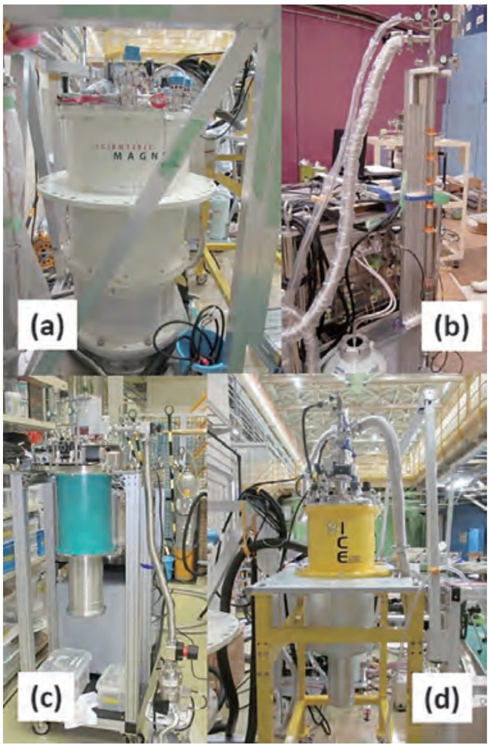

Figure 1. Photographs of the BL-common equipment managed by the SE cryogenic and magnet sub-team: (a) superconducting magnet, (b) DR insert, (c) ^{3}He cryostat, (d) ^{4}He cryostat.

To make the operation of the cryostats convenient for users, we plan to introduce IROHA2, the common software framework for the instrument control in MLF. In JFY2016, we will start it with the super-conducting magnet.

3. High temperature equipment

The high temperature sub-team has a niobium furnace and a furnace for small-angle neutron scattering (SANS) and neutron reflectivity (NR) as the BL-common SE equipment. The niobium furnace is available in vacuum and in rare gas. Until last year, only argon gas was available as rare gas. In this year, we improved the system and helium gas is available for high temperature experiments. The maximum temperature is 800°C under rare gas atmosphere and is 1600°C in vacuum. The sample rotation controller has been upgraded and the sample rotation can be controlled easily with a touch panel. The improved furnace sys-tem was used on BL14 for users' experiment in JFY2015. The furnace for SANS and NR was installed as the second BL-common furnace and operated on BL15 up to 800°C in February, 2016 (Fig. 2).

4. A pulse magnet system

The activities of the SE pulsed magnet team started in the second half of JFY2014. We have developed a prototype of a pulse magnet system in J-PARC MLF. The pulse magnet system consists of a pulsed power supply, a solenoid coil and a sample stick. The coil is installed in the sample stick and is connected with the power supply through a coaxial cable. Figures. 3 (a) and (b) show the developed sample stick and coil, respectively. The stick is to be installed in the orange cryostats. The pulse test had been performed on the coil. In the experiment, the coil was cooled to 77 K by liquid nitrogen. When

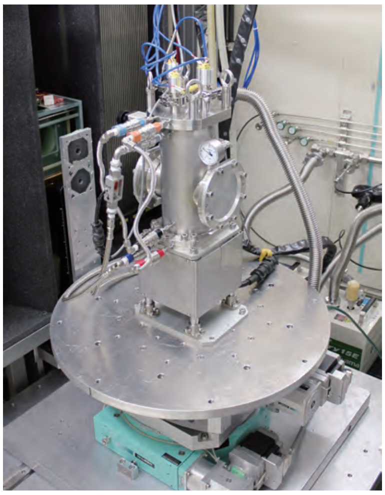

Figure 2. New furnace used on BL15.

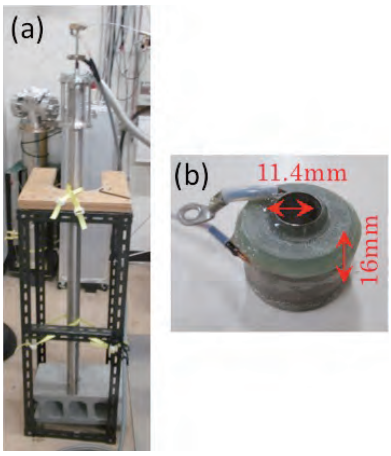

Figure 3. (a) The developed sample stick and (b) the coil.

the maximum charged voltage in the capacitors of the pulsed power supply was 1.4 kV, output current of approximately 4.5 kA in the coil was obtained. Linear B-I characteristics of the coil were obtained up to 30 Tesla. The system is to be employed to perform neutron scattering experiments in the MLF in the near future.

5. High pressure

We introduced the VX-6 type Paris-Edinburgh (PE) press as the first BL-common equipment to comply with users' requests. In this FY, we have started its commissioning at room temperature. It was confirmed that the pressurization was carried out successfully and safely within the range of specification. The jig stands for mounting the PE press to goniometer stage of BL11 and BL15 were also prepared (Fig. 4). We have started the design of the cryostat for cooling the PE press in order to realize a low temperature and high pressure environment. It is planned to be introduced in the next FY.

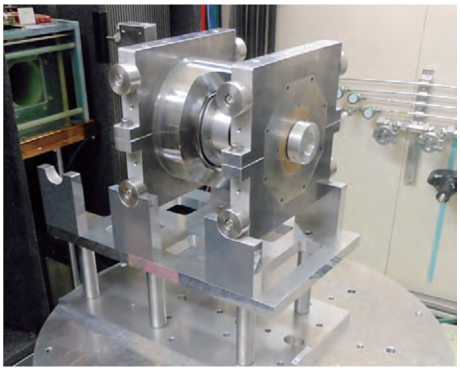

Figure 4. PE press mounted on the goniometer stage of BL15.

6. Soft-matter

A rheometer is the most powerful tool for the study of the viscoelasticity behavior of soft matter, such as polymer solutions, gels, and liquid crystals. As shown in Fig. 5, the rheometer (MCR302), purchased from Anton Paar, and a box capable of preventing condensation were installed for Rheo-SANS experiments on BL15 in JFY2015. The system can operate in the temperature range from 223 K to 423 K with vaporizer system using liquid nitrogen.

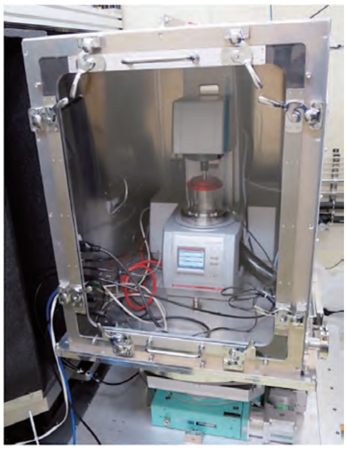

Figure 5. The rheometer and its box on the goniometer stage of BL15.

T. Aso[1], Y. Yamauchi[2], M. Ishikado[3], S. Ohira-Kawamura[4], M. Watanabe[2], K. Munakata[3], S. Takata[4], Y. Sakaguchi[3], K. Ohuchi[3], M. Obinata[3], R. Takahashi[5], S. Isomae[5], and T. Oku[2]

[1]*Neutron Source Section, Materials and Life Science Division, J-PARC Center;* [2]*Technology Development Section, Materials and Life Science Division;* [3]*Neutron R&D Division, CROSS-Tokai;* [4]*Neutron Science Section, Materials and Life Science Division, J-PARC Center;* [5]*Nippon Advanced Technology co.*

Progress of Data Analysis Software

1. Progress in FY2015

We will report our work in several fields: the improvement of the NeXus [1] interface prepared in Manyo Library [2, 3] between data-containers and NeXus files, the publication of User's Manual of Manyo Library and the production of the Utsusemi binary package installer.

2. Manyo Library

Our basic concept of maintaining the analysis environment for neutron scattering experiments in MLF is to provide a framework, which has common and generic analysis functionalities for that type of experiments. The framework, "Manyo Library" (ML), is a standard framework for developing data analysis software, which has been installed on the 16 instruments in MLF. ML is a high-performance C++ framework and class library designed to handle large amounts of data. The class library is wrapped by the Python user interface created by SWIG. Users can perform data reduction and analysis on the C++ library through the Python interface. The framework is available on various operating systems: Linux, MacOSX and Windows. The binary installer and packages have also been prepared.

"ElementContainer"(EC) is a simple and fundamental data container in ML, and a one-dimensional histogram where the error values can be stored in an EC, where any number of vector<double> objects are handled with their names. Basic mathematical arithmetic-operators and statistical operators provided in ML can operate ECs with error-propagation. Data containers for two- and three-dimensional histograms, "ElementContainerArray" (ECA) and "ElementContainerMatrix" (ECM), are prepared, and raw data and analysis data are stored in the EC family on ML. Figure 1 shows the structure of ECM. The number of vector objects in an EC is Nv. Any number of EC and ECA objects can be stored in an ECA and ECM, and the number of EC and ECA in a container is N_{EC} and N_{ECA}, respectively. The procedures for memory allocations and their garbage collections have been prepared in the containers. Users can build data analysis software in Python environment by using the operators prepared in the C++ library; ML provides a rapid prototyping environment for data analysis software.

3. New Binary File Format

The size of data files handled on ML is getting larger with increasing the intensity of proton beams producing pulsed neutron beams in MLF. Currently, our concern is how to improve the efficiency of reading and writing data files on the framework. Histogram data stored in containers can be stored in NeXus format by using NeXus C-API on ML. The NeXus format is a standard format in many neutron, X-ray and muon facilities in the world and can be read by any operating system. A new interface between the EC family and NeXus files was developed by using the HDF5 C-API library [4], and a new data file structure was also defined while preserving the NeXus format. The new data structure, where the number of groups and depth of the hierarchical structure have been decreased, will be simpler than the one used now.

We completed the prototype of the new interface in ML. The efficiency values of reading and writing three-dimensional histograms stored in ECM from/to NeXus files with the present and new interface have been obtained and shown in Table 1. The measurements were performed on Ubuntu Linux (64-bit) with an Intel Core i5-4460 3.2 GHz processor and 16 GB memory. The size of vectors stored in an EC is 4000, and the data size of the NeXus files are 4.0 and 1.3 GB at (N_v,N_{EC},N_{ECA})=(3,100,300) and (3,10000,1), respectively. The structures and dimensions of the former and latter data sets are the same as those of the three-dimensional histogram data produced by the chopper- spectrometer and the powder diffractometer in MLF. The writing and reading efficiency of the new interface is about 1.6 and 4 times larger than that of the present one.

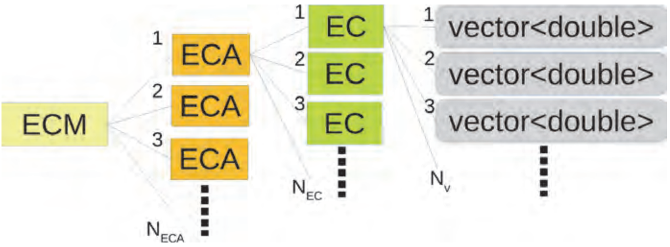

Figure 1. Structure of the EC family defined in ML. The number of vectors, EC and ECA in an EC, ECA and ECM are N_v, N_{EC} and N_{ECA}, respectively.

Table 1. Comparison between the new and present interfaces regarding the efficiency of reading and writing NeXus files from/to ECM. Tw and Tr are the writing and reading times in seconds with the interface developed in this study, and the numbers in the parentheses are those with the present interface. Nv, N_{EC} and N_{ECA} indicate the dimensions of ECM.

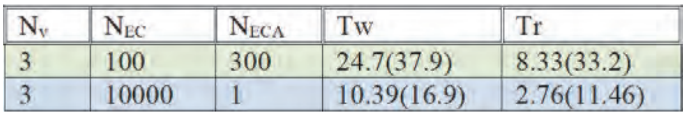

N_v	N_{EC}	N_{ECA}	Tw	Tr
3	100	300	24.7(37.9)	8.33(33.2)
3	10000	1	10.39(16.9)	2.76(11.46)

The data I/O rate on ML can be increased with the new interface, and we will develop and integrate it into ML in 2016. We also decided to keep the present interface to allow reading of the older data files in the MLF file archiver.

4. User's Manual

A User's Manual of ML in Japanese was published as a JAEA report, and can be obtained from "http://dx.doi.org/10.11484/jaea-testing-2016-001". The table of contents of the manual is shown in Table 2. An English version of the User's Manual will be completed in near future.

Table 2. Table of Contents of the User's Manual.

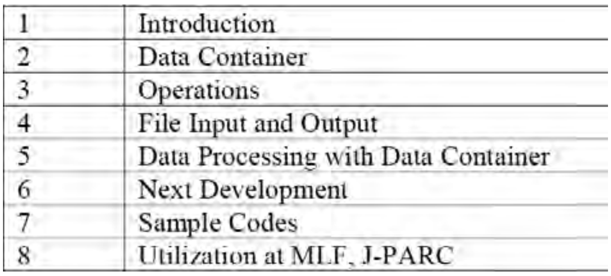

1	Introduction
2	Data Container
3	Operations
4	File Input and Output
5	Data Processing with Data Container
6	Next Development
7	Sample Codes
8	Utilization at MLF, J-PARC

5. Utsusemi and Binary-Packaging

ML is widely utilized as a base architecture in data treatment and analysis of actual measurements in MLF at J–PARC. One of the applications of ML to data analysis and visualization is the 'Utsusemi' software [5].

Utsusemi is the series of software written in C++, based on the ML framework and Python, to analyze and visualize the neutron scattering data with a graphical interface (GUI). Utsusemi has been adopted extensively by a lot of instruments and users in MLF because it offers useful functions, for example a flexible histogram creation from event recorded data, produced by the common data acquisition system in MLF.

However, the general users have difficulties installing and using Utsuemi, including ML, on their own PCs, because the software and the codes run only on the Linux OS. This means that the users must construct a Linux environment before using our software. Such a complex installation hinders users' ability to analyze data at their offices and to prepare quickly their results' output.

To solve this problem, we have produced a binary application and installer software executable on Windows and Mac OS, as shown in Figures 2 and 3. The binary installers are easy to use because they conform with the rules for each OS and include all binary applications of both ML and Utsusemi with the required software libraries. They work on 64-bit Windows 7, 8.2 and 10 or Mac OS 10.10 (Yosemite) and 10.11 (El Capitan).

After the installation, the users can launch several GUI applications by double clicks and run many functional codes with command-line interface (CUI). The main GUI application, called 'SequenceEditor', enables the users to execute step-by-step commands for data reduction with Utsusemi. Also installed are some visualization software applications with GUI, such as 1 or 2-dimension plotters and data-slice software for a single crystal sample. In addition, CUI on Python Interpreter to handle functions is also available by using the command prompt application on Windows or the terminal application on Mac OS. So, the installed software environment with SequenceEditor as central software is the same as the one used on the actual instruments. Therefore, users can not only start analysis without confusion but also execute users' own analysis scripts, if needed.

Although these binary applications and installers have worked very well, only the MLF staffs and a limited number of users are able to use them because of some ongoing problems with the license. We have initiated a procedure at JAEA to make Utsusemi an open-source software for effective distribution among users.

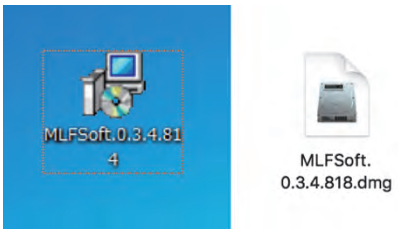

Figure 2. Binary Installers, for Windows on the left and for MacOS on the right.

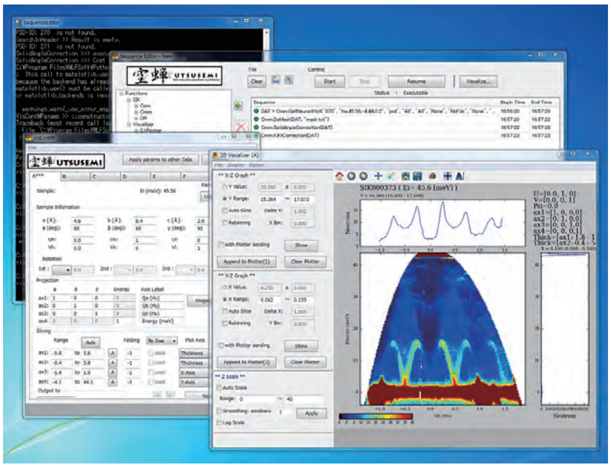

Figure 3. Screenshot of Utsusemi running on Windows 7.

6. Future Plans

As shown above, our data analysis software has been steadily developed to reach a high degree of perfection. On the other hand, we know that our distribution of information, especially the documentation concerning our work, is still insufficient. Therefore, we continue to produce documents and have a plan to prepare immediately a portal web site. On that site, we will show the information about our software, including the ML User's Manual and provide binary software to be downloaded by users. The site will be launched in FY 2016.

References

[1] http://www.nexusformat.org/

[2] Jiro Suzuki *et al.*, Nucl. Instr. and Meth. A 534, 175 (2004).

[3] Jiro Suzuki *et al.*, Nucl. Instr. and Meth. A 600, 123 (2009).

[4] https://www.hdfgroup.org/

[5] Y. Inamura, T . Nakatani, J. Suzuki and T. Otomo, J. Phys. Soc. Jpn. 82 (2013), SA031-1 – SA031-9.

J. Suzuki[1,2], Y. Inamura[3], T. Ito[4], and T. Nakatani[3]

[1]*Computing Research Center, KEK;* [2]*Information System Section, J-PARC Center;* [3]*Neutron Science Section, Materials and Life Science Division, J-PARC Center;* [4]*Neutron R&D Division, CROSS-Tokai*

High-Pressure Operation of Two-Dimensional Gaseous Neutron Detector

1. Introduction

In a two-dimensional gas-based neutron detector, the thickness of the conversion gap should be made as small as possible to prevent the occurrence of the parallax effect of incident neutrons. Therefore, it is necessary to increase the gas pressure of the detector to achieve high detection efficiency. However, increasing the gas pressure decreases the output signal strength. To measure the small output signals, the supply voltage must be increased to boost the gas gain of the detector element. Therefore, we have developed a pressure vessel and a dedicated two-dimensional multiwire-type detector element for individual signal line readout to ensure satisfactory detector system operation even at high pressure.

2. Developed system and irradiation tests

A developed neutron detection system consists of a 256-channel detector element (x: 128 lines, y: 128 lines) equipped into a pressure vessel, amplifier-shaper-discriminator boards, optical signal transmission devices, position encoders, and a fast data-acquisition device. The specially-fabricated pressure vessel has 256 feedthroughs, insulated by alumina ceramics, for signals and 6 connectors for high voltage. The vessel could withstand pressures of up to 0.8 MPa. A dedicated detector element with 256 output connectors was also fabricated for use in the pressure vessel. Experiments were performed using a gaseous mixture of He and carbon tetrafluoride (CF_4) at a total pressure of 0.8 MPa ($He/CF_4 = 0.71/0.09$). Under this gas condition, the thermal neutron detection efficiency was 87%. Neutron irradiation was performed by using a Cf-252 neutron source.

3. Results

Figure 1 shows the pulse-height distributions under neutron irradiation by changing the supplied voltage to anode wires. A signal-pulse peak of neutrons can be observed clearly. This result indicates that the majority of the spurious events generated in the lower channels as a result of electronic noise and gamma events can be easily suppressed using a discriminator. A flat-field image and the histogram of the pixel contents of the flat-field image are shown in Fig. 2. The histogram was evaluated by fitting it with a Gaussian function. The image showed good homogeneity, and the average pixel count was 262, with a standard deviation of $\sigma = 20.3$, corresponding to an average gain spread of approximately 7.7%. The measured gamma-ray sensitivity of the detector was 1.1×10^{-7} by using a Co-60 gamma-ray source with the intensity of 7.0×10^5 Bq.

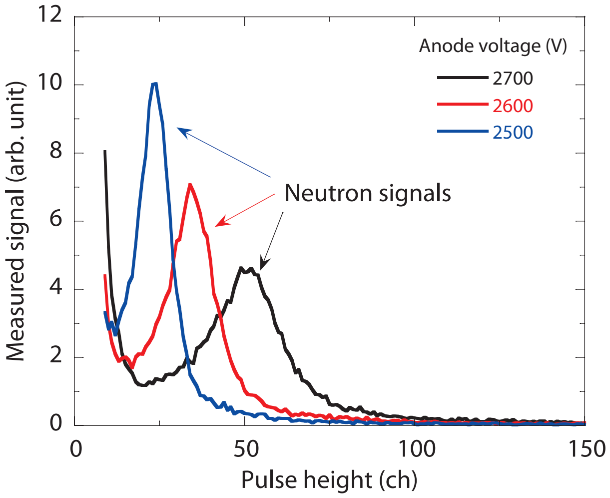

Figure 1. Pulse-height distribution of anode lines.

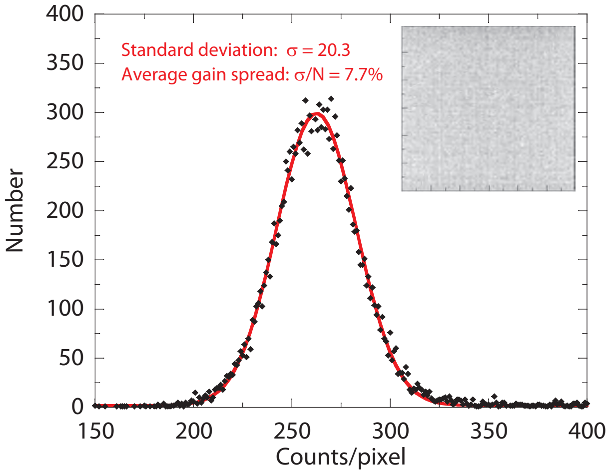

Figure 2. Histogram of count distribution of the flat-field image and measured flat-field image under Cf-252 neutron irradiation.

K. Toh[1], T. Nakamura[1], K. Sakasai[1], and H. Yamagishi[2]
[1]*Neutron Instrumentation Section, Materials and Life Science Division, J-PARC center;* [2]*Nippon Advanced Technology*

Accessible Length Scale of the In-Plane Structure in Polarized Neutron Off-Specular Scattering Measurement

1. Introduction

Layered magnetic structures exhibit interesting and important magnetic properties, such as exchange coupling between layers, giant magnetoresistance, and tunnel magnetoresistance, which are not present in the bulk. These anomalous magnetic behaviors arise from the structure in the out-of-plane and/or in-plane directions reduced to the nm range. To elucidate those mechanisms and to open the possibility of new applications, it is important to obtain information on the in-plane magnetic structure. Off-specular scattering (OSS) using polarized neutrons is a unique and powerful technique to observe correlations of small magnetic objects in layered systems. Since the OSS has its own accessible range and resolution of the lateral component of the momentum transfer $\boldsymbol{q}$, it is important to verify, if the length scale of the in-plane structure of the sample matches the in-plane $\boldsymbol{q}$-range and resolution. The in-plane $\boldsymbol{q}$-resolution corresponds to the in-plane component of the coherence volume or, in other words, the length scale of the measurement,. The interpretation of the data can be different, if the lateral dimension of the in-plane structure of the sample is sufficiently small or large compared with the in-plane component of the coherence volume in that dimension. OSS only measures a limited range of the in-plane component of $\boldsymbol{q}$ due to the restriction in the scattering geometry, making difficult the access to the lateral correlation length smaller than 100 nm. This study discusses the accessible in-plane $\boldsymbol{q}$-range of the OSS using polarized neutrons to illustrate the limitation of the accessible lateral correlation length of the OSS.

2. Results

Let us assume a scattering geometry where sample surface is parallel to the (x, y) plane and neutrons incident on the sample are scattered within the (x, z) plane [1]. The OSS data can be analyzed in the framework of the distorted wave Born approximation given by Toperverg et al [2]. The lateral correlation length for the magnetic scattering ξ, corresponding to the length of an area, in which the spins are aligned to the same direction, can be determined by the scattering intensity dependence on q_x. Since $\boldsymbol{q}$ is oriented close to parallel to the z-axis in the OSS, q_x is smaller than a few percent of $|\boldsymbol{q}|$ for most cases. Although the q_x-range can be increased by increasing q_z, this causes another problem - reduction of the scattering intensity. In general, it is difficult to obtain enough scattering intensity over the full q_x-range for $q_z > 0.5$ nm^{-1}. This limits the accessible q_x-range to $|q_x| < 0.01$ nm^{-1}. To understand this, let us consider the q_x-dependence of the structure factor in the simulation. Since the coupled areas with uniform orientation of the spins are modeled as rectangular boxes with lengths of 2ξ within the plane, the structure factor is found to be proportional to the Lorentzian function, $1/\{1+(q_x \cdot \xi)^2\}$. Figure 1 shows the structure factors proportional to the Lorentzian profiles

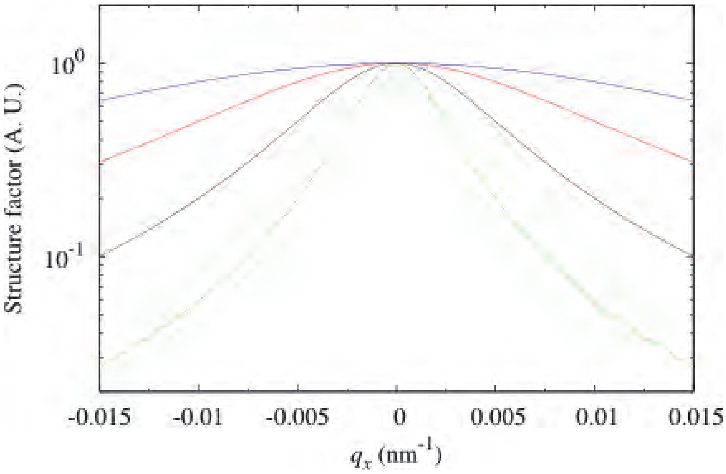

Figure 1. Structure factors proportional to the Lorentzian function, $1/\{1+(q_x \cdot \xi)^2\}$. Green, black, red, and blue lines indicate the profile with ξ = 400, 200, 100, and 50 nm, respectively.

for different values of ξ. The full width at half maximum of the Lorentzian function becomes comparable to the accessible q_x-range with decreasing ξ. This means that only a small part of the full peak profile is measured, making the determination of ξ more ambiguous. The condition of $q_{x,\max} \cdot \xi \gg 1$ needs to be taken into account when performing the OSS measurement, where $q_{x,\max}$ is the maximum value of $|q_x|$ in the measurement [3].

3. Conclusions

We discussed the accessible range of the in-plane component of $\boldsymbol{q}$ and the relation between the in-plane component of the coherence volume and length scale of the in-plane structure of the sample for the OSS measurement using polarized neutrons. To determine accurately ξ, the condition of $q_{x,\max} \cdot \xi \gg 1$ has to be satisfied, which usually corresponds to $\xi > 100$ nm. Grazing incidence small angle scattering measurement is needed to obtain qualitative information on the in-plane structure with a length scale smaller than that.

References

[1] R. Maruyama, T. Bigault, A. R. Wildes, C. D. Dewhurst, K. Soyama, and P. Courtois, Nucl. Instr. and Meth. Phys. Res. A819 37 (2016).

[2] B. P. Toperverg, Appl. Phys. A74 (Suppl.) S1560 (2002).

[3] R. Maruyama, T. Bigault, A. R. Wildes, C. D. Dewhurst, T. Saerbeck, D. Honecker, D. Yamazaki, K. Soyama, and P. Courtois, submitted to J. Phys.Conf. Series, (Proceedings of PNCMI 2016).

R. Maruyama
Neutron Instrumentation Section, Materials and Life Science Division, J-PARC Center

Muon Scinece

Status of J-PARC MUSE

Because of the fire caused by the power supply for the septum magnet at the muon D-line on January 16, 2015, we had to stop all operations of J-PARC for one and a half months. Thanks to the tremendous efforts by the members of the J-PARC task force, it became possible to restart the neutrino and neutron operations in the end of February, 2015. Although we were about to restart the muon experiments in the end of April, we faced another problem due to a water leakage from the neutron target. This shortened the period of the MLF beam time in October, 2015, but unfortunately, we had a third problem with the neutron target in November. Finally, we managed to restart the MLF operation in the end of February, 2016. Since MLF had to adopt the No.2 neutron target which cannot accept beams with power higher than 300 kW, the proton intensity was restricted to be less than 200 kW.

1. A new superconducting decay muon solenoid at the D-Line

For Phase 1, one graphite target was installed, from which four sets of the secondary lines were designed to be extracted and extended into two experimental halls (toward the west wing, one decay-surface muon line, the D-line and one ultra slow muon line, the U-line, and towards the east wing surface muon line, the S-line, and possibly one high-momentum muon line, the H-line). In the beginning, we managed to install the D-line, a superconducting decay/surface channel with a modest-acceptance (about 40 mSr) pion injector. The D-line was originally constructed with the re-used superconducting magnet that had been utilized at KEK-MSL for more than 30 years, which had cold bore (inner bore radius of ϕ 12), with beam windows at the inlet and outlet. In the summer shutdown period of 2015, we replaced the re-used superconducting magnet with a new one that has warm bore (inner bore radius of ϕ 20), without a beam window, with the purpose to extract lower momentum intense negative muons, which otherwise are stopped at the beam windows. Details of the beam commissioning results will be introduced on another occasion.

2. S-line

On October 29, 2015, we extracted successfully at the S-line surface muons with a momentum of 28 MeV/c. Figure 1 shows the extracted positron and muon beams signals, exhibiting the double-bunched pulse structure observed by using a thin scintillating counter situated at the beam extraction window at the S1 area. The beamline commissioning was further accelerated by installing a μ SR spectrometer, which was fabricated for the element strategy research project for electron materials. The automatic tuning program, called ForTune, can tell the beamline parameters to provide a well-focused muon beam at the sample position by gathering μ-e decay events, which are counted by Kalliope μ SR detectors assembled in the spectrometer.

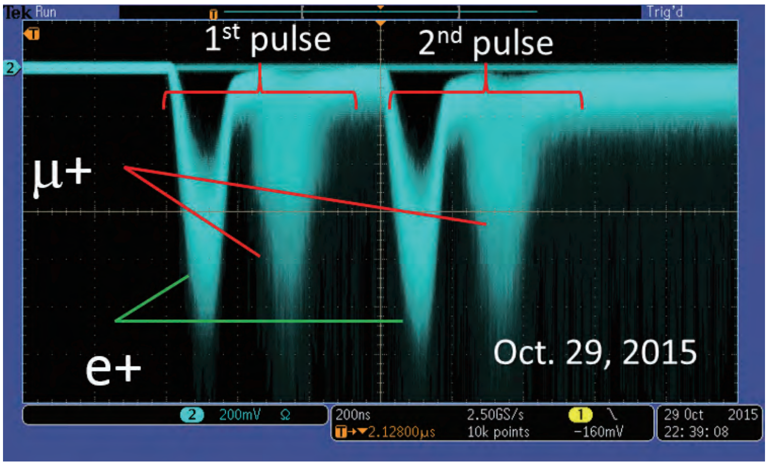

Figure 1. The extracted positron and muon beams signals, exhibiting the double-bunched pulse structure observed by using a thin scintillating counter situated at the beam extraction window in S1.

3. U-Line

At the U-line, we have successfully observed ultra-slow muons on February 21, 2016, as shown in Fig. 2. As many as 35 ultra-slow muons per second by laser resonant ionization of muoniums evolved from hot tungsten (2000 K) were experimentally detected by a MCP, a number, which is higher than the one detected by the devices developed by KEK and RAL (20 μ^+/s) at the RIKEN/RAL. In addition to reaching the highest intensity in the world, it is expected that with the quality improvement of the pulsed laser, we can achieve an ultra-slow muon beam with narrower energy width, which has the potential to improve the depth resolution in the sample. After further enhancement of the laser power (Lyman-α 1.7 μJ/pulse to 71 μJ/pulse and 355 nm laser ~100 μJ/pulse/cm^2 to 350 μJ/pulse/cm^2) and improving the transmission efficiency of the ultra-slow muon, we expect to generate a much more intense ultra-slow muon beam at the experimental ports to pioneer new techniques, which will allow the muon science to be expanded into a variety of new nano-scientific fields.

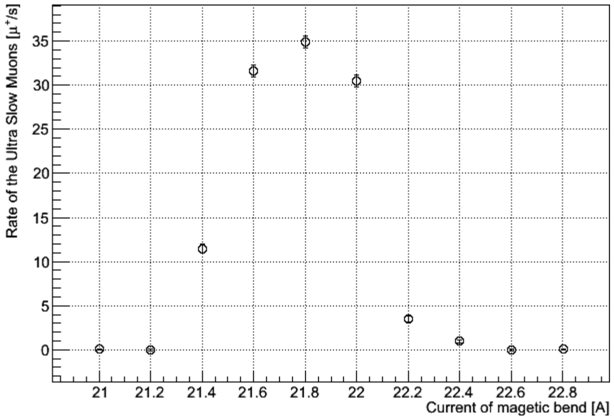

Figure 2. Rate of the ultra-slow muons with current of magnetic bending (mass separating) magnet.

Y. Miyake[1,2], N. Kawamura[1,2], K. Shimomura[1,2], P. Strasser[1,2], A. Koda[1,2], Y. Ikedo[1,2], H. Fujimori[1,2], S. Makimura[1,2], Y. Kobayashi[1,2], J. Nakamura[1,2], H. Ooishi[1,2], K. M. Kojima[1,2], R. Kadono[1,2], W. Higemoto[2,3], and T. U. Ito[2,3]

[1]*Muon Science Laboratory, High Energy Accelerator Research Organization (KEK);* [2]*Muon Science Section, Materials and Life Science Division, J-PARC center;* [3]*Advanced Science Research Center, Japan Atomic Energy Agency (JAEA)*

Muon Target System - Renovation of a Scraper Unit

A variety of materials and life science research has been carried out with the pulsed muon beams with the world's highest intensity, generated using the pulsed proton beams from the accelerator (3 GeV, 25 Hz, 333 μA) at J-PARC. A rotating target made of an isotropic graphite for muon generation is located in the proton beam line between the 3-GeV Rapid Cycle Synchrotron (RCS) and a neutron target. In the summer maintenance period of 2014, the spent fixed target was replaced with the rotating target [1]. This rotating target is running in full working order with beam power of 0.5 MW.

Two scrapers made of oxygen-free copper, used for stopping scattered components of the proton beam, are placed at the downstream of the muon rotating target in series. The upstream scraper is called scraper No. 1, hereinafter referred to as SC. The approximate dimensions of the SC are 300 mm width, 700 mm height, and 700 mm length in the direction of the beam axis. Circular through-hole of the inlet with diameter 74 mm has been drilled in the SC with a beam axis as the center. The radius of the hole is increasing toward the beam downstream. The heat load on the SC, due to scattering of the proton beam on the target, is about 19 kW in the 1-MW beam power operation. This heat is removed with two cooling water lines. The cooling water pipes are embedded in the SC with a hot isostatic press method to avoid thermal resistance on the interface of the bonding. K-type thermocouples, enclosed in stainless steel sheathes, are mounted on the upstream and side surfaces of the SC to measure the temperature of the SC. The temperatures with thermocouples mounted on the upper and lower sides of the upstream surface of the SC and the temperatures at the inlet and outlet of the cooling water flowing through the SC are all shown in Table 1 in the case of the fixed and the rotating targets.

Table 1. Temperatures of SC at 0.3 MW (°C).

(°C)	Upper	Lower	Side	Water inlet	Water outlet
Fixed target	45	32	28	22.4	23.6
Rotating target	73	41	26	19.4	21.1

Temperatures after the updates to the rotating target, especially the upper one, were higher than the ones before the updates. The temperature differences inside the SC must be less than 100°C, so that the thermal stress does not exceed the elastic limit of a copper. If the temperatures measured with the thermocouples are correct, the beam power for the SC could be increased to 0.6 MW. The beam losses of the fixed and the rotating targets should be the same since both targets have the same thickness (2 cm). Therefore, the scattered components of the proton beam do not contribute to the temperature rise. Then, we evaluated carefully the reason why the temperatures of the SC when the rotating target was used were higher than those in the case of the fixed target. When using the fixed target, the copper jacket jointed to the graphite is cooled directly with the cooling water. On the other hand, the rotating target is cooled only by thermal radiation. Then, the temperature of the rotating target is higher than that of the fixed target. A halo monitor for measuring scattered components of the proton beam is mounted on the upstream surface of the SC, as shown in Fig. 1. To avoid charge-up of the signal cables of the halo-monitor, a cover is located, facing the rotating target. The temperature of the cover is increased by thermal radiation from the rotating target. The heat of the cover is hardly dissipated because it is in vacuum. Therefore, the halo monitor cover is hot during the beam irradiation. The thermal radiation from the hot cover raises the temperature of the thermocouples. Because the temperatures are utilized for interlocks to protect the SC, it is decided to replace the SC.

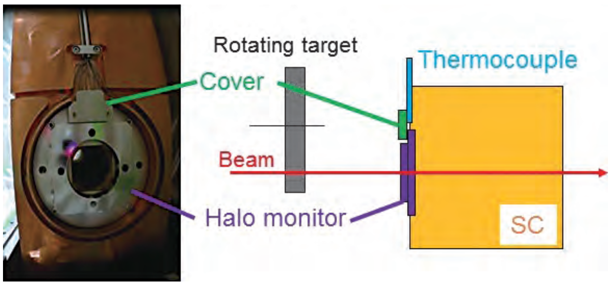

Figure 1. Picture and schematic view of the used SC.

In the summer maintenance period of 2015, we replaced the SC. This replacement work is similar to the change of the fixed target with a rotating target in 2014. A halo monitor was not installed in the newly-manufactured SC. Thermocouples were attached behind the boring structure, as shown in Fig. 2, so that thermocouples do not receive direct thermal radiation from the rotating target.

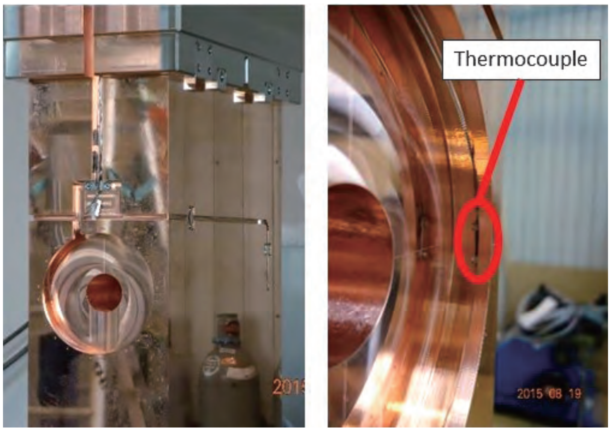

Figure 2. Pictures of the new SC (left) and enlarged view near the thermocouple (right).

The evaluation of the induced radioactivity, generated by the beam irradiation, has been carried out with a Monte Carlo code PHITS version 2.76 and an induced radioactivity calculation code DCHAIN-SP [2]. We evaluated the accumulated radioactivity in the SC, and then measures were taken to reduce the radiation dose on the surface of the cask storing the SC to reduce the radiation exposure of workers during the transportation of the SC. Table 2 shows the induced radioactivity of the SC after 14 cooling days, followed by irradiation with a proton beam at 0.3 MW for 10 years, including the safety margin. The total radioactivity, which is the sum of all of the radionuclides was about 20 TBq. Shielding of the cask with an iron wall with a thickness of 20 cm has been calculated for this radioactivity with PHITS. The estimated dose rate at the surface of the cask was 0.43 mSv/h and is not too high for the work.

Table 2. Induced radioactivity of the SC at 0.3-MW operation.

no.	nuclide	[Bq]	[%]	γ-ray energy	half life
1	Co 58	3.85E+12	19.25	811keV	71d
2	Co 60	3.13E+12	15.67	1332keV 1173keV	5.3y
3	H 3	2.36E+12	11.81		12y
4	Co 57	2.26E+12	11.29	122keV	272d
5	Ni 63	2.11E+12	10.54	beta17keV	100y
6	Fe 55	1.31E+12	6.56	5.9keV	2.7y
7	Mn 54	1.22E+12	6.08	835keV	312d
8	Cr 51	7.70E+11	3.85	320keV	28d
9	V 49	6.08E+11	3.04	4.5keV	330d
10	Co 56	5.87E+11	2.94	847keV 1238keV	77d

In July and August of 2015, the cooling water pipes, electrical wires, the vertical drive mechanism unit and the vacuum flange were removed, and a cask base for the cask installation was mounted over the SC assembly. The new SC and vacuum storage container (made by MIRAPRO Co., Ltd.) were delivered on August 25. The vacuum storage container for storing the used SC was installed in the temporary storage. On September 3, the cask was mounted on the cask base and the used SC was pulled out from the proton beam line using a crane in the cask by remote control. The SC was stored in the vacuum storage container with a shielding in the temporary storage. The radiation dose rate of the used SC was 1.5 Sv/h at a distance of 7 cm from the SC surface. The radiation dose rate at the cask surface was 0.15 mSv/h. It was estimated that the residual radioactivity of the SC was around 7 TBq from comparison with calculations with PHITS and DCHAIN-SP. The difference between the original estimate (20 TBq) and the measured values (7 TBq) was primarily due to the fact that the excessively setting the beam irradiation period on the safe side in the calculation with PHITS. The new SC with the cask was introduced into the proton beam line on September 8.

The removal of the cask and the cask base, the restoration of the cooling water pipes and electrical wires, vacuum pumping (ultimate vacuum: $3*10^{-5}$ Pa or less) and the interlock test were completed by the end of October. As of 2016, the new SC is running smoothly in the 0.2-MW operation. The measured temperature of the new SC at 0.5-MW operation in the second half of 2015 was 42°C, which is close to the design value. It was confirmed that the temperature measurement of the new SC was suitable even at 2-MW operations.

If the halo monitor is removed, the used SC can be used as a spare SC. We are planning to remove the halo monitor by remote control after the next fiscal year.

[1] S. Makimura *et al.,* Development of Muon Rotating Target at J-PARC/MUSE, Journal of Radioanalytical and Nuclear Chemistry **305** (2015) 811-815.

[2] T. Sato *et al*., Particle and Heavy Ion Transport Code System PHITS, Version 2.52, J. Nucl. Sci. Technol. 50:9, 913-923 (2013).

S. Matoba[1, 2], S. Makimura[1,2], N. Kawamura[1,2], Y. Matsuzawa[1, 3], and M. Tabe[1, 4]

[1]Muon Science Section, Materials and Life Science Division, J-PARC; [2]Muon Science Laboratory, High Energy Accelerator Research Organization (KEK); [3]Nippon Advanced Technology Co., LTD (NAT); [4]Seekel Co., LTD

Development of a Kicker System and Safety Measures for the Septum Power Supply at D-line

1. Introduction

Kicker and the following septum are used at the D-line to separate a double pulse muon beam into two single pulses and feed them simultaneously to two experimental areas (D1, D2). However, the kicker noise associated with the ignition of the kicker power supply has been affecting adversely the nearby particle detectors. A saturable inductor was installed at the output of the pulse forming network, and was tested whether it could eliminate the noise.

As for the septum power supply, a small-size auxiliary transformer was newly added in the winter of 2015 to feed a low current for lower energy muons. However, the transformer (AC 420 V to 38 V) was burned during the first commissioning of the low-output current mode operation when the AC 420 V was turned on at the main breaker. After the accident, a review committee was organized to investigate its cause and to consider the necessary safety measures.

2. Kicker System

2.1 Saturable Inductor

The kicker noise source is the surge voltage at about 10 MHz that occurs with the ignition of the thyratron to discharge the charged Pulse Forming Network (PFN). Alternatively, a saturable inductor (SI) was considered to eliminate the surge without delaying the rise-time. The SI is made of saturable ferrite cores, and has the ability to work as a large inductance at the onset of the surge voltage/current. Subsequently, the inductance decreases sharply due to saturation of the ferrite as the current increases. In the circuit simulation code, SPICE, the SI can be modeled as

$$L_{sat}(I) = L_0 (Ae^{-\alpha|I|} + 1),$$

where L_0 is the air-core inductance and I the current. Two kinds of ferrite were tested and their characteristics are summarized in Table 1. The present parameters are optimized for the initial charging voltage of PFN at 20 kV. The diagram of the kicker system with the SI is shown in Fig. 1.

Table 1. Parameters of the saturable inductors optimized for 20 kV operation.

Type	A	α	Bandwidth	Power loss
I	29.0	0.0013	>80 MHz	12.5 W
II	189.0	0.0023	12 MHz	2.6 W

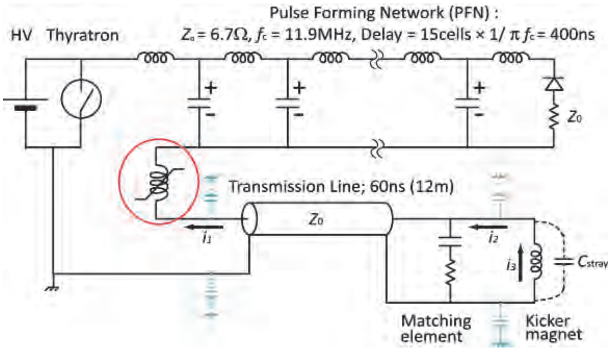

Figure 1. Kicker system with the saturable inductor.

Figure 2 shows the results of the SPICE calculations and the installed saturable inductor. It can clearly be seen that the surge current peaks due to a multiple reflection at both ends of the transmission line are eliminated, while the rising point is shifted, but the rise-time of the kicker current is unchanged. From top are shown the currents I_1, I_2 and I_3 as indicated in Fig. 1.

The saturable inductor is composed of a stack of 10 ferrite cores with 161 and 61 mm in outer and inner diameters, respectively, and 25 mm in thickness. The housing cavity is shown in Fig. 2 (right).

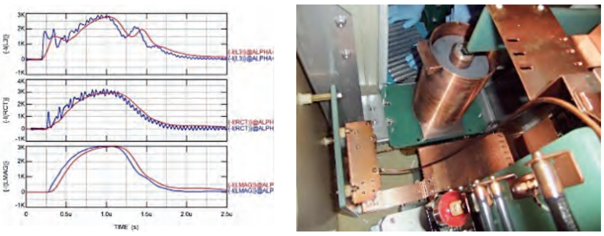

Figure 2. Analysis results with SPICE for the case with (red) and without (blue) SI, and a stack of 10 ferrite cores and its housing cavity installation.

2.2 Results and Discussion

The results obtained in this trial did not reproduce the smooth load current that was expected in the calculations. Figure 3 shows the excitation curve with/without SI. The flat top has a ringing of about 10 MHz for both cases. It was found that the frequency characteristic of the ferrite described in the manufacturer's data sheet was only valid for excitation of 10 Gauss. The actual flux density in our system, however, reaches ~1.5 T. Therefore, it could be assumed that the saturable inductor would not block the high frequency surge current.

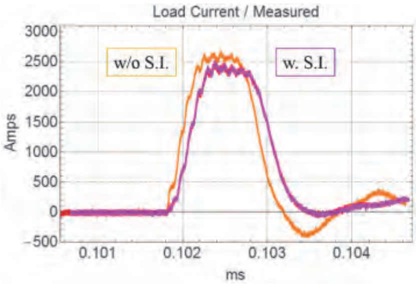

Figure 3. Kicker load current (I_2) with/without SI.

3. Safety Measures for the Septum Power Supply

3.1 Safety Measures

The power supply, modified by adding a small-size auxiliary transformer, is shown in Fig. 4. If the thermal interlock of the transformer and the switch at the secondary winding are implemented correctly, these measures would be sufficient from a safety point of view. It was found that the output current could not be stabilized by using the added transformer because of a difference in the feedback parameters between the low and high current modes. Then, the new power supply comprises two independent power supplies for high and low current modes. Their outputs are connected in parallel to the load, as shown in Fig. 5. The selection of high or low current mode is made by exclusive switching at the output. Even if the exclusive switching fails, like in the case when both switches are switched on simultaneously, a fast-blow fuse (300 A) protects the low output current power supply from damages.

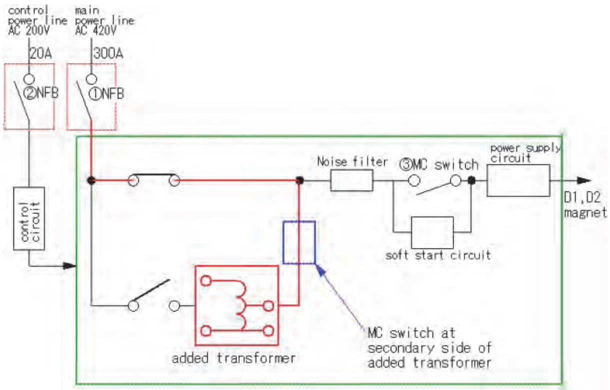

Figure 4. The AC input part of the modified power supply to include the low output current mode.

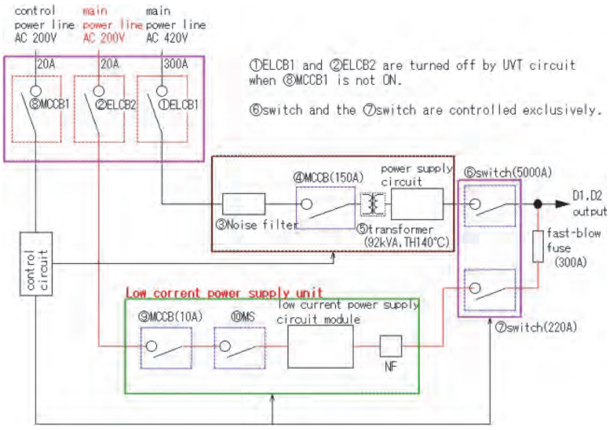

Figure 5. New design of the septum power supply. Two independent power supplies for high and low current modes are connected in parallel to the load through an exclusive switch.

3.2 Control of the two-power-supply system

A PLC (programmable logic controller) is used to control the septum power supply. For the low current power supplies, PLCs of the same series (Yokogawa FA-M3) were adopted, and they are connected through an FA-Link, as shown in Fig. 6.

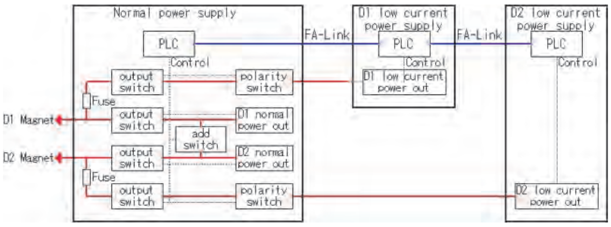

Figure 6. New control system of the septum power supply.

The typical interlock items of the septum power supply are listed in Table 2.

Table 2. Typical interlock items of the septum power supply.

Switch failure
Fuse failure
Overheat of transformer and switching transistor
MC (IC-contactor) answer back error
Output over current and voltage
Fan alarm
Low current power supply output over current and voltage
Low current power supply output fuse failure
Low current power supply over heat
Low current power supply fan alarm
PLC link error

4. Summary

A saturable inductor was installed and tested for its ability to eliminate the kicker noise upon the nearby particle detectors. It was found, however, that the saturable inductor could not block the surge current due to the insufficient frequency bandwidth. A plan to install a Low-Pass-Filter in place of the saturable inductor is in progress. As for the septum power supply, an independent power supply system was adopted to cover a wide range of output current, instead of using an auxiliary transformer.

Acknowledgements

Concerning the issue of the safety measures for the septum power supply, the authors express their gratitude to Dr. T. Takayanagi and Mr. N. Kubo from the J-PARC Accelerator division and Materials and Life Science Facility (MLF) division, respectively, for their thorough discussions at the review committee on safety and technical issues.

H. Fujimori[1], Y. Kobayashi[1], Y. Irie[1], K. Kojima[1], N. Kawamura[1], A. Koda[1], Y. Ikedo[1], S. Sakata[2], M. Meguro[2], M. Tampo[1], K. Hamada[1], N. Kurosawa[2], T. Adachi[1], P. Strasser[1], W. Higemoto[3], K. Shimomura[1], and Y. Miyake[1]

[1]*Muon Science Laboratory, High Energy Accelerator Research Organization (KEK-MUSE);* [2]*Nippon Advanced Technology Co. Ltd. (NAT);* [3]*Advanced Science Research Center, Japan Atomic Energy Agency*

The Status of U-Line

We generated successfully the Ultra Slow Muon beam for the first time at J-PARC in fiscal year 2015. This result was accomplished by many upgrades, especially improvement of the laser system and optimization of the muonium (Mu) production target.

The Ultra Slow Muon beamline at J-PARC

The Ultra Slow Muon beam, which has quite low kinetic energy, small beam size, and small time distribution, is desired to probe surface, interface, and multi-layer properties of materials. In J-PARC, a muon beamline was constructed for it [1, 2].

The layout of the Ultra Slow Muon beamline is shown in Fig. 1. Surface muons are transported to the Mu production target. A part of the muons stopped in the target evaporate as muoniums. The pulsed lasers ionize them to generate the Ultra Slow Muons. Static voltage applied to the target accelerates them up to 30 kV. A dipole magnet, electrical bends, and electrical quadruples transport them to μSR setups.

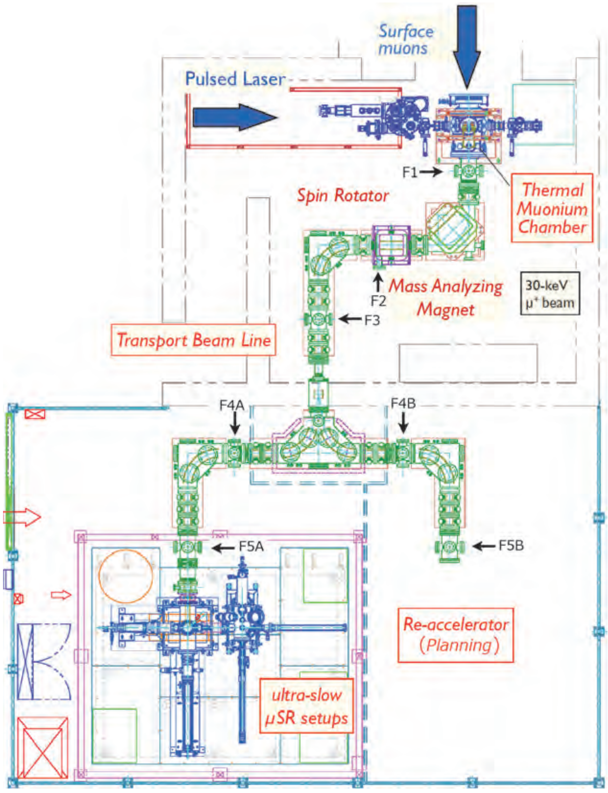

Figure 1. Layout of the Ultra Slow Muon beamline at J-PARC. The focus points in the beamline are shown as F1, F2, F3, F4A, and F5A.

The progress in fiscal year 2015

In this fiscal year, we installed the positron counters to measure the number of muons stopped around the Mu production target. By using them, we tuned the surface muon beam to the Mu production target.

By using simulation code SRIM [3], we estimated the best thickness of the muonium target, which maximizes the density of the stopping muons around the rear surface of the target. Based on the simulation, we exchanged the target from 100 μm (50 μm degrader + 50 μm target) to 75 μm (25 μm degrader + 50 μm target).

We tuned the Ultra Slow Muon beamline by using the thermal ionized Li^+ and the laser ionized H^+. The laser ionized H^+ was also used to optimize the overlap of the lasers.

After implementing these updates and improving the laser system, we generated successfully the Ultra Slow Muon beam on February 21st, 2016. As shown in Fig. 2, the time of flight (TOF) of the Ultra Slow Muon to the focusing point F3 was 0.7 μs, which agrees with the simulated TOF. The yield of the Ultra Slow Muon was below 0.01 [μ^+/s] in the beginning. By the end of March, it rose up to 7 [μ^+/s] at the focusing point F3.

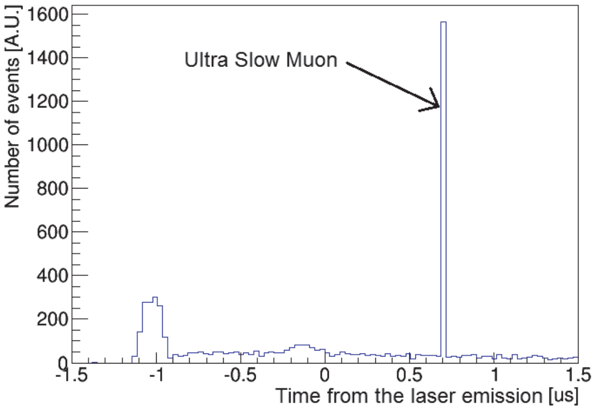

Figure 2. Time distribution of the events measured by the detector at F3. Laser emitted at 0 ns.

Laser system for Ultra Slow Muon generation

Ultra-slow muons can be generated in resonant optical ionization by simultaneous irradiation of 122.09 nm light, which is the muonium Lyman-α resonance wavelength and corresponds to the 1S-2P transition of muonium, and 355 nm light. Therefore, the high-energy coherent Lyman-α light source is a very important element for the generation of high-power ultra-slow muon.

In order to generate intense Lyman-α light, we chose a method of two-photon resonance four-wave-mixing in Krypton. A coherent 212.556 nm pulse for two-photon excitation and a tunable near-infrared pulse are required for the method. The tunable near-infrared source can tune the wavelength around 820.649 nm and 845.015 nm to generate resonant Lyman-α for a muonium and a hydrogen atom, respectively.

The output pulses at 212.556 nm and the near-infrared from all-solid-state laser and subsequent wavelength conversions were independently loosely focused and coaxially superposed in the middle of a 1-m long krypton-argon mixture gas cell to make the interaction length long and the suitable mode-matching. Kr and Ar gas mixing ratio was adjusted to satisfy the phase matching in four-waves, since the Kr gas has negative dispersion at the Lyman-α wavelength region. The calculated susceptibility of Kr and Ar is shown in Fig. 3.

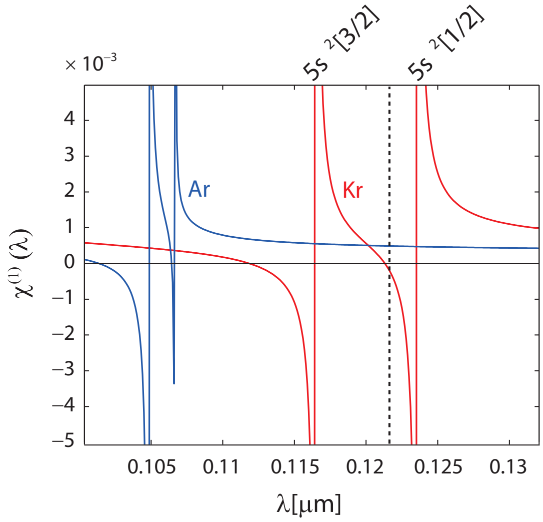

Figure 3. Calculated dispersion near the electric dipole resonances of Kr and Ar.

In our last report, the optimized mixture ratio for hydrogen Lyman-α was $P_{Ar}/P_{Kr} \approx 5$ when the maximum pulse energy was obtained [4]. However, we had problem not only with the reproducibility but also with the long-term instability, due to the gases mixing process. The Ar and Kr gases were sequentially supplied from a high-pressured gas cylinder to the gas cell. However, the process cannot produce a perfect gas mixture at the gas cell and the result is a different gas mix ratio distribution, which depends on the location of the gas cell. To overcome the problem, we introduced a gas mixer, which consists of mass flow controllers and a static-mixer, to simultaneously fill krypton and argon gases, as seen in Fig. 4. Accordingly, the optimized P_{Ar}/P_{Kr} ratio was changed to 3 for hydrogen Lyman-α. The value of the ratio is almost the same as the theoretical prediction of the phase matching condition [5]. The stability of the Lyman-α output pulse energy was also improved. The time evolution of the Lyman-α pulse energy is shown in Fig. 5. A slow variation of output energy was obtained when the gas mixer was not applied. On the other hand, a rapid increase and stable output were obtained using gas mixer.

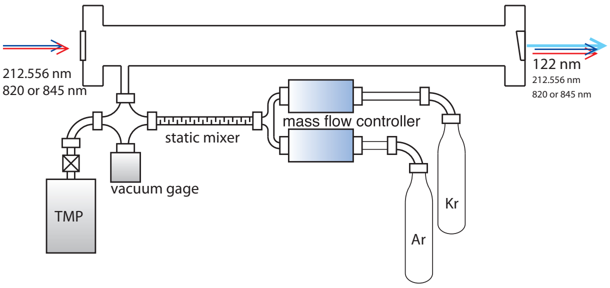

Figure 4. The newly installed Ar-Kr gas mixer and mixture gas cell for stable Lyman-α generation.

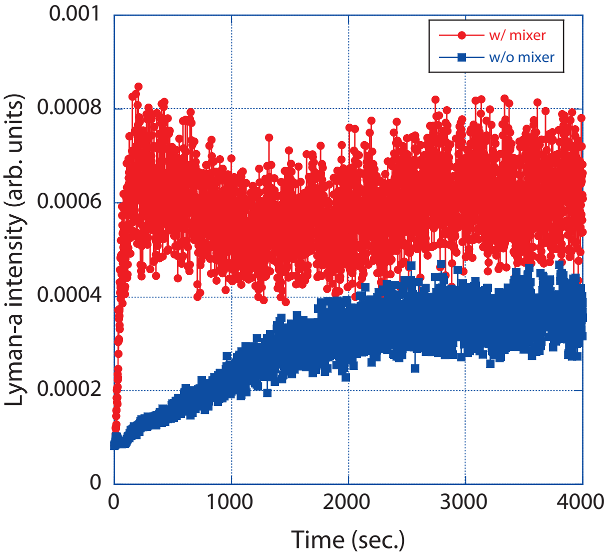

Figure 5. Time evolution of measured Lyman-α pulse energy for hydrogen without (blue plots) and with (red plots) gas mixer when the gas ratio and total pressure were fixed to $P_{Ar}/P_{Kr} \approx 3$ and 2400 Pa.

The generation of muonium Lyman-α was also carried out using the gas mixer. The optimum gas ratio of argon and krypton and the total pressure were $P_{Ar}/P_{Kr} \approx 5.5$ and 3600 Pa, respectively. Even if we use the gas mixer, the Lyman-α output decreasesafter a continuous operation over 10s hours. We are investigating the problem under the assumption that there is a contamination inside the gas cell and/or a deterioration of the gas cell windows.

In conclusion, we installed an efficient gas mixer to improve the stability of Lyman-α generation. Thus, we ensured a continuous successful operation of the laser system to generate ultra-slow muons and subsequent beam line tuning.

References

[1] P. Strasser et. al., J. Phys.: Conf. Ser. **551** 012065 (2014).
[2] T. Nagatomo et. al., JPS Conf. Proc. **2** 010102 (2014).
[3] J. F. Ziegler, http://www.srim.org/
[4] N. Saito *et al.*. *Opt. Exp.* 24 (2016) 7566-7574.
[5] O.A. Louchev *et al.*. *Phys. Rev. A* 84 (2011) 033842(1-9).

T. Adachi[1,2], Y. Oishi[1,2], W. Higemoto[2,3], Y. Ikedo[1,2], T. U. Ito[2,3], T. Iwashita[4], M. Iwasaki[5], R. Kadono[1,2], Y. Miyake[1,2], J. G. Nakamura[1,2], A. D. Pant[1,2], N. Saito[5], K. Shimomura[1,2], P. Strasser[1,2], E. Torikai[3,6], S. Wada[5], A. Yabuuchi[7], and I. Yamauchi[8]
[1]*High Energy Accelerator Research Organization (KEK);* [2]*J-PARC Center;* [3]*Japan Atomic Energy Agency (JAEA);* [4]*Nippon Advanced Technology Co., Ltd. (NAT);* [5]*RIKEN;* [6]*University of Yamanashi;* [7]*University of Kyoto;* [8]*University of Saga*

Commissioning of the Muon S-Line and the General Purpose μSR Spectrometer ARTEMIS

1. Introduction

The surface muon beamline (S-Line) in experimental hall No.1 was installed and endorsed for muon beam delivery by the facility inspection in FY2014 [1]. Beamline commissioning was resumed after a long suspension period of summer shutdown and safety inspection of the beamline magnets; at last, a muon beam was successfully delivered to the S1 area on October 29, 2015. A thin scintillating detector (50 mm in diameter, 1.5 mm in thickness) was placed at the beam extraction window (180 mm in diameter), and the beam was observed as in Fig. 1 (top panel). Utilizing the time of flight (TOF) difference between the prompt positron and muon signals, we were able to tune the beamline transmission momentum; the momentum distribution of the muon was thus obtained as in Fig. 1 (bottom panel).

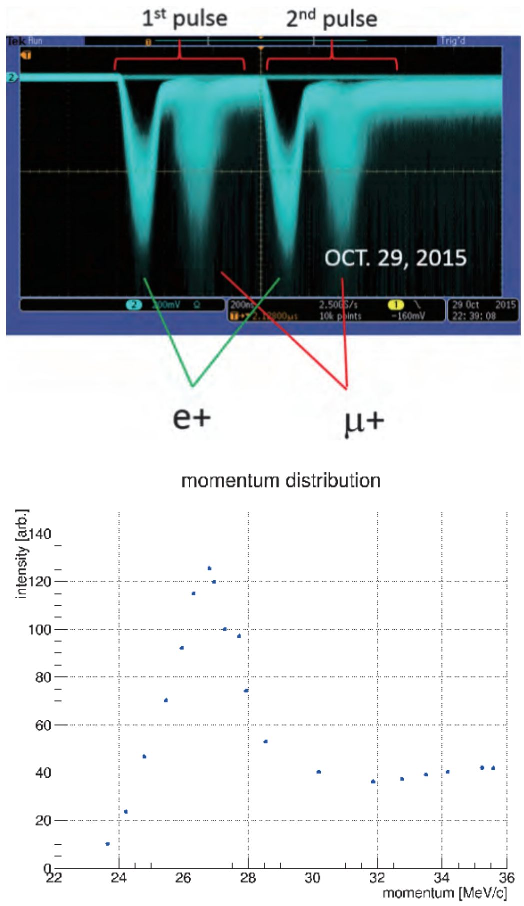

Figure 1. Top: time spectrum of the first beam at the S1 experimental area, as measured by the light output of a scintillator placed at the beam exit. Bottom: muon beam momentum distribution, as derived from TOF method.

2. Beamline tuning

The tuning process of the muon beam was accelerated by the installation of the automatic tuning program *ForTune*, which had been developed at the U-line and generalized for usage at any muon beamline described by the parameter files. The beam profile, as measured by a scintillator screen furnished with gated image-intensifier and cooled CCD camera [2], is shown in Fig. 2.

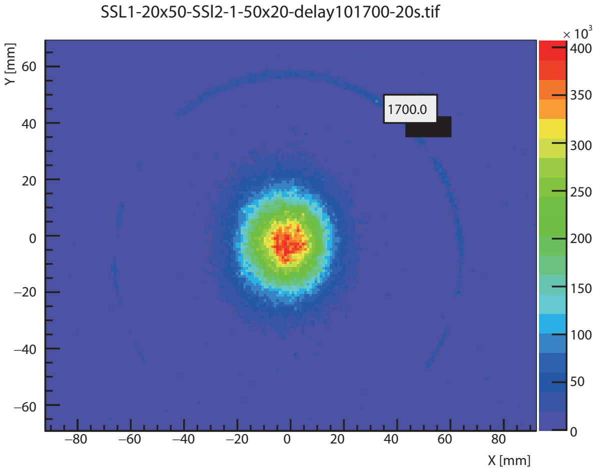

Figure 2. Muon beam profile after tuning. The spot size is ~28 mm FWHM in x and y direction.

3. ARTEMIS: General purpose μSR spectrometer

The μSR spectrometer's manufacture was sponsored by the Element Strategy grant and it had the same hardware design as the D1-μSR spectrometer, which had been used for the user programs since 2014. The 1280 channels of positron counters, covering 21.2% of the 4π solid angle, have all been constructed by the Kalliope detector system [3]. As shown in Fig. 3, the installed μSR spectrometer is equipped with a fly-past chamber, a vacuum chamber, in which the sample on a conduction-type cryostat cold head is suspended in vacuum, so that the muon flies away from the sample measurement area, if it misses the sample.

After the tuning of the beamline to maximize the rate for regular-sized sample of 16 × 16 mm, the measurement rate became approximately 40 M events/hour, which is comparable to the rate available at the similarly powered (200 kW) facility RIKEN/RAL port 2.

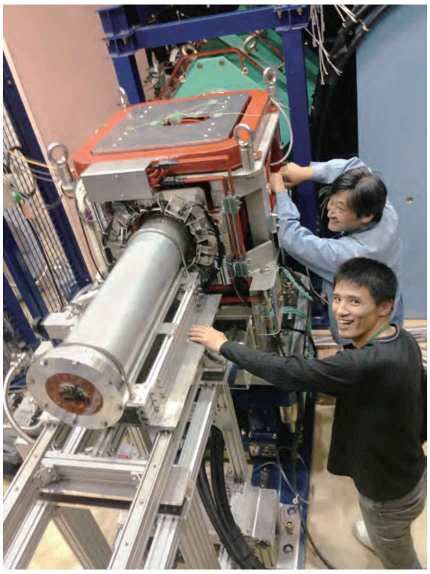

Figure 3. The S1 spectrometer with the flypast chamber installed. Drs. Koda (in blue jacket) and Hiraishi are working on sample installation to the flypast chamber.

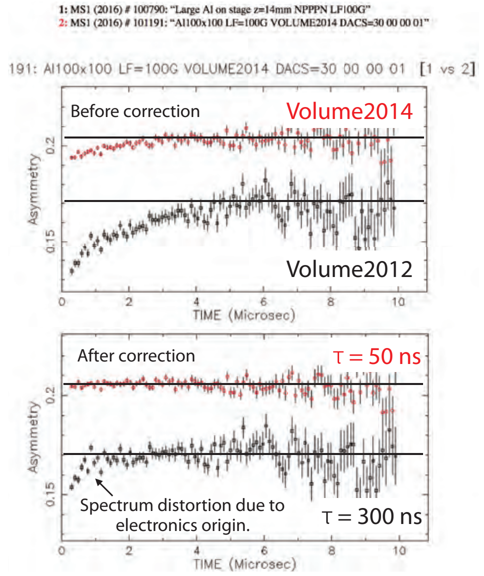

Figure 4. Comparison of the μSR time spectra between the older Volume2012 and the newer Volume2014 analog boards. The top panel is before, and the bottom after the pileup correction.

4. Upgrade of Kalliope detector system

With the previous operation of the D1-spectrometer, we know that the Kalliope detector system has a dead time of τ~300 ns, with a poor 2nd pulse detection efficiency due to a transient property (undershooting) of the analog signal. These features originate from the Volume2012 ASIC (Application Specific Integrated Circuit) used in Kalliope. With the 200 kW operation of MLF, the distortion of the pulsed μSR spectrum is not as severe, as we have experienced in the 500 kW operation in 2014. However, in preparation for the 1 MW operation in the coming years, we have developed a new ASIC called Volume2014, and installed a new analog board, which has the same input/output characteristics as the older Volume2012 design.

In Fig. 4, we compare the μSR spectrum of silver, which is supposed to be time independent. As shown in the top panel, the spectrum (asymmetry plot of the forward/backward counters along the beamline) bends down early in the process, due to the count-loss of positron events with a non-zero dead time of the detectors. The count-rate of this measurement is 200 M events/hour, which is the measurement with full-open slit setting and large enough specimen to stop the full beam. This count rate is equivalent to the regular sized specimen (16 × 16 mm) in the 1 MW operation. We corrected the count-loss using the well-known formula with the detector deadtime τ,

$$N_{corr} = N_{obs}/(1-R_{obs}\,\tau)$$

where, R_{obs} is the instantaneous count rate and N_{obs} and N_{corr} are observed and corrected counts. For Volume2012, the deadtime parameter τ~300 nsec is required to correct the count loss. For Volume2014, the parameter is improved to τ~50 nsec. What is more important is that the spectrum distortion at < 1 μsec is eliminated in Volume2014 with better transient signal properties. With the upgrade to Volume2014, the S1 μSR spectrometer is ready to be used at the 1 MW operation; we named this S1 μSR spectrometer ***ARTEMIS*** (Advanced Research Targeted Experimental Muon Instrument at S-line). It will be used for measurement of Element Strategy materials under the S1-type experiment 2013MS01.

References

[1] A. Koda *et al.*, MLF Annual report (2014).
[2] T. U. Ito *et al.*, *Nucl. Inst. Method* A, **754** (2014) 1.
[3] K. M. Kojima *et al.*, *J. Phys: Conf. Ser.*, **551** 012063, (2014).

A. Koda[1,3], P. Strasser[1,3], K. M. Kojima[1,3], Y. Nakatsugawa[1,3], T. U. Ito[2,3], M. Aoki [4], H. Lee[1,3], M. Hiraishi[1,3], H. Okabe[1,3], S. Takeshita[1,3], R. Kadono[1,3], and J-PARC Muse staff and Open-It collaboration

[1]*Muon Science Laboratory, High Energy Accelerator Research Organization(KEK);* [2]*Advanced Science Research Center,Japan Atomic Energy Agency (JAEA);* [3]*Muon Section, Materials and Life science Division, J-PARC Center*

Present Status of the H-line

A brand-new beam line, the H-line, is planned to be constructed as the 4th beam line in MUSE. The new beam line is designed to have a large acceptance, momentum tunability, and ability of kicker magnet and Wien filter use. This beam line will provide an intense beam for experiments, which require high statistics and need to occupy the experimental areas for relatively long period. Several experiments in the field of fundamental physics studies have been proposed for the H-line [2-4].

In MUSE, it is possible to extract 4 muon beam lines from the existing muon production target. The H-line is extracted to the south-east direction in experimental hall #1.

At the primary stage of the MUSE construction, only the D-line and the frontend magnets in the S-line were installed, and then the frontend magnets in the U-line were installed in 2009. In the H-line, temporary radiation-shield blocks were placed. J-PARC has been operated since 2008, and thus, the activation around the muon production target becomes more and more serious by each passing year. According to the evaluation using a Monte-Carlo code [5], the dose rate beside the target chamber was estimated to be close to 1 Sv/h, and the summer shutdown in 2012 was the actual time limit to install the frontend magnets in the H-line. Thus, the installation of the frontend devices was completed mainly in 2012 and partially in 2014, as shown in Fig. 2 and 3.

In the other high-intensity beam line in MUSE, the U-line, we adopted only axial focusing magnets to obtain high transmission efficiency [6]. On the other hand, in the H-line, the beam captured by an axial focusing large-aperture solenoid magnet is transmitted through bending magnets, although these non-axial focusing magnets increase the beam loss. To compensate for this and improve the transmission efficiency, large aperture magnets and other devices are adopted in the H-line. A typical size of the aperture is 600 mm in diameter.

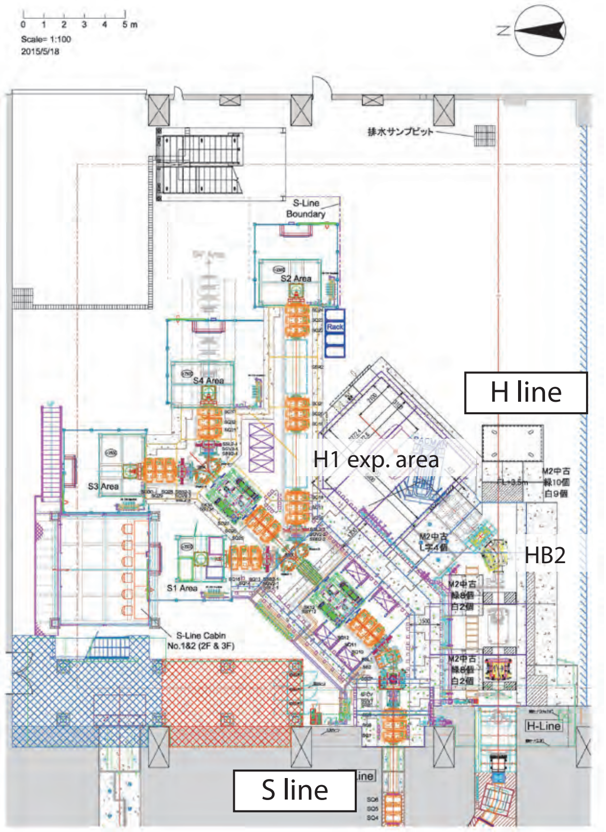

Figure 1. A layout plan of experimental hall #1 in the first phase.

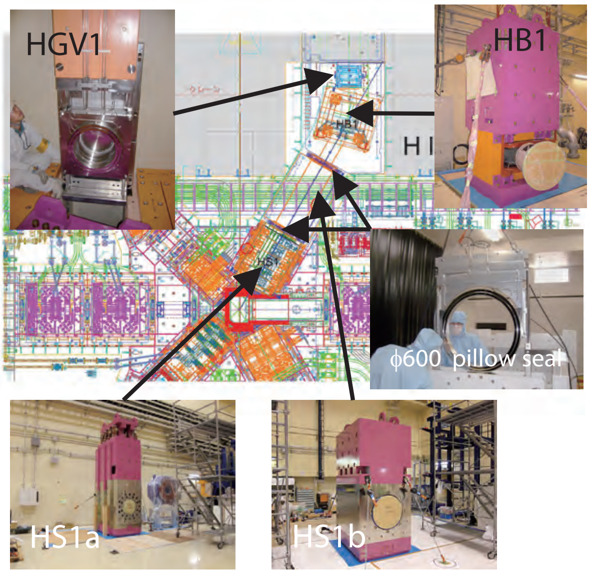

Figure 2. Installed frontend devices in the H-line.

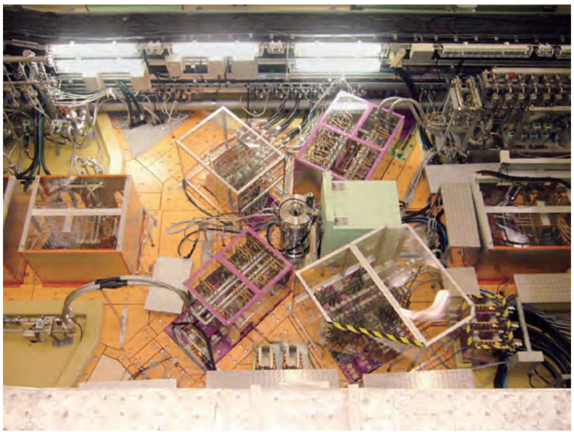

Figure 3. Picture taken after completing the installation of the frontend devices in the H-line.

The conceptual design work of the major components in the experimental hall, *i.e.* magnets, vacuum components and so on, has been almost converged for the first phase of the H-line, in which the beam line is constructed up to the first experimental area, as shown in Fig. 1. Currently, the detailed mechanical design work is in progress. In order to provide a sufficient muon beam to all planed experiments in the H-line, design work is performed with the collaborators of the proposed experiments.

The designing work of the radiation shield was performed in the same way in the other beam lines [5]. Along the beam line, a few meter-thick concrete shields will be necessary to enclose the streaming neutrons and other radiation sources. Because the H-line adopts large aperture devices, the effect of the streaming neutrons will be more serious than on the other beam lines. The evaluation of the streaming neutrons is important not only for radiation safety but also to check its effect on the detectors and other devices in the experimental area. Figure 4 shows a typical result of the simulation. While the proton beam is on, the dose rate in the experimental area is expected to reach 100 μSv/h, and no one can enter to the area even if no beam is delivered. By inserting a beam blocker which is a 40-cm thick copper block, the dose rate is decreased by a factor of ten. Both the beam blocker and switching off HB2 guarantee the personnel's safety from the radiation, and compose the personal protection interlock system.

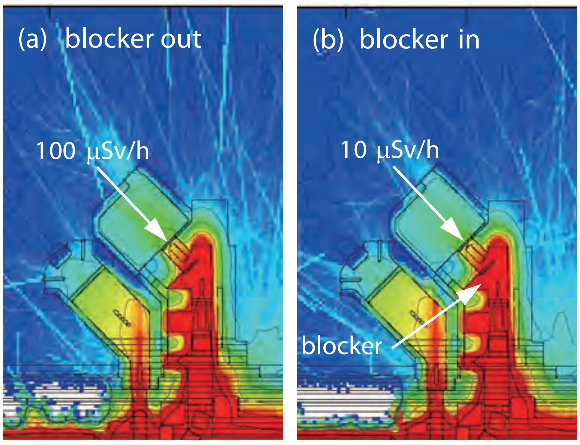

Figure 4. A typical simulated result of the radiation dose around the H-line. To enter the experimental area, a beam blocker is inserted on the right while no blocker is used on the left.

In 2014JFY, a supplemental budget was secured to reinforce the radiation shield against a 1-MW proton beam. A part of H-line's shield was designed and fabricated to unite the reinforcement shield in experimental hall #1. These shield blocks were delivered in the end of March, 2015, and temporarily stored in the experimental hall and they are still there at present, as shown in Fig. 5. With regard to the radiation safety, the modification of the shield, shown in Fig. 6, was submitted to the regulatory agency.

In the summer shutdown of 2015, these blocks will be assembled in the H-line shield.

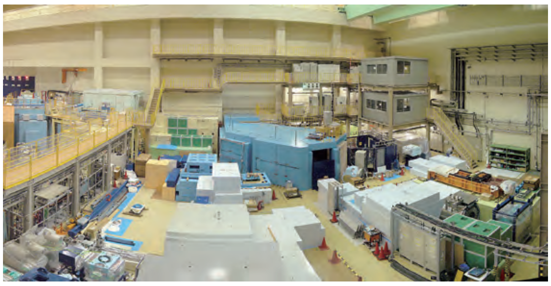

Figure 5. The radiation shield, temporarily stored in experimental hall #1.

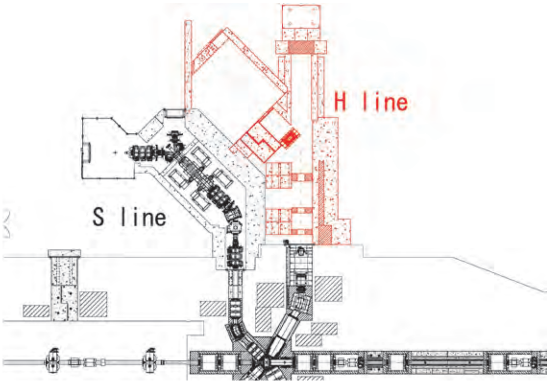

Figure 6. Drawing of the shield modifications awaiting approval.

[1] N. Kawamura *et al., 2013 Journal of Physics: Conference Series* **408** 012072.

[2] K. Shimomura *et al., ibid.*

[3] N. Saito *et al., ibid.*

[4] S. Mihara *et al., ibid.*

[5] N. Kawamura *et al.*, 2009 *NIM A* **600** 114.

[6] K. Nakahara *et al.*, 2010 AIP Conf. Proc. **1222** 420.

N. Kawamura[1,2], MuHFS collab., DeeMe collab., and g-2/EDM collab.

[1]*Muon Science Section, Materials and Life Science Division, J-PARC;* [2]*Muon Science Laboratory, High Energy Accelerator Research Organization (KEK)*

MLF Safety

Research Safety

1. Radiation safety

(Measurement of shieling performance of all neutron beamlines with increase of the proton beam power)

Toward the 1-MW operation permitted in the radiological license issued last year, we plan to measure the dose rates at all estimation points in MLF, following the increase of the proton beam power in order to confirm the shielding performance. In 2015, we measured the dose rates at the 450-kW operation in March and at the 560-kW operation in April. As a result, it was confirmed that the dose rates measured at all estimation points in the operation were lower than the entered values in the application, even if the measured values were scaled to the 1-MW operation.

(Periodic Inspection)

In 2015, the Nuclear Regulatory Commission conducted its periodic inspection of MLF. To keep the radiological license, the periodic inspection at MLF must be conducted every 5 years. During the periodic inspection, several examinations of dose rates, interlocks and signs and document confirmation were done in May, July and November. Although several troubles at the accelerators and MLF caused a delay in the examination schedule, the periodic inspection did not find any serious problems and the radiological license was extended.

(Radiological License Upgrade)

Although we normally have two chances to apply for a radiological license upgrade in a year, only one application was submitted in FY2015.

The application for a radiological license upgrade was approved on April 18, 2016, with updates for the following items:

(1) Installation of neutron beam line BL23 (POLANO),
(2) Addition of storage and usage of several sealed radioisotopes (RI) (Am-241 and Am-243),
(3) Extension of the usage area of RI after the new beam line installation and
(4) Interlock for entering the proton beam line areas after operation.

2. Chemical safety

The chemical-safety team performed successfully safety checks of chemical materials brought by users, such as specimen and reagents, to determine the toxicity and the chemical stability of substances with actual physical form, such as powder, solid, liquid and gas. The safety of those materials was confirmed by the individual beamline staffs. As a result, there were no serious problems when the experiments were performed. Figure 1 shows a trend for a number of chemical materials for safety check. In 2015, because of shorter available beam time (approximately 62 days), the total number of chemical materials decreased, compared with 2014 (approximately 118 days).

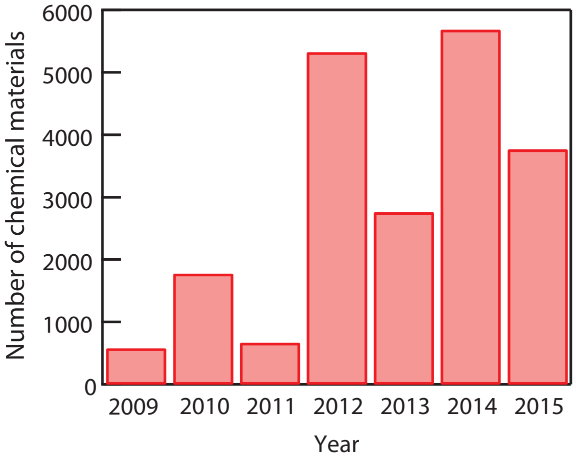

Figure 1. Trend of chemical materials for chemical safety check.

The risk assessment of chemical materials for various works at the office is mandated from 2016, so the chemical-safety team has conducted a study of a method for it.

3. User brought equipment safety

There are many user-brought pieces of equipment in MLF, for example cryostats, magnets, furnaces, gas chamber systems, etc. So, the equipment safety team, which consists of electrical safety staff, mechanical safety staff and general technical staff, checks various user-brought pieces of equipment. The total number of safety checks was 49 in 2015.

The approved equipment is permitted to be used in experiments for 1 year. Firstly, the safety check is performed about the specifications of the interlock system, electric circuits, cable specifications and terminal treatments, monitor system, etc. Next, it is confirmed whether the interlock system operates correctly or not. Figure 2 shows parts of the permission sheet as an example.

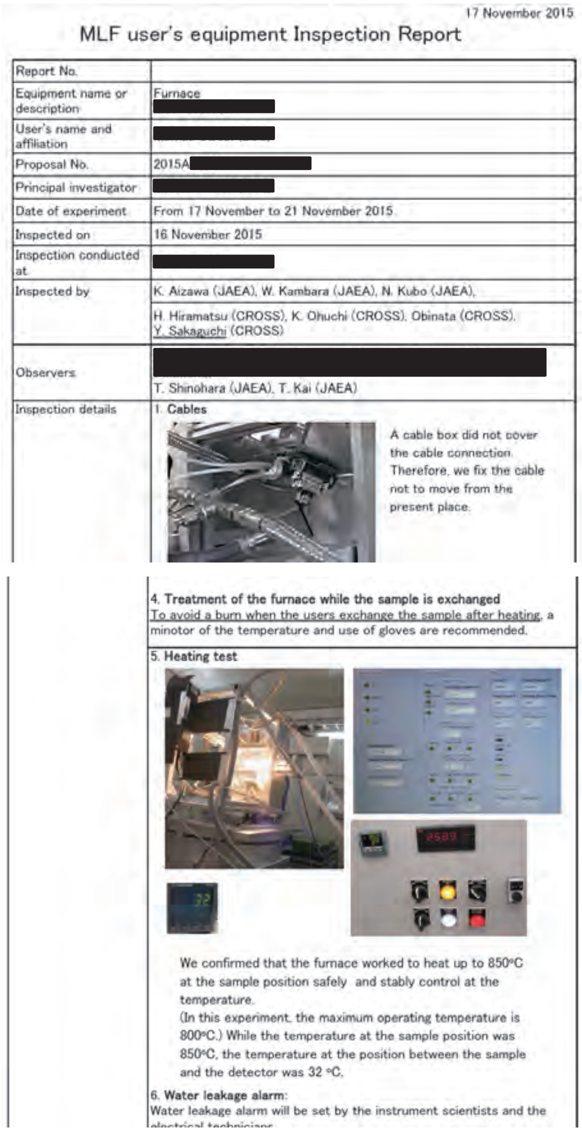

17 November 2015

MLF user's equipment Inspection Report

Report No.	
Equipment name or description	Furnace [redacted]
User's name and affiliation	[redacted]
Proposal No.	2015A[redacted]
Principal investigator	[redacted]
Date of experiment	From 17 November to 21 November 2015
Inspected on	16 November 2015
Inspection conducted at	[redacted]
Inspected by	K. Aizawa (JAEA), W. Kambara (JAEA), N. Kubo (JAEA), H. Hiramatsu (CROSS), K. Ohuchi (CROSS), Obinata (CROSS), Y. Sakaguchi (CROSS)
Observers	[redacted] T. Shinohara (JAEA), T. Kai (JAEA)
Inspection details	1. Cables

A cable box did not cover the cable connection. Therefore, we fix the cable not to move from the present place.

4. Treatment of the furnace while the sample is exchanged
To avoid a burn when the users exchange the sample after heating, a minotor of the temperature and use of gloves are recommended.

5. Heating test

We confirmed that the furnace worked to heat up to 850°C at the sample position safely and stably control at the temperature.
(In this experiment, the maximum operating temperature is 800°C.) While the temperature at the sample position was 850°C, the temperature at the position between the sample and the detector was 32 °C.

6. Water leakage alarm:
Water leakage alarm will be set by the instrument scientists and the

Figure 2. Permission sheet for user-brought equipment.

4. Crane safety

There are 2 cranes in each experimental hall (experimental hall No.1 and experimental hall No.2). These cranes are used by technical staffs or constructors to change an experimental setup during the beam time and perform maintenance in the summer season. Figure 3 shows the statistics of total crane usage in both experimental halls as a function of every month. The usage frequency is highest in October, because the maintenance must be completed in October. The trend and numbers of every month are similar to those of 2014.

The safety and effective schedules of crane usage are planned by the crane safety team. Also, that team checks the mechanical sling, lifting sling, etc., every month and replaces the old ones with new ones, if necessary. Furthermore, a crane operator, who wants to use the cranes in the experimental halls, needs to attend hands-on training by the crane safety team staff before the actual operation. A crane work team, to comply with the rules, is required to include a crane operator, slinging operator and observer.

As a result, there are no serious troubles in the crane operations.

Figure 3. Trend of the total crane usage in one year.

M. Harada[1], **M. Ooi**[1], **M. Sekijima**[1], **T. Kai**[2], **Y. Kasugai**[3], **K. Aizawa**[4], **S. Ono**[4], **N. Kubo**[4], **W. Kambara**[4], **M. Sawabe**[4], **K. Suzuya**[2], **N. Kawamura**[5], **Y. Sakaguchi**[6], **and T. Yamashita**[6]

[1]*Neutron Source Section;* [2]*Neutron Science Section, Materials and Life Science Division, J-PARC center;* [3]*Radiation Safety Section, Safety Division, J-PARC Center;* [4]*Technology Development Section, Materials and Life Science Division, J-PARC center;* [5]*Muon Science Section, Materials and Life Science Division, J-PARC Center;* [6]*Neutron R&D Division, CROSS-Tokai*

MLF Operations in 2015

Beam Operation Status at MLF

In Japanese Fiscal Year (JFY) 2015, the beam operation at the MLF started on April 19, 2015, with a beam power of 500 kW. Table 1 shows the scheduled time and availability in JFY 2015, which reflects the original plan made before JFY 2015. On April 14, just before the start of JFY 2015, the beam power was increased from 400 kW to 500 kW after confirmation of the beam loss status. The radiation dose around the target station for 600 kW was confirmed to be smaller than the conservative designated value.

Two failures of the cooling water channel at the mercury target (Target #5 and #7) occurred in JFY 2015, so the overall availability shown in Table 1 was worse than in the past years. The first malfunction of the cooling channel at Target #5 happened on April 30. Due to the first failure, we had to stop the beam until the end of June, although it was planned to be supplied up to the end of that month. On November 20, the second malfunction happened at Target #7, which was just exchanged during the summer shutdown period. Three months were required to rectify this failure, including checking the health of the replaced target, which was Target #2. Since the replaced target did not have the helium bubbler to mitigate cavitation erosion at the target vessel, the beam power was determined to be lower than 200 kW.

Additionally, a relatively long beam stop period was required to complete the purification of the cryogenic system for the neutron moderator. In JFY 2015, the purification was done twice, from Nov 12th to Nov 16th and from Mar 7th to Mar 14th. Figure 1 shows the trend of the beam power and its availability during JFY 2015. After replacement of Target #2, relatively high availability was achieved, except during the cryogenic system refreshment period.

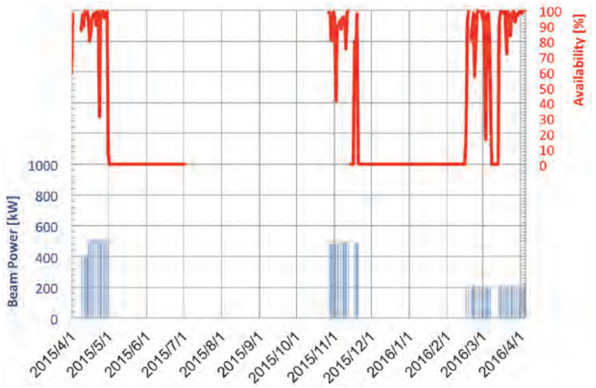

Figure 1. Beam power trend (shown in blue line) at MLF and availability per day (shown in red line).

Table 1. Run cycle, scheduled time and availability.

Run	Duration	Scheduled time (h)	Modified schedule time (h)	Beam time (h)	Availability to modified schedule (%)
62	Apr 19 – May19	655	655	221.2	25.0
63	May 22 – Jun 25	730	730	0	0
64	Oct 29 – Nov 11	324	324	281.7	86.9
65	Nov 15 – Dec 24	889	899	59.2	6.6
66	Jan 16 – Feb 27	880	210	33.4	15.9
67	Feb 21 – Apr 4	941	941	735.8	78.2
Overall		4429	3759	1331.2	35.4

Users at the MLF

In the fiscal year 2015, there were two long periods (total 5 months) of shutdown of neutron and muon beam operation due to target incidents occurred in April and November, 2015. Therefore, the number of the MLF users in this fiscal year decreased by 30 percent compared with that of the previous year. The beam operation was resumed in February 2016 with beam power of 200 kW. The unconducted experiments in 2015A due to these incidents were postponed to 2015B by cancelling the call for the proposals in 2015B. The transition of the number of users at the MLF is summarized in Table and Figure for domestic and foreign users of neutron and muon experimental facilities.

Table 1. The number of domestic and foreign users in the period of fiscal year.

	FY2008		FY2009		FY2010		FY2011		FY2012		FY2013		FY2014		FY2015	
	Domestic Users	Foreign Users	Domestic Users	Foreign Users	Domestic Users	Foreign Users	Domestic Users	Foreign Users	Domestic Users	Foreign Users	Domestic Users	Foreign Users	Domestic Users	Foreign Users	Domestic Users	Foreign Users
Neutron	107		317		476		259		708		449		824		559	
	95	12	303	14	432	44	238	21	628	80	399	50	711	113	476	83
Muon	18		40		50		23		56		61		91		69	
	18	0	38	2	42	8	21	2	46	10	50	11	78	13	59	10

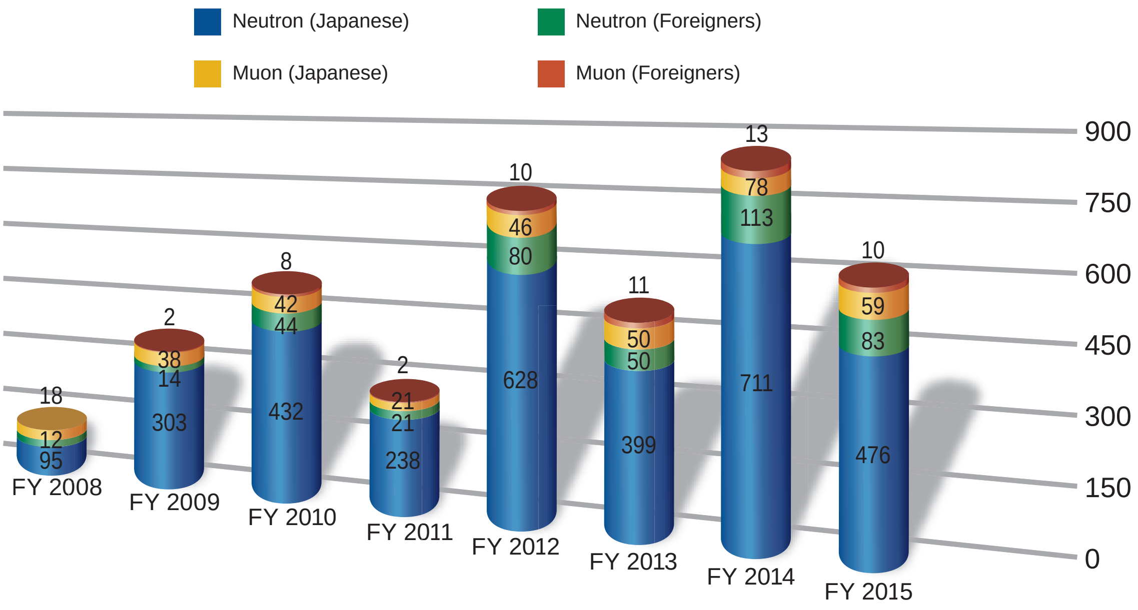

Figure 1. The number of domestic and foreign users in the period of fiscal year.

MLF Proposals Summary – FY2015

The call for J-PARC MLF 2015B General Use Proposals were canceled, because of the long downtime for maintenance of the neutron target, machine time allocated to 2014B and 2015A was shifted to 2015B.

Table 1. Breakdown of Proposals Numbers for the 2015A Rounds.

Beam-line	Instrument		2015A		Full Year					
			Submitted	Approved	Submitted			Approved		
			GU	GU	PU/S	IU	ES	PU/S	IU	ES
BL01	4D-Space Access Neutron Spectrometer - ***4SEASONS***		18(2)	13(1)	3	1	2	3	1	2
BL02	Biomolecular Dynamics Spectrometer - ***DNA***		20(1)	17(1)	2	1	0	2	1	0
BL03	Ibaraki Biological Crystal Diffractometer - ***iBIX***	$(100\text{-}\beta)^{\ddagger}$	6	3	0	0	0	0	0	0
		$(\beta)^{\dagger}$	3	3	16	0	0	15	0	0
BL04	Accurate Neutron-Nucleus Reaction Measurement Instrument - ***ANNRI***		12	7	2	1	0	2	1	0
BL05	Neutron Optics and Physics - ***NOP***		5	3	1	0	0	1	0	0
BL08	Super High Resolution Powder Diffractometer - ***S-HRPD***		11	7	2	0	0	2	0	0
BL09	Special Environment Neutron Power Diffractometer - ***SPICA***		0	0	1	0	0	1	0	0
BL10	Neutron Beamline for Observation and Research Use - ***NOBORU***		8	7	3	1	0	3	1	0
BL11	High-Pressure Neutron Diffractometer - ***PLANET***		9	8	0	1	0	0	1	0
BL12	High Resolution Chopper Spectrometer - ***HRC***		13	8	4	0	0	4	0	0
BL14	Cold-neutron Disk-chopper Spectrometer - ***AMATERAS***		25	10	4	1	1	4	1	1
BL15	Small and Wide Angle Neutron Scattering Instrument - ***TAIKAN***		29(2)	15(2)	4	2	2	4	2	2
BL16	High-Performance Neutron Reflectometer with a horizontal Sample Geometry - ***SOFIA***		14	13	1	0	0	1	0	0
BL17	Polarized Neutron Reflectometer - ***SHARAKU***		13	9	1	1	1	1	1	1
BL18	Extreme Environment Single Crystal Neutron Diffractometer - ***SENJU***		24	12	2	2	1	2	2	0
BL19	Engineering Diffractometer - ***TAKUMI***		28	13	3	1	1	3	1	1
BL20	Ibaraki Materials Design Diffractometer - ***iMATERIA***	$(100\text{-}\beta)^{\ddagger}$	15	6	0	0	0	0	0	0
		$(\beta)^{\dagger}$	23	23	14	0	0	14	0	0
BL21	High Intensity Total Diffractometer - ***NOVA***		22	12	4	0	0	4	0	0
BL22	Energy Resolved Neutron Imaging System - ***RADEN***		10	7	2	1	0	2	1	0
D1	Muon Spectrometer for Materials and Life Science Experiments - ***D1***		29(1)	20(1)	3	1	0	3	1	0
D2	Muon Spectrometer for Basic Science Experiments - ***D2***		12(2)	9(1)	2	1	0	2	1	0
U	Muon U		0	0	1	0	0	1	0	0
Total			**349**	**225**	**75**	**15**	**8**	**74**	**15**	**7**

GU : General Use
PU : Project Use or Ibaraki Pref. Project Use
S : S-type Proposals
IU : Instrument Group Use
ES : Element Strategy
† : Ibaraki Pref. Exclusive Use Beamtime ($\beta = 80\%$ in FY2014)
‡ : J-PARC Center General Use Beamtime ($100 - \beta = 20\%$ in FY2014)
( ) : Proposal Numbers under Trial Use Access System or P-type proposals (D1,D2) in GU

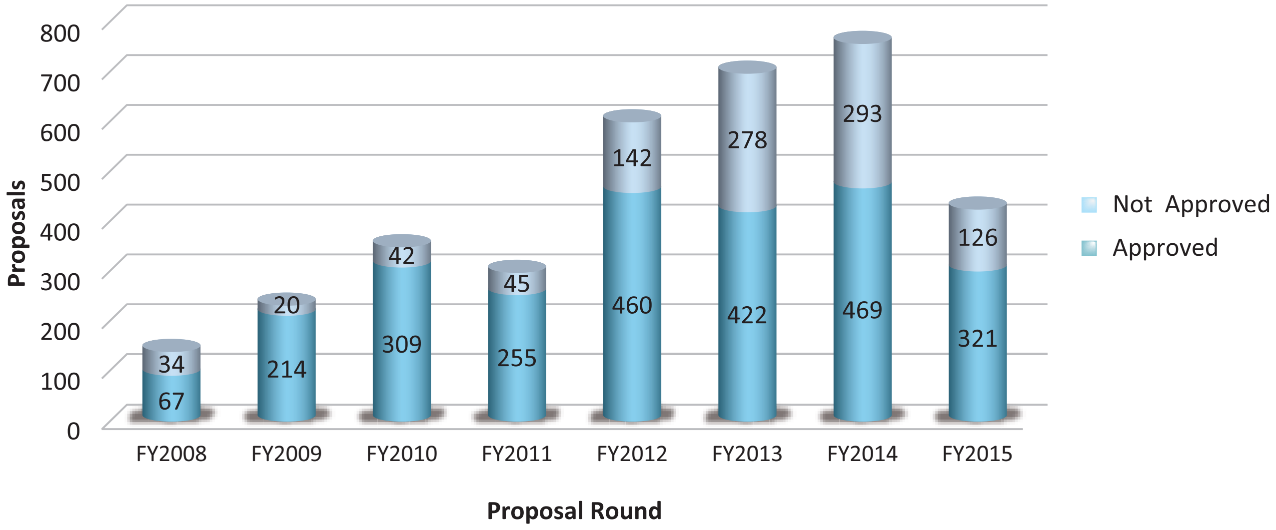

Figure 1. MLF Proposal Numbers over Time.

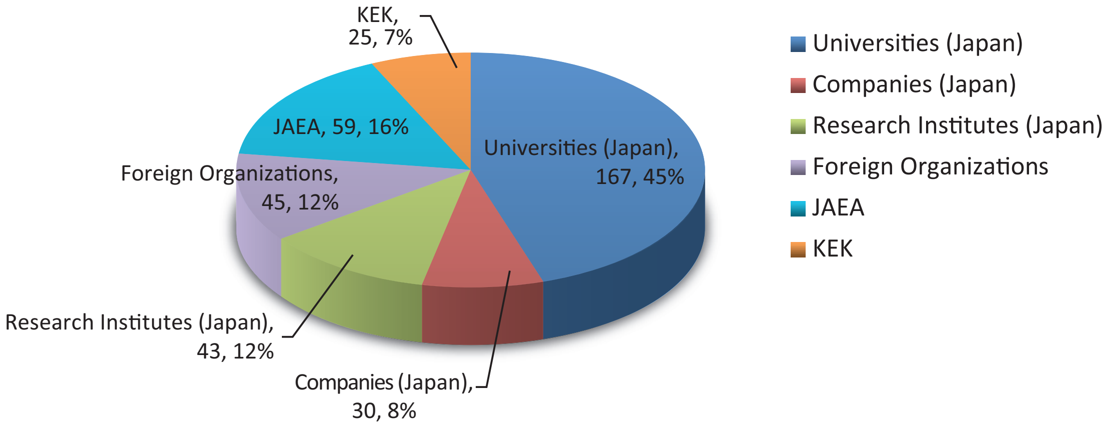

Figure 2. Origin of Submitted Proposals by affiliation - FY2015.

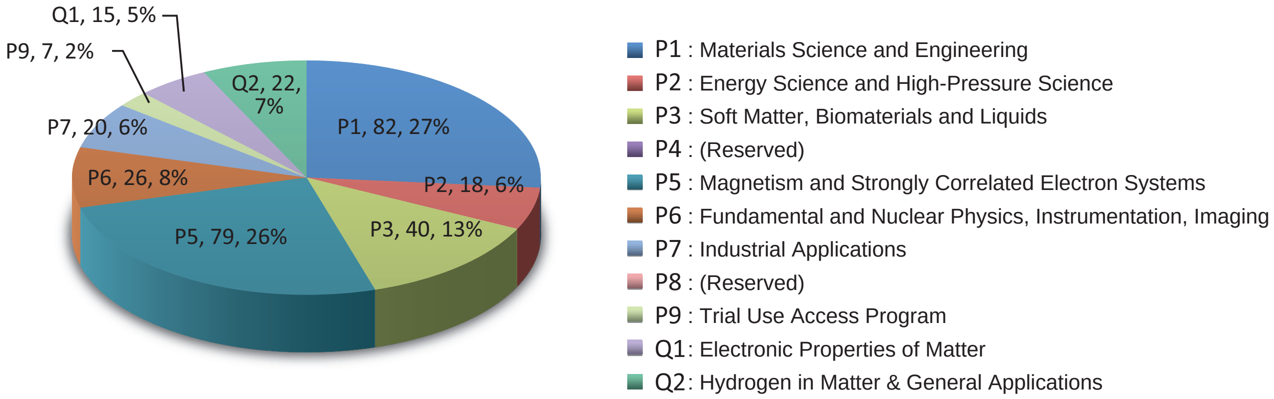

Figure 3. Submitted Proposals by Sub-committee/Expert Panel – FY2015.

MLF Division Staff 2015

Head	**Masatoshi Futakawa (Until May, 2015)**
	Toshiji Kanaya (From June, 2015)
Deputy Head	**Hideki Seto**
	Kazuhiko Soyama

Neutron Source Section

*: additional duties

<JAEA>

Hiroshi Takada (Leader)
Katsuhiro Haga (Sub-Leader)
Katsuhiro Aoyagi
Tomokazu Aso
Shinpei Fukuda
Kouhei Hanano
Masahide Harada
Shoichi Hasegawa *
Mitsunori Hirane
Miyuki Hoshino
Masato Ida
Kenji Imahashi
Tetsuya Kai *
Yuko Kato
Tomoyuki Kawasakii
Hidetaka Kinoshita
Hiroyuki Kogawa
Kazuma Maekawa
Shin-ichiro Meigo
Hideki Muto
Takashi Naoe
Norio Narui
Masaaki Nishikawa
Gaku Noguchi
Kazutaka Nomura
Ken-ichi Oikawa *
Motoki Ohi
Kenji Sakai
Masakazu Seki
Mitsuaki Sekijima
Hideki Tatsumoto
Makoto Teshigawara
Toshitsugu Uchida
Hideki Ueno
Takashi Wakui
Zhihong Xiong
Shizuka Yoshinari

Neutron Science Section

*: additional duties

<JAEA>

Kenji Nakajima (Leader)
Yukinobu Kawakita (Sub-Leader)
Kazuya Aizawa *
Koichi Akita *
Kazuhiro Aoyama
Satoru Fujiwara *
Hideo Harada *
Masahide Harada *
Stefanus Harjo
Takanori Hattori
Kousuke Hiroi
Tomonori Hosoya
Yasuhiro Inamura
Takaaki Iwahashi
Nobuyuki Iwamoto *
Tetsuya Kai
Ryoichi Kajimoto
Wataru Kambara *
Kouji Kaneko *
Chiho Katagiri
Seiko Kawamura
Takuro Kawasaki
Naoko Kawase
Tatsuya Kikuchi
Atsushi Kimura *
Ryoji Kiyanagi
Masato Kubota *
Kazuo Kurihara *
Bing Li
Futoshi Minato *
Hiroshi Nakagawa *
Shoji Nakamura *
Mitsutaka Nakamura
Takashi Ohhara
Ken-ichi Oikawa
Asami Sano
Kunieda Satoshi *
Mariko Segawa *
Kaoru Shibata
Naoko Shimizu
Takenao Shinohara
Yuhua Su
Kentaro Suzuya
Shin-ichi Takata
Tarou Tamada *

Itaru Tamura *
Yousuke Tou *
Shuichi Wakimoto *
Masao Watanabe *
Dai Yamazaki *

<KEK>

Shinichi Ito (Sub-Leader)
Hideki Seto
Hitoshi Endo
Haruhiro Hiraka
Takashi Honda
Soshi Ibuka
Kazutaka Ikeda
Takashi Ino
Takashi Kamiyama
Naokatsu Kaneko
Kenji Mishima
Fumiya Nemoto
Hidetoshi Oshita
Toshiya Otomo
Kaoru Taketani
Shuki Torii
Norifumi Yamada
Testuya Yokoo
Masao Yonemura

Technology Development Section

*: additional duties

<JAEA>

Kazuya Aizawa (Leader)
Takayuki Oku (Sub-Leader)
Tomokazu Aso
Chikako Doda
Wu Gong
Katsuhiro Haga *
Masahide Harada *
Yasuhiro Inamura *
Tetsuya Kai *
Wataru Kambara
Kazuhiro kawakami
Hiroyuki Kogawa *
Naoya Kubo
Kentaro Moriyama
Mitsutaka Nakamura *
Tatsuya Nakamura *
Takeshi Nakatani
Shino Ono
Motoki Ohi *
Kenji Sakai *
Kaoru Sakasai *
Masaki Sawabe
Kentaro Suzuya *
Shin-ichi Takata *
Kazue Tanaka
Masao Watanabe
Yasuhiro Yamauchi

<KEK>

Masataka Sakaguchi
Hiroshi Fujimori *
Takashi Ino *
Naokatsu Kaneko *
Naritoshi Kawamura *
Kenji Kojima *
Shunsuke Makimura *
Setsuo Sato
Tomohiro Seya
Kaoru Taketani *
Shuki Torii *
Testuya Yokoo *

Neutron Instrumentation Section

*: additional duties

<JAEA>

Kaoru Sakasai (Leader)
Noriko Amezawa
Masumi Ebine *
Katsunori Honda
Ryuji Maruyama
Tatsuya Nakamura
Kentaro Toh
Dai Yamazaki

Muon Science Section

*: additional duties

<KEK>

- Ryosuke Kadono (Leader)
- Naritoshi Kawamura (Sub-Leader)
- Taihei Adachi
- Pant Amba Datt
- Hiroshi Fujimori
- Koji Hamada
- Masatoshi Hiraishi
- Li Hua
- Yutaka Ikedo
- Yasuo Kobayashi
- Akihiro Koda
- Kenji Kojima
- Shunsuke Makimura
- Shiro Matoba
- Yasuhiro Miyake
- Junpei Nakamura
- Yohei Nakatsugawa
- Yasuhisa Nemoto
- Yu Oishi
- Hirotaka Okabe
- Koichiro Shimomura
- Patrick Strasser
- Masato Tabe
- Soshi Takeshita
- Yutaka Taniguchi
- Motonobu Tanpo
- Atsushi Yabuuchi
- Ichihiro Yamauchi

<JAEA>

- Wataru Higemoto *
- Takashi Ito *

CROSS-Tokai Staff 2015

Director **Hideaki Yokomizo**

Science Coordinators

Masatoshi Sato

Yoshiaki Fukushima

Neutron R&D Division

*: additional duties

Jun-ichi Suzuki (Head)
Kenichi Funakoshi (Head (Deputy))

<BL01 Group>
Kazuya Kamazawa (Leader)
Kazuhiko Ikeuchi
Kazuki Iida

<BL02 Group>
Masato Matsuura (Leader)
Takeshi Yamada
Taiki Tominaga

<BL11 Group>
Kenichi Funakoshi * (Leader)
Jun Abe
Shinichi Machida

<BL15 Group>
Kazuki Ohishi (Leader)

Jun-ichi Suzuki *
Hiroki Iwase

<BL17 Group>
Jun-ichi Suzuki * (Leader)
Noboru Miyata (Sub Leader)
Tazuko Mizusawa
Kazuhiro Akutsu

<BL18 Group>
Akiko Nakao (Leader)
Koji Munakata
Takayasu Hanashima
Taketo Moyoshi

<BL22 Group>
Hirotoshi Hayashida (Leader)
Joseph Don PARKER
Yoshihiro Matsumoto
Shuoyuan Zhang

<Technical Support Group>
Koji Kiriyama (Leader)
Takayoshi Ito (Sub-Leader)
Yoshifumi Sakaguchi
Yukihiko Kawamura
Hiroshi Kira
Motoyuki Ishikado
Nobuo Okazaki
Makoto Kobayashi
Satoshi Kasai
Toshiaki Morikawa
Hideyuki Hiramatsu
Yutaka Ebara
Tetsuya Kuroda
Keiichi Ohuchi
Masae Sahara
Masashi Obinata

Health and Safety Division

*: additional duties

Toshiyuki Yamashita (Head)
Yukihiko Kawamura *

Rei Ohuchi *
Koji Kiriyama *

Utilization Promotion Division

*: additional duties

Junichi Sato(Head)
Kenichi Funakoshi *(Head (Deputy))
Asuko Ariga
Toshiki Asai
Yoshiaki Fukushima *
Megumi Kawakami
Keiko Mikami
Junko Ohta
Rei Ohuchi
Sayaka Suzuki
Emi Takaha
Aya Yamada
Shinichi Yamaguchi

Admin and Finance Division

Yasuo Seishi (Head)
Masaru Yokoyama (Head (Deputy))
Mika Gunji
Takashi Hikita
Mutsumi Shiraishi
Tomoyuki Yabana

Proposals Review System, Committees and Meetings

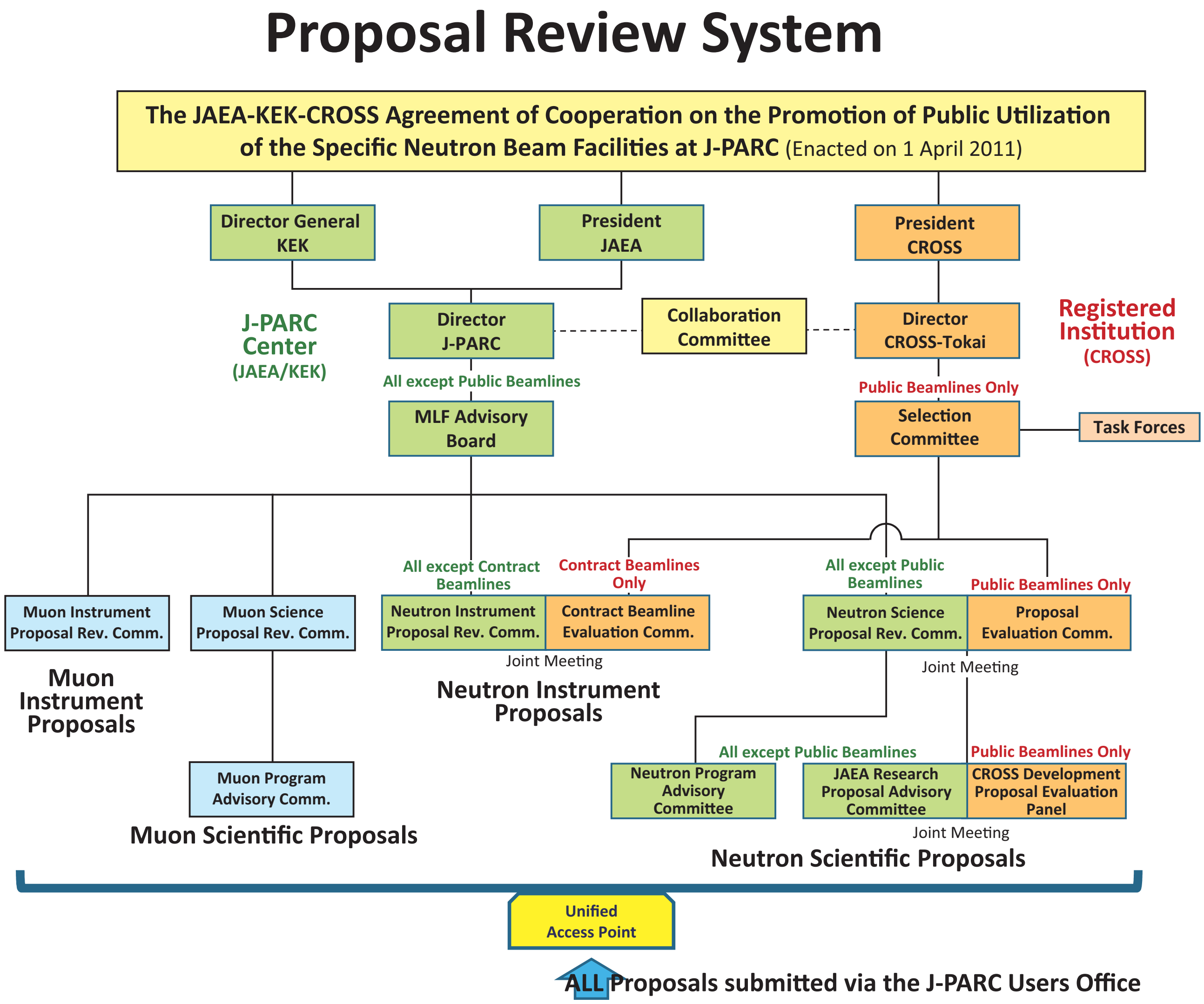

Figure 1. Proposals Review System Framework.

Materials and Life Science Facility Advisory Board

Kazuya Aizawa	Japan Atomic Energy Agency, Japan
Jun Akimitsu	Okayama University, Japan / Hiroshima University, Japan
Hiroshi Amitsuka	Hokkaido University, Japan
Masaki Fujita	Tohoku University, Japan
Michihiro Furusaka	Hokkaido University, Japan
Masatoshi Futakawa	Japan Atomic Energy Agency, Japan
Ryosuke Kadono	High Energy Accelerator Research Organization, Japan
Takashi Kamiyama	High Energy Accelerator Research Organization, Japan
Toshiji Kanaya	High Energy Accelerator Research Organization, Japan
Yuji Kawabata	Kyoto University, Japan
Yukinobu Kawakita	Japan Atomic Energy Agency, Japan
Yoshiaki Kiyanagi	Nagoya University, Japan
Kenya Kubo	International Christian University, Japan
Tetsurou Minemura	Ibaraki Prefecture, Japan
Yasuhiro Miyake	High Energy Accelerator Research Organization, Japan
Atsushi Nakagawa	Osaka University, Japan
Kenji Nakajima	Japan Atomic Energy Agency, Japan
Toshiya Otomo	High Energy Accelerator Research Organization, Japan
Hideki Seto	High Energy Accelerator Research Organization, Japan
Mitsuhiro Shibayama	The University of Tokyo, Japan
Kazuhiko Soyama	Japan Atomic Energy Agency, Japan
Jun Sugiyama	Toyota Central R&D Labs., Inc., Japan
Jun-Ichi Suzuki	Comprehensive Research Organization for Science and Society, Japan
Masayasu Takeda	Japan Atomic Energy Agency, Japan
Toshio Yamaguchi (Chair)	Fukuoka University, Japan

Term: through March 31, 2017

Selection Committee (CROSS)

Jun Akimitsu	Okayama University, Japan / Hiroshima University, Japan
Masaki Fujita	Tohoku University, Japan
Michihiro Furusaka	Hokkaido University, Japan
Yasuhiro Iye (Chair)	Japan Society for Promotion of Science, Japan
Yuji Kawabata	Kyoto University, Japan
Hiroyuki Kishimoto	Sumitomo Rubber Industries, LTD., Japan
Naoki Kishimoto	Research Center for Strategic Materials, Japan
Yoshiaki Kiyanagi	Nagoya University, Japan
Tetsurou Minemura	Ibaraki Prefecture, Japan
Atsushi Nakagawa	Osaka University, Japan
Mitsuhiro Shibayama	The University of Tokyo, Japan
Jun Sugiyama	Toyota Central R&D Labs., Inc., Japan
Shinji Tsuneyuki	The University of Tokyo, Japan
Toshio Yamaguchi	Fukuoka University, Japan

Term: through March 31, 2017

Neutron Advisory Committee (NAC)

NAC convened 23-24 February, 2016 at the J-PARC Research Center, Tokai

Group photo of NAC

Neutron Advisory Committee (23-24 Feb. 2016)

Jean-Michel Poutissou (chair)	Canada's National Laboratory for Particle and Nuclear Physics
Hiroshi Amitsuka	Hokkaido University
Thomas Roser	Brookhaven National Laboratory
Shinian Fu	Institute of High Energy Physics
Sergio Bertolucci	The European Organization for Nuclear Research
Robert Tschirhart	Fermi National Accelerator Laboratory
Robert Tribble	Brookhaven National Laboratory
Donald F. Geesaman	Argonne National Laboratory
Horst Stoecker	GSI Helmholtzzentrum für Schwerionenforschung GmbH
Hamid Aït Abderrahim	Belgian Nuclear Research Centre
Paul Langan	Oak Ridge National Laboratory
Hidetoshi Fukuyama	Tokyo University of Science
Robert Robinson	Australian Nuclear Science and Technology Organisation
Andrew Dawson Taylor	Science and Technology Facilities Council

Muon Advisory Committee (MAC)

MAC convened 14-15 February, 2016 at the KEK Tokai Campus, Tokai

Group photo of MAC

Muon Advisory Committee (14-15 Feb. 2016)

Francis Pratt (Chair)	Rutherford Appleton Laboratory
Toshiyuki Azuma	RIKEN
Klaus Jungmann	University of Groningen
Kenya Kubo	International Christian University
Andrew MacFarlane	The University of British Columbia
Yasuo Nozue	Osaka University
Prokscha Thomas	Paul Scherrer Institute
Jun Sugiyama	Toyota Central R & D Labs. Inc.

Workshops, Conferences, Seminars and Schools in 2015

International Symposiums held jointly by J-PARC MLF and CROSS-Tokai

The 8th Meeting on Collective Action for Nomadic Small Angle Scatterers (canSAS VIII)

14-16 Apr. 2015, IBARAKI Quantum. Beam Research. Center, Ibaraki

Group Photo of canSAS-VIII

The seventh workshop on NEUtron WAVElength-dependent imaging (NEUWAVE-7)

31 May - 3 Jun. 2015, Ibaraki Prefectural Culture Center, Ibaraki

Group Photo of NEUWAVE-7

The 15th Japan-Korea Meeting on Neutron Science

6-8 Jan. 2016, Hotel Nongshim, Busan Korea

Conferences held jointly by J-PARC MLF and CROSS-Tokai

Collaborative Symposium of Elements Strategy Initiative and Large Research Institutions 2015

21-22 Jan. 2016, Ito International Research Center, Tokyo

2015 Quantum Beam Science Festa, (The 7th MLF symposium and The 33th PF symposium)

15-16 Mar. 2016, Tsukuba International Congress Center, Ibaraki

Group Photo of 2015 Quantum Beam Science Festa

Workshops held by KEK

6th Progress report meeting of J-PARC MUSE

27 Jul. 2015, KEK Tokai Campus, Ibaraki

Workshop for Neutron Optics and Physics (BL05)

19 Nov. 2015, Nagoya University, Aichi

Workshop for neutron total scattering (BL21)

24 Nov. 2015, KEK Tokai Campus, Ibaraki

Workshop for Neutron Optics and Physics (BL05,BL10)

1 Dec. 2015, KEK Tsukuba Campus, Ibaraki

Workshop for neutron inelastic scattering (BL12)

4 Dec. 2015, KEK Tokai Campus, Ibaraki

Workshop for polarized neutron scattering (BL23)

8 Dec. 2015, KEK Tsukuba Campus, Ibaraki

Workshops held by CROSS-Tokai

The 15th CROSSroads of Users and J-PARC "structures and functions of materials"

7-8 Sep. 2015, IBARAKI Quantum. Beam Research. Center, Ibaraki

Group Photo of CROSSroads 15

The 16th CROSSroads of Users and J-PARC "Recent progress on strongly correlated electron systems and its future"

14-15 Oct. 2015, IBARAKI Quantum. Beam Research. Center, Ibaraki

Group Photo of CROSSroads 16

The 17th CROSSroads of Users and J-PARC "Condensed States of Strongly Correlated Electron Systems"

18-19 Jan. 2016, IBARAKI Quantum. Beam Research. Center, Ibaraki

Group Photo of CROSSroads 17

Workshops and Seminars held by CROSS-Tokai and other organizations

2015 1st Workshop on Analytical Methods In Small Angle Scattering

8 Jul. 2015, KENKYUSHA EIGO Center, Tokyo

Photo of 2015 1st Workshop on Analytical Methods In Small Angle Scattering

2015 Workshop on Materials Science

30 Jul. 2015, Essam Kanda Hall, Tokyo

Photo of 2015 Workshop on Materials Science

2nd Collaborative Symposium of Large Research Institutions and Super computer KEI 2015

2 Sep. 2015, Akihabara UDX, Tokyo

Photo of 2nd Collaborative Symposium of Large Research Institutions and Super computer KEI 2015

Seminar About The Industrial Application by SPring-8 in Kanagawa

3-4 Sep. 2015, KAWASAKI Sangyo Shinko Hall, Kanagawa

2015 Workshop on Surfaces and Interfaces

1 Oct. 2015, KENKYUSHA EIGO Center, Tokyo

Ibaraki Society for Promotion of Use of Neutrons" 2015 Meeting of Magnetic Materials"

6 Oct. 2015, Essam Kanda Hall, Tokyo

2015 1st Workshop on Residual Stress and Strain

13 Oct. 2015, Essam Kanda Hall, Tokyo

Users Meeting of the CROSS Trial Use and Ibaraki Beam Line FY2014

23 Oct. 2015, Kagaku-kaikan Hall, Tokyo

2015 1st Workshop on Structural Biology

17 Nov. 2015, Essam Kanda Hall, Tokyo

2015 Workshop on Neutron Science

25 Nov. 2015, KENKYUSHA EIGO Center, Tokyo

Seminar About The Industrial Application by The Neutron in Saitama

11Dec. 2015, Cultural Center "Sanazeria", Saitama

Ibaraki Society for Promotion of Use of Neutrons 2015 "Workshop on Texture Evaluation of Metal Material"

15 Dec. 2015, KENKYUSHA EIGO Center, Tokyo

2015 Workshop on Magnetic Materials

21 Dec. 2015, Essam Kanda Hall, Tokyo

2015 Workshop on Battery Materials

12 Jan. 2016, KENKYUSHA EIGO Center, Tokyo

2015 Workshop on Non-destructive Visualization and Analysis Methods

20 Jan. 2016, Essam Kanda Hall, Tokyo

Photo of 2015 Workshop on Non-destructive Visualization and Analysis Methods

2015 Workshop on Metallographic Structure

29 Jan. 2016, Essam Kanda Hall, Tokyo

2015 Workshop on Organic and Polymeric Materials Neutron Structure Elucidation

16 Feb. 2016, Essam Kanda Hall, Tokyo

2nd Synchrotron Radiation・Neutron Linkage Use Seminar

19 Feb. 2016, KENKYUSHA EIGO Center, Tokyo

Photo of 2nd Synchrotron Radiation・Neutron Linkage Use Seminar

2015 2nd Workshop on Structural Biology

10 Mar. 2016, KENKYUSHA EIGO Center, Tokyo

2015 2nd Workshop on Residual Stress and Strain

1 Mar. 2016, KENKYUSHA EIGO Center, Tokyo

2015 Workshop on Soft Matter Neutron Scattering

22 Mar. 2016, Essam Kanda Hall, Tokyo

2015 Z-Code Training Course

28-30 Mar. 2016, LMJ Tokyo, Tokyo

Schools in 2015

The 9th KEK Summer Challenge

18-26 Aug. 2015, KEK Tsukuba Campus, Ibaraki

Group Photo of the 9th KEK Summer Challenge
Credit : KEK

The 7th AONSA Neutron School 2015 / 3rd MLF School

1-5 Dec. 2015, J-PARC Center, Ibaraki

Award List

Particle Accelerator Society of Japan, Presentation Award

Study of a corrosion resistant coating layer for metal magnetic cores using neutron reflectometry

Kazuhiro Akutsu (CROSS), August 2015

JAEA President's Awards 2015, Research and Development Prizes

The realization of high-pressure and high-temperature neutron experiments on high-pressure neutron diffractometer PLANET

Takanori Hattori and Asami Sano (JAEA), October 2015

The JSNS Technology Award

Construction of high-pressure neutron diffractometer PLANET and the realization of high-pressure and high-temperature neutron experiments

Takanori Hattori, Asami Sano (JAEA) & Hiroshi Arima (Tohoku Univ.), December 2015

The JSNS Achievement Award

Observation of Quantum States of Hydrogen in Matter Using a Pulsed Neutron Source

Susumu Ikeda (KEK), December 2015

The JSNS Best Poster Award

Neutron inelastic scattering study of magnetic excitation in quasi- one-dimensional quantum spin system of BaCu2V2O8

Yuta Ishii, Hiroyuki Kimura (Tohoku Univ.), Kazuhiko Ikeuchi (CROSS), Ryoichi Kajimoto (JAEA), Zhangzhen He (CAS) and Mitsuru Itoh (Titech)

MLF Publication 2015

1 S. Ohisa, Y.-J. Pu, N. L Yamada, G. Matsuba, and J. Kido
Molecular Interdiffusion between Stacked Layers by Solution- and Thermal Annealing-Process in Organic Light Emitting Devices
ACS Appl. Mater. Interfaces **7** 20779 (2015)

2 K. Komatsu, S. Machida, T. Matsubayashi, M. Watanabe, H. Kagi, A. Sano-Furukawa, and T. Hattori
Crystal structure of magnesium dichloride decahydrate determined by X-ray and neutron diffraction under high pressure
Acta Crystallographica **B71** 74-80 (2015)

3 W. Gong, Y. Tomota, S. Harjo, Y. H. Su, and K. Aizawa
Effect of prior martensite on bainite transformation in nanobainite steel
Acta Materialia **85** 243-249 (2015)

4 T. Okuchi, N. Purevjav, N. Tomioka, J. Lin, T. Kuribayashi, L. Schoneveld, H. Hwang, N. Sakamoto, N. Kawasaki, and H. Yurimoto
Synthesis of large and homogeneous single crystals of water-bearing minerals by slow cooling at deep-mantle pressures
American Mineralogist **100(7)** 1483-1492 (2015)

5 K. Ninomiya, M. K. Kubo, T. Nagatomo, W. Higemoto, T. U. Ito, N. Kawamura, P. Strasser, K. Shimomura, Y. Miyake, T. Suzuki, Y. Kobayashi, S. Sakamoto, A. Shinohara, and T. Saito
Nondestructive Elemental Depth-Profiling Analysis by Muonic X-ray Measurement
Analytical Chemistry **87** 4597-4600 (2015)

6 H. Mizoguchi, S. Park, H. Hiraka, K. Ikeda, T. Otomo, and H. Hosono
An anti CuO2-type metal hydride square net structure in Ln2M2As2H(x) (Ln=La or Sm, M=Ti, V, Cr, or Mn)
Angewandte Chemie International Edition **54** 2932-2935 (2015)

7 S. Takagi, Y. Iijima, T. Sato, H. Saitoh, K. Ikeda, T. Otomo, K. Miwa, T. Ikeshoji, K. Aoki, and S.-I. Orimo
True Boundary for the Formation of Homoleptic Transition-Metal Hydride Complexes
Angewandte Chemie International Edition **54** 5650-5653 (2015)

8 H. Shishido, S. Miyajima, Y. Narukami, K. Oikawa, M. Harada, T. Oku, M. Arai, M. Hidaka, A. Fujimaki, and T. Ishida
Neutron detection using a current biased kinetic inductance detector
Applied Physics Letters **107** 23601 (2015)

9 T. Matsuo, T. Arata, T. Oda, K. Nakajima, S. Ohira-Kawamura, T. Kikuchi, and S. Fujiwara
Internal dynamics of F-actin and myosin subfragment-1 studied by quasielastic neutron scattering
Biochemical and Biophysical Research Communications **459** 493-497 (2015)

10 M. Sugiyama, N. Horikoshi, Y. Suzuki, H. Taguchi, T. Kujirai, R. Inoue, Y. Oba, N. Sato, A. Martel, L. Porcar, and H. Kurumizaka
Solution structure of variant H2A.Z.1 nucleosome investigated by small-angle X-ray and neutron scatterings
Biochemistry and Biophysics Reports **4** 28-32 (2015)

11 S. Taminato, M. Hirayama, K. Suzuki, N. L. Yamada, M. Yonemura, J. Y. Son, and R. Kanno
Highly reversible capacity at the surface of a lithium-rich manganese oxide: a model study using an epitaxial film system
Chemical Communications **51** 1673 (2015)

12 M. Mitsumi, K. Ezaki, Y. Komatsu, K. Toriumi, *et al.*
Proton Order-Disorder Phenomena in a Hydrogen-Bonded Rhodium-η(5)-Semiquinone Complex: A Possible Dielectric Response Mechanism
Chemistry A European Journal **21** 9682-9696 (2015)

13 T. Matsukawa, Y. Yoshida, A. Hoshikawa, S. Okada, and T. Ishigaki
Neutron crystal structure analysis of stilbazolium derivatives for terahertz-wave generation
CrystEngComm **17** 2616-2619 (2015)

14 M. G. Makowska, M. Strobl, E. M. Lauridsen, H. L. Frandsen, A. S. Tremsin, T. Shinohara, and L. T. Kuhn
Phase Transition Mapping by Means of Neutron Imaging in SOFC Anode Supports during Reduction under Applied Stress
ECS Transactions **68** 1103 (2015)

15 Y. Mizuno, Y. Matsuda, K. Suzuki, M. Yonemura, M. Hirayama, and R. Kanno
Synthesis, crystal structure, and electrochemical properties of Li1.2+xMn0.3Co0.2Ni0.3O2 (x > 0) for lithium-ion battery cathodes
Electrochemistry **83** 820-823 (2015)

16 Y. Idemoto, Y. Sera, N. Ishida, and N. Kitamura
Average and Local Crystal Structure and Electronic Structure of 0.4Li2MnO3-0.6LiMn1/3Ni1/3Co1/3O2 Using First-principles Calculations and Neutron Beam and Synchrotron X-Ray Sources
Electrochemistry **83** 879-884 (2015)

17 K. Nakajima, S. Ohira-Kawamura, T. Kikuchi, R. Kajimoto, N. Takahashi, M. Nakamura, K. Soyama, and T. Osakabe
Beam-transport optimization for cold-neutron spectrometer
EPJ Web of Conferences **83** 03011 (2015)

18 J. Hori, H. Yashima, S. Nakamura, K. Furutaka, K. Y. Hara, H. Harada, K. Hirose, M. Igashira, T. Katabuchi, A. Kimura, K. Kino, F. Kitatani, Y. Kiyanagi, M. Koizumi, M. Mizumoto, T. Sano, Y. Takahashi, and Y. Toh
Neutron Capture Cross Section Measurement on 91Zr at J-PARC/MLF/ANNRI
EPJ Web of Conferences **93** 2004 (2015)

19 T. Yokoo, K. Ohoyama, S. Itoh, K. Iwasa, N. Kaneko, J. Suzuki, M. Ohkawara, K. Aizawa, S. Tasaki, T. Ino, K. Taketani, S. Ishimoto, M. Takeda, T. Oku, H. Kira, K. Hayashi, H. Kimura, and T. J. Sato
Polarized neutron spectrometer for inelastic experiments at J-PARC : Status of POLANO Project
EPJ Web of Conferences **83** 03018 (2015)

20 H. Harada, O. Iwamoto, N. Iwamoto, A. Kimura, K. Terada, T. Nakao, S. Nakamura, K. Mizuyama, M. Igashira, T. Katabuchi, T. Sano, Y. Takahashi, K. Takamiya, C. H. Pyeon, S. Fukutani, T. Fujii, J. Hori, T. Yagi, and H. Yashima
Accuracy Improvement of Neutron Nuclear Data on Minor Actinides
EPJ Web of Conferences **93** 6001 (2015)

21 A. Kimura, H. Harada, S. Nakamura, O. Iwamoto, Y. Toh, M. Koizumi, F. Kitatani, K. Furutaka, M. Igashira, T. Katabuchi, M. Mizumoto, J. Hori, K. Kino, and Y. Kiyanagi
Current activities and future plans for nuclear data measurements at J-PARC
The European Physical Journal A **51** 180 (2015)

22 K. Komatsu, K. Munakata, K. Matsubayashi, Y. Uwatoko, Y. Yokoyama, K. Sugiyama, and M. Matsuda
Zr-based bulk metallic glass as a cylinder material for high pressure apparatuses
High Pressure Research **35** 254-262 (2015)

23 K. Shimomura
Muonium in J-PARC; from fundamental toapplication
Hyperfine Interactions **235** 89-95 (2015)

24 K. Kawamura, M. Yashima, K. Fujii, K. Omoto, K. Hibino, S. Yamada, J. R. Hester, M. Avdeev, P. Miao, S Torii, T. Kamiyam
Structural Origin of the Anisotropic and Isotropic Thermal Expansion of K2NiF4-Type LaSrAlO4 and Sr2TiO4
Inorganic Chemistry **54** 3896-3904 (2015)

25 M. L. Baker, T. Tanaka, R. Murakami, S. Ohira-Kawamura, K. Nakajima, T. Ishida, and H. Nojiri
Relationship between Torsion and Anisotropic Exchange Coupling in a TbIII-Radical-Based Single-Molecule Magnet
Inorganic Chemistry **54** 5732-5738 (2015)

26 K. Iwase, K. Mori, S. Tashiro, H. Yokota, and T. Suzuki
Crystal Structure Analysis of La2Ni6CoDx During Deuterium Absorption Process
Inorganic Chemistry **54** 8650-8655 (2015)

27 K. Li, H. Zheng, T. Hattori, A. Sano-Furukawa, C. Tulk, J. Molaison, M. Feygenson, I. N. Ivanov, W. Yang, and H-K. Mao
Synthesis, Structure, and Pressure-Induced Polymerization of Li3Fe(CN)6 Accompanied with Enhanced Conductivity
Inorganic Chemistry **54** 11276-11282 (2015)

28 M. Futakawa
Material issues relating to high power spallation neutron sources
IOP Conference Series: Materials Science and Engineering **74** 12001 (2015)

29 S. He, Y. Tomota, Y. Su, W. Gong, S. Harjo, and G. Zhao
Unusal Tempering Behavior of Fe-Cr-C Martensite
ISIJ International **55** 686-690 (2015)

30 Y. Oba, S. Morooka, H. Sato, K. Ohishi, J. Suzuki, and M. Sugiyama
Simultaneous characterization of precipitates and matrix in a steel using small-angle neutron scattering and Bragg-edge transmission analysis
ISIJ International **55** 2618 (2015)

31 R. Kajimoto, M. Nakamura, Y. Inamura, K. Kamazawa, K. Ikeuchi, K. Iida, M. Ishikado, K. Nakajima, S. Ohira-Kawamura, T. Nakatani, W. Kambara, H. Tanaka, Y. Yamauchi, K. Aoyama, T. Hosoya, K. Kiriyama, K. Aizawa, and M. Arai
Recent progress in the chopper spectrometer 4SEASONS at J-PARC
JAEA-Conf **2015-002** 319-329 (2015)

32 M. Nakamura, K. Ikeuchi, R. Kajimoto, W. Kambara, Th. Krist, T. Shinohara, M. Arai, K. Iida, K. Kamazawa, Y. Inamura, and M. Ishikado
MAGIC chopper: basic concept and experimental evaluation
JAEA-Conf **2015-002** 339-348 (2015)

33 Q. H. Zhang, Z. Zhai, Z. H. Nie, S. Harjo, D. Y. Cong, M. G. Wang, J. Li, and Y. D. Wang
An in situ neutron diffraction study of anomalous superelasticity in a strain glass Ni43Fe18Ga27Co12 alloy
Journal of Applied Crystallography **48** 1183-1191 (2015)

34 O. Kwon, M. Hirayama, K. Suzuki, Y. Kato, T. Saito, M. Yonemura, T. Kamiyama, and R. Kanno
Synthesis, structure, and conduction mechanism of the lithium superionic conductor Li10+δGe1+δP2−δS12
Journal of Materials Chemistry A **3** 438-446 (2015)

35 K. Fujii, M. Shiraiwa, Y. Esaki, M. Yashima, S. J. Kimc, and S. Leec
Improved oxide-ion conductivity of NdBaInO4 by Sr doping
Journal of Materials Chemistry A **3** 11985-11990 (2015)

36 T. Yokoyama, M. Mizuguchi, A. Ostermann, K. Kusaka, N. Niimura, T. E. Schrader, and I. Tanaka
Protonation State and Hydration of Bisphosphonate Bound to Farnesyl Pyrophosphate Synthase
Journal of Medicinal Chemistry **58** 7549-7556 (2015)

37 T. Wan, T. Naoe, and M. Futakawa
In-situ structural integrity evaluation for high-power pulsed spallation neutron source – Effects of cavitation damage on structural vibration
Journal of Nuclear Materials **468** 321-330 (2015)

38 H. Kogawa,T. Naoe, H. Kyotoh, K. Haga, H. Kinoshita, and M. Futakawa
Development of microbubble generator for suppression of pressure waves in mercury target of spallation source
Journal of Nuclear Science and Technology **52** 1461-1469 (2015)

39 K. Ikeuchi, M. Sato, S. Li, M. Toyoda, Y. Kobayashi, M. Itoh, P. Miao, S. Torii, Y. Ishikawa, and T. Kamiyama
Detailed Study of the Phase Diagram of Fe-based Superconductor Ba(Fe1-xCox)2As2 by Super High-Resolution Neutron Diffraction Measurements
Journal of Physics **592** 12071 (2015)

40 Y. Ikeda, H. Yoshizawa, S. Konishi, S. Araki, T. C. Kobayashi, T. Yokoo, and S. Itoh
Caracterization of Ferromagnetic Order in CePd2P2
Journal of Physics: Conference Series **592** 012013 (6 pages) (2015)

41 S. Konno, A. Suzuki, K. Nihei, K. Kuwahara, D. Kawana, T. Yokoo, and S. Itoh
Intermultiplet transitions in filled skutterudite SmFe4P12
Journal of Physics: Conference Series **592** 012029 (6 pages) (2015)

42 Y. Sakaguchi, H. Asaoka, Y. Uozumi, Y. Kawakita, T. Ito, M. Kubota, D. Yamazaki, K. Soyama, M. Ailavajhala, M. R. Latif, K. Wolf, M. Mitkova, and M. W. A. Skoda
Dynamics of silver photo-diffusion into Ge-chalcogenide films: time-resolved neutron reflectometry
Journal of Physics; Conference Series **619** 012046 (2015)

43 G. Yoshida, K. Ninomiya, M. Inagaki, W. Higemoto, T. U. Ito, N. Kawamura, K. Shimomura, Y. Miyake, T. Miura, K. M. Kubo, and A. Shinohara
Muonic atom formation processes for carbon containing molecules
Journal of Physics: Conference Series **635** 052047 (2015)

44 K. Tomoyori, Y. Hirano, K. Kurihara, and T. Tamada
Background elimination using the SNIP method for Bragg reflections from a protein crystal measured by a time-of-flight single-crystal neutron diffractometer
Journal of Physics: Conference Series **664** 072049 - 042055 (2015)

45 Y. Idemoto, R. Kawai, N. Ishida, and N. Kitamura
Characterization, average and electronic structures during charge–discharge cycle in 0.6Li2MnO3–0.4Li(Co1/3Ni1/3Mn1/3)O2 solid solution of a cathode active material for Li-ion battery
Journal of Power Sources **273** 1023-1029 (2015)

46 G. Yoshida, K. Ninomiya, T. U. Ito, W. Higemoto, T. Nagatomo, P. Strasser, N. Kawamura, K. Shimomura, Y. Miyake, T. Miura, K. M. Kubo, and A. Shinohara
Muon capture probability of carbon and oxygen for CO, CO2, and COS under low-pressure gas conditions
Journal of Radioanalytical and Nuclear Chemistry **303** 1277-1281 (2015)

47 S. Makimura, N. Kawamura, S. Onizawa, Y. Matsuzawa, M. Tabe, Y. Kobayashi, R. Shimizu, Y. Taniguchi, H. Fujimori, Y. Ikedo, R. Kadono, A. Koda, K. M. Kojima, K. Nishiyama, J. Nakamura, K. Shimomura, P. Strasser, Y. Nakatsugawa, and Y. Miyake
Development of muon rotating target at J-PARC/MUSE

Journal of Radioanalytical and Nuclear Chemistry **305** 811-815 (2015)

48 H. Tatsumoto, Y. Shirai, M. Shiotsu, Y. Naruo, H. Kobayashi, and Y. Inatani
Heat Transfer Characteristics of a Horizontal Wire in Pools of Liquid and Supercritical Hydrogen
Journal of Superconductivity and Novel Magnetism **28** 1185-1188 (2015)

49 M. Unno, K. Ishikawa-Suto, K. Kusaka, T. Tamada, Y. Hagiwara, M. Sugishima, K. Wada, T. Yamada, K. Tomoyori, T. Hosoya, I. Tanaka, N. Niimura, R. Kuroki, K. Inaka, M. Ishihara, and K. Fukuyama
Insights into the Proton Transfer Mechanism of a Bilin Reductase PcyA Following Neutron Crystallography
Journal of the American Chemical Society **137** 5452-5460 (2015)

50 Y. Ikeda, S. Suzuki, T. Nakabayashi, H. Yoshizawa, T. Yokoo, and S. Itoh
Transport and Thermodynamic Studies of Stripe and Checkerboard Ordering in Layered Nickel Oxides R2-xSrxNiO4 (R = La and Nd)
Journal of the Physical Society of Japan **84** 023706 (5 pages) (2015)

51 R. Kajimoto, K. Tomiyasu, K. Nakajima, S. Ohira-Kawamura, Y. Inamura, and T. Okuda
Development of Spin Correlations in the Geometrically Frustrated Triangular-Lattice Heisenberg Antiferromagnet CuCrO2
Journal of the Physical Society of Japan **84** 074708 (2015)

52 K. Kamazawa, M. Ishikado, S. Ohira-Kawamura, K. Kakurai, K. Nakajima, Y. Kawakita, K. Yamada, M. Arai, and M. Sato
Spin Fluctuation in YBaFe4O7+δ with Geometrically Frustrated Pyrochlore Lattice of Fe Spins
Journal of the Physical Society of Japan **84** 104711 (2015)

53 Y. Ikeda, D. Ueta, H. Yoshizawa, A. Nakao, K. Munakata, and T. Ohhara
Single-Crystal Neutron Diffraction Study of the Heavy-Electron Superconductor CeNiGe3
Journal of the Physical Society of Japan **84** 123701 (2015)

54 Y. Kobayashi, S. Kototani, K. Ohishi, M. Itoh, A. Hoshikawa, T. Ishigaki, and M. Sato
Identification of Various Coexisting Phases in Superconducting and Non-superconducting Samples of RbxFe2−ySe2
Journal of the Physical Society of Japan **84** 44710 (2015)

55 M. Futakawa
Targetry overview — Various target concepts and expectable next generation targets in power frontier applications —
JPS Conference Proceedings **8** 001002 (2015)

56 S. Harjo, T. Kawasaki, T. Hemmi, T. Ito, T. Nakamoto, and K. Aizawa
Thermal Strain in Superconducting Nb3Sn Strand at Cryogenic Temperature
JPS Conference Proceedings **8** 031001 (2015)

57 S. Hosokawa, J. Stellhorn, W.-C. Pilgrim, N. Boudet, N. Blanc, S. Kohara, H. Tajiri, H. Kato, Y. Kawakita, and T. Otomo
A Combination of Anomalous X-ray Scattering and Neutron Diffraction for Structural Characterizations of Zr45Cu45Ag10Metallic Glass
JPS Conference Proceedings **8** 31002 (2015)

58 K. Furuta, K. Mori, Y. Onodera, and T. Fukunaga
Local Structure of Lithium Ion Conducting Germanium Sulfide Glass: (Li2S)40(GeS2)60
JPS Conference Proceedings **8** 31004 (2015)

59 S. Harjo, T. Kawasaki, W. Gong, K. Aizawa, and T. Iwahashi
Metastable Austenitic Steel Deformation at Low Temperature
JPS Conference Proceedings **8** 031005 (2015)

60 H. Suzuki, K. Kusunoki, M. Kanematsu, A. Tasai, Y. Hatanaka, N. Tsuchiya, S. Bae, S. Shiroishi, S. Sakurai, T. Kawasaki, and S. Harjo
Application of Neutron Stress Measurement to Reinforced Concrete Structure
JPS Conference Proceedings **8** 031006 (2015)

61 K. Maruyama, Y. Arai, S. Sato, M. Sanada, T. Otomo, K. Suzuya, and K. Itoh
Neutron Diffraction Study of Isotope Enriched Glassy Sm4Ti9O24
JPS Conference Proceedings **8** 31007 (2015)

62 S. Tahara, Y. Kawakita, M. Nakamura, H. Shimakura, T. Kikuchi, Y. Inamura, K. Nakajima, S. Ohira-Kawamura, T. Sunakawa, and T. Fukami
Two Low-Energy Excitations in Superionic Conductors of RbAg4I5 and KAg4I5
JPS Conference Proceedings **8** 031008 (2015)

63 T. Kawasaki, S. Harjo, W. Gong, K. Aizawa, T. Iwahashi, Z. Shi, J. Li, Y. Tomota, and T. Ungár
Dislocation Characteristics of Martensitic Steel Studied by In-Situ Neutron Diffraction Experiment
JPS Conference Proceedings **8** 031009 (2015)

64 R. Kiyanagi, Y. Matsuo, T. Ohhara, T. Kawasaki, K. Oikawa, *et al.*
Phase Transition and Internal Crystal Structure of Superprotonic Conductor, Rb3-xKxH(SeO4)2
JPS Conference Proceedings **8** 31012 (2015)

65 Y. Onodera, H. Nakashima, K. Mori, T. Otomo, and T. Fukunaga
Structure and conductivity of Na-P-S superionic conducting glasses studied by neutron and X-ray diffraction
JPS Conference Proceedings **8** 31013 (2015)

66 Y. Su, K. Oikawa, T. Kawasaki, T. Kai, Y. Shiota, H. Sato, T. Shinohara, Y. Tomota, M. Harada, Y. Kiyanagi, and M. Arai
Microstructure and Residual Strain Distribution in Cast Duplex Stainless Steel Studied by Neutron Imaging
JPS Conference Proceedings **8** 31015 (2015)

67 D. S. Adipranoto, M. Yonemura, Y. Ishikawa, A. Hoshikawa, T. Ishigaki, T. Kamiyama, Y. Uchimoto, and Z. Ogumi
Crystal-Local Structure Analyses for Cathode LIBs LiNi1−xCoxO2(0 ≤x≤ 1) by Neutron Diffraction
JPS Conference Proceedings **8** 031017 (2015)

68 H. Arima, T. Kawamata, Y. Yokoyama, K. Sugiyama, and T. Otomo
Structural Study of Fe80B20 Amorphous Alloy by Anomalous X-ray Scattering Coupled with Neutron Diffraction
JPS Conference Proceedings **8** 31019 (2015)

69 K. Kino, M. Yonemura, Y. Ishikawa, and T. Kamiyama
Application of the J-PARC Neutron Beam to the Transmission Measurement for a Li Ion Battery during Charge and Discharge
JPS Conference Proceedings **8** 031021 (2015)

70 P. Xu, S. Harjo, T. Ito, Y. Morii, W. Gong, H. Suzuki, K. Akita, T. Suzuki, Y. Tomota, and L. Lutterotti
Progress in Bulk Texture Measurement Using Neutron Diffraction
JPS Conference Proceedings **8** 031022 (2015)

71 Y. Sakaguchi, H.hito Asaoka, Y. Uozumi, Y. Kawakita, T. Ito, M. Kubota, D. Yamazaki, K. Soyama, M. Ailavajhala, K. Wolf, M. Mitkova, and M. W. A. Skoda
Measurement of Transient Photo-Induced Changes in Thin Films at J-PARC — Time-Resolved Neutron Reflectivity Measurements of Silver Photo-Diffusion into Ge-Chalcogenide Films
JPS Conference Proceedings **8** 031023 (2015)

72 A. Hoshikawa, Y. Yoshida, T. Matsukawa, and T. Ishigaki
Structure Analysis of Propane Hydrates
JPS Conference Proceedings **8** 32001 (2015)

73 H. Abe, T. Takekiyo, M. Shigemi, Y. Yoshimura, S. Tsuge, T. Hanasaki, K. Ohishi, S. Takata, and J. Suzuki
Size-tunable confined water in a room temperature ionic liquid
JPS Conference Proceedings **8** 033001 (2015)

74 Y. Sekine, R. Kobayashi, S. Chi, J. A. Fernandez-Baca, K. Suzuya, F. Fujisaki, K. Ikeda, T. Otomo, T. Ikeda-Fukazawa, H. Yamauchi, and H. Fukazawa
Neutron Diffraction of Ice and Water in Hydrogels
JPS Conference Proceedings **8** 33009 (2015)

75 H. Fukazawa, M.i Arakawa, H. Yamauchi, Y. Sekine, R. Kobayashi, Y. Uwatoko, S. Chi, and J. A. Fernendez-Baca
Properties of Ferroelectric Ice
JPS Conference Proceedings **8** 033010 (2015)

76 K. Akutsu, H. Iwase, Y. Nakatani, and T. Yoshimura
Structural study of gold nanoparticle/surfactant complex by SANS, SAXS, TEM, and EXAFS Techniques
JPS Conference Proceedings **8** 033011 (2015)

77 H. Iwase, N. K. Kawano, K. Akutsu, and T. Yoshimura
SANS and SAXS studies on the aggregates properties of a Gemini-type amphiphilic dendrimer in solution
JPS Conference Proceedings **8** 33012 (2015)

78 K. Azuma, N. Hariyama, Y. Kamata, N. L. Yamada, N. Torikai, and M. Kawaguchi
Depth Distribution of Component for the Thin Films of Binary Polystyrene Blends with Different Molecular Weights
JPS Conference Proceedings **8** 033013 (2015)

79 K. Kodama, N. Igawa, S.-I. Shamoto, K. Ikeda, H. Ohshita, N. Kaneko, T. Otomo, K. Suzuya, A. Hoshikawa, and T. Ishigaki
Local Lattice Distortion Caused by Short-Range Charge Ordering in Transition Metal Oxides
JPS Conference Proceedings **8** 034002 (2015)

80 K. Amemiya, M. Sakamaki, M. Mizusawa, and M. Takeda
Magnetic Field Dependence of the Canted Spin Moment around the Interface between Ferromagnetic Ni and Antiferromagnetic FeMn Revealed by the Polarized Neutron Reflectivity
JPS Conference Proceedings **8** 34004 (2015)

81 S. Lee, Y. Ishikawa, P. Miao, S. Torii, and T. Kamiyama
Time of Flight Neutron Diffraction on NiO
JPS Conference Proceedings **8** 034007 (2015)

82 T. Ueno, K. Saito, N. Inami, T. Kojima, M. Mizuguchi, N. Miyata, K. Akutsu, M. Takeda, K. Takanashi, and K. Ono
Structural and Magnetic Depth Profile Analysis of L10 FeNi Film by Polarized Neutron Reflectometry
JPS Conference Proceedings **8** 034008 (2015)

83 T. Mochiku, Y. Hata, A. Hoshikawa, T. Ishigaki, H. Yasuoka, and K. Hirata
Crystal Structure of the Fe1−xSr2YCu2+xO6+δ Magnetic Superconductor
JPS Conference Proceedings **8** 34009 (2015)

84 A. Nakao, H. Nakao, K. Ohoyama, S. Torii, J. Zhang, T. Kamiyama, Y. Murakami, W. Kobayashi, and I. Terasaki
Magnetic and Crystal Structures of the Room Temperature Ferrimagnet Sr3YCo4O10.5
JPS Conference Proceedings **8** 034010 (2015)

85 S. Wakimoto, K. Ikeuchi, M. Arai, M. Fujita, R. Kajimoto, S. Kawamura, M. Matsuura, K. Nakajima, and K. Yamada
Neutron Scattering Study of Spin Fluctuations in La2−xSrxCuO4 by Four-Dimensional Mapping of Neutron Cross-Sections Using the 4SEASONS Chopper Spectrometer
JPS Conference Proceedings **8** 034013 (2015)

86 K. Hiroi, T. Shinohara, H. Hayashida, N. Wada, K. Oikawa, M. Harada, T. Kai, and M. Arai
Development of AC Magnetic Field Imaging Technique Using Polarized Pulsed Neutrons at J-PARC
JPS Conference Proceedings **8** 35001 (2015)

87 M. Harada, J. D. Parker, K. Oikawa, T. Kai, and T. Shinohara
Inner Observation of Canning Cadmium by Energy-Selective Neutron Imaging at NOBORU
JPS Conference Proceedings **8** 35002 (2015)

88 R. Kajimoto, M. Nakamura, Y. Inamura, K. Kamazawa, K. Ikeuchi, K. Iida, M. Ishikado, K. Nakajima, M. Harada, and M. Arai
Background Caused by Continuously Emitted High-Energy Neutrons at the Chopper Spectrometer 4SEASONS
JPS Conference Proceedings **8** 036001 (2015)

89 K. Oikawa, M. Harada, T. Shinohara, T. Kai, M. Ooi, and Y Kiyanagi
Custom-Made Shutter Block for Imaging Instrument "RADEN" at J-PARC
JPS Conference Proceedings **8** 036002 (2015)

90 N. L. Yamada, K. Mitamura, H. Sagehashi, N. Torikai, S. Sato, H. Seto, M. Furusaka, T. Oda, M. Hino, T. Fujiwara, M. Kobayashi, and A. Takahara
Development of Sample Environments for the SOFIA Reflectometer for Seconds-Order Time-Slicing Measurements
JPS Conference Proceedings **8** 036003 (2015)

91 K. Tomoyori, K. Kurihara, T. Tamada, and R. Kuroki
Evaluation of the Resolvable Capacity of Bragg Reflections for a New Diffractometer at J-PARC/MLF Designed for Protein Crystals with Large Unit Cells
JPS Conference Proceedings **8** 036004 (2015)

92 M. Segawa, M. Ooi, T. Kai, T. Shinohara, H. Satoh, and M. Kureta
Development of a Three-Dimensional Computed Tomography System using High-Speed Camera at a Pulsed Neutron Source
JPS Conference Proceedings **8** 36006 (2015)

93 M. Ooi, K. Sakai, A. Watanabe, A. Akutsu, S. Meigo, and H. Takada
Upgrade of Monitoring and Operation Systems for the MLF-GCS Base on EPICS and CSS
JPS Conference Proceedings **8** 036007 (2015)

94 H. Kira, H. Hayashida, H. Iwase, K. Ohishi, J. Suzuki, T. Oku, K. Sakai, K. Hiroi, S. Takata, T. Ino, K. Ohoyama, M. Ohkawara, T. Shinohara, K. Kakurai, K. Aizawa, and M. Arai
Demonstration study of small-angle polarized neutron scattering using polarized 3He neutron spin filter
JPS Conference Proceedings **8** 036008 (2015)

95 T. Oku, H. Hayashida, H. Kira, K. Sakai, K. Hiroi, T. Shinohara, Y. Sakaguchi, T. Ino, K. Ohoyama, L.-J. Chang, M. Nakamura, J. Suzuki, K. Aizawa, M. Arai, Y. Endoh, and K. Kakurai
Development of Compact Laser Optics for an In-Situ Spin-Exchange Optical Pumping 3He Neutron Spin Filter
JPS Conference Proceedings **8** 036009 (2015)

96 N. Suzuki, M. Katano, M. Yonemura, and T. Kamiyama
Optimization of Radial Collimators for a Powder Diffractometer SPICA
JPS Conference Proceedings **8** 036010 (2015)

97 M. Nakamura, Y. Kawakita, W. Kambara, K. Aoyama, R. Kajimoto, K. Nakajima, S. Ohira-Kawamura, K. Ikeuchi, T. Kikuchi, Y. Inamura, K. Iida, K. Kamazawa, and M. Ishikado
Oscillating Radial Collimators for the Chopper Spectrometers at MLF in J-PARC
JPS Conference Proceedings **8** 036011 (2015)

98 K. Ishizuka, T. Kai, T. Shinohara, M. Segawa, and K. Mochiki

Super-Resolution Processing for Pulsed Neutron Imaging System Using a High-Speed Camera
JPS Conference Proceedings **8** 36012 (2015)

99 T. Nakatani, Y. Inamura, T. Ito, and T. Otomo
The Control Software Framework of the Web Base
JPS Conference Proceedings **8** 036013 (2015)

100 K. Sakai, T. Oku, H. Hayashida, H. Kira, K. Hiroi, T. Ino, K. Ohoyama, M. Ohkawara, K. Kakurai, T. Shinohara, K. Oikawa, M. Harada, K. Aizawa, M. Arai, Y. Sakaguchi, and J. Suzuki
Development Status of the NMR System for the Polarized 3He Neutron Spin Filter (NSF) in the MLF at J-PARC
JPS Conference Proceedings **8** 36015 (2015)

101 T. Ohhara, R. Kiyanagi, K. Kaneko, I. Tamura, A. Nakao, *et al.*
Current Status of an Extreme Environment Single Crystal Neutron Diffractometer SENJU at J-PARC
JPS Conference Proceedings **8** 36018 (2015)

102 H. Ohshita, M. Ishiwata, K. Iwase, F. Fujisaki, S. Muto, S. Satoh, T. Seya, M. Sakaguchi, T. Otomo, K. Ikeda, N. Kaneko, and K. Suzuya
New Neutron Beam Monitor Based on GEM
JPS Conference Proceedings **8** 36019 (2015)

103 S. Takata, J. Suzuki, T. Shinohara, T. Oku, T. Tominaga, K. Ohishi, H. Iwase, T. Nakatani, Y. Inamura, T. Ito, K. Suzuya, K. Aizawa, M. Arai, T. Otomo, and M. Sugiyama
The design and q resolution of the small and wide angle neutron scattering instrument (TAIKAN) in J-PARC
JPS Conference Proceedings **8** 36020 (2015)

104 M. Arai, M. Futakawa, H. Takada, K. Haga, S. Meigo, Y. Miyake, M. Harada, K. Nakajima, R. Kajimoto, M. Nakamura, K. Suzuya, K. Shibata, J. Suzuki, S. Takata, T. Nakatani, Y. Inamura, T. Nakamura, T. Oku, K. Aizawa, K. Soyama, and Y. Kawakita
Present Status of the Materials and Life Science Experimental Facility of J-PARC
JPS Conference Proceedings **8** 036021 (2015)

105 K. Shibata, N. Takahashi , Y. Kawakita, M. Matsuura , T. Yamada, T. Tominaga, W. Kambara, M. Kobayashi, Y. Inamura, T. Nakatani, K. Nakajima, and M. Arai
The Performance of TOF near Backscattering Spectrometer DNA in MLF, J-PARC
JPS Conference Proceedings **8** 36022 (2015)

106 S. Satoh
Development of a New Exclusive Function for a 2012 Model 6Li Time Analyzer Neutron Detector System
JPS Conference Proceedings **8** 51001 (2015)

107 Y. Narukami, S. Miyajima, H. Shishido, A. Fujimaki, M. Hidaka, K. Oikawa, M. Harada, T. Oku, M. Arai, and T. Ishida
Signal from a Single Neutron by using Current-Biased Kinetic Inductance Detector made of Superconducting Nb Nanowire
JPS Conference Proceedings **8** 051003 (2015)

108 S. Miyajima, Y. Narukami, H. Shishido, N. Yoshioka, A. Fujimaki, M. Hidaka, K. Oikawa, M. Harada, T. Oku, M. Arai, and T. Ishida
Time-Dependent Flux from Pulsed Neutrons Revealed by Superconducting Nb Current-Biased Kinetic Inductance Detector with 10B Converter Operated at 4 K
JPS Conference Proceedings **8** 051004 (2015)

109 K. Haga, T. Naoe, T. Wakui, H. Kogawa, H. Kinoshita, and Masatoshi Futakawa
Thermal Hydraulic Design of a Double-walled Mercury Target Vessel
JPS Conference Proceedings **8** 051008 (2015)

110 D. Yamazaki, M. Nagano, R. Maruyama, H. Hayashida, K. Soyama, and K. Yamamura
Neutron Focusing by a Kirkpatrick–Baez Type Super-Mirror
JPS Conference Proceedings **8** 051009 (2015)

111 C. Ohmori, A. Koda, Y. Miyake, K. Nishiyama, K. Shimomura, A. Schnase, E. Ezura, K. Hara, K. Hasegawa, M. Nomura, T. Shimada, K. Takata, F. Tamura, M. Toda, M. Yamamoto, and M. Yoshii
High Temperature μSR Experiments for Accelerator Developments
JPS Conference Proceedings **8** 012025(1-5) (2015)

112 T. Osawa, K. Ninomiya, G. Yoshida, M. Inagaki, K. M. Kubo, N. Kawamura, and Y. Miyake
Elemental Analysis System with Negative-Muon Beam
JPS Conference Proceedings **8** 025003(1-6) (2015)

113 S. Kanda, M. Aoki, Y. Fukao, Y. Higashi, T. Higuchi, H. Iinuma, Y. Ikedo, K. Ishida, M. Iwasaki, R. Kadono, O. Kamigaito, D. Kawall, N. Kawamura, A. Koda, K. M. Kojima, K. Kubo, Y. Matsuda, T. Mibe, Y. Miyake, T. Mizutani, K. Nagamine, K. Nishiyama, T. Ogitsu, R. Okubo, N. Saito, K. Sasaki, K. Shimomura, P. Strasser, M. Sugano, M. Tajima, K. S. Tanaka, D. Tomono, H. A. Torii, E. Torikai, A. Toyoda, K. Ueno, Y. Ueno, M. Yoshida, and A. Yamamoto
Precision Measurement of Muonium Hyperfine Splitting at J-PARC and Integrated Detector System for High-Intensity Pulsed Muon Beam Experiment
JPS Conference Proceedings **8** 025006(1-6) (2015)

114 Y. Nakatsugawa, M. Aoki, D. Bryman, M. Ikegami, Y. Irie, S. Ito, N. Kawamura, M. Kinsho, H. Kobayashi, S. Makimura, H. Matsumoto, S. Meigo, T. Mibe, S. Mihara, Y. Miyake, H. Natori, H. Nishiguchi, T. Numao, C. Ohmori, S. Ritt, P. K. Saha, N. Saito, Y. Seiya, K. Shimizu, K. Shimomura, P. Strasser, Y. Takezaki, N. Teshima, N. D. Thong, N. M. Truong, K. Yamamoto, K. Yamamoto, and M. Yoshii
Silicon Carbide Target for a Muon-Electron Conversion Search at J-PARC MLF
JPS Conference Proceedings **8** 025013(1-5) (2015)

115 R. Kitamura, G. Beer, K. Ishida, M. Iwasaki, S. Kanda, H. Kawai, N. Kawamura, W. Lee, S. Lee, G. M. Marshall, Y. Matsuda, T. Mibe, Y. Miyake, S. Nishimura, Y. Oishi, S. Okada, A. Olin, M. Otani, N. Saito, K. Shimomura, P. Strasser, M. Tabata, D. Tomono, K. Ueno, and E. Won
Studies on Muonium Production from Silica Aerogel with Substructure for the Muon g-2/EDM Experiment
JPS Conference Proceedings **8** 025016(1-6) (2015)

116 H. A. Torii, H. A. Torii, M. Aoki, Y. Fukao, Y. Higashi, T. Higuchi, H. Iinuma, Y. Ikedo, K. Ishida, M. Iwasaki, R. Kadono, O. Kamigaito, S. Kanda, D. Kawall, N. Kawamura, A. Koda, K. M. Kojima, K. Kubo, Y. Matsuda, T. Mibe, Y. Miyake, T. Mizutani, K. Nagamine, K. Nishiyama, T. Ogitsu, R. Okubo, N. Saito, K. Sasaki, K. Shimomura, P. Strasser, M. Sugano, M. Tajima, K. S. Tanaka, D. Tomono, E. Torikai, A. Toyoda, K. Ueno, Y. Ueno, A. Yamamoto, and M. Yoshida
Precise Measurement of Muonium HFS at J-PARC MUSE
JPS Conference Proceedings **8** 025018(1-6) (2015)

117 M. Inagaki, K. Ninomiya, K. Fujihara, G. Yoshida, Y. Kasamatsu, M. K. Kubo, W. Higemoto, N. Kawamura, T. Nagatomo, Y. Miyake, T. Miura, and A. Shinohara
Muonic Atom Formation by Muon Transfer Process in C6H6 or C6H12 and CCl4 Mixtures
JPS Conference Proceedings **8** 033004(1-6) (2015)

118 K. Ninomiya, M. K. Kubo, P. Strasser, T. Nagatomo, Y. Kobayashi, K. Ishida, W. Higemoto, N. Kawamura, K. Shimomura, Y. Miyake, T. Suzuki, A. Shinohara, and T. Saito
Elemental Analysis of Bronze Artifacts by Muonic X-ray Spectroscopy
JPS Conference Proceedings **8** 033005(1-6) (2015)

119 A. D. Pant, Y. Sugawara, I. Yanagihara, G. P. Khanal, I. Shiraki, W. Higemoto, K. Shimomura, K. Ishida, F. L. Pratt, E. Torikai, and K. Nagamine
Hydration Effect on Electron Transfer in Cytochrome c Monitored by μSR

JPS Conference Proceedings **8** 033007(1-5) (2015)

120 S. Itoh, T. Yokoo, T. Masuda, H. Yoshizawa, M. Soda, Y. Ikeda, D. Kawana, T. J. Sato, Y. Nambu, K. Kuwahara, S. Yano, J. Akimitsu, Y. Kaneko, Y. Tokura, M. Fujita, M. Hase, K. Iwasa, H. Hiraka, T. Fukuda, K. Ikeuchi, K. Yoshida, T. Yamaguchi, K. Ono, and Y. Endoh
Science from the initial operation of HRC
JPS Conference Proceedings **8** 034001 (6 pages) (2015)

121 K. Ohishi, Y. Kousaka, E. Proskurina, T. Ogura, A. Koda, J. Akimitsu, and K. Inoue
Relation between Crystallographic and Magnetic Chiralities in a Chiral Helimagnet CsCuCl3
JPS Conference Proceedings **8** 034006(1-5) (2015)

122 T. U. Ito, W. Higemoto, K. Ninomiya, M. K. Kubo, N. Kawamura, and K. Shimomura
Online Monitoring of Negative Muon Beam Profiles at J-PARC MUSE using a Gated Image Intensifier
JPS Conference Proceedings **8** 036014(1-5) (2015)

123 M. Tampo, K. Hamada, N. Kawamura, M. Inagaki, T. U. Ito, K. M. Kojima, K. M. Kubo, K. Ninomiya, P. Strasser, G. Yoshida, and Y. Miyake
The Development of a Non-Destructive Analysis System with Negative Muon Beam for Industrial Devices at J-PARC MUSE
JPS Conference Proceedings **8** 036016(1-6) (2015)

124 T. Adachi, Y. Ikedo, K. Nishiyama, A. Yabuuchi, T. Nagatomo, P. Strasser, T. U. Ito, W. Higemoto, K. M. Kojima, S. Makimura, J. Nakamura, K. Shimomura, N. Kawamura, Y. Kobayashi, R. Kadono, Y. Miyake, and E. Torikai
Tuning of Ultra-Slow Muon Transport System
JPS Conference Proceedings **8** 036017(1-4) (2015)

125 S. Makimura, N. Kawamura, S. Onizawa, Y. Matsuzawa, M. Tabe, Y. Kobayashi, R. Shimizu, H. Fujimori, Y. Ikedo, R. Kadono, A. Koda, K. M. Kojima, K. Nishiyama, J. Nakamura, K. Shimomura, P. Strasser, M. Aoki, Y. Nakatsugawa, and Y. Miyake
Present Status of Muon Production Target at J-PARC/MUSE
JPS Conference Proceedings **8** 051002(1-8) (2015)

126 T. Hirata, H. Matsuno, D. Kawaguchi, T. Hirai, N. L. Yamada, M. Tanaka, and K. Tanaka
Effect of Local Chain Dynamics on a Bioinert Interface
Langmuir **31** 3661 (2015)

127 Y. Oda, D. Kawaguchi, T. Hirata, N. L. Yamada, S. Kanaoka, S. Aoshima, and K. Tanaka
Density Profiles of Well-Defined Poly(methyl 2-propenyl ether) (PMPE) Near Water Interface
Macromol. Symp. **350** 99 (2015)

128 F. Chen, D. Peng, Y. Ogata, K. Tanaka, Z. Yang, Y. Fujii, N. L. Yamada, C.-H. Lam, and O. K. C. Tsui
Confinement Effect on the Effective Viscosity of Plasticized Polymer Films
Macromolecules **48** 7719 (2015)

129 Z. M. Shi, W. Gong, Y. Tomota, S. Harjo, J. Li, B. Chi, and J. Pu
Study of tempering behavior of lath martensite using in situ *neutron diffraction*
Materials Characterization **107** 29-32 (2015)

130 C. I. Cheon, H. W. Joo, K. W. Chae, J. S. Kim, S. H. Lee, S. Torii, and T. Kamiyama
Monoclinic ferroelectric NaNbO3 at room temperature: Crystal structure solved by using super high resolution neutron powder diffraction
Materials Letters **156** 214-219 (2015)

131 Z. Shi, Y. Tomota, S. Harjo, Y. Su, B. Chi, J. Pu, and L. Jian
Effect of non-isothermal deformation of austenite on ferrite transformation behavior studied by in-situ neutron diffraction
Materials Science and Engineering:A **631** 153-159 (2015)

132 H. Sato, T. Sato, Y. Shiota, T. Kamiyama, A. S. Tremsin, M. Ohnuma, and Y. Kiyanagi
Relation between Vickers Hardness and Bragg-Edge Broadening in Quenched Steel Rods Observed by Pulsed Neutron Transmission Imaging
Materials Transactions **56** 1147 (2015)

133 Y. Nii, T. Nakajima, A. Kikkawa, Y. Yamasaki, K. Ohishi, J. Suzuki, Y. Taguchi, T. Arima, Y. Tokura, and Y. Iwasa
Uniaxial stress control of skyrmion phase
Nature Communications **6** 8539 (2015)

134 M. Segawa, M. Ooi, T. Kai, T. Shinohara, M. Kureta, K. Sakamoto, and T. Imaki
Development of a pulsed neutron three-dimensional imaging system using a highly sensitive image-intensifier at J-PARC
Nuclear Instruments and Methods in Physics Research A **769** 97 (2015)

135 H. Hasemi, M. Harada, T. Kai, T. Shinohara, M. Ooi, H. Sato, K. Kino, M. Segawa, T. Kamiyama, and Y. Kiyanagi
Evaluation of nuclide density by neutron resonance transmission at the NOBORU instrument in J-PARC/MLF
Nuclear Instruments and Methods in Physics Research A **773** 137 (2015)

136 T. Nakamura, K. Toha, T. Kawasaki, M. Ebine, A. Birumachi, K. Sakasai, and K. Soyama
A two-dimensional scintillation-based neutron detector with wavelength-shifting fibers and incorporating an interpolation method
Nuclear Instruments and Methods in Physics Research A **784** 202 (2015)

137 M. Hino, T. Oda, M. Kitaguchi, N. L. Yamada, S. Tasaki, and Y. Kawabata
The ion beam sputtering facility at KURRI: Coatings for advanced neutron optical devices
Nuclear Instruments and Methods in Physics Research A **797** 265 (2015)

138 T. Hattori, A. Sano-Furukawa, H. Arima, K. Komatsu, A. Yamada, Y. Inamura, T. Nakatani, Y. Seto, T. Nagai, W. Utsumi, T. Iitaka, H. Kagi, Y. Katayama, T. Inoue, T. Otomo, K. Suzuya, T. Kamiyama, M. Arai, and T. Yagi
Design and performance of high-pressure PLANET beamline at pulsed neutron source at J-PARC
Nuclear Instruments and Methods in Physics Research A **780** 55-67 (2015)

139 Y. Arimoto, N. Higashi, Y. Igarashi, Y. Iwashita, T. Ino, R. Katayama, R. Kitahara, M. Kitaguchi, H. Matsumura, K. Mishima, N. Nagakura, H. Oide, H. Otono, R. Sakakibara, T. Shima, H. M. Shimizu, T. Sugino, N. Sumi, H. Sumino, K. Taketani, G. Tanaka, M. Tanaka, K. Tauchi, A. Toyoda, T. Tomita, T. Yamada, S. Yamashita, H. Yokoyama, and T. Yoshioka
Development of time projection chamber for precise neutron lifetime measurement using pulsed cold neutron beams
Nuclear Instruments and Methods in Physics Research A **799** 187–196 (2015)

140 T. Hirata, H. Matsuno, D. Kawaguchi, N. L. Yamada, M. Tanaka, and K. Tanaka
Effect of interfacial structure on bioinert properties of poly(2-methoxyethyl acrylate)/poly(methyl methacrylate) blend films in water
Physical Chemistry Chemical Physics **17** 17399 (2015)

141 K. Mori, K. Enjuji, S. Murata, K. Shibata, Y. Kawakita, M. Yonemura, Y. Onodera, and T. Fukunaga

Direct Observation of Fast Lithium-Ion Diffusion in a Superionic Conductor: Li7P3S11 Metastable Crystal
Physical Review Applied **4** 054008 (2015)

142 S. Hayashida, M. Soda, S. Itoh, T. Yokoo, K. Ohgushi, D. Kawana, H. M. Rønnow, and T. Masuda
Magnetic model in multiferroic NdFe3(BO3)4 investigated by Inelastic Neutron Scattering
Physical Review B **92** 054402 (9 pages) (2015)

143 I. Yamauchi, K. Nawa, M. Hiraishi, M. Miyazaki, A. Koda, K. M. Kojima, R. Kadono, H. Nakao, R. Kumai, Y. Murakami, H. Ueda, K. Yoshimura, and M. Takigawa
Structural anomalies and short-range magnetic correlations in the orbitally degenerate system Sr2 VO4
Physical Review B **92** 064408(1-7) (2015)

144 K. Shimomura, R. Kadono, A. Koda, K. Nishiyama, and M. Mihara
Electronic structure of Mu-complex donor state in rutile TiO2
Physical Review B **92** 075203(1-6) (2015)

145 T. U. Ito, W. Higemoto, A. Sakai, M. Tsujimoto, and S. Nakatsuji
Perturbation on hyperfine-enhanced 141Pr nuclear spin dynamics associated with antiferroquadrupolar order in PrV2Al20
Physical Review B **92** 125151(1-5) (2015)

146 I. Umegaki, H. Tanaka, N. Kurita, T. Ono, M. Laver, C. Niedermayer, C. R üegg, S. Ohira-Kawamura, K. Nakajima, and K. Kakurai
Spinon, soliton, and breather in the spin-1/2 antiferromagnetic chain compound KCuGaF6
Physical Review B **92** 174412 (2015)

147 M. Hase, K. Nakajima, S. Ohira-Kawamura, Y. Kawakita, T. Kikuchi, and M. Matsumoto
Magnetic excitations in the spin-1/2 tetramer substance Cu2 114Cd11B2O6 obtained by inelastic neutron scattering experiments
Physical Review B **92** 184412 (2015)

148 T. Katabuchi, T. Matsuhashi, K. Terada, M. Igashira, M. Mizumoto, K. Hirose, A. Kimura, N. Iwamoto, K. Y. Hara, H. Harada, J.-i. Hori, T. Kamiyama, K. Kino, F. Kitatani, Y. Kiyanagi, S. Nakamura, and Y. Toh
Misassigned neutron resonances of Nd-142 and stellar neutron capture cross sections
Physical Review C **91** 37603 (2015)

149 K. Kino, M. Yonemura, Y. Kiyanagi, Y. Ishikawa, J. D. Parker, T. Tanimori, and T. Kamiyama
First Imaging Experiment of a Lithium Ion Battery by a Pulsed Neutron Beam at J-PARC/MLF/BL09
Physics Procedia **69** 612-618 (2015)

150 S. Hayashida, M. Soda, S. Itoh, T. Yokoo, K. Ohgushi, D. Kawana, and T. Masuda
Inelastic neutron scattering on multiferroics NdFe3(BO3)4
Physics Procedia **75** 127 -133 (2015)

151 K. Iwasa, A. Yonemoto, S. Takagi, S. Itoh, T. Yokoo, S. Ibuka, C. Sekine, and H. Sugawara
Nd-ion substitution effect on f-electron multipole order of PrRu4P12
Physics Procedia **75** 179 -186 (2015)

152 H. Lee, S. Jo, T. Hirata, N. L. Yamada, K. Tanaka, E. Kim, and D. Y. Ryu
Interpenetration of Chemically Identical Polymer onto Grafted Substrates
Polymer **74** 70 (2015)

153 T. Hirata, H. Matsuno, D. Kawaguchi, N. L. Yamada, M. Tanaka, and T. Tanaka
Construction of a blood-compatible interface based on surface segregation in a polymer blend
Polymer **78** 219 (2015)

154 Z. Xiong, T. Naoe, T. Wan, M. Futakawa, and K. Maekawa
Mechanical Property Change in the Region of Very High-cycle Fatigue
Procedia Engineering **101** 552-560 (2015)

155 Y. Nakatsugawa
Search for muon to electron conversion at J-PARC MLF : Recent status on DeeMe
PROCEEDINGS of SCIENCE(NUFACT2014) 93 (2015)

156 K. Akutsu, M. Sahara, N. Miyata, T. Niizeki, S. Nagayama, Y. Hasegawa, A. Shimomura, and M. Yoshii
Study of a Corrosion Resistant Coating Layer for Metal Magnetic Cores Using Neutron Reflectometry
Proceedings of the 12th Annual Meeting of Particle Accelerator Society of Japan 72-76 (2015)

157 S. Makimura, *et al.*
PRESENT STATUS OF MUON ROTATING TARGET AT J-PARC/MUSE
Proceedings of the 12th Annual Meeting of Particle Accelerator Society of Japan 261-264 (2015)

158 K. Terada, T. Katabuchi, M. Mizumoto, T. Arai, T. Saito, M. Igashira, K. Hirose, S. Nakamura, A. Kimura, H. Harada, J. Hori, K. Kino, and Y. Kiyanagi
Measurement of neutron capture cross sections of Pd-107 at J-PARC/MLF/ANNRI
Progress in Nuclear Energy **82** 118-121 (2015)

159 S. Ajimura, *et al.*
On-site background measurements for the J-PARC E56 experiment: A search for the sterile neutrino at J-PARC MLF
Progress of Theoretical and Experimental Physics **6** 063C01 (2015)

160 D. Payra, M. Naito, Y. Fujii, N. L. Yamada, S. Hiromoto, and A. Singh
Bioinspired adhesive polymer coatings for efficient and versatile corrosion resistance
RSC Advances **5** 15977 (2015)

161 A. Nakamura, T. Ishida, K. Kusaka, T. Yamada, S. Fushinobu, I. Tanaka, S. Kaneko, K. Ohta, H. Tanaka, K. Inaka, Y. Higuchi, N. Niimura, M. Samejima, and K. Igarashi
"Newton's cradle" proton relay with amide–imidic acid tautomerization in inverting cellulase visualized by neutron crystallography
Science Advances **1** e1500263 (2015)

162 N. Funamori, K. M. Kojima, D. Wakabayashi, T. Sato, T. Taniguchi, N. Nishiyama, T. Irifune, D. Tomono, T. Matsuzaki, M. Miyazaki, M. Hiraishi, A. Koda, and R. Kadono
Muonium in Stishovite: Implications for the Possible Existence of Neutral Atomic Hydrogen in the Earth's Deep Mantle
Scientific Reports **5** 8437(1-5) (2015)

163 K. Mori, K. Furuta, Y. Onodera, K. Iwase, and T. Fukunaga
Three-dimensional structures and lithium-ion conduction pathways of (Li2S)x(GeS2)100−x superionic glasses
Solid State Ionics **280** 44-50 (2015)

164 K. Osamura, S. Machiya, S. Harjo, T. Nakamoto, N. Cheggour, and A. Nijhuis
Local strain exerted on Nb 3 Sn filaments in an ITER strand
Superconductor Science and Technology **28** 45016 (2015)

Editorial Board - MLF Annual Report 2015

Chief Editor
Toshiki Asai
CROSS-Tokai

Kaoru Sakasai
Neutron Instrumentation Section

Shin-ichiro Meigo
Facility and Application Development Section

Takashi Naoe
Neutron Source Section

Asami Sano-Furukawa
Neutron Science Section

Kenji Mishima
Neutron Science Section

Kenji M. Kojima
Muon Science Section

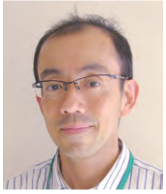

Naritoshi Kawamura
Muon Science Section

Kenichi Funakoshi
CROSS-Tokai

Taiki Tominaga
CROSS-Tokai

Kazuhiko Ikeuchi
CROSS-Tokai

J-PARC

JAPAN PROTON ACCELERATOR RESEARCH COMPLEX

High Energy Accelerator Research Organization (KEK)
Japan Atomic Energy Agency (JAEA)

---

http://j-parc.jp/

Materials and Life Science Division
J-PARC Center

http://j-parc.jp/MatLife/

CROSS

Comprehensive Research Organization for Science and Society
http://www.cross-tokai.jp/

J-PARC 17-01